TELAC REPORT 96-13

HIGH TEMPERATURE DEGRADATION MECHANISMS IN POLYMER MATRIX COMPOSITES

Ronan A. Cunningham
Research Assistant

December, 1996

HIGH TEMPERATURE DEGRADATION MECHANISMS IN POLYMER MATRIX COMPOSITES

by

Ronan A. Cunningham

Submitted to the Department of Aeronautics and Astronautics on December 23, 1996 in partial fulfillment of the requirements for the Degree of Master of Science in Aeronautics and Astronautics

ABSTRACT

Polymer matrix composites are increasingly used in demanding structural applications in which they may be exposed to harsh environments. The durability of such materials is a major concern, potentially limiting both the integrity of the structures and their useful lifetimes. The goal of the current investigation is to develop a mechanism-based model of the chemical degradation which occurs, such that given the external chemical environment and temperatures throughout the laminate, laminate geometry, and ply and/or constituent material properties, we can calculate the concentration of diffusing substances and extent of chemical degradation as functions of time and position throughout the laminate. This objective is met through the development and use of analytical models, coupled to an analysis-driven experimental program which offers both quantitative and qualitative information on the degradation mechanism. Preliminary analyses using a coupled diffusion/reaction model are used to gain insight into the physics of the degradation mechanisms and to identify crucial material parameters. An experimental program is defined based on the results of the preliminary analysis which allows the determination of the necessary material coefficients. Thermogravimetric analyses are carried out in nitrogen, air, and oxygen to provide quantitative information on thermal and oxidative reactions. Powdered samples are used to eliminate diffusion effects. Tests in both inert and oxidative environments allow the separation of thermal and oxidative contributions to specimen mass loss. The concentration dependency of the oxidative reactions is determined from the tests in pure oxygen. Short term isothermal tests at different temperatures are carried out on neat resin and unidirectional macroscopic specimens to identify diffusion effects. Mass loss, specimen shrinkage, the formation of degraded surface layers and surface cracking are recorded as functions of exposure time. Geometry effects in the neat resin, and anisotropic diffusion effects in the composites, are identified through the use of specimens with different aspect ratios. The data is used with the model to determine reaction coefficients and effective diffusion coefficients. The empirical and analytical correlations confirm the preliminary model results which suggest that mass loss at lower temperatures is dominated by oxidative reactions and that these reaction are limited by diffusion of oxygen from the surface. The mechanism-based model is able to successfully capture the basic physics of the degradation phenomena under a wide range of test conditions. The analysis-based test design is successful in separating out oxidative, thermal, and diffusion effects to allow the determination of material coefficients. This success confirms the basic picture of the process; however, a more complete understanding of some aspects of the physics are required before truly predictive capability can be achieved.

Thesis Supervisor: Hugh L. McManus
Title: Class of 1943 Assistant Professor
Department of Aeronautics and Astronautics
Massachusetts Institute of Technology

ACKNOWLEDGMENTS

While there is only one name underneath the title on the first page of this thesis, a multitude of people contributed in one way or another to producing what you have in your hands. First, I would like to thank my advisor Prof. Hugh McManus for giving me the opportunity to come to MIT and work with people whose knowledge of the areas they work in is unparalleled, and whose levels of interest, enthusiasm and commitment to their work is something that everyone should aspire to. Hugh is one of those unique people who are engineers in the true sense of the word, with a wealth of knowledge on a tremendous number of aspects of engineering, a real intuitive sense of what is going on, and communication skills which can allow anybody (even me) to understand highly complex ideas. The knowledge I gained from Hugh over the last two and a half years goes far beyond what you will see in this thesis and his guidance is greatly appreciated.

I would also like to thank Paul, Mark and Prof. Dugundji for all their input during my presentations and for making sure that I never got away with anything that wasn't up to par. Special thanks to Mark for insisting that everyone who took his class had to pronounce the word "composites" properly - between both our efforts we're finally making some progress. I think "tomato" should be next on our list. Thanks to Ping for all her help in dealing with the four hundred requisition forms (filled out in triplicate, approved by a purchasing committee, signed by the pope, and folded exactly three times along the length) that you have to submit to buy a box of staples at MIT. Many thanks to Deb for helping me to keep track of Hugh's movements (and believe me, that in itself is a full time job) and for keeping me company while I waited outside Hugh's office for hours, and hours, and hours.....

One person who deserves a huge amount of credit for every piece of research that has come out of TELAC, and this thesis is no exception, is Al Supple. Al is the epitome of a gentleman, has the patience of a saint, is always ready to help, and knows more about manufacturing and testing than the rest of the lab put together. I would also like to thank Lenny Rigione for letting me use, and eventually break, a huge variety of test equipment which greatly assisted this work. Thanks also to all my UROPers – Greg, Sean and in

particular Jim (who always managed to squeeze me into his busy sleeping schedule) – who are responsible for a huge amount of the work shown here.

As is the case with everyone who goes to grad school here, the people you learn most from are the other grad students you work, eat, drink, and complain with. And we're not just talking about school here. While everyone in TELAC is great there are a few people who really made my time here worthwhile. Huge thanks to my office mates and drinking buddies, Mark (a.k.a. the Norm Peterson of the Cambridgeport Saloon) and Brian, who were initially very disappointed to find out that Ronan is in fact the name of a fella and not a girl, but who (after much debate) decided to let me stay anyway and canceled their request to have me replaced with a member of the fairer sex. It was fun, boys. I can't think of two other people, at least not of the male persuasion, who I would rather have to work on problem sets and research with until all of hours of the night, seven days a week, fifty two weeks a year..... Hang on, did I just say it was fun? Big thanks also to Bethany, my perennial lunch date, who's still trying to convince me that a good diet and exercise are in fact conducive to good health. Sounds dodgy to me - hey, pass the double-cheese pizza, and don't knock over my beer while you're doing it. Cheers to Mongo, who was always good for a laugh, and Hari, who's basically a really nice guy underneath that wild and crazy exterior.

Finally I want to thank my parents who have supported me completely throughout my time here, as they have done with everything else I have ever been involved in, and who never once complained about having to listen to me rant on about the seemingly never ending problems with my research during our weekly phone calls. Couldn't have done it without you.

FOREWORD

This work was conducted in the Technology Laboratory for Advanced Composites (TELAC) in the Department of Aeronautics and Astronautics at the Massachusetts Institute of Technology. This work was sponsored by the National Science Foundation under NSF Grant 9257612-CMS, and the NASA Lewis Research Center under NASA Grants NAG3-1760 and NAG3-1893.

TABLE OF CONTENTS

LIST OF FIGURES

LIST OF TABLES

NOMENCLATURE

A	total surface area
A_i	area of surface i
b	mass loss metric
c_{ox}	relative concentration of oxygen
c_s	relative concentration of species s
C	diffusivity exponential constant
C_{ij}	anisotropic diffusivity exponential constant
D	diffusion coefficient
D_{ij}^s	anisotropic diffusivity tensor
D_o	pre-exponential diffusivity constant
D_z^{ox}	through-thickness oxygen diffusivity
$\left(D_{ij}\right)_o$	anisotropic pre-exponential diffusivity constant
E_i	activation energy of reaction acting on component i
E_{ij}	activation energy of reaction j acting on component i
F	rate of transfer of diffusing substance per unit area
$F'(T)$	temperature-dependence function
$F(\alpha_i)$	conversion-dependence function for component i
h	half-thickness of specimen
I	Kissinger plot intercept
k_i	rate constant for reaction acting on component i
k_{ij}	rate constant for reaction j acting on component i

l	specimen length
m_f	final mass of unreacting mass fractions
m_i	mass lost due to completion of reactions on component i
m_{ij}	concentration-dependency of reaction j acting on component i
m_o	original mass of material in an infinitesimal control volume
m_{si}	concentration-dependency of reaction acting on species s
m_{fi}	final mass of component i
m_{oi}	original mass of component i
n_i	order of reaction acting on component i
n_{ij}	order of reaction i acting on component i
N	number of data points
N_q	number of heating rates
P	pressure
Q	heating rate
r_i	rate of consumption of oxygen by reactions on component i
r_{ox}	total rate of consumption of oxygen
r_s	rate of consumption of species s
R	real gas constant
R_i	oxygen consumption constant for reactions on component i
S_i	surface i
t	time
T	absolute temperature
V	specimen volume

V^k	volume contained inside node k
w	specimen width
y_i	mass fraction of component i
z	distance from exposed surface
α_i	mass loss metric for component i
α_{ij}	mass loss metric for reaction j acting on component i
Δm	total mass lost from control volume
$\Delta m'$	normalized mass lost from control volume
Δm_i	mass lost from component i
ΔM	total mass lost from volume V
ΔM^k	mass loss at node k
ΔM_i	mass loss per unit surface area through surface i
Δz	finite difference grid spacing
σ_i	standard deviation at data point i
τ	diffusion time through thickness h
χ^2	cost function
χ_j^2	cost function evaluated at heating rate j
χ_{total}^2	mean cost function for all heating rates
ζ	normalized ratio of chemical reaction rate to diffusion rate

CHAPTER 1

INTRODUCTION

As a result of the growing need for high-strength, low-density, high temperature materials in the aerospace industry, composite materials are increasingly used in demanding structural applications in which they may be exposed to harsh environmental conditions. High temperatures, thermal cycling and exposure to moisture, oils, and solvents all significantly accelerate the degradation of polymer matrix composites (PMCs). Hence, the durability of such materials is a major concern, potentially limiting both the integrity of the structures and their useful lifetimes. In fact, the durability of these materials in the use environment may ultimately be the limiting factor in such applications as engine supports and cowlings, reusable launch vehicle components, and primary and secondary structures in high speed aircraft. The proposed High Speed Civil Transport (HSCT) is one example of an application with an extreme environment. The expected thermal environment of the Mach 2.4 HSCT includes maximum skin temperatures between 120°C and 150°C (248°F and 302°F) on the majority of the surfaces, and leading edge temperatures as high as 177°C (350°F). These temperatures will be sustained for 75% of the flight, corresponding to the supersonic cruise portion of the flight profile. Lifetimes for the HSCT are required to have in excess of 60,000 hours of flight time if the program is to be economically viable.

Programs such as the HSCT have resulted in a growing need within

the aerospace industry for PMCs which have upper use temperatures in excess of 150°C. This has led to a concerted effort to develop suitable matrix materials. Candidate materials must possess good mechanical properties over a wide temperature range and be capable of withstanding large fluctuations in temperature. The materials must also be chemically resistant to the degrading environment, demonstrating a low mass loss at extended aging times at their upper use temperatures. Coupled with the development of these new materials is the need to understand and quantify the effects of long term exposure to the use environments.

Presently, the performance of PMCs under continuous thermal exposure is still poorly understood. Observed effects of prolonged exposure of matrix materials to elevated temperatures include specimen mass loss, specimen shrinkage, the development of a severely degraded surface layer, the development of surface microcracks, and the degradation of mechanical properties. In the case of composite materials, the problem is further complicated by the anisotropy of the material. For instance, neat resin will experience only external cracking while cracks also form at fiber/matrix interfaces in unidirectional and general composite laminates. General composite laminates also experience thermally (or mechanically) induced intraply microcracks in the matrix material. Cracks can then provide new pathways into the interior of the material for the external environment, resulting in more severe degradation of the laminate as a whole.

The interaction of these effects during the aging period results in a highly complex, coupled problem where the identification of individual mechanisms and their contributions becomes extremely difficult. It has been found that even comparatively simple tests of materials subjected to environmentally-induced degradation are difficult to interpret. The observed

spatially non-uniform degradation results in specimens which have non-uniform chemical and mechanical states. This makes reduction of measurable specimen responses (such as failure loads and total mass losses) to desired material properties (such as failure stresses and local mass losses) very difficult.

Design of high temperature structures would be greatly improved through the development of a model which could incorporate known quantities such as laminate geometry, material properties, temperatures and chemical environment, and from these determine quantities such as the material degraded state as functions of exposure time and position within the material. A schematic of the desired coupled analysis which could provide this capacity is shown in Figure 1.1. The analysis consists of several individual modules which address different aspects of the problem. Inputs to the model include the exposure environment and the applied mechanical loads. For a comprehensive analysis, it is necessary to calculate the thermal response, diffusion and reaction chemistry, and the thermo-mechanical response of the system from the input variables. The thermal analysis supplies the diffusion and reaction chemistry model with the necessary temperatures. This module can then provide the thermo-mechanical analysis with predictions of the chemical state within the material. Results from these analyses can then be used to determine whether damage (and ultimately failure) occurs. The effects of damage on material properties, thermal response and the reaction chemistry is accounted for in an incremental fashion, allowing a truly coupled representation of the problem.

Several modules of this proposed analysis scheme are already quite well developed. For instance, temperatures may be calculated given the thermal environment and material properties, and the thermo-mechanical

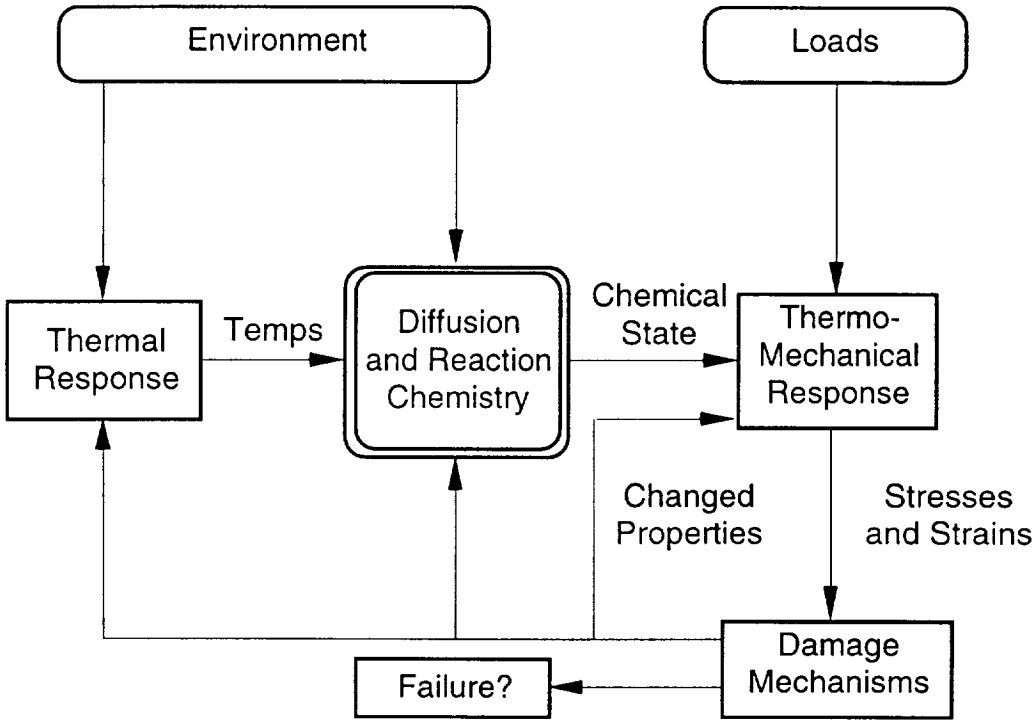

Figure 1.1 Desired coupled analysis

response may be predicted when the loads and material properties (at each point within the system) are known, using standard methods. However, the current limited understanding of the diffusion and reaction chemistry involved in the degradation of composites represents a weak link in this framework and needs to be addressed.

The goal of the current research is to establish an analytical methodology which can be used to predict the degradation states at all points within a composite laminate as functions of exposure time and environment. The analysis uses Arrhenius reaction kinetics to model the chemical reactions which occur within the material, while Fickian diffusion solutions are used to model the diffusion of the external environment into the material. Multiple, simultaneously occurring chemical reactions, including both purely thermal reactions and reactions that depend on diffusing substances, are taken into account. The concentration of diffusing substances and the degradation state of the material are predicted as functions of exposure time and location within the material. The analysis is integrated into a computer code which allows calculations to be performed for any user-defined thermal environment.

Preliminary studies were carried out using a one-dimensional diffusion model and a single concentration-dependent reaction. Extensive parametric studies were performed to examine trends predicted by the model and to establish the relative importance of material coefficients in generating accurate predictions for the degraded state of the material. Initial results from these studies, and previous experimental work, suggest that the degradation of PMCs in oxidative environments is controlled by the diffusion of oxygen into the material from the external environment.

Experimental studies were carried out to quantify crucial material

coefficients and to verify the analysis at each stage. Both PMR-15 neat resin and its composites were studied. Comprehensive dynamic heating thermogravimetric analyses (TGAs) were carried out on finely ground neat resin powders in both thermal and oxidative environments. The use of finely ground powders, which have very large surface area to volume ratios, effectively eliminated the dominance of diffusion effects witnessed in finite-sized specimens. Mass losses and mass loss rates were measured and the required chemical reaction coefficients for the model were determined from the data.

Short-term isothermal tests were also carried out on rectangular neat resin and unidirectional composite macroscopic specimens. Samples which had different aspects ratios in each of the three principal directions were used to quantify the anisotropic nature of degradation. Mass losses and dimensional changes were recorded, as was the growth of degraded surface layers and the initiation and propagation of surface cracks. Neat resin diffusion coefficients and estimates of the diffusion in each of the principal directions in composites, were determined through the use of this data and the knowledge of the reaction coefficients gained from the TGA studies. The experimentally determined material coefficients were incorporated into the analytical model.

The thermogravimetric data collected for PMR-15 under a wide variety of conditions provided an understanding of the degradation mechanisms and allowed the development of chemical reaction models which provided accurate predictions under the test conditions. Collection of data from macroscopic specimens allowed the modeling of effective diffusion coefficients for the diffusion of oxygen into finite-sized specimens. This data also provided a large amount of qualitative and quantitative information on the

anisotropic effects which occur in unidirectional specimens. Through this study, a framework for a comprehensive predictive model has been developed. Some issues still remain unresolved, in particular the confident extrapolation of the models developed here to use conditions, and these need to be addressed before a comprehensive predictive model can be developed.

Previous work relevant to the current research is described in Chapter 2. This includes analytical and experimental studies on the degradation of high temperature PMCs as well as a background on the analytical chemistry used in the course of this work. The problem statement and approach for the current research is presented in Chapter 3. The analytical methodology is developed in Chapter 4. Chapter 5 describes the experimental procedures which were used to measure required material coefficients. Experimental results, as well as correlations between experimental data and model predictions, and parametric studies are presented and discussed in Chapter 6. Finally, conclusions and recommendations for future work are presented in Chapter 7.

CHAPTER 2

BACKGROUND

The potential advantages of high temperature polymer matrix composites for applications in the aerospace industry have long been recognized. However, the performance of these materials is limited by their durability. Traditional polymers are highly vulnerable to thermal and oxidative degradation, and exhibit a rapid decrease in structural integrity, when exposed to high temperatures for extended periods of time. This has resulted in a need for polymers that are resistant to chemical attack and capable of maintaining their mechanical properties when exposed to these conditions. Extensive research in the field of polymer chemistry in recent years has led to the development of several candidate materials which possess the required mechanical properties and thermo-oxidative stability characteristics [1-4]. However, while these materials offer significant advantages over the previous generation of polymers, they are still subject to degradation over long periods of time at elevated temperatures.

Extensive experimental studies have been carried out on neat resin and fiber-reinforced composite materials to identify, and qualitatively describe, the effects of long term exposure at elevated temperatures. More recent empirical work has concentrated on trying to quantify these mechanisms and correlating their effects with changes in material properties. However, most studies to date have only dealt with the problem on a qualitative level with little effort being devoted to sufficiently quantifying the

phenomena so that accurate analytical models may be developed. Current analytical work primarily consists of empirical data fits, which allow trends to be captured for particular sets of experimental data, rather than mechanism-based modeling of the observed phenomena. As a result, while case-specific models of high-temperature degradation have been developed, the need for a truly quantitative, mechanistic-based predictive tool still exists.

In this chapter, the experimental studies relevant to the problem will be reviewed. A brief review of current analytical approaches is included for the purposes of background. As a considerable amount of the work presented in this thesis deals with an attempt to quantify the degradation phenomenon at a chemical level, relevant studies in the area of polymer chemistry will also be discussed. For the purposes of clarity, a summary of the implications of the previous work, in terms of an engineering understanding of the problem, is presented at the end of the chapter.

2.1 PREVIOUS EXPERIMENTAL STUDIES

There is extensive literature available on the behavior of macroscopic neat resin and composite samples undergoing long term degradation. Mass loss, shrinkage, and changes in thermal, mechanical and viscoelastic behavior have been reported. Various investigations have studied the effects of aging on neat resin [5, 6], bare fibers [7-10] and composite materials [7-16]. Only limited correlation exists between individual studies.

A study by Bowles [6] on the effects of aging on neat PMR-15 resin revealed that several coupled mechanisms proceed simultaneously in the early stages of degradation at elevated temperatures in air. Samples exposed for up to 3000 hours at temperatures ranging between 288°C and 343°C

exhibited mass loss, specimen shrinkage, the formation of a distinct surface layer, development of surface microcracks and the degradation of mechanical properties. Mass loss occurs throughout the duration of the aging periods observed, and in the presence of oxygen results in the formation of a distinctive thin layer on the exposed surfaces of the polymer. This layer progresses inwards to the core of the material as aging time increases. Through analysis of aged specimens by X-ray diffraction (XD) scans and infrared scanning microprobes (IRSM), it was determined that the surface layer formed in this manner exhibits a different chemical composition to that of the core material [6, 17]. Voids develop within the surface layer and increase in size and density over time, acting as starter points for cracks which grow from the exposed surfaces. The similarity between the observed surface layer growth rates and mass loss rates [6] suggests that degradation-induced mass loss primarily occurs within this thin surface layer which develops and grows during aging, while the core of the material is relatively protected from oxidative degradation. Shrinkage of the polymer is also observed, resulting in dimensional changes which are sensitive to specimen geometry.

Similar investigations on the effects of aging at elevated temperatures on bare fibers have also been conducted [7-10]. Bowles [9] found that extended exposure in air resulted in mass loss from graphite fibers. Through the use of Braunauer-Emmet-Teller (BET) nitrogen/krypton adsorption techniques, the exposed surface areas of the fibers were measured and the mass loss was found to be accompanied by a rapid increase in the exposed fiber surface area and a similar increase in the porosity of the fibers. Data from this study suggested that carbon fibers such as Celion 6000 consist of a layered microstructure which has a relatively non-porous outer skin

surrounding a porous core. As the outer layer degrades the environment gains access to the inner, porous core, resulting in an acceleration of the degradation process.

This effect was also noted by Wong *et al.* [10] in a study on the thermo-oxidative stability of IM6 fibers in air. At low temperatures (below 371°C) mass loss from the fibers was not significant and followed a linear relationship with aging time, suggesting that the fiber oxidation is controlled by a surface reaction at these temperatures. At higher temperatures (above 371°C) a dramatic increase in mass loss rate was observed, with complete degradation of the fibers occurring after 150 hours at 398°C. The surface morphology of the fibers was examined using a Scanning Electron Microscope (SEM) at different stages of the aging process at 316°C. At times in excess of 700 hours at this temperature, a significant reduction in the fiber diameter was observed and severe pitting was found on the fiber surface. These changes were correlated with the mass loss from the fibers at this temperature. The dramatic change in the oxidation rate at higher temperatures was attributed to a significant increase in the surface available for reactions, most likely as a result of the formation of voids and cracking of the fiber surface. In contrast, fibers in composites are protected – virtually no surface area is exposed to the environment and no mass loss is observed [8].

Unidirectional composites demonstrate similar degradation mechanisms to neat resin, although the mass loss is less severe. Mass loss appears to be dependent on the matrix volume fraction [16], suggesting that preferential degradation of the matrix takes place. A study on the effects of different aging environments on the mass loss from unidirectional graphite-fiber/PMR-15 composites recorded significant differences in the mass loss

behavior in inert and oxidative atmospheres [3]. Mass losses in inert atmospheres asymptotically approached stable values over a period of time at each of the test temperatures. The majority of the mass loss occurs within the first few hundred hours of aging and appears to be a bulk mechanism, depending only on specimen volume. After the first 150 hours of aging, mass losses from the specimens at each of the aging temperatures have essentially reached their final values, which increases with exposure temperature. This behavior suggests that only the initial portion of the mass loss curves reflect thermally activated processes. In contrast, specimens exposed to oxidative atmospheres will continually lose mass over the entire aging period. Notably higher mass loss rates are demonstrated in air than in an inert atmosphere at the same temperature.

There is little evidence to suggest that thermal aging alone results in any significant changes in the physical nature of the matrix, with the exception of a marked increase in the flexural properties at higher temperatures [3]. Thermo Mechanical Analysis (TMA) of PMR-15 composites aged in nitrogen indicated a large increase in the glass transition temperature (a change of over 130°C after 24 hours at 371°C) which correlated with greatly improved mechanical properties at high temperatures. No significant density changes, surface cracking or warping, or porosity were observed in specimens aged in inert atmospheres [3]. Whether metrics such as these can offer any true indication of the material chemical state after aging is still not clear.

In contrast to aging in inert atmospheres, aging in oxidative atmospheres always results in the formation of degraded surface layers. Surface cracking is also observed to occur in unidirectional composites at extended aging times (in excess of 1000 hours at 288°C) [13]. As aging time

is increased, a distinct layer of degraded matrix forms at the surfaces and advances into the composite. Cracking is initiated perpendicular to these surfaces and grows inwards between the reinforcing fibers, resulting in the degradation of composite mechanical properties, such as flexural strength, which are matrix-dependent or surface-dependent [13]. This layer growth is similar to that observed in neat resin, however, cracking is not always evident in neat resin samples which have been exposed at the same temperatures and for the same amount of time, as their composite counterparts which exhibit cracking [6].

Studies of PMR-15 composites reinforced with various continuous fibers [7-9, 11, 13, 15] revealed significant geometric effects when exposed to oxidative environments, with the three different types of specimen surfaces (molded surfaces, surfaces with cut fiber ends, and surfaces cut parallel to fibers) exhibiting different mass loss rates. This geometric effect is not observed when samples are aged in inert atmospheres [3]. Nam and Seferis [18] determined the mass loss rates in the three principal directions for unidirectional carbon-fiber reinforced bismaleimide composites and concluded that, while it is traditionally measured through scalar mass loss measurements, the degradation of these materials is (in their approximation) a tensorial-based property depending on both magnitude and direction. This anisotropy has also been measured in optical microscopy of aged composites [9, 11, 18, 19], where the thickness of the degraded surface layer, and hence its possible contribution to the mass loss of the system, differs greatly depending on the type of exposed surface under examination. Growth of surface layers on the molded surface and surfaces cut parallel to the fibers, and the mass loss rate from these surfaces, is significantly slower than that of the surface with exposed cut fiber ends [20] except when resin-rich molded

surfaces are present. When resin-rich surfaces are present, the mass loss rate from these surfaces will initially be higher than either of the other two surfaces, due to the greater availability of resin for degradation. As time progresses, however, the mass loss rate from this surface decreases to that observed for the surfaces cut parallel to the fibers [18].

The strong influence of the fiber reinforcements on thermo-oxidative stability has been addressed by several research efforts [7, 8, 13, 16] in an effort to explain the accelerating effect of exposed graphite fiber ends on mass loss rates in composites. Bowles studied the effects of various fiber reinforcements on the mass loss in PMR-15 composites at elevated temperatures [8] and attributed the accelerating effect to a detrimental fiber/matrix interaction. Differences in mass loss, matrix cracking, and geometry dependency effects were recorded for different fiber types. A similar study by Alston [16] linked this effect to impurities on the fiber surfaces which allow oxygen to diffuse from the external environment at a faster rate along the fiber/matrix interface than would otherwise occur. PMR-15 composites reinforced with fibers known to possess low levels of contaminants, primarily sodium ions, demonstrated smaller mass losses than those reinforced with other fibers. Both of these studies noted a strong synergistic effect between different fiber/matrix combinations. The most thermally stable fibers do not necessarily result in the most stable composites, and in some cases result in the least thermo-oxidatively stable configurations [9]. This effect has been attributed to the quality of the interfacial bond between the fiber and matrix – fibers that are less oxidatively stable in the bare form may in fact possess the necessary surface topography and chemical composition to ensure a tight interfacial bond which slows the diffusion of oxygen along the fibers into the material bulk [9].

Laminated composites which have plies at different angles exhibit a more rapid mass loss than is found in unidirectional composites. As before, an altered surface layer forms and microcracks develop at the surface at extended times. However, microcracks now also develop in the interior of the composite [13]. Tensile stresses may develop in the matrix due to high residual thermal stresses from curing and possible degradation-induced stress gradients caused by physical changes in the surface layer [7], leading to cracking of the matrix throughout the laminate. These cracks enhance oxidation of the composite by providing additional paths for air to penetrate into the material. This can lead to a vicious circle, where oxidation promotes cracking which in turn allows more oxidation, and so on. For example, the mass loss in cross-ply laminates at longer aging times depends only on specimen volume rather than exposed surface area once internal microcracking develops [13].

2.2 PREVIOUS ANALYTICAL WORK

Attempts have been made to analyze and model various aspects of this problem. Mass loss rates have been empirically fit to Arrhenius rate curves [21, 22]. Arrhenius rate kinetics represent an important, established method of reporting and comparing kinetic data. The Arrhenius rate equation expresses material conversion/degradation rate as a function of both temperature and conversion state. The true versatility of this model lies in the generality of the conversion-dependence function used in the rate equation [23], allowing a large variety of experimental rate measurements to be modeled in this manner. This type of approach provides a simple means to model the stability of different systems but is useful only for comparative purposes if data is not collected and reduced in a rigorous manner. Other

degradation models such as Coats/Redfern, Ingraham/Marier, and Horowitz/Metzger have also been fit to mass loss rate data [24]. These models are less general than the Arrhenius form, placing specific assumptions on the mechanisms which are being modeled. As such they are less versatile than the Arrhenius approach and are more commonly used as methods for comparing the stability of similar polymer systems subjected to isothermal exposures than for determining kinetic parameters for predictive modeling.

More sophisticated models have combined modeling of the diffusion of oxygen into the material with chemical reaction rate equations to predict the mass loss and growth of degraded surface layers. In many such cases effective diffusion coefficient models are used [18, 25] where an apparent diffusivity is found by fitting to experimental mass loss curves for a composite. Models of this kind allow the anisotropic nature of the degradation to be simulated but offer little insight to the true physics of the problem, effectively smearing many possible mechanisms together into the observed global effects.

Kim *et al.* [26] incorporated a one-dimensional form of the Fickian diffusion model into a finite element method based on the assumption that the degradation of the material is controlled by slow diffusion of oxygen into the material bulk. The use of higher order interpolation functions allowed for a non-linear concentration of oxygen within an element and hence non-uniform degradation states. Nam and Seferis [27] developed a generalized methodology for composite degradation based on two elementary reaction mechanisms, hence allowing for both reaction and diffusion controlled degradation mechanisms. Several independent reaction mechanisms may be accounted for through the use of weighting factors. These weighting factors

assign certain proportions of the overall mass loss to individual reactions, each with its own set of kinetic parameters, and thus allow a variety of complex chemical degradation processes to be modeled.

Cracking of the degraded layers has been predicted by modeling the degraded layers as layers with different material properties in a finite element model [28]. The effects of matrix cracking at elevated temperatures have also been analyzed by extending models, originally developed for cracking in an elastic laminate, to viscoelastic polyimide systems through application of an elastic-viscoelastic correspondence principle [29]. Aging induced changes in viscoelastic properties have been incorporated into standard viscoelastic analysis techniques [30]. Micromechanical models allow for the prediction of composite properties and behavior given the matrix and fiber properties, facilitating the prediction of the effects of temperature on composite properties [31, 32].

Other existing semi-empirical methods for predicting composite durability, which use highly simplified closed-form equations to model hygral, thermal and mechanical effects [33], could be applied to some aspects of this problem. These methods are based on composite micromechanics and ply-stress influence coefficients, making them generic and applicable to a large number of fiber/polymer-matrix composites. The effects of thermal cycling (cycles required to initiate transverse microcracking), and hygro-thermo-mechanical cyclic loading (number of cycles to failure) on specific composites have been predicted using these models. However, extensive validation of these models is required before any confidence can be placed in their predictions. The success of these methods in the current problem is unlikely as they cannot adequately account for the unique physics observed in the high temperature degradation process.

2.3 POLYIMIDE CHEMISTRY

The degradation behavior which has been observed empirically is dependent upon the chemistry of the matrix material. The PMR-15 material considered in the course of this work is chemically quite complex. PMR polyimides are addition-type thermosetting polymers prepared by the polymerization of monomer reactants (PMR). Resin solutions consist of three individual monomers - a nadic ester (NE), the dimethyl ester of 3,3',4,4'-benzophenotetracarboxylic acid (BTDE), and 4,4'-methylenedianiline (MDA) dissolved in methanol. When these monomers are combined in a 2.000/2.087/3.087 molar ratio respectively, the formulated weight after imidization, but before crosslinking, is 1500. Resin of this composition is designated PMR-15 [34]. The chemistry of the formation of this building block is quite well understood [35], however the chemistry involved in the polymerization and later cross-linking of the material is still subject to much debate with no definitive answer as yet available [5, 36]. The chemistry involved in the degradation of this and other related systems is under investigation [24, 36] but it is not yet understood to a level which would allow definite conclusions to be drawn and predictive calculations to be made.

Evidence suggests that cross-linking within the material is not complete at the end of the post-cure period, and hence one aspect of the aging process is the completion of cross-linking reactions. Studies have linked this increase in cross-link density within the material to the initial increase in material properties such as the glass transition temperature and compressive modulus [37, 38]. The amount of cyclopentadiene (CPD) which is evolved as a degradation product has been used as a metric to estimate the extent of the cross-linked structure within the polymer chains [5], with good correlation existing between the amount of CPD evolved and the increase in the glass

transition temperature during the curing process and the very early stages of high-temperature aging. For prolonged aging times, however, the amount of CPD evolved quickly drops to negligible levels while the specimens continue to lose mass.

The fully cross-linked material is subject to both oxidative attack and thermal degradation at a variety of sites, both in the cross-links and in the main polymer chain itself at a variety of vulnerable links [36, 39]. The mass loss over extended aging times is attributed to the degradation of the nadic ester and MDA components of the main polymer chain while the BTDE component remains relatively unaffected [34, 36, 40]. The nadic ester appears to be the most vulnerable to oxidative attack and is thus the weak link in the thermo-oxidative stability of these materials, with an increase in the nadic ester content in the PMR formulation resulting in a decrease in the thermo-oxidative stability of the compound [41]. Efforts to reformulate the PMR polyimides with monomers possessing greater thermo-oxidative stability have largely been unsuccessful due a strong synergistic effect which exists between the individual monomers [39]. PMR formulations using the MDA component demonstrated lower mass loss and higher material property retention than PMRs formulated using more a stable monomer in place of MDA. This effect has been attributed to a synergy between the MDA/NE components which provides sites vulnerable to oxidation in the PMR polymer chain. These sites promote weight-gaining reactions (such as carbonyl formation) and thermo-oxidative cross-linking in surfaces exposed to air, resulting in the polymer possessing a higher thermo-oxidative stability as a whole [39].

Degradation of this and other related polymers ultimately results in the release of large quantities of carbon monoxide and carbon dioxide along

with smaller quantities of a large variety of low molecular mass volatiles, suggesting that degradation occurs at a multitude of sites along the chain simultaneously [24, 42, 43]. The release of these volatiles are greatly accelerated in the presence of oxygen but will occur even in an inert atmosphere. Releases of larger fragments of the polymer may follow. In an inert atmosphere such as nitrogen, approximately 60% of the initial mass of the polymer will remain as char up to 800°C. In air, the more aggressive nature of the environment results in all of the mass being eventually consumed at these temperatures [24]. While the basic theory behind the chemistry of this degradation behavior is currently receiving considerable attention, the efforts in this area to develop a more complete understanding of this phenomenon remain too diverse to allow the development of a definitive model of the mechanisms which occur. A more concerted, concentrated effort in the study of this behavior is required if progress towards this goal is to be achieved.

2.4 RECENT WORK

It has been found that even comparatively simple tests of material subjected to environmentally-induced degradation are difficult to interpret due to the complexity caused by the non-uniformity of the degradation. A second degree of complexity is added by the fact that most of these mechanisms proceed at very slow rates in the use environment and so acceleration methods (through the use of higher temperatures, increased pressures or other accelerating mechanisms in the test environment) must be employed if time-efficient experiments are to be conducted. As a result, the majority of recent work has concentrated upon attempting to accurately quantify the phenomena which have been observed empirically, correlating

these phenomena with physical effects such as changes in material properties, and developing accelerated test methods which will allow these results to be scaled accurately to the real environment.

Considerable work has recently been carried out in the area of developing phenomenologically correct kinetic models which can allow the prediction of degradation under a variety of different environments. Thermogravimetric analyses (TGAs) of both neat resin [22, 24, 42] and composite materials [19, 44-47] have been conducted to identify and characterize primary mass loss mechanisms. Thermogravimetric analyses allow the measurement of minute changes in mass loss and mass loss rates during the aging of specimens. Both isothermal [19, 45] and dynamic heating [22, 24, 42, 44, 46, 47] experiments have been carried out. Through the study of changes in the mass loss rates from the materials at different temperatures and/or heating rates, it is possible to evaluate reaction kinetics and activation energies for the degradation process [44]. Thermogravimetric analyses on different forms of neat polyimide resin [22] revealed that significant differences in the magnitude and location of mass loss rate peaks exist between bulk and finely-divided powdered forms of the resin subjected to dynamic heating analyses. Bulk specimens displayed extra peaks in the mass loss rate curves, with these peaks being attributed to complicated combinations of chemical reactions, diffusion, and volatilization processes as temperature was increased. Hence in order to isolate the reaction kinetics from mass transfer (diffusion) effects, it is necessary to use specimens which have very large exposed surface area to volume ratios.

Isothermal TGAs on powdered specimens in nitrogen, air and oxygen [45] yielded activation energies in air which were approximately one-half of those in nitrogen, indicating that significantly less energy is required for

oxidation as opposed to thermal degradation. Comparison between tests in air and oxygen have revealed a strong effect of relative oxygen concentration on reaction rate, with rates being greatly accelerated with increasing oxygen concentration [45]. However only comparative data was detailed in this study - data was not reduced to a set of kinetic coefficients which could be used in analytical models.

Kamvouris *et al.* [48] studied the feasibility of using shear stress relaxation for determining the extent of aging in PMR-15 and found that both physical (reversible) aging effects and chemically induced (mass loss) effects occur during long term exposure at elevated temperatures. Results from the investigation revealed that the shifts in stress relaxation curves, and the extent of reversibility of aging effects, can provide quantitative information about the physical and chemical aging which occurs in PMR-15 at temperatures up to 316°C. However, the exact cause of the shifts recorded for specimens aged in air is still open to debate. It was not possible to determine if the shifts were a result of a decrease in molecular mobility (caused by cross-linking and physical aging), or as a consequence of the non-uniform degradation of specimens in air. While the method possesses some potential for use as a metric for aging in composites, the effects of non-uniform oxidation near the surface of specimens aged in air need further consideration before a reliable test can be established.

A similar combination of physical and chemical aging effects were reported by Bowles *et al.* [37] in a study of the effects of isothermal aging on the compression strength of PMR-15 composites. At lower temperatures, the degradation in compression strength was attributed to physical aging effects, while at higher temperatures the loss in compression strength was shown to be directly related to the mass loss from the material. Variations of

compression strength with specimen thickness were also recorded, again suggesting that chemical change does not occur evenly throughout the entire volume of the material. However, this effect could be structural, with changes in failure mechanisms occurring as specimen thickness is increased, e.g. a transition from failure due to fiber kinking and delamination to failure caused by brooming at the specimen ends. Comparison of the compression strengths of these different failure modes, and particularly their application as a metric for degradation, is dangerous without further investigation.

Changes in the glass transition temperature and bending strength of other high-temperature material systems [49] have also been attributed to a combination of physical and chemical aging, with ambient air environments causing a greatly accelerated decrease in mechanical properties as compared to the changes exhibited in inert environments. The effects of isothermal aging on transverse crack development are also under investigation. Changes in glass transition temperature, composite weight loss, crack density, and mode I intralaminar fracture toughness were monitored during isothermal aging of bismaleimides in air at 177°C [50]. A reduction of 50% in the mode I intralaminar fracture toughness was recorded for specimens aged in excess of 2000 hours. A normalization of the results with aging, taking into account the change in cross-sectional area due to surface degradation, could not account for the majority of the decrease in fracture toughness and the reductions were attributed to possible changes in the fiber/matrix interface over the aging time.

Accelerated test methods which can provide useful data for analytical models of both the chemical and physical aging mechanisms and their effects on material properties are currently under investigation [25, 51-53]. While the methodology behind the design of these accelerated tests is well

developed, the analytical models as yet possess a limited accuracy and remain for the most part case-specific. Models which can calculate [54] degraded composite laminate properties and behaviors based on known degradation states within the material have been developed. However, these models require accurate chemical degradation and diffusion information, and require careful verification at all levels before they will be useful for predictive calculations.

2.5 SUMMARY

Extended exposure at elevated temperatures leads to the degradation of polymer matrix composites, primarily in the matrix component. While extensive empirical investigations of the effects of aging on these materials have been carried out, their performance under continuous thermal exposure is still not fully understood. Neat resin suffers mass loss, shrinkage, the development of degraded surface layers, surface cracking, and degradation of mechanical properties when exposed to oxidative environments at high temperatures. In the case of composites, the material anisotropy adds further complexity to the problem. Cracks form not only at the surface but along the fiber/matrix interface in unidirectional and general composite laminates. Cracks also form parallel to the fibers in the interior of general laminates, allowing oxygen from the environment to penetrate deep into the material, resulting in degradation throughout the material volume at long exposure times. The coupling between the chemical degradation, changes in mechanical properties, mechanical and degradation-induced stresses, and cracking of the material results in a highly complex problem where the individual components are very difficult to separate out.

Evidence from a number of empirical and analytical studies suggest

that the degradation of these polymers is controlled by the slow diffusion of oxygen from the exposed surfaces into the material bulk. The rate at which the oxygen diffuses into the material bulk is different in each of the principal directions in a composite. Diffusion is fastest through surfaces which have exposed cut fiber ends, possibly due to impurities on the fiber surface which allow the oxygen to diffuse more quickly along the fiber length than would otherwise be possible. As the oxygen progresses into the material it attacks the polymer chain at certain vulnerable sites causing fragments of the polymer to be released as volatiles, a process which is reflected by mass loss in the material and the significantly altered chemistry of the surface layer. This oxidative attack is accompanied simultaneously by a less aggressive thermal degradation which occurs throughout the material bulk. Thermal degradation also results in the release of volatiles, although mass loss due to this mechanism is significantly less than that due to the oxidative degradation.

As the surface layer grows with aging time, the changing chemical structure of the surface layer (as opposed to that of the core material) appears to cause stress gradients in the material which may result in cracking perpendicular to the surfaces. The problem is exacerbated when residual thermal stresses and applied mechanical loads are also present, with wide-spread cracking of the material occurring. This leads to a vicious circle where degradation induces damage, this damage in turn accelerates the degradation by exposing more of the material to the environment, which leads to more damage and so on. Both the degradation itself, and the damage it induces, have deleterious effects on the mechanical properties of the material, with significant decreases in matrix-dominated and surface-dominated material properties (such as flexural strength and compression

strength) being recorded after long-term exposure in air at elevated temperatures.

While the effects of these mechanisms have been studied on a qualitative level by numerous research efforts, no study has yet dealt with these phenomena satisfactorily at a quantitative level. Comparative, qualitative studies offer great insight into the physics of the mechanisms, however they do not allow predictive models to be generated. Design of high temperature structures would be greatly improved through the development of a predictive tool which could determine material state and changes in material properties from known quantities such as laminate geometry, material properties, exposure temperatures and chemical environment. In order to do this, a greater understanding, particularly on a quantitative level, of each of the components involved in the degradation of these materials must be developed. This goal can only be achieved through intelligent selection of appropriate models for the individual mechanisms and careful design of experimental programs which allow particular effects to be separated out and quantified. Until the individual components and their effects are well understood, the generation of a comprehensive model which can accurately simulate all of the observed phenomena is unlikely.

CHAPTER 3

PROBLEM STATEMENT AND APPROACH

3.1 PROBLEM STATEMENT

In this work, we will endeavor to develop a model of the chemical degradation of a polymer matrix composite such that, given the external chemical environment and temperatures throughout the laminate, laminate geometry, and ply and/or constituent material properties throughout, we can calculate the concentration of diffusing substances, and metrics of chemical degradation, as functions of time and position throughout the laminate.

3.2 APPROACH

Available literature on the phenomena and preliminary models are used to develop an understanding of the probable degradation mechanisms. This understanding is used to develop analytical models and experimental techniques which offer both qualitative confirmation of the mechanisms and quantitative material properties. Extensive analytical and experimental investigations are carried out to explore the validity of the models and to collect the necessary material properties.

The analysis has three fundamental goals. The analysis is used to identify key parameters associated with the assumed degradation mechanisms, as well as the sensitivity of the analysis to these parameters. Secondly, the analysis provides insight into the physical mechanisms and aids in the intelligent design of an experimental program which can provide

quantitative data for predictive modeling. The models are also useful for interpreting and reducing test data. The ultimate goal of the analysis is to provide a design capability such that the degradation state at any point can be predicted as a function of exposure time and position.

The purposes of the experimental program are to allow a greater qualitative understanding of the mechanisms involved, to provide material parameters for the analysis, and to provide verification of the analysis. The experimental program is analysis driven, in that preliminary studies using the analytical models are used to design test matrices which allow crucial parameters to be measured. This approach allows the development of a well structured methodology for the collection and reduction of experimental data.

3.3 ANALYTICAL TASKS

The analysis is composed of two basic models which describe the chemical reaction and diffusion phenomena. Figure 3.1 shows a schematic of this analytical model, integrated with the other aspects of the comprehensive model discussed in Chapter 1. Both thermal (bulk) and oxidative reactions are considered. Thermal reactions are assumed to be described by an Arrhenius reaction model, while a concentration-dependent form of this model is used to describe the oxidative reactions. Diffusion of oxygen into the material bulk is modeled using the Fickian law of diffusion. The reaction and diffusion models are coupled through the concentration-dependency of the oxidative reactions.

The analysis is implemented through the use of an explicit time-step finite difference computer code. Inputs to the analysis are the environment temperature and relative oxygen concentration at the surface of the laminate. Degradation state and oxygen concentration within the material are

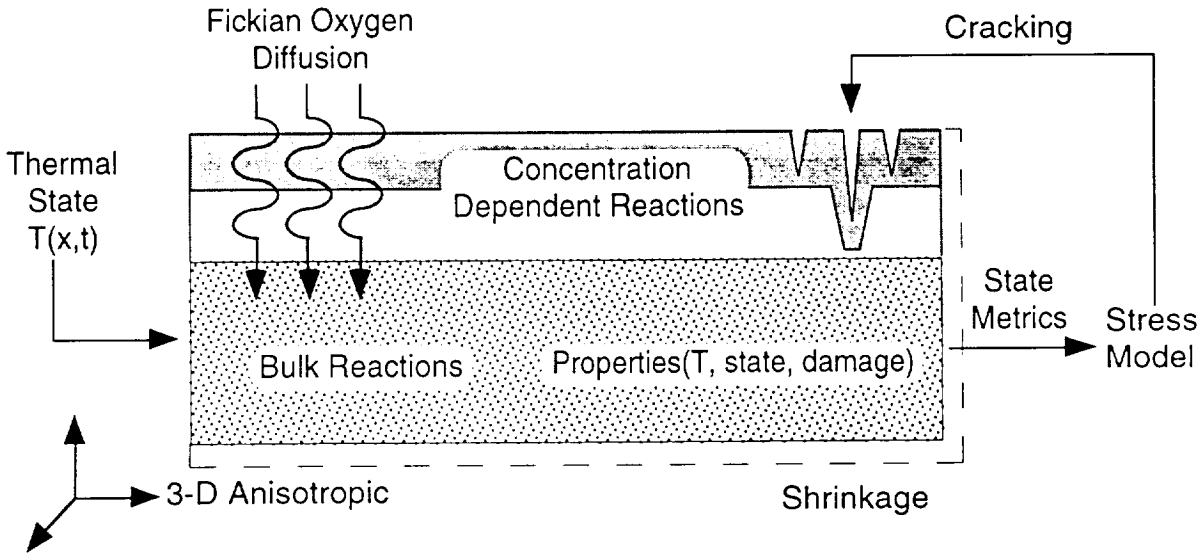

Figure 3.1 Assumed degradation mechanisms

calculated as functions of exposure time and distance from the exposed surface. The thickness of the degraded layer in each of the principal directions is also predicted.

Preliminary parametric studies using a single oxidative reaction were used to identify critical material parameters and to aid in the design of the experimental test matrices. Parametric studies using more complete models were carried out to determine the sensitivity of the analysis to the different material coefficients and to gain a more complete understanding of the mechanisms under consideration. The analysis was used to reduce mass loss data from powdered specimens to a set of chemical reaction constants, and to reduce the observed growth of degraded surface layers to a set of effective diffusion coefficients. Finally, model predictions incorporating both chemical reactions and diffusion were correlated with the mass loss from macroscopic neat resin and unidirectional composite specimens.

3.4 EXPERIMENTAL TASKS

All materials used in the course of this research were manufactured at the NASA Lewis Research Center. Neat PMR-15 resin and unidirectional T650-35/PMR-15 composites are considered. Thermogravimetric analyses on powdered resin specimens are carried out in both inert and oxidative environments. Both dynamic heating and isothermal tests are conducted. The use of powders allows the decoupling of purely chemical effects from diffusion controlled effects. The inert atmosphere provides data for the purely thermal effects. Tests in oxidative atmospheres provide data for the combined thermal and oxidative effects. The study of both these phenomena separately allows an effective decoupling of the oxidative and thermal reactions.

Short-term isothermal tests are carried out on both unidirectional and neat resin macroscopic specimens to provide data on the diffusion mechanisms. Three different sizes of rectangular specimen are used for both the unidirectional and neat resin specimens in order to investigate geometry (surface area to volume ratio) effects and to separate out diffusion effects in the three principal directions in the composite specimens. Two different exposure temperatures were used. Samples were periodically removed and mass loss and dimensional changes were recorded. Specimens were sectioned and photomicrographs of the cross-section were taken. The growth of the surface layer with aging time and the formation of surface cracks were recorded through optical analysis of these photomicrographs. At each stage the experimental data is used to provide the analysis with the required coefficients. Analytical predictions are subsequently correlated with test results to validate the model and provide insight into the details of the mechanics of the problem.

CHAPTER 4

ANALYTICAL METHODS

In this chapter a detailed engineering model of the diffusion of oxygen into a polymer matrix composite, and the oxidative and non-oxidative reactions which occur in the polymer matrix, is presented. The model uses Arrhenius reaction kinetics to describe chemical reactions within the material, and the Fickian diffusion law to model diffusion of oxygen into the material bulk. The methods in which the models are implemented, along with the data fit procedures used to obtain key material parameters for the analysis from the experimental data, are described here. Several key examples of the data fit procedures are also presented in this chapter for the purposes of illustration.

4.1 DEGRADATION MODEL

A wide, thin plate of composite material is considered. The plate has thickness $2h$, and is composed of unidirectional composite plies. One or both faces of the plate are exposed to the environment at time-varying temperature T and pressure P. The diffusion of oxygen from the environment is considered, as is the chemical degradation of the matrix material. The fibers are assumed to be stable, with only the matrix component degrading over time. It is assumed that the thermal transient time of the plate is small compared to that of all degradation mechanisms, so the temperature throughout the plate is assumed to be that of the environment. Oxygen

concentration and matrix chemical state are predicted at a point within the material as functions of distance from the surface z and exposure time t.

4.1.1 Diffusion Model

This section presents a brief synopsis of the analytical theory behind diffusion. A more complete description of the theory presented here may be found in [55]. The theory of diffusion is directly analogous to the theory used to describe the transfer of heat by conduction. Fick was the first to quantify diffusion by adopting the mathematical equation of heat conduction. The mathematical theory of diffusion in isotropic substances is based on the hypothesis that the rate of transfer of a diffusing substance through a unit of surface is proportional to the concentration gradient measured normal to that surface, as described by Fick's first law

$$F = -D\frac{\partial c_s}{\partial x} \tag{4.1}$$

where c_s is the relative concentration of the diffusing species s, D is called the diffusion coefficient, and F is the rate of transfer per unit area. The fundamental differential equation of diffusion in a three-dimensional isotropic medium is given by [55]

$$\frac{\partial c_s}{\partial t} = D\left(\frac{\partial^2 c_s}{\partial x^2} + \frac{\partial^2 c_s}{\partial y^2} + \frac{\partial^2 c_s}{\partial z^2}\right) \tag{4.2}$$

In tensor notation this can be written as

$$\frac{\partial c_s}{\partial t} = \frac{\partial}{\partial x_i}\left(D\frac{\partial c_s}{\partial x_i}\right) \tag{4.3}$$

In anisotropic media, such as composite materials, the diffusion properties may not be the same in different directions. For such media, it is not always the case that the direction of flow of the diffusing species at any

point is normal to the surface of constant concentration through that point. The Fickian diffusion law for a species diffusing into the material bulk from the surrounding environment is then described by

$$\frac{\partial c_s}{\partial t} = \frac{\partial}{\partial x_i}\left(D_{ij}^s \frac{\partial c_s}{\partial x_j} \right) \tag{4.4}$$

where D_{ij}^s is the non-isotropic tensor of diffusivity of species s through the composite material. In cases where the diffusing species may be consumed by chemical reactions, it is necessary to account for this consumption in the diffusion model. Hence

$$\frac{\partial c_s}{\partial t} = \frac{\partial}{\partial x_i}\left(D_{ij}^s \frac{\partial c_s}{\partial x_j} \right) - r_s \tag{4.5}$$

where r_s is the rate of consumption of species s by the reactions. The diffusivity constants are strongly dependent on temperature and are typically described by [56]

$$D_{ij}^s = \left(D_{ij}\right)_o \exp\left(\frac{-C_{ij}}{T} \right) \tag{4.6}$$

where $\left(D_{ij}\right)_o$ and C_{ij} are constants, and T is the absolute temperature. In general, these constants will be different for each component of the diffusivity tensor (for example, the diffusivity in the fiber direction of the composite is known to be much greater than the diffusivity in the through-thickness direction), and for each substance s. The diffusivities will also be functions of the chemical state and stress state, and will be affected strongly by the presence of damage such as microcracking.

Eq. 4.5 represents the general, fully three-dimensional case. Based on the empirical observations presented in Chapter 2, we assume here that the thickness of the degraded layers which form in a composite material, and

hence the distance through which oxygen diffuses, is small compared to the overall dimensions of finite sized specimens. The contribution of effects at the corners between surfaces, where the diffusion is truly anisotropic, is not significant and thus is not accounted for. This results in Eq. 4.5 becoming uncoupled in the principal directions. Diffusion of oxygen through each of the exposed surfaces is then considered to be one-dimensional, with a gradient of concentration perpendicular to the exposed surface only. For the current work, a diffusivity which does not vary spatially is also assumed. The diffusion through a single surface of the composite is then described by

$$\frac{\partial c_{ox}}{\partial t} = D_z^{ox} \frac{\partial^2 c_{ox}}{\partial z^2} - r_{ox} \tag{4.7}$$

where D_z^{ox} is the diffusivity perpendicular to the surface being considered. Figure 4.1 illustrates the coordinate system for the one-dimensional case. As in the case of the anisotropic diffusion coefficient, D_z^{ox} is also temperature dependent

$$D_z^{ox} = D_o \exp\left(\frac{-C}{T}\right) \tag{4.8}$$

4.1.2 Reaction Chemistry Model

The reaction is considered to take place inside an infinitesimal control volume containing a mass m_o of matrix material. The fibers are assumed to be stable. The matrix material is assumed to consist of different components that are available for various reactions. A mass m_i is defined as the mass that would be lost due to the completion of a set of reactions involving component i. A mass fraction y_i is defined as the ratio between the mass of component i and the overall mass

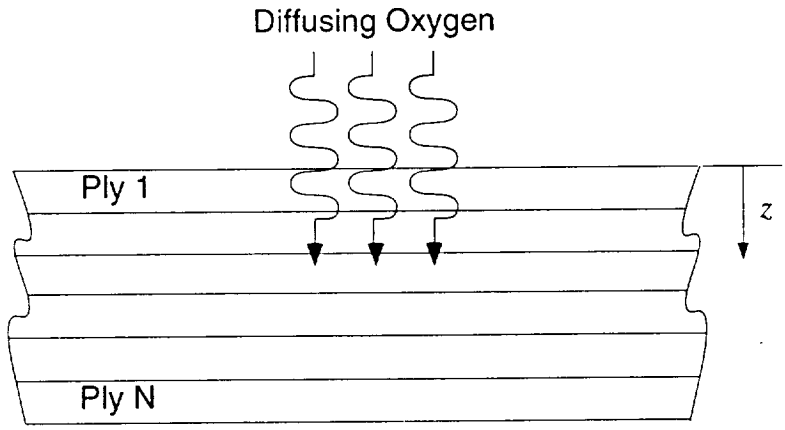

Figure 4.1 Coordinate system for one-dimensional Fickian diffusion model.

$$y_i = \frac{m_i}{m_o} \tag{4.9}$$

All of the mass is assigned to one of the possible mass fractions, so

$$\sum_{\text{all } i} y_i = 1 \tag{4.10}$$

A conversion metric α_i is used to keep track of the degradation of mass fraction y_i. When α_i is equal to zero, no degradation has taken place; when α_i is equal to one, the mass fraction is entirely lost. The rate at which mass is lost from the control volume due to loss of component i is

$$-\frac{\partial m_i}{\partial t} = m_o y_i \frac{\partial \alpha_i}{\partial t} \tag{4.11}$$

Note that summation notation is not used here. The total mass lost from component i is

$$\Delta m_i = -\int_0^t \frac{\partial m_i}{\partial t} dt \tag{4.12}$$

Finally, the mass lost from the control volume is

$$\Delta m = \sum_{\text{all } i} \Delta m_i \tag{4.13}$$

It is often convenient to express the total mass loss as a proportion of the initial mass. In the notation of McManus and Chamis [54]

$$b = \frac{\Delta m}{m_o} \tag{4.14}$$

All of the above considers the mass loss at a point within the material, which is not a measurable quantity. In a finite specimen of volume V, we measure the total mass loss and mass loss rate

$$\Delta M = \int_V \Delta m dV \tag{4.15}$$

$$\frac{\partial(\Delta M)}{\partial t} = \int_V \frac{\partial(\Delta m)}{\partial t} dV \tag{4.16}$$

Finally, in some cases certain mass fractions will not react. A final mass m_f is defined as the sum of the unreacting mass fractions

$$m_f = m_o \sum_{i \subset unreacting} y_i \tag{4.17}$$

A normalized mass loss, which reaches a value of one when all reactions have completed, is then defined as

$$\Delta m' = \frac{\Delta m}{m_o - m_f} \tag{4.18}$$

The conversion metric, α_i, is defined here in terms of the normalized mass loss from each component i at any time t

$$\alpha_i = \Delta m_i' = \frac{\Delta m_i}{m_{o_i} - m_{f_i}} \tag{4.19}$$

where m_{o_i} and m_{f_i} represent the initial and final masses of component i respectively.

It is convenient to express some experimental results as a normalized mass loss rate, expressed either as a time derivative or, in the case of a constant heating rate test (with a heating rate Q expressed in °C/sec), as a temperature derivative. These quantities are related by

$$\frac{\partial(\Delta m')}{\partial T} = \frac{1}{Q}\frac{\partial(\Delta m')}{\partial t} \tag{4.20}$$

Arrhenius reaction kinetics are assumed for the chemical reactions acting on the different mass fractions. Reaction rates for each material component i are related to the conversion metric, α_i, and to the absolute temperature, T, by different and independent functions. A complete kinetic description of a chemical reaction requires the characterization of both expressions [23]

$$\frac{\partial \alpha_i}{\partial t} \propto F(\alpha_i) F'(T) \tag{4.21}$$

where $F'(T)$ is the rate (temperature-dependence) function, and $F(\alpha_i)$ is the conversion-dependence function. Generally, reaction rates increase with temperature. At high values of α_i the reaction rate will typically slow down due to the decreasing amount of material available to the reaction.

The rate constant $F'(T)$ is a function of temperature only, whereas $F(\alpha_i)$ is some function of conversion, α_i. Typically, $F'(T)$ is assumed to follow an Arrhenius-type expression, and so

$$F'(T) = k_i \exp\left(\frac{-E_i}{RT}\right) \tag{4.22}$$

where k_i is the reaction rate constant defining the frequency of occurrence of the particular reaction configuration, E_i is the activation energy which represents the energy barrier which must be surmounted during transformation of reactants into products, and R is the real gas constant. $F(\alpha_i)$ is commonly expressed as $(1-\alpha_i)^{n_i}$ assuming nth-order kinetics, giving

$$\frac{\partial \alpha_i}{\partial t} = k_i (1-\alpha_i)^{n_i} \exp\left(\frac{-E_i}{RT}\right) \tag{4.23}$$

In cases where the reactions are controlled by the concentration of a diffusing substance, a modified form of Eq. 4.23 is used

$$\frac{\partial \alpha_i}{\partial t} = k_i (1-\alpha_i)^{n_i} c_s^{m_{si}} \exp\left(\frac{-E_i}{RT}\right) \tag{4.24}$$

where c_s is the concentration of the diffusing species and m_{si} defines the order of the concentration dependency.

All of the expressions derived thus far assume that only a single reaction acts on each of the mass fractions. For the general case where multiple reactions can occur, each mass fraction y_i can be attacked by a number of reactions j. The reactions rates in, say, an oxidative atmosphere

can then be fully described by

$$\frac{\partial \alpha_{ij}}{\partial t} = k_{ij}\left(1-\alpha_i\right)^{n_{ij}} c_{ox}^{m_{ij}} \exp\left(\frac{-E_{ij}}{RT}\right) \tag{4.25}$$

The reaction rate k_{ij}, activation energy E_{ij}, and reaction order n_{ij} are needed to fully characterize each reaction. The oxygen concentration dependence m_{ij} is zero for thermal (non-oxidative) reactions, and must be specified for oxidative reactions. The reduction of mass fraction i is computed from

$$\frac{\partial \alpha_i}{\partial t} = \sum_{\text{all } j} \frac{\partial \alpha_{ij}}{\partial t} \tag{4.26}$$

$$\alpha_i = \int_0^t \frac{\partial \alpha_i}{\partial t} dt \tag{4.27}$$

Note that none of the quantities in Eqs. 4.25 or 4.26 are tensors. The notation employed in these equations was chosen as a convenient method in which to express the occurrence of multiple, simultaneous reactions.

4.1.3 Coupling of Diffusion and Reaction Models

The diffusion and reaction models are coupled through the oxygen concentration term in Eq. 4.25, and the oxygen consumption term in Eq. 4.7. The consumption term is calculated from

$$r_i = \frac{\partial \alpha_i}{\partial t} R_i \qquad r_{ox} = \sum_{\text{all } i} r_i \tag{4.28}$$

where r_i describes the amount of oxygen consumed by the oxidative reactions acting on component i at a point in the material at a given time t, and R_i is a constant which represents the total amount of oxygen required to bring the reaction to completion at that point. Here, as all concentrations used in the course of the analysis are normalized, R_i is dimensionless. In cases where actual concentration values are used, R_i has units of mol/m^3.

4.2 DETERMINATION OF KINETIC CONSTANTS

The necessary kinetic constants may be derived from experimental data through the use of Kissinger's method. This method allows the reduction of the data to a useful set of kinetic constants through the use of the time derivative of Eq. 4.23. An experiment which measures Δm and $\partial m/\partial t$ of a sample as functions of time is assumed. The experiment uses a constant heating rate Q, such that $T = Qt$ where T is the absolute temperature. Tests are carried out at several different heating rates. Multiple reactions may exist, however only a single reaction will be considered here for the purposes of illustration. The reduction technique employed to reduce data which results from multiple reactions is addressed in Section 4.4. At the maximum degradation rate for a particular mass fraction

$$\frac{\partial}{\partial t}\left(\frac{\partial \alpha_i}{\partial t}\right) = 0 \tag{4.29}$$

Manipulation of the resulting equations allows for the calculation of the activation energy and pre-exponential constant. When the heating rate is constant, time and temperature derivatives of the mass loss rate are linearly related. As a result, data may be plotted as a function of time or temperature, and then analyzed using Kissinger's method. For a constant heating rate, Q, Eq. 4.23 may be rewritten as

$$\frac{\partial \alpha_i}{\partial T} = \frac{k_i}{Q}\left(1-\alpha_i\right)^{n_i} \exp\left(\frac{-E_i}{RT}\right) \tag{4.30}$$

At the maximum degradation rate, the temperature derivative of Eq. 4.30 is given by

$$\frac{\partial}{\partial T}\left(\frac{\partial \alpha_i}{\partial T}\right)=\frac{k_i}{Q}n_i(1-\alpha_i)^{n_i-1}\exp\left(\frac{-E_i}{RT}\right)\left(-\frac{\partial \alpha_i}{\partial T}\right)+\frac{k_i}{Q}(1-\alpha_i)^{n_i}\exp\left(\frac{-E_i}{RT}\right)\frac{E_i}{RT^2} \quad (4.31)$$

Simplifying for $\partial\alpha_i/\partial T$ through the use of Eq. 4.30 gives

$$k_i \exp\left(\frac{-E_i}{RT}\right)n_i(1-\alpha_i)^{n_i-1}=\frac{E_i Q}{RT^2} \quad (4.32)$$

Taking logarithms of both sides of Eq. 4.32 and rearranging, we get

$$\ln\frac{Q}{T^2}=\frac{-E_i}{RT}+\ln\left[\frac{k_i R}{E_i}n_i(1-\alpha_i)^{n_i-1}\right] \quad (4.33)$$

Given data at several different heating rates, the required parameters may be obtained from Eq. 4.33 by plotting $\ln(Q/T^2)$ as a function of $1/T$, where T is the temperature at the maximum mass loss rate for each of the different heating rates. The activation energy can then be obtained from the slope $(-E_i/R)$ and the pre-exponential constant, k_i, from the intercept assuming that the order of the reaction n_i is known. When n_i equals one, k_i becomes independent of conversion, α_i, at the maximum degradation rate.

For cases where $n_i \neq 1$ then it is necessary to find n_i in the following manner. From Eq. 4.33, the intercept of a plot of $\ln(Q/T^2)$ as a function of $1/T$ at the maximum mass loss rate is given by

$$I=\ln\left[\frac{k_i R}{E_i}n_i(1-\alpha_i)^{n_i-1}\right] \quad (4.34)$$

Solving for k_i, we get

$$k_i=\frac{E_i \exp(I)}{R}\frac{1}{n_i(1-\alpha_i)^{n_i-1}} \quad (4.35)$$

Substitution into Eq. 4.30, and rearranging, then gives an expression for n_i

$$n_i=\left(\frac{\partial \alpha_i}{\partial T}\right)^{-1}\frac{E_i \exp(I)}{QR}(1-\alpha_i)\exp\left(\frac{-E_i}{RT}\right) \quad (4.36)$$

Hence, the reaction order, n_i, can be obtained from Eq. 4.36 once the

activation energy and intercept value have been determined from Eq. 4.33. Note that in addition to the heating rate, Q, and the temperature at which the maximum mass loss rate occurs, it is also necessary to determine $\partial\alpha_i/\partial T$ and α_i from the experimental data at this point. Resubstitution of n_i into Eq. 4.35 then allows the determination of k_i.

4.3 MODEL IMPLEMENTATION

The model was implemented in several different ways, for different purposes. A preliminary model was used to correlate with the results of degradation tests which had previously been carried out on macroscopic neat resin specimens [6]. This model consisted of a single concentration-dependent reaction coupled with a Fickian diffusion model and was implemented using a one-dimensional through-thickness explicit time-step finite difference computer code. The constants used for the single reaction model, described in Eq. 4.24, and the one-dimensional diffusion model, described in Eq. 4.7, were estimated from the available literature on similar polymers. These equations were solved through the explicit finite difference scheme to predict oxygen concentrations, reaction rates, reaction states, and mass loss as functions of time and position, and total mass loss as a function of time.

Initial conditions were $c_{ox} = 0$ and $\alpha_i = 0$ everywhere. Boundary conditions were $c_{ox} = 1$ at the surface ($z = 0$) and no mass flux, $\partial c_{ox}/\partial z = 0$, occurred across the mid-plane of the plate ($z = h$). The analysis considered a plate of the same mass and thickness as the test specimens. The thickness of the surface layer was considered to be very thin by comparison to the dimensions of the specimen, allowing the contribution of the corners between surfaces to be ignored. The surface layer was considered to be of the same

thickness on each of the exposed surfaces. One-dimensional mass loss predictions were generated using a very fine finite-difference grid. The mass loss from the actual specimens was then calculated from the one-dimensional predictions. The mass loss from a specimen of length l, width w, and thickness $2h$, was calculated from

$$V^k = \big(l - (2(k-1)\Delta z)\big)\big(w - (2(k-1)\Delta z)\big)\big(2h - (2(k-1)\Delta z)\big) \tag{4.37}$$

$$\Delta M_{actual} = \frac{1}{V}\sum_{k=1}^{N-1}\left(V^k - V^{k+1}\right)\left(\frac{\Delta M^k - \Delta M^{k+1}}{2}\right) \tag{4.38}$$

where Δz is the grid spacing, N is the total number of nodes, V is the specimen volume, ΔM^k is the mass loss at node k, and ΔM^{k+1} is the mass loss at node $k+1$. The quantity $V^k - V^{k+1}$ represents a very thin layer of material, of thickness Δz, whose outer surface lies at a depth $(k-1)\Delta z$ from each of the specimen surfaces. The mass loss within this layer is assumed to be the average of the mass loss from the nodes at the top and bottom surfaces of the layer, $\left(\Delta M^k - \Delta M^{k+1}\right)/2$. The summation of the mass loss from all of these thin layers allows the actual total mass loss of the specimen to be determined.

To model the chemical reactions observed in the thermogravimetric experimental work, discussed in Chapter 5, a more detailed chemical model was implemented. A single oxidative reaction, coupled with multiple thermal reactions were modeled. The normalized mass loss and mass loss rate for constant heating rate experiments were predicted using a numerical time integration. As these tests were carried out on finely ground powders which minimize mass transfer effects and ensure a uniform degradation state throughout the sample, diffusion effects were not considered in this model.

Finally, once reliable chemical constants had been established, a three dimensional degradation model was assembled which incorporated both

oxidative and thermal reactions for finite-sized neat resin plates. Correlations between the model predictions and data collected from the isothermal exposure of neat resin allowed the necessary diffusion coefficients to be determined. Analytical predictions of the mass loss for the actual specimens were generated in the same manner as was used in the preliminary model, using a one dimensional model to generate predictions for the three dimensional specimens. Once again, the model was implemented as an explicit time-step finite difference code with the same set of initial and boundary conditions as used in the preliminary model. The source code for this analytical model is presented in Appendix A.

4.4 DATA REDUCTION IMPLEMENTATION

4.4.1 Thermogravimetric Data in Nitrogen

During the course of the experimental study it was determined that mass loss from PMR-15 and its composites is composed of mass loss from several different material components. However, due to the current lack of understanding of the degradation phenomenon at a chemical level, the relative contribution of each of the mass loss components to the overall mass loss is not known, i.e. the particular material components which are losing mass, and hence the mass fraction y_i for each of the material components, is unknown. As knowledge of the correct mass fractions are an integral part of determining the correct reaction coefficients, this prevents a direct reduction of the thermogravimetric data to a set of useful kinetic constants. Consequently, it was necessary to use an iterative data fit procedure which would allow the optimum mass fractions and reaction coefficients to be derived. A particular case, in which two individual Arrhenius-type reactions govern the mass loss from a system, are used here to illustrate the technique

which was employed.

The combined mass loss rate for two Arrhenius-type reactions, at a number of different heating rates, was compared to the data by means of the following cost function

$$\chi^2 = \sum_{i=1}^{N} \frac{1}{1000} \left(\frac{(\partial\alpha/\partial T)_i - (\partial\alpha/\partial T)_{i,predicted}}{\sigma_i} \right)^2 \tag{4.39}$$

where N is the total number of data points, $(\partial\alpha/\partial T)_i$ and $(\partial\alpha/\partial T)_{i,predicted}$ are the mean actual and predicted values, respectively, for the total mass loss rate at data point i, and σ_i is the standard deviation at data point i.

Conceptually, this method is equivalent to plotting the mean of the normalized experimental data and the analytical predictions on the same graph. The error for each data point is found from the absolute distance between each data point and the analytical prediction corresponding to the temperature of that data point. Once the cost function at each heating rate has been determined, the cost functions are then averaged across all the heating rates to provide an evaluation of the set of reaction coefficients as a whole

$$\chi^2_{total} = \frac{1}{N_q} \sum_{j=1}^{N_q} \chi^2_j \tag{4.40}$$

where N_q is the total number of heating rates and χ^2_j is the cost function evaluated at heating rate j.

The procedure is started by assuming a mass fraction for the second reaction. Thermogravimetric data for a two reaction system will typically exhibit two mass loss rate peaks, the height and locations of these peaks being dependent on the contribution from each of the individual reactions. An initial set of reaction coefficients is determined for the second reaction by

assuming that the second mass loss rate peak in the data is due only to the second reaction with no contribution from the first reaction. Mass loss rate curves for this assumed reaction at a number of different heating rates are calculated through the use of Eqs. 4.23 and 4.27. These curves are then subtracted from the data. Eqs. 4.33-4.36 are used to derive a set of kinetic constants for the first reaction from the remaining mass loss rate curves which are produced in this manner. The cost function is then evaluated for the combined set of reactions.

The mass loss rate curve for the first reaction is subtracted from the data to produce an improved estimate for the second reaction, and the entire procedure is repeated until (i) the solution converges, i.e. further iterations result in the same reaction coefficients being returned and the cost function remains the same, or (ii) the solution begins to diverge with the an increase in the cost function being experienced. In situations where the solution begins to diverge, the set of coefficients which produced the smallest cost function before divergence occurred are taken to be the solution for that particular set of mass fractions. Once a set of coefficients has been established for a given mass fraction, the mass fraction for the second material component is incremented and the procedure is repeated with the minimum cost function for each set of mass fractions being recorded. The mass fractions (and hence reaction coefficients) which return a global minimum for the cost function are taken to be the optimum set of parameters. A flowchart of this data fit procedure is shown in Figure 4.2. The source code is given in Appendix B. The implementation, and validity, of this data fit procedure is illustrated in the Section 4.5.

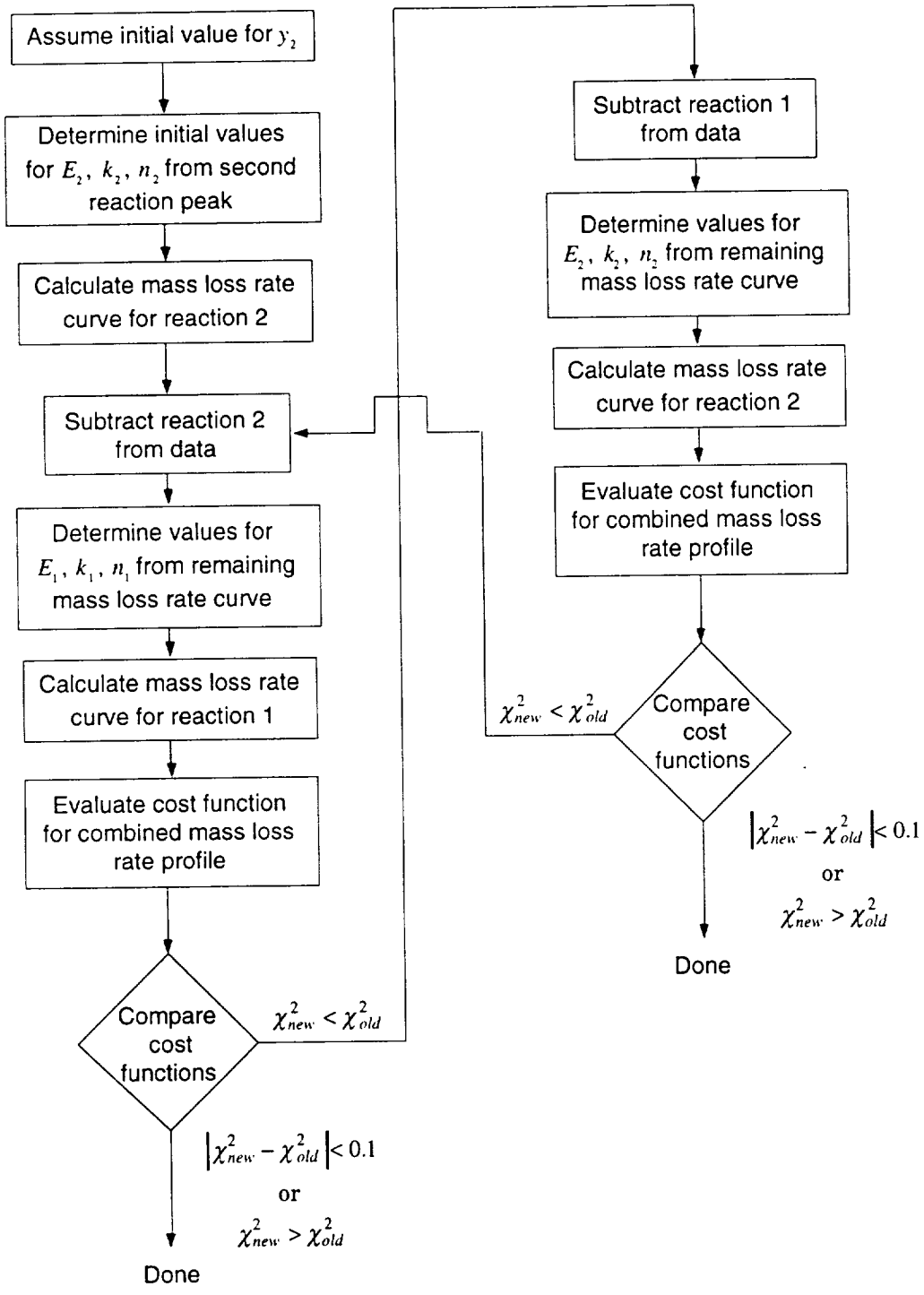

Figure 4.2 Flowchart of data fit algorithm for an assumed mass fraction y_2.

4.4.2 Thermogravimetric Data in Air

The χ^2 cost function was also used to fit to the data in air and separate out the oxidative reactions. However, due to the presence of highly rate insensitive reactions, and secondary reactions which could not be accounted for in the current model, it was not possible to obtain an estimate for the oxidative reaction coefficients through the iterative method used to determine the optimum reaction coefficients for a given mass fraction in the nitrogen data. Instead an exhaustive search of suitable reaction coefficients for the assumed oxidative reaction was carried out, with the cost function being evaluated for each combination of coefficients. The reaction coefficients used in this search were bounded as follows: $110\text{x}10^3\text{kJ/mol} < E_{12} < 170\text{x}10^3\text{kJ/mol}$, $1\text{x}10^5\text{s}^{-1} < k_{12} < 1\text{x}10^{10}\text{s}^{-1}$, and $1 < n_{12} < 3$. Based on the empirical data, the first oxidative reaction was assumed to consume some of the same material components as the first thermal reaction. The best fit to the data was achieved through the evaluation of the χ^2 cost function over a range of mass fractions for the first oxidative reaction. The combination of reaction coefficients which resulted in the minimum cost function was chosen as the optimum set.

4.5 DATA FIT VALIDATION AND PARAMETRIC STUDY

4.5.1 Validation

The purpose behind this section is to illustrate the validity of the data fit procedure, described in Section 4.4, in reducing mass loss data which results from Arrhenius-type degradation chemistry. Figure 4.3 illustrates the typical behavior of the mass loss rate with respect to temperature for a single Arrhenius-type reaction at a number of different heating rates. The corresponding mass loss curves are shown in Figure 4.4. As the heating rate

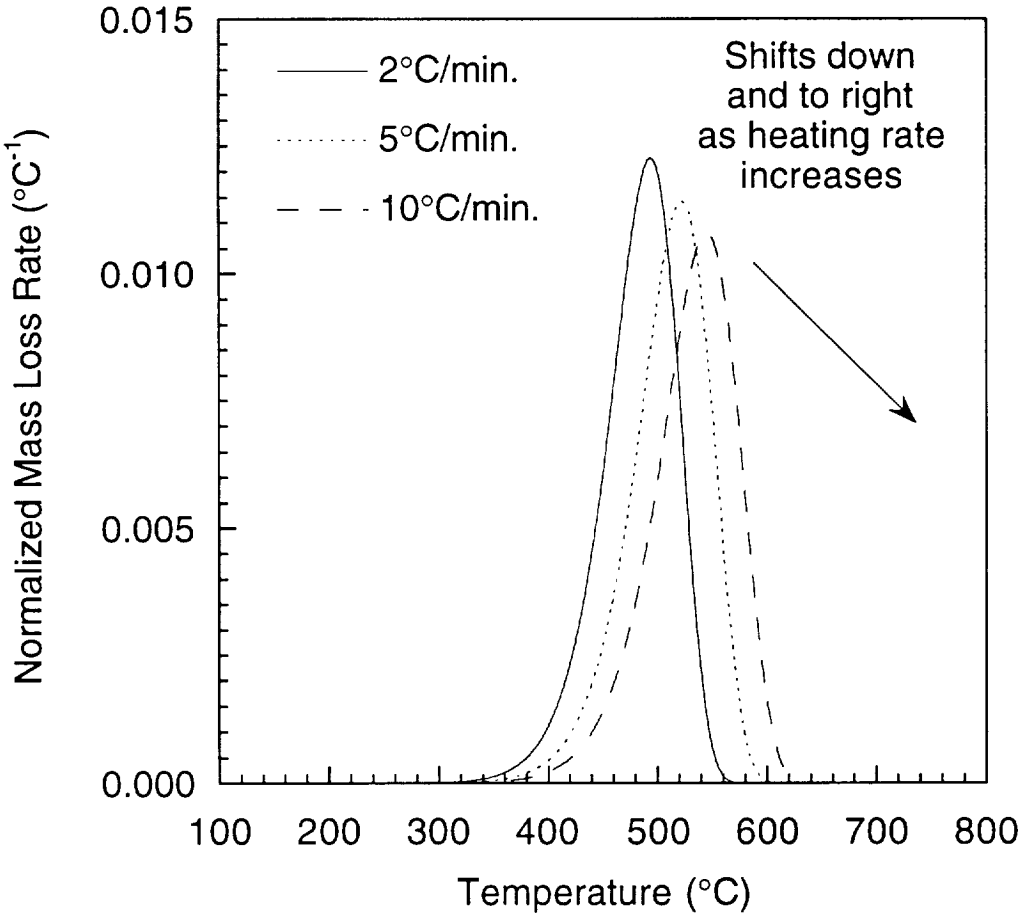

Figure 4.3 Arrhenius reaction mass loss rates at different heating rates.

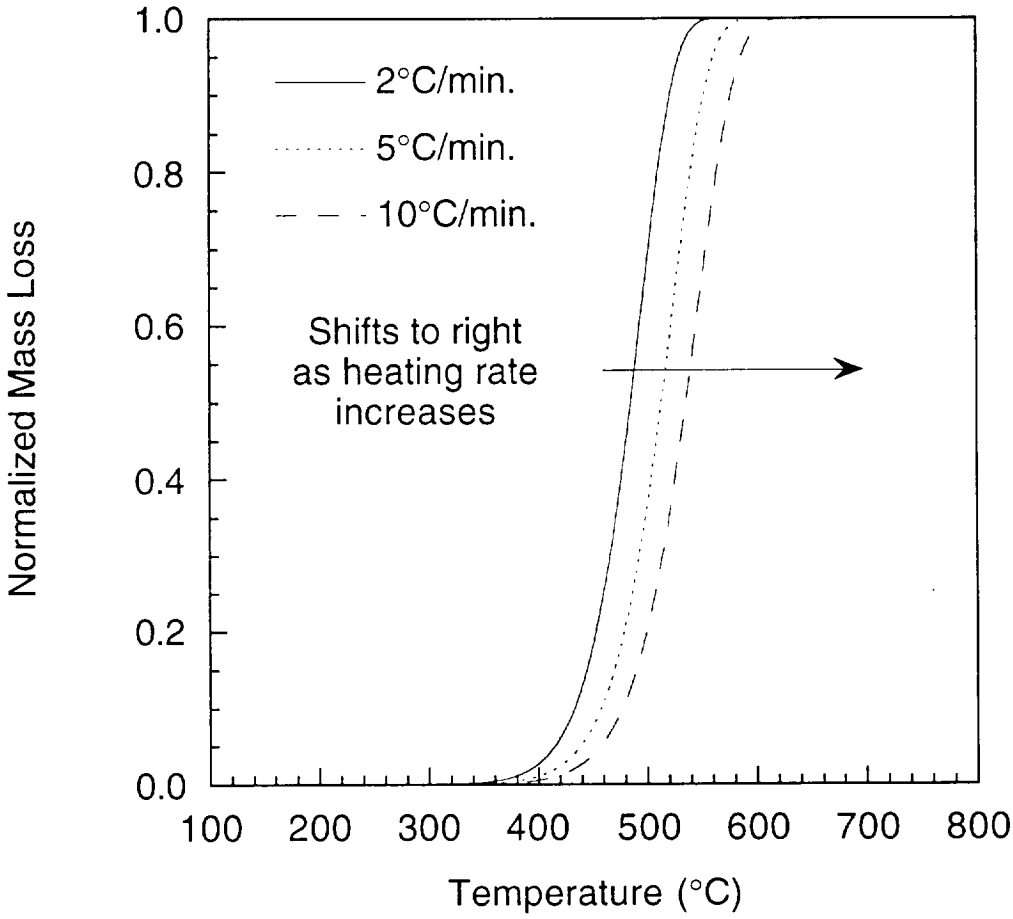

Figure 4.4 Arrhenius reaction mass loss at different heating rates.

is increased then the mass loss rate curve shifts to the right and the magnitude of the peak decreases. At higher heating rates less degradation will occur at the lower temperatures. The mass loss rates at the lower temperatures are small and, as the heating rate is increased, the periods which the samples spend at these temperatures become progressively smaller. Hence, the amount of degradation which occurs at these temperatures will decrease as the heating rate is increased. Note that the mass loss rates in Figure 4.3 have been normalized with respect to temperature and have units of $^{\circ}C^{-1}$. A renormalization of this data on a per unit time basis will more clearly illustrate the features discussed above.

To validate the data fit method, for the purposes it was used for in the current study, two cases were considered. The first considers only a single Arrhenius reaction while the second considers a two reaction system. Pseudo-data was generated using Eqs. 4.22 and 4.27, and the data fit method was then used to recover the coefficients. Table 4.1 shows a comparison between the reaction constants used to generate the single reaction pseudo-data shown in Figures 4.3 and 4.4, and those which were analytically derived by reducing this data through the use of Eqs. 4.33-4.36. As the pseudo-data is generated directly from the Arrhenius rate equations, one would expect the data reduction procedure to return the exact solution for the reaction coefficients. While there are minor differences between the two sets of coefficients, excellent agreement is found between the predicted mass loss rates and those of the pseudo-data. Mass loss rates at two different heating rates are shown in Figure 4.5. The temperatures at which the maximum mass loss rate occurs, and the magnitude of the maximum mass loss rate, for the two sets of coefficients are shown in Table 4.1.

The data fit procedure for the two-reaction model is illustrated here

Table 4.1 Single Arrhenius Reaction Data - Pseudo vs. Predicted

	Pseudo-Data	Predicted
E (kJ/mol)	150	148.4
k (min.$^{-1}$)	1 x 10^9	0.78 x 10^9
n	1.0	0.96
Q=2°C/min.		
T_{max} †	494	494
$(\partial\alpha/\partial T)_{max}$	0.0123	0.0124
Q=10°C/min.		
T_{max} †	546	546
$(\partial\alpha/\partial T)_{max}$	0.0108	0.0109

† Temperature, in °C, at which the maximum mass loss rate occurs.

Units for $(\partial\alpha/\partial T)$ are in °C^{-1}.

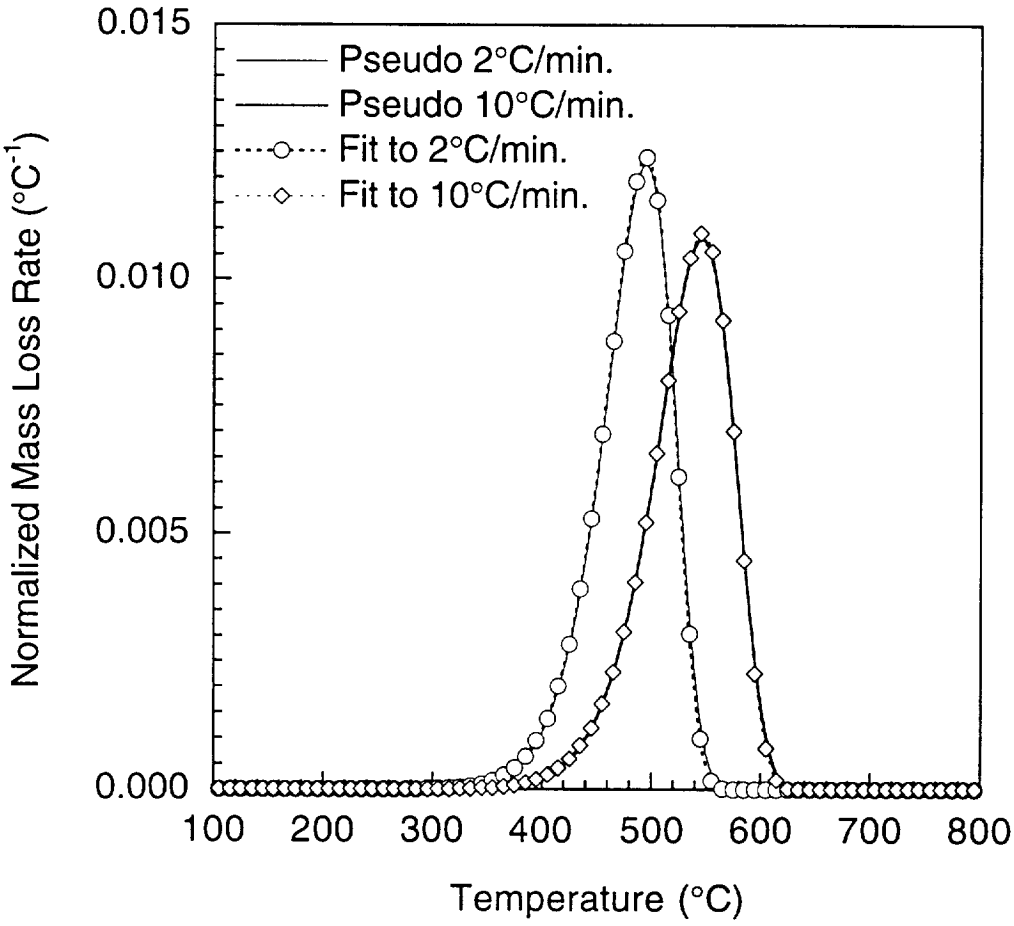

Figure 4.5 Pseudo-data and predicted mass loss rates for single reaction.

using pseudo-data which is similar to the data which was recorded during the course of the thermogravimetric analyses used in this work. Data for a two reaction degradation process was generated using the reaction constants shown in Table 4.2. The individual mass loss rates along with their combined effect, at a heating rate of 2°C/min., are shown in Figure 4.6. A uniform standard deviation was assumed across all the data points. The analysis begins with y_1=0.20 and $y_2 = 1 - y_1$. The best fit to the data, for the given mass fractions, was determined using the data-fit procedure outlined in Section 4.4. The assumed value for y_1 was then incremented (in this case an increment of 0.005 is used) and the entire procedure was repeated.

A plot of the variation of the cost function with mass fraction for the fit to the pseudo-data is shown in Figure 4.7. The shape of the curve is essentially concave with a single, clearly defined minimum occurring at y_1=0.305. The exact solution has y_1=0.30. The reaction constants which were derived using the data-fit procedure are shown in Table 4.2. Again, some minor differences exist between the sets of coefficients. However, excellent agreement is found between the model and the data across the entire temperature range and across all heating rates. A comparison between the pseudo-data and the model predictions at two different heating rates, generated using the coefficients given in Table 4.2, is shown in Figure 4.8. The locations and magnitudes of the normalized mass loss rate peaks at these heating rates are also shown in Table 4.2.

While this demonstrates that the procedure is valid, it should be noted that it is not very sensitive to the activation energy, with a 1% error in E resulting in almost no error in the data fit. The cost function for these optimum parameters is negligible. This was also the case in the data fit to the single Arrhenius reaction. However, the small error in E results in much

Table 4.2 Two-Reaction Kinetic Constants - Pseudo vs. Predicted

	Pseudo-Data	Predicted‡
E_1 (kJ/mol)	150	148.4
E_2 (kJ/mol)	185	186.6
k_1 (min.$^{-1}$)	1 x 10^9	0.78 x 10^9
k_2 (min.$^{-1}$)	1 x 10^{10}	1.27 x 10^{10}
n_1	1.0	0.98
n_2	2.0	1.99
y_1	0.30	0.305
y_2	0.70	0.695
Q=2°C/min.		
$T_{1,max}$ †	504	503
$T_{2,max}$ ††	586	586
$(\partial\alpha/\partial T)_{1,max}$	0.0047	0.0047
$(\partial\alpha/\partial T)_{2,max}$	0.0057	0.0057
Q=10°C/min.		
$T_{1,max}$ †	561	561
$T_{2,max}$ ††	638	637
$(\partial\alpha/\partial T)_{1,max}$	0.0045	0.0045
$(\partial\alpha/\partial T)_{2,max}$	0.0051	0.0051

‡ A standard deviation of 1 x 10^{-4} was used for all data points in the cost function evaluation.

† Temperature, in °C, at which the first peak in the *combined* mass loss rate curve occurs.

†† Temperature, in °C, at which the second peak in the *combined* mass loss rate curve occurs.

Units for $(\partial\alpha/\partial T)$ are in °C^{-1}.

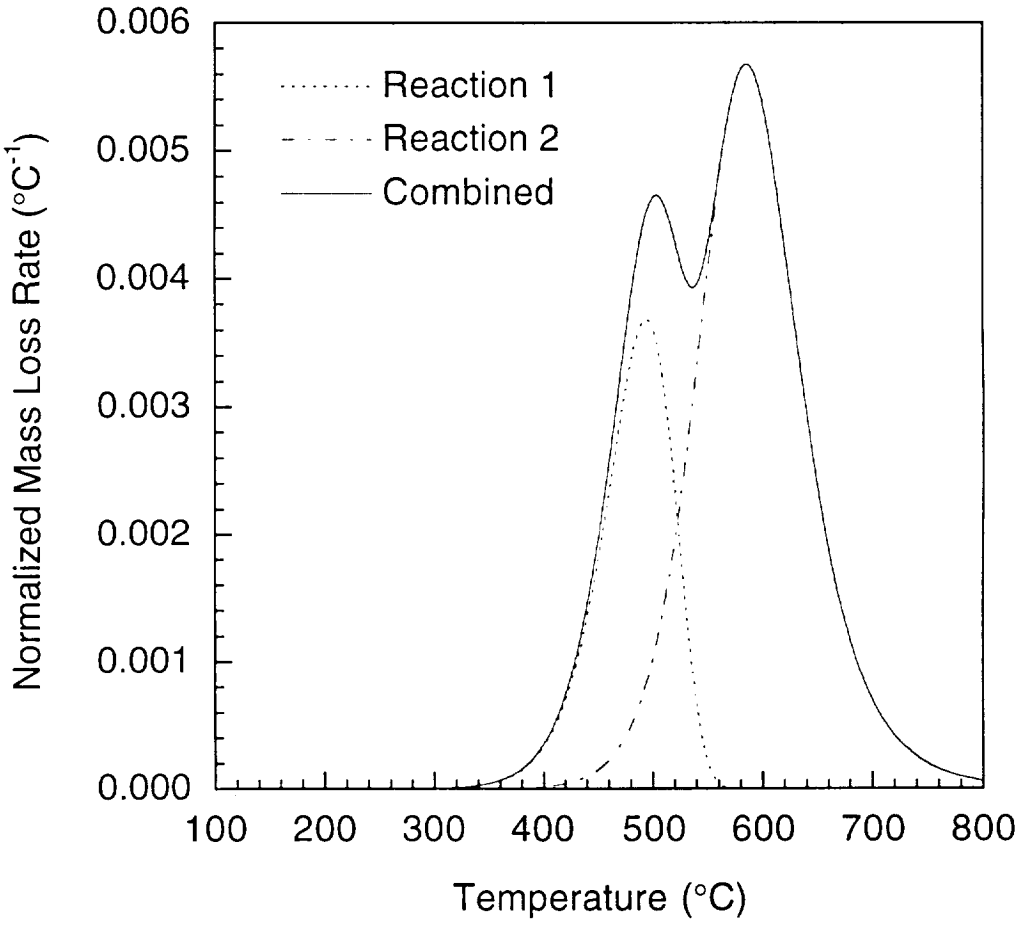

Figure 4.6 Two reaction degradation mechanism.

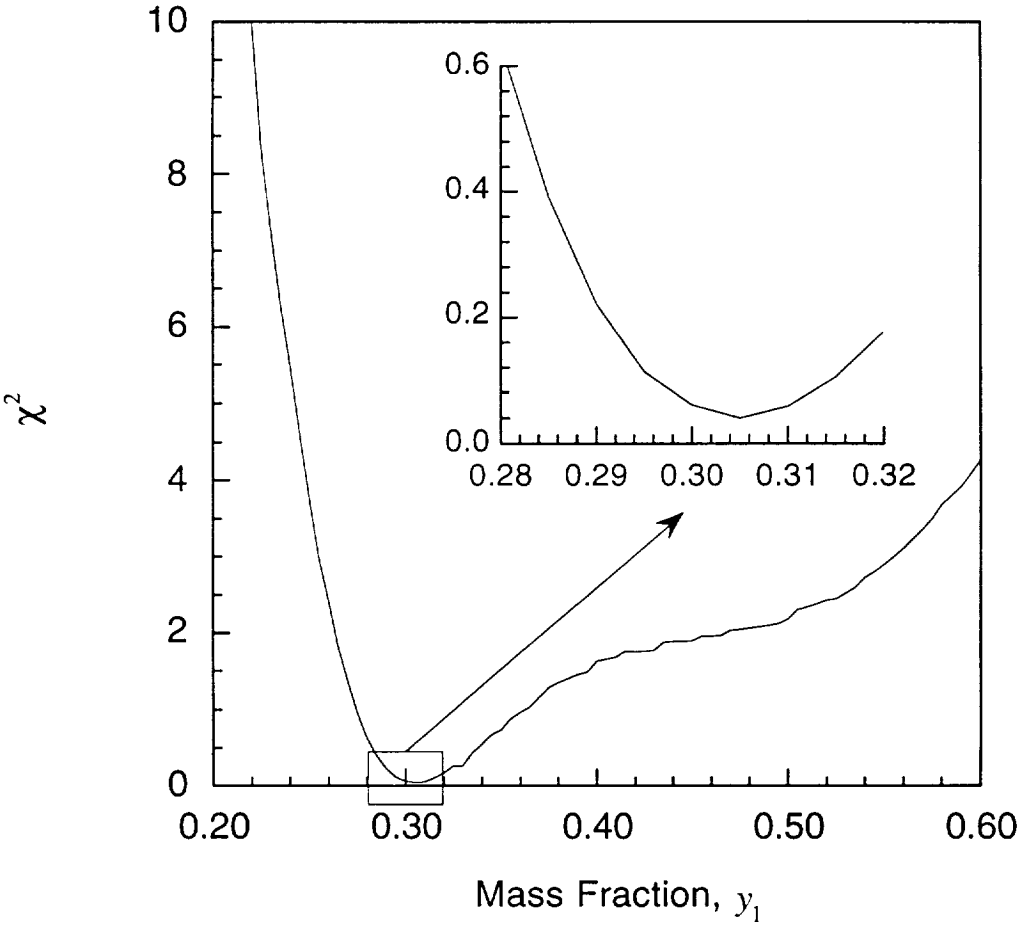

Figure 4.7 Cost function for two-reaction pseudo-data.

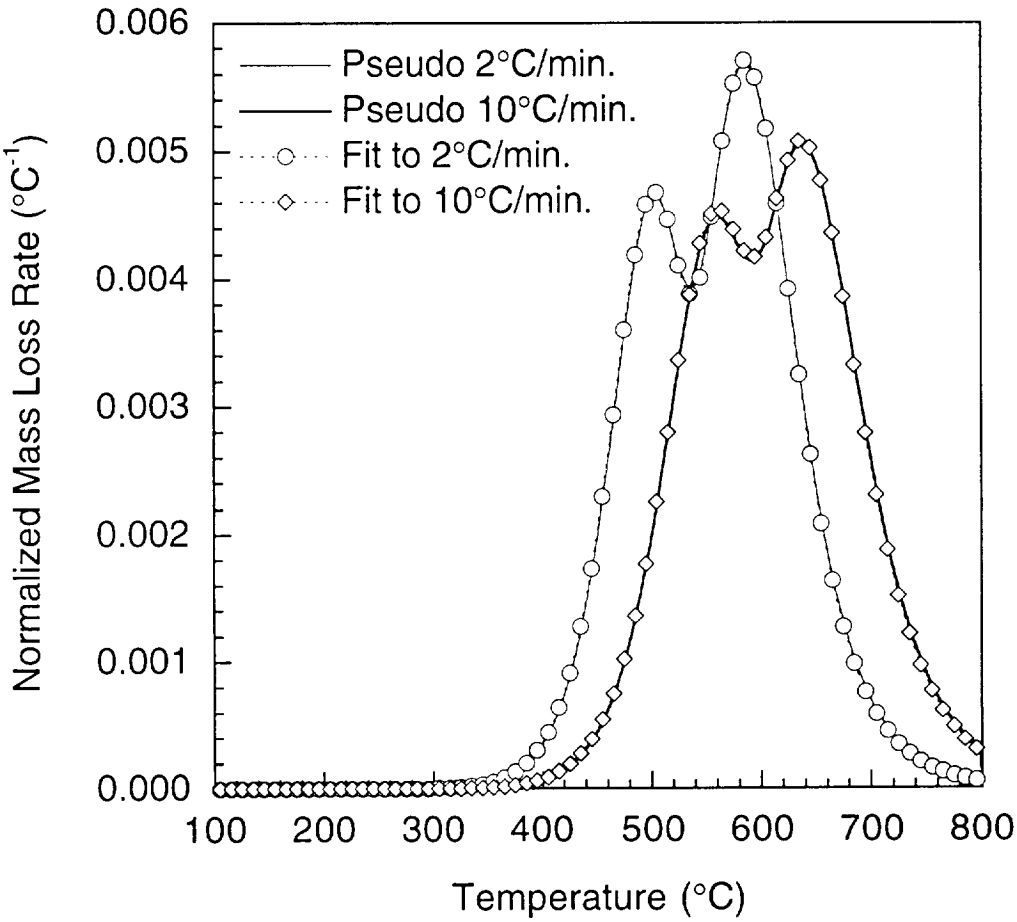

Figure 4.8 Pseudo-data and predicted mass loss rates for two reactions.

larger variations in k. In fact, the values returned for both of the reaction rate constants in the two reaction case have errors of greater than 20%. In contrast, the percentage error in the reaction orders is approximately the same as their respective activation energies. In order to gain a more complete understanding of the relative sensitivities of each of these parameters, a parametric study was carried out.

4.5.2 Arrhenius Model Sensitivity Analysis

Before modeling of the empirical data, a sensitivity analysis was carried out to determine the relative sensitivities of the Arrhenius model to each of the reaction coefficients. Figures 4.9-4.11 illustrate the sensitivity of the model to the activation energy, reaction rate, and reaction order respectively. The baseline reaction used in each case had material properties with E = 150 kJ/mol, k = 1 x 10^9 $min.^{-1}$, and n = 1. A heating rate of 5°C/min. was used to generate each of the profiles.

Three quite different behaviors are apparent. The height and location of the peak, as well as the resulting shape of the mass loss rate curve, is highly dependent on the activation energy, with small changes in E producing significant changes in the mass loss rate curves. As the activation energy decreases the curves tend to shift to the left due to less energy being required to initiate the reaction. The magnitude of the peak also increases, along with a narrowing of the temperature range which is required to bring the reaction to completion. Higher activation energies cause a shift to the right and also result in a shallower, more broad profile than before. This is a result of the higher energy which is now required to activate (and accelerate) the degradation mechanism.

A similar change in the mass loss rate profiles is observed when the

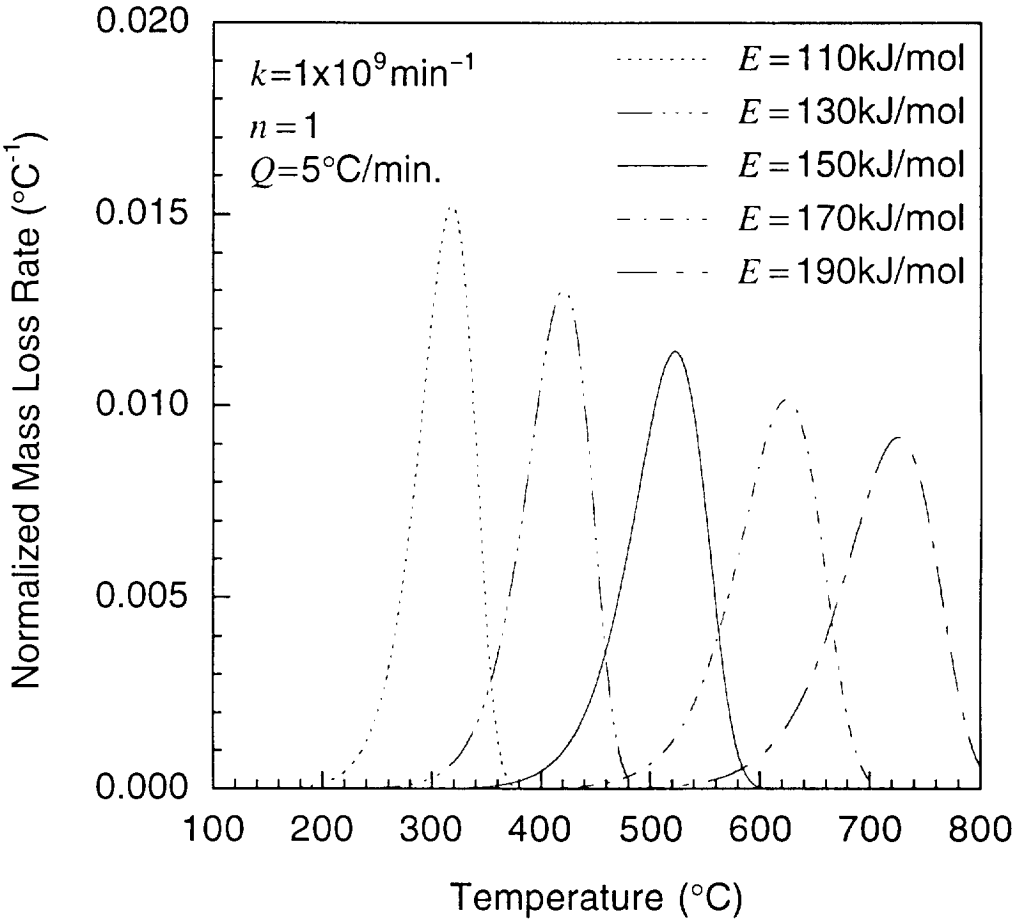

Figure 4.9 Sensitivity of mass loss rate to activation energy.

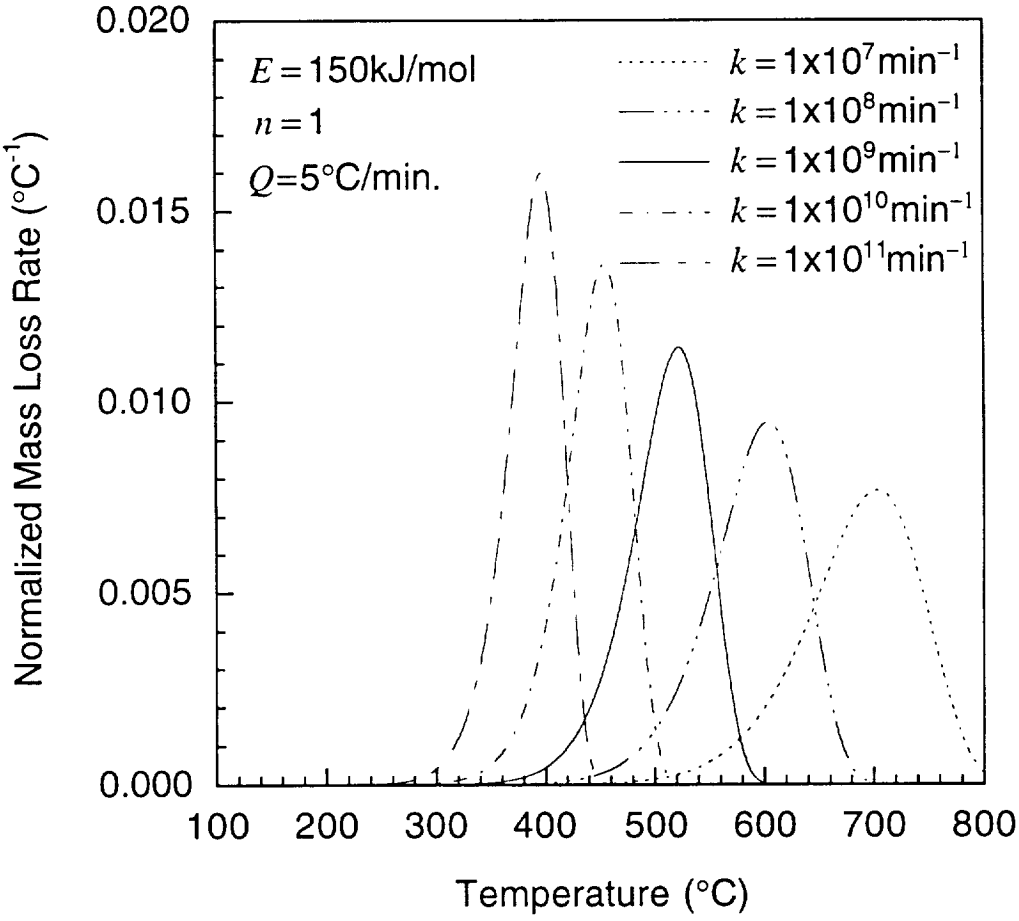

Figure 4.10 Sensitivity of mass loss rate to reaction rate constant.

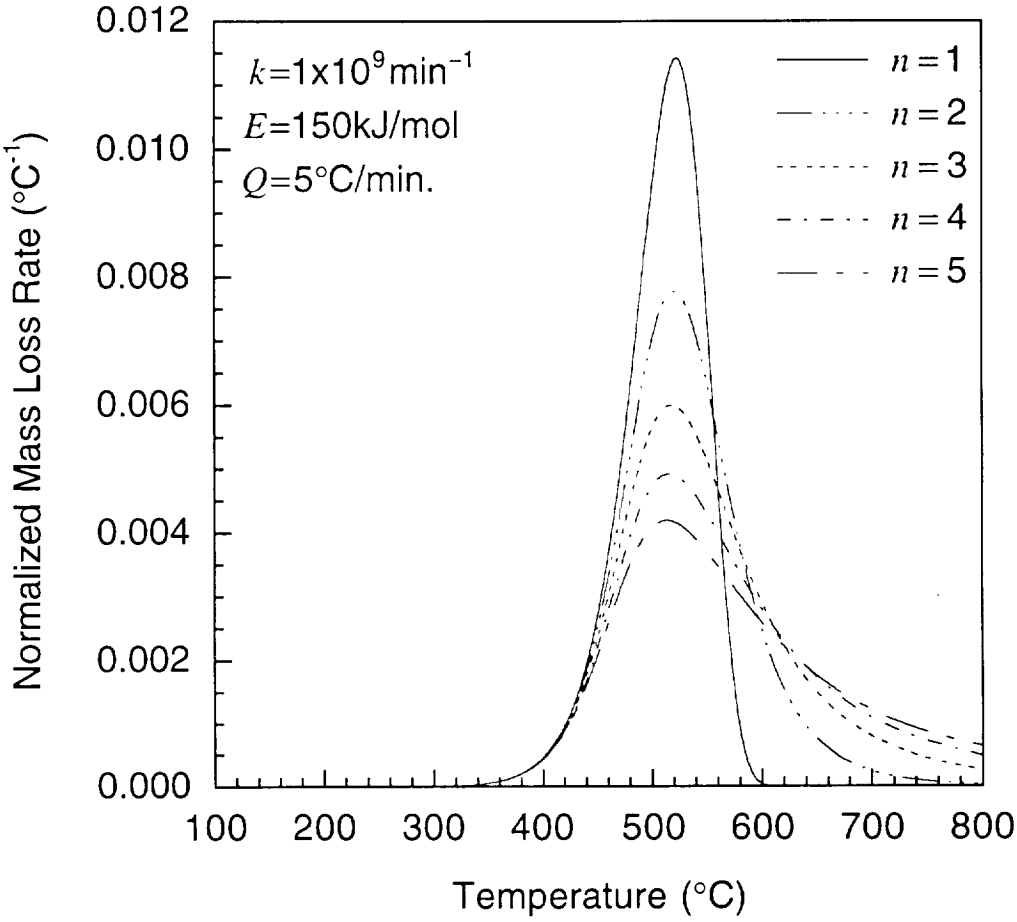

Figure 4.11 Sensitivity of mass loss rate to reaction order.

reaction rate constant is changed. The reaction rate is indicative of the frequency at which a particular degradation mechanism occurs. Hence as k is increased, the reaction rate at lower temperatures will also increase. This produces the same shifts in the profiles as occur when the activation energy is decreased. However, the sensitivity to changes in the reaction rate constant is considerably less than that for the activation energy, with a change of at least an order of magnitude required to produce a similar effect to that found for a 10% change in the activation energy.

When the reaction order is varied, the mass loss rate peak demonstrates a change in magnitude but not in location. As the reaction order is increased from unity, the magnitude of the peak decreases rapidly at first, and then more slowly as the reaction order becomes increasingly higher. This change in magnitude is accompanied by a broadening of the tail of the reaction, although the initial portion of the curve remains relatively unaffected. The reason for this is that low values of α, the $(1-\alpha)^n$ term does not change significantly as the reaction order increases. However, as α becomes non-trivial the behavior of the curve becomes dominated by the $(1-\alpha)^n$ term for high reaction orders. This causes a rapid suppression of the reaction rate early in the reaction process and results in a longer tail with the reaction slowly burning itself out at the higher temperatures.

The sensitivities shown here are also reflected in the reaction coefficients which were returned from the data fit to the pseudo-data. In the case of the two reaction model, the activation energy of the first reaction is underestimated by 1%. This underestimation causes a slight shift of the mass loss curves to the left, a shift which is compensated for by a decrease in the reaction rate constant which will cause the curve to shift back to the right. However, because the mass loss rates are much less sensitive to the

reaction rate constant, a significantly larger change in k is required (in this case a 22% decrease in k is necessitated). In the case of the second reaction, the activation energy is overestimated by approximately 1% causing a shift of the mass loss rate curves to the left. This shift is compensated for by a 27% increase in k which shifts the mass loss rate curve back to the right. In each of these cases the high sensitivity of the model to low values of the reaction order n, results in only minor errors in the reaction order.

The sensitivity analysis indicates that, due to the nature in which E and k interact, several combinations of different values of E and k may exist which will allow very close fits to data at a variety of heating rates. However, the high sensitivity of the model to parameters such as the activation energy and reaction order forces a solution in which E and n are very close to the exact values. Any minor errors which may occur in the activation energy may be compensated for by an appropriate increase or decrease in the reaction rate constant while still maintaining excellent agreement with the data. This is clearly the case for the reaction coefficients recovered from the pseudo-data.

Figure 4.12 shows an extrapolation of the behavior of the data fit coefficients for the first reaction in Table 4.2 to very high and very low heating rates. The curves for the pseudo-data and the data fit coefficients are indistinguishable. It is interesting to note that it is also possible to extrapolate from these coefficients to the extreme case of isothermal behavior with very good confidence. Figure 4.13 shows a comparison between the isothermal behaviors of the pseudo-data reaction coefficients and those of the data fit derived reaction coefficients for the first Arrhenius reaction. As in the dynamic heating case, excellent agreement is found.

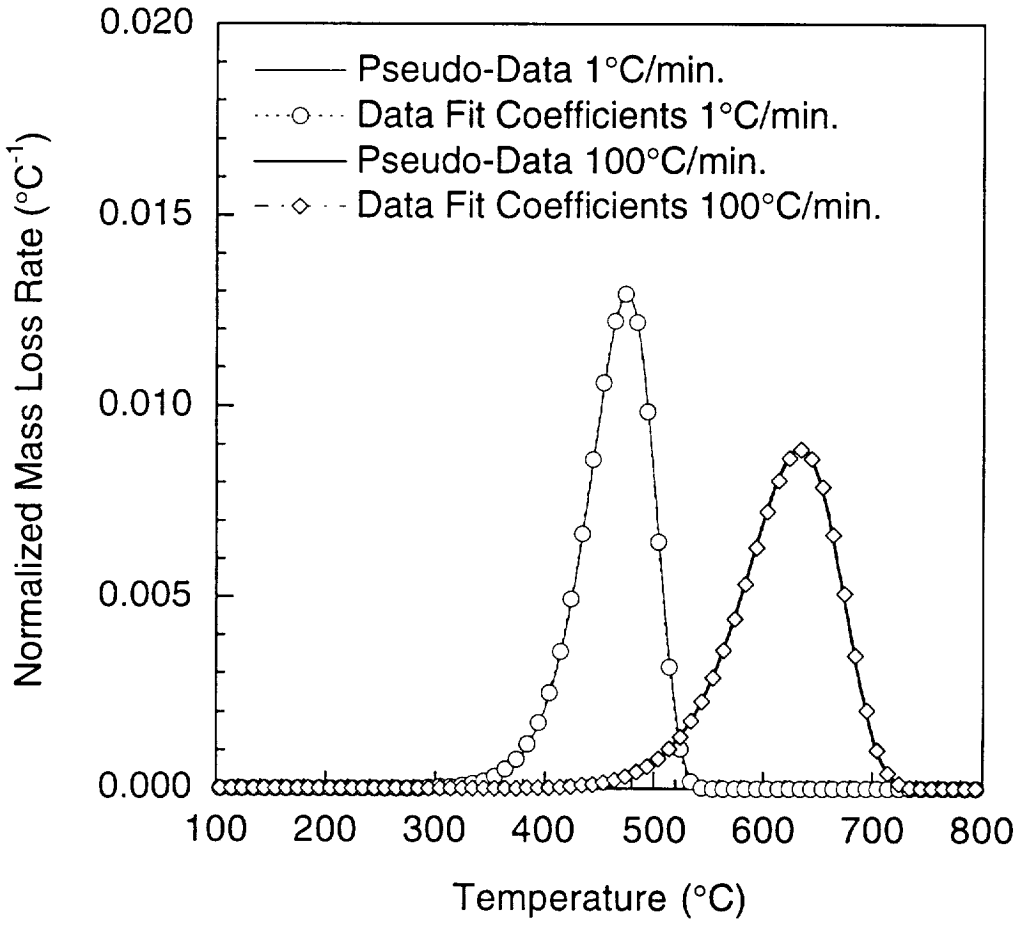

Figure 4.12 Comparison between mass loss rates for pseudo-data and data fit derived reaction coefficients at 1°C/min. and 100°C/min.

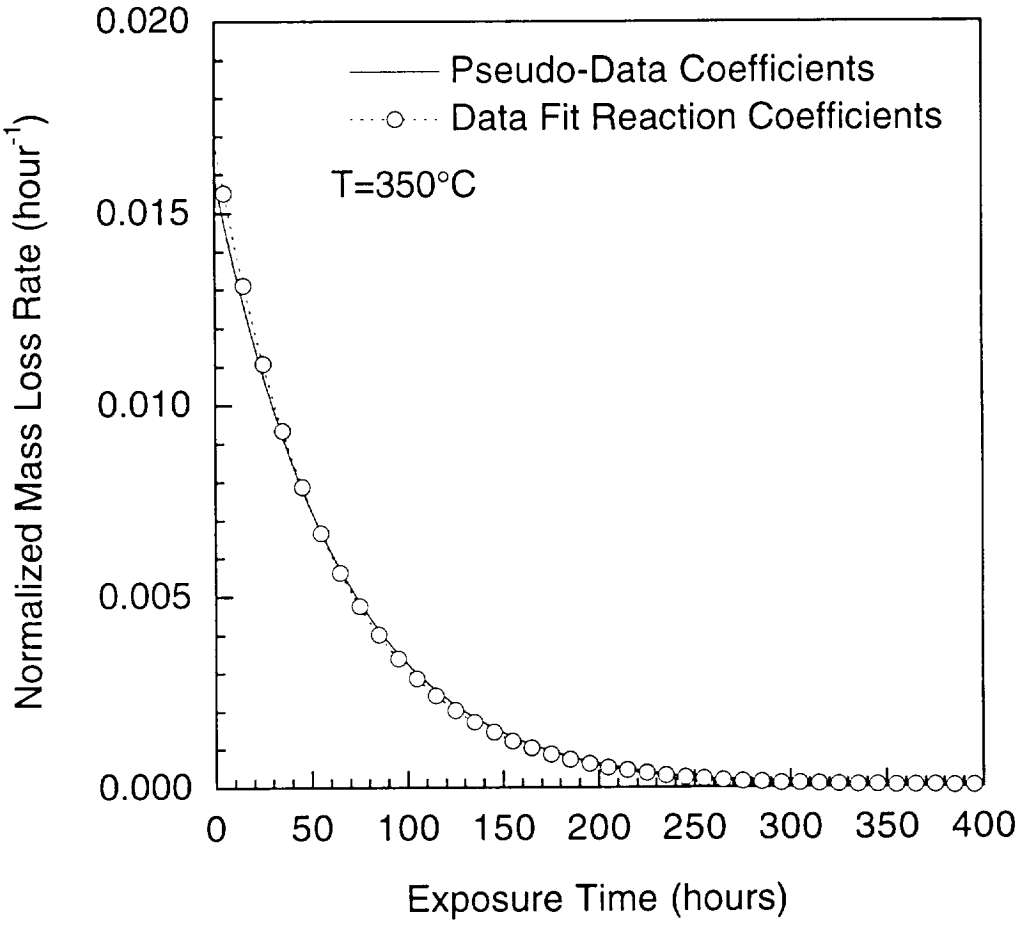

Figure 4.13 Comparison between isothermal behavior of pseudo-data and data fit derived reaction coefficients at 350°C.

CHAPTER 5

EXPERIMENTAL PROCEDURES

An experimental study was carried out to provide quantitative data for the analytical models described in Chapter 4. The empirical data not only provides the necessary coefficients for the analysis but also allows us to gain important insights into the physics involved in the degradation of composite laminates. In this chapter the test matrices, and the justification behind their design, are presented. Both neat PMR-15 resin and T650-35/PMR-15 unidirectional composites were considered. The details of specimen preparation, experimental set-up, experimental procedures and data collection are also described.

5.1 TEST MATRICES

Both neat resin and unidirectional specimens were used in the experimental investigation. Neat resin in both a powder form and in the form of rectangular macroscopic specimens was considered. The test matrices were designed based on preliminary parametric studies which were carried out using the analytical model. Correlation of the results from these studies with previously collected empirical data suggested that matrix degradation is limited by the diffusion of oxygen from the surrounding environment into the material bulk. As a result, the reaction coefficients determined from finite-sized specimens may be confounded by mass transfer effects and thus cannot be used to quantify the degradation at a point in the material. This effect has also

been noted by Tsotsis [45], who suggested the use of specimens with large surface area to volume ratios in determining kinetic parameters. Through the use of these parametric studies it became very clear that if a mechanistic approach was to be used to model the degradation of these materials then both accurate reaction and diffusion coefficients would be required. The test matrices presented here were designed in such a way as to allow the necessary coefficients to be extracted from the data and also to provide sufficient data to allow a complete validation of the modeling approach. Emphasis was placed on obtaining data which would provide both qualitative and, more importantly, quantitative data on the degradation mechanisms while also illustrating interesting trends.

The material systems used in this study were PMR-15 neat resin, and T650-35/PMR-15 unidirectional specimens. All materials were manufactured at the NASA Lewis Research Center. Dynamic heating thermogravimetric analyses (TGAs) were carried out on PMR-15 neat resin powder or shavings in nitrogen, air and oxygen atmospheres. This allowed the quantification of the kinetic parameters in both thermal and oxidative atmospheres without the additional complications introduced by diffusion dominated effects. The material used in the thermogravimetric analyses was initially cured in plates and was then reduced to powder or shaving form. This ensured that the initial chemical state of the material was the same as that used in real structures. The test matrix used for the thermogravimetric analyses in shown in Table 5.1. Several isothermal TGAs were also carried out in nitrogen to validate coefficients derived from the dynamic heating tests.

Small rectangular neat resin and unidirectional composite specimens were subjected to short-term isothermal aging to identify diffusion effects. Samples with different aspect ratios were used to separate out both geometry

Table 5.1 Neat Resin[Δ] TGA Test Matrix

	Atmosphere		
Heating Rate[†] (°C/min.)	Nitrogen	Air	Oxygen
2	3		
5	3		
7	3		
10	5	3	3
15	5	3	3
20	5	3	3
Isothermal Exposure Temperature[††] (°C)			
300	1		
340	1		
380	1		

[Δ] All specimens in form of fine powders or shavings.

[†] Dynamic heating TGAs heated to a maximum of 800°C.

[††] Exposure time of 10 hours at isothermal TGA temperature.

effects and the diffusion effects in different directions. Mass loss from the specimens was recorded periodically, as were the dimensional changes. The growth of the degraded surface layers in the interiors of the specimens were analyzed by optical microscopy. The test matrix for these tests is shown in Table 5.2. Specimen sizes were carefully chosen to maximize the surface area to volume ratio effects and also, in the case of the composite specimens, to maximize the contribution of different exposed surfaces to the overall degradation mechanisms. Through the use of such an approach, it is possible to separate out the individual contributions of each exposed surface during the data reduction procedures. The notation use in Table 5.2 is illustrated in Figure 5.1.

5.2 TEST SPECIMEN MANUFACTURE AND PREPARATION

All specimens were manufactured at the NASA Lewis Research Center using standard manufacturing procedures developed for the PMR polyimides. The details of these procedures may be found in [7]. These procedures have been shown to yield low-void, high quality laminates [57]. A total of three PMR-15 neat resin panels (one 102 mm x 102 mm (4" x 4") panel and two 152 mm x 152 mm (6" x 6") panels) and two 12 ply, 305 mm x 305 mm (12" x 12") unidirectional T650-35/PMR-15 panels were obtained. Nominal ply thickness for the unidirectional specimens was 0.2 mm (0.008"). All composite laminates had a fiber volume fraction equal to 0.50. After curing, all specimens were subjected to a 16 hour free-standing post-cure in air at 316°C. Ultrasonic C-scan traces of the unidirectional panels before and after post-cure indicated that the quality of both laminates was very good.

Specimens were taken from each of the three neat resin plates for use in the thermogravimetric analyses. Narrow strips (approximately 5 mm wide)

Table 5.2 Short-Term Isothermal Exposure Test Matrix

	316°C (600°F)	343°C (650°F)	$A^{\dagger}/V$ (mm^{-1})	$A_1/A^{\dagger}$	$A_2/A^{\dagger}$	$A_3/A^{\dagger}$
Neat Resin						
76.2 x 3.2 x 3.2	8	8	1.29	0.490	0.490	0.020
76.2 x 6.4 x 3.2	8	8	0.97	0.649	0.324	0.027
25.4 x 25.4 x 3.2	8	8	0.79	0.800	0.100	0.100
Unidirectional[††]						
76.2 x 3.2 x 2.5	8	8	1.44	0.546	0.436	0.018
3.2 x 76.2 x 2.5	8	8	1.44	0.546	0.018	0.436
25.4 x 25.4 x 2.5	8	8	0.94	0.833	0.083	0.083

All dimensions in mm.

[†] Total cross-sectional area of specimen.

[††] All unidirectional specimens are 12 ply T650-35/PMR-15 composites.

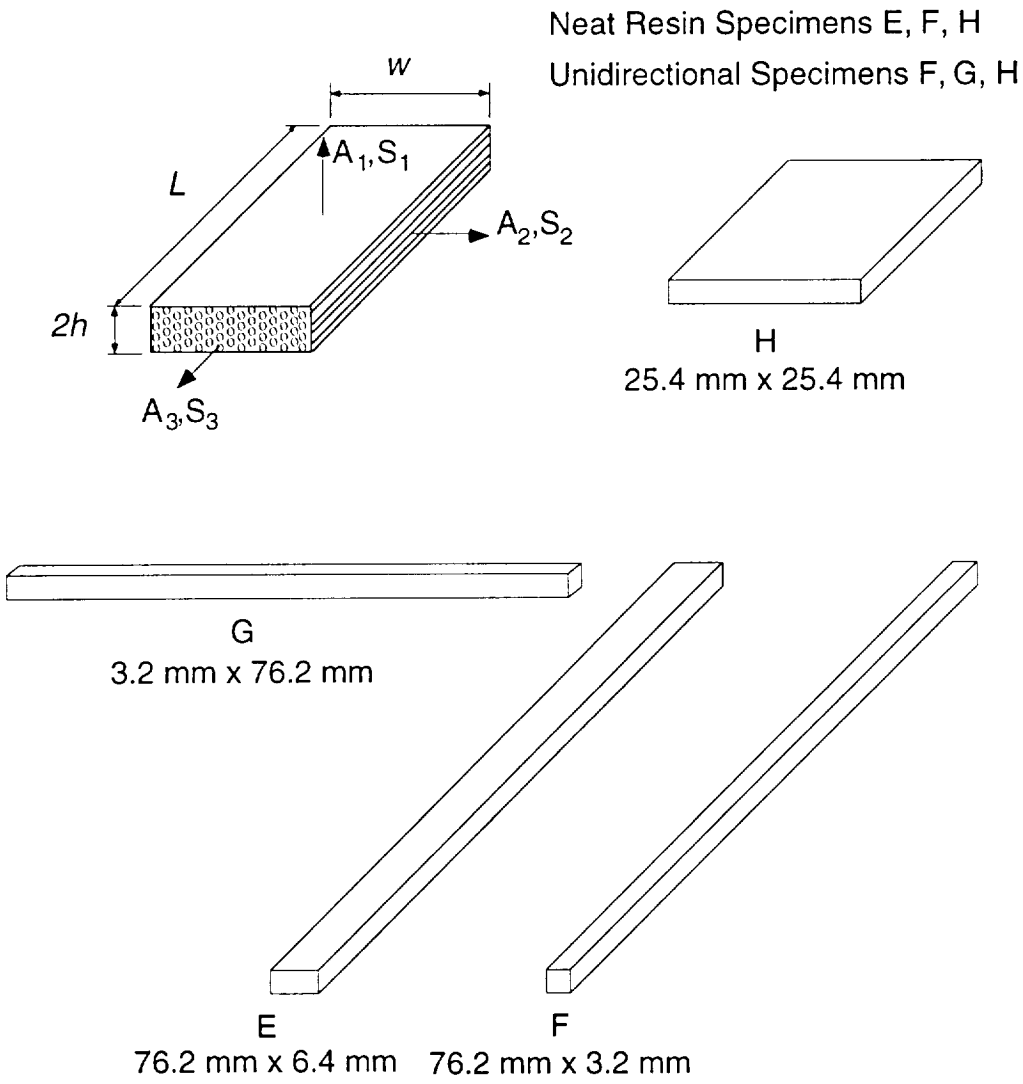

Figure 5.1 Specimen dimensions.

were cut from the neat resin plates using a water-cooled diamond blade. These strips were then broken into several small pieces and placed into a standard coffee grinder, along with some dry ice. As the neat resin is extremely tough, it is necessary to use dry ice in the grinding process in order to make the polymer more brittle and easier to grind. Specimens were then ground for approximately five minutes, with more dry ice being added if the previous batch had evaporated before the grinding process was complete. The powder which was produced in this manner was then sifted through calibrated sieves to obtain the required grade of powder for analysis. A fine, light-brown powder was obtained from each sample through the use of this technique. The use of dry ice in the grinding procedure also ensured that no residue would be left on the powder once the samples had been dried after grinding.

One batch of powder produced in this manner produced highly atypical mass loss rates curves when tested in oxygen. Upon inspection of this batch of powder, which had been ground from plaque C specifically for the tests in pure oxygen, small particles of another polymer were found mixed into the neat resin. It was determined that these particles had come from several shards of the plastic blade casing in the grinder which had broken off during the grinding of that batch. The grinder was replaced and the results obtained for that batch of powder were disregarded in further analyses. This batch of powder was the only one which experienced this problem.

The use of a ball-milling machine was also investigated as a means for producing a fine powder, however, the heptane solution which was used to prevent particles from sticking to the walls of the container during the milling procedure resulted in the formation of a thick residual coating on the PMR-15 powder at the end of the process. This residue could not be separated from the powder and so the powder had to be discarded.

Initially, several thermogravimetric analyses were carried out in air on unsieved particles as well as particles which had been separated out using a number of different sieves. These tests indicated that the particles obtained through the use of a No. 40 U.S.A. Standard Testing Sieve (425 micron grating) was sufficiently small to ensure that the effects of diffusion on the weight loss behavior in oxidative environments would be negligible. Analyses carried out using particles obtained from a No. 80 sieve (180 micron grating) revealed no measurable differences in the magnitude and location of the peaks in the TGA mass loss rate curves over those found for the No. 40 sieve.

All powders produced in this manner were placed in small, unsealed glass jars into the post-cure oven for 2 hours at 125°C to remove any residual moisture. Due to the large surface area of the particles, the removal of moisture from the specimens is achieved in relatively small amounts of time (compared to the macroscopic specimens). This large surface area also has a secondary effect which is to allow moisture to diffuse very quickly back into the specimen. The neat resin powder was found to be very hygroscopic, rapidly absorbing moisture from the air upon removal from the post-cure oven. The glass jars were immediately sealed after removal from the post-cure oven and the specimens were stored like this until testing. Shavings from each of the neat resin panels were also produced for use in the TGAs in nitrogen. These shavings were obtained from the specimen edges by drawing a clean, sharp stainless-steel blade along the edges of the specimens. Very thin shavings (less than 100 microns thick) were obtained in this manner. All shavings were dried and stored in the same manner as the powdered specimens.

Unidirectional and neat resin specimens for use in the short-term isothermal tests were manufactured from each of two unidirectional and two neat resin panels as per the cutting plan shown in Figure 5.2. The designation

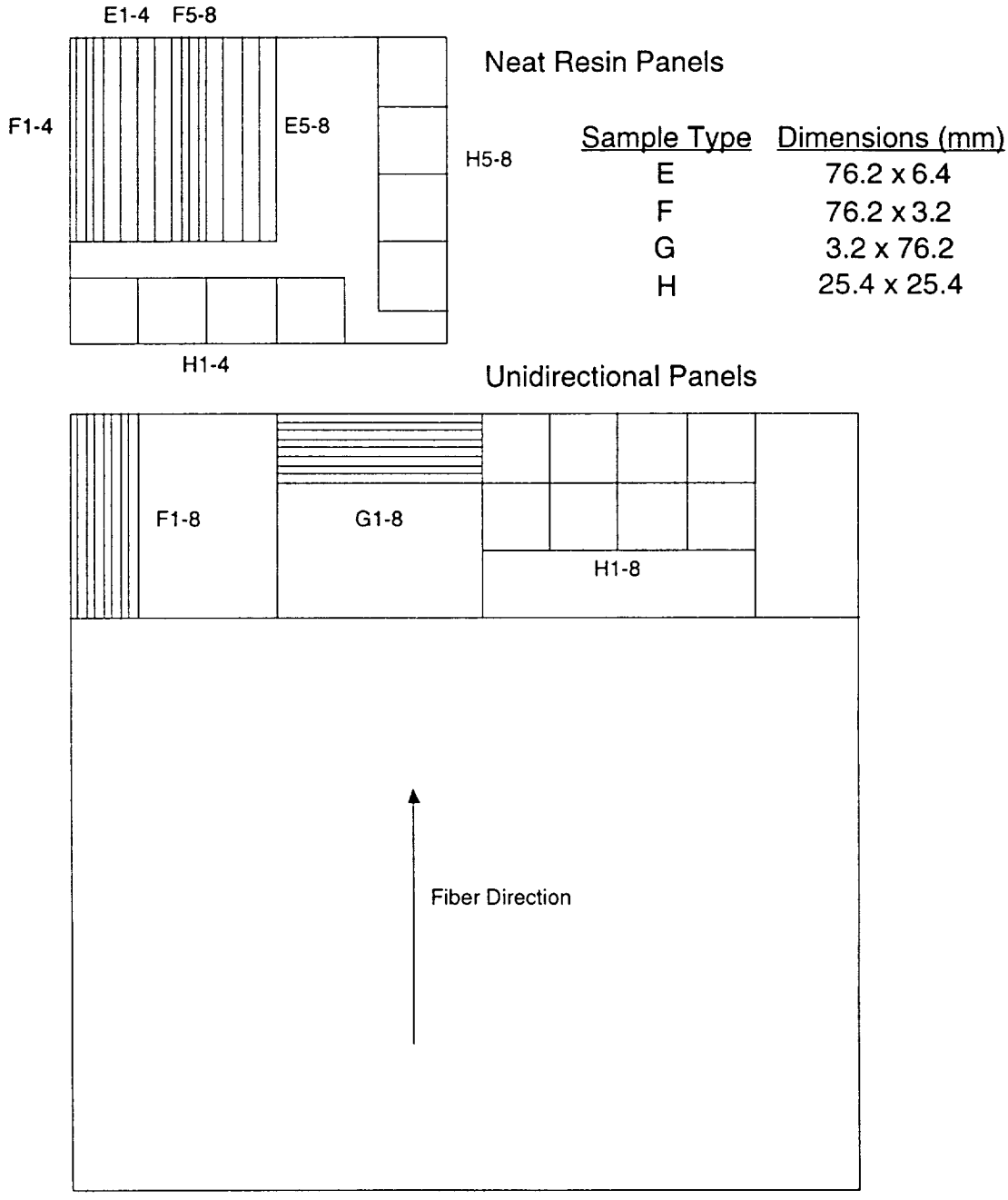

Figure 5.2 Cutting plan for all panels.

used for each of the specimen types is also included in this figure. Two neat resin and two unidirectional panels were used to allow inherent batch-to-batch variations to be accounted for, with half of the total number of specimens being taken from each panel. All specimens were cut to the required dimensions using a water-cooled diamond blade. In the case of the F and G type specimens cut from the unidirectional panels, two 76.2 mm x 76.2 mm (3" x 3") squares were first cut from the panels. Specimens were then manufactured from these sections. A similar approach was used for the neat resin E and F type specimens.

After cutting, the dimensions and masses of all the specimens were recorded. Width and length measurements were taken using a dial calipers with a resolution of ±10 microns. Thickness measurements were taken using a micrometer with a resolution of ±1 micron. A single width and length measurement were taken for each sample. All samples possessed an inherent variation in thickness and so three thickness measurements were taken along the length of each specimen. One reading was taken at each end, and a third was taken in the center of the specimen. The average thickness of each specimen was used in all subsequent calculations. All mass measurements were made using a Mettler AE100 balance which has an accuracy of ±0.1 milligrams. Dimensional and mass measurements were all recorded manually and then entered into a spreadsheet for reduction at a later stage. After manufacture, all specimens were dried in the post-cure oven for a minimum of 18 hours at 125°C prior to testing. After drying, dimensional and mass measurements were again recorded and the samples were then placed immediately into the thermal environment chamber for subsequent testing.

It was found during isothermal testing that some of the samples aged at 316°C had not been completely dried out before testing. Samples aged at

316°C had been dried for a total of 18 hours. However, it was noticed that some specimens demonstrated a rather large mass loss in the first 24 hours of aging. A comparison between the amount of moisture which had been desorbed from the different sample groups revealed that significantly different amounts of moisture had been desorbed from each during the drying period. The percentage moisture desorbed from the neat resin groups E, F, and H were 1.85%, 1.97%, and 1.77% respectively, while the percentage moisture desorbed from unidirectional groups F, G, and H were 0.68%, 0.79%, and 0.54% .

The samples which were prepared for aging at 343°C were then dried for a total of 30 hours, with the samples being weighed periodically to determine whether all of the moisture had been desorbed. A survey of this data revealed that after 18 hours only the neat resin F type specimens and unidirectional G type specimens had completely dried out. All other sample groups still retained moisture up to 24 hours at 125°C. As a result all the 316°C data which was used in subsequent analyses was corrected to compensate for residual moisture retained after the 18 hour drying period. It was assumed that the correct initial moisture content was measured while drying the F resin specimens and G unidirectional composites and hence the other specimen groups started with a known level of moisture. The initial mass loss due to this moisture was discounted in the corrected data. The uncorrected measurements from all specimens are reported in Appendix D. All raw dimensional and mass measurements recorded over the duration of the two isothermal aging runs are contained in this appendix.

5.3 THERMOGRAVIMETRIC EXPERIMENTAL PROCEDURE

5.3.1 TGA 7 Thermogravimetric Analyzer

Thermogravimetric measurements were performed using a Perkin-

Elmer TGA 7 Thermogravimetric Analyzer coupled to a Perkin-Elmer Series 7500 data collection computer. Thermogravimetric analyzers permit the measurement of mass changes in a sample material, resulting from chemical reactions, decomposition or water and solvent desorption, as a function of temperature or time. The TGA 7 is comprised of two major components - a sensitive microbalance and a furnace element. A high temperature furnace, with operating temperatures from 50°C to 1500°C, was used in the current study. A user-programmable controller connected to the furnace allows both isothermal and dynamic heating experiments to be carried out. Heating rates ranging from 0.1°C/min. to 100°C/min. in 0.1°C/min. increments may be used with this furnace. A sensitive platinum-rhodium thermocouple in close proximity to the sample is used to measure sample temperature during an analysis. Temperature at the sample pan may be controlled to within ±5°C of the user-defined temperature.

The microbalance operates as a high gain electromechanical servo system which permits the measurement of mass changes as small as 10 micrograms. When a sample is placed in the sample pan, the beam that supports the sample pan deflects. A beam position detector measures the deflection with an optical sensor and uses current to return the beam to its original position, with the amount of current required being a direct measure of the mass on the beam. The microbalance is isolated from the furnace so that temperature effects on the mass measurements are minimized. A schematic of the analyzer, with the furnace retracted from the sample pan, is shown in Figure 5.3. During operation, the furnace completely surrounds the sample pan and hang-down wire. A platinum sample pan is used in the tests due to the ability of platinum to withstand high temperatures and also because it is chemically inert and thus will not react with the samples under examination.

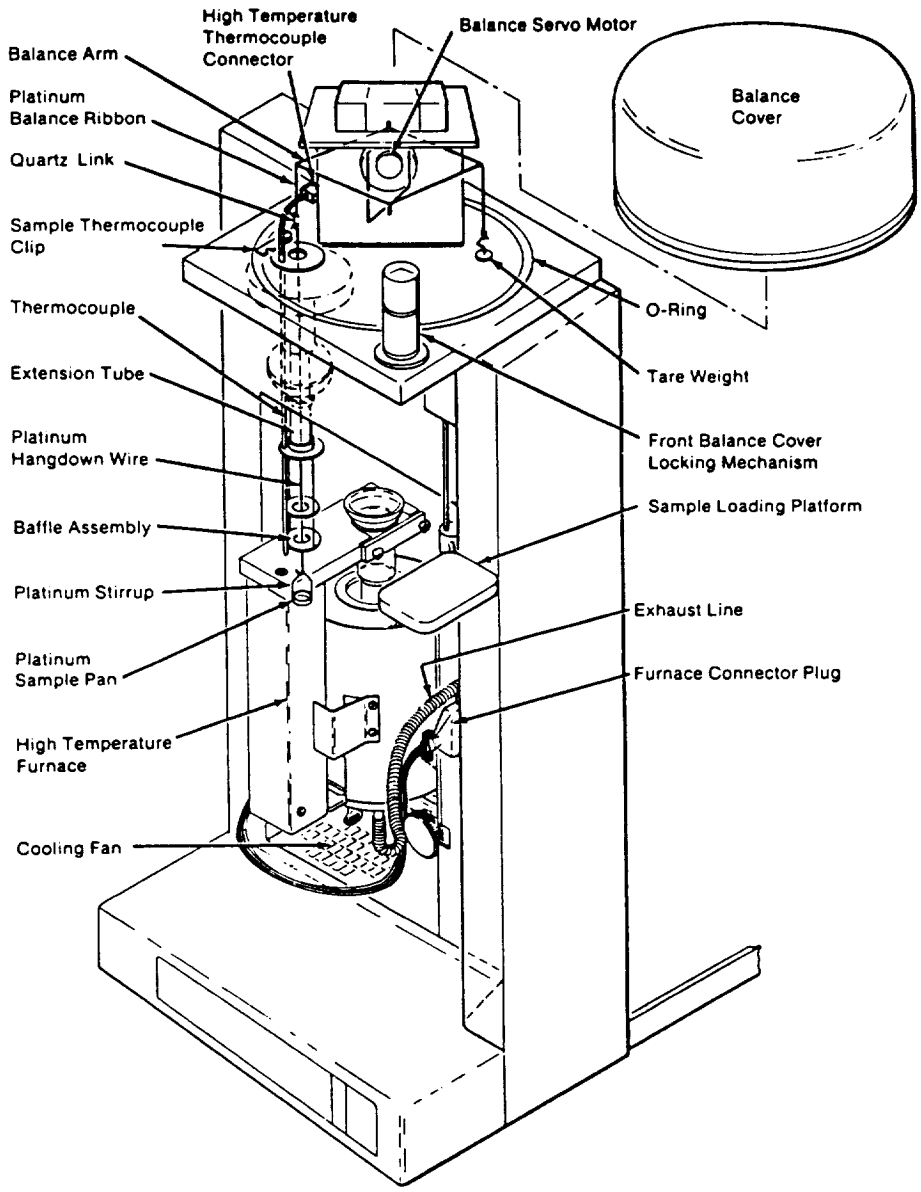

Figure 5.3 Schematic of TGA 7 with high temperature furnace [58].

Data from the thermocouple and microbalance is collected by the data acquisition computer at a frequency which is dependent upon the duration of the test being conducted. Between 500 and 1,000 data points are collected during each analysis.

Several preliminary tests were carried out in order to assess whether the high temperatures alone would affect the microbalance circuitry resulting in a shift or float of the zero set-point. Dynamic heating analyses were carried out at 5°C/min. and 10°C/min. with no sample mounted in the sample pan. The output from the microbalance was set to zero at the beginning of each test. The data collected over the duration of both of these tests is illustrated in Figure 5.4. The maximum deviation from zero occurs at 800°C in both cases. However, the magnitude of this deviation is negligible when compared to the masses and mass losses of the specimens used in the actual analyses. A minimum mass loss of 12 milligrams was recorded at 800°C in dynamic heating tests for samples with an initial mass of 30 milligrams. The change in the zero set-point for isothermal exposures of the sample pan at temperatures in the range of the isothermal tests (300°C to 380°C) was less than 0.01 milligrams. Hence, the temperature-induced fluctuation in the microbalance zero set-point is not a significant source of error in the current investigation.

5.3.2 Dynamic Heating TGA Experiments

Dynamic heating rate experiments were carried out from room temperature up to 800°C at all heating rates. Three different gaseous atmospheres - nitrogen, air and oxygen - were used in the course of testing. Flow rates of 1700 cm^3/hr were used for all test atmospheres. A total of six heating rates ranging from 2°C/min. to 20°C/min. were used in the nitrogen atmosphere, while three heating rates ranging from 10°C/min. to 20°C/min.

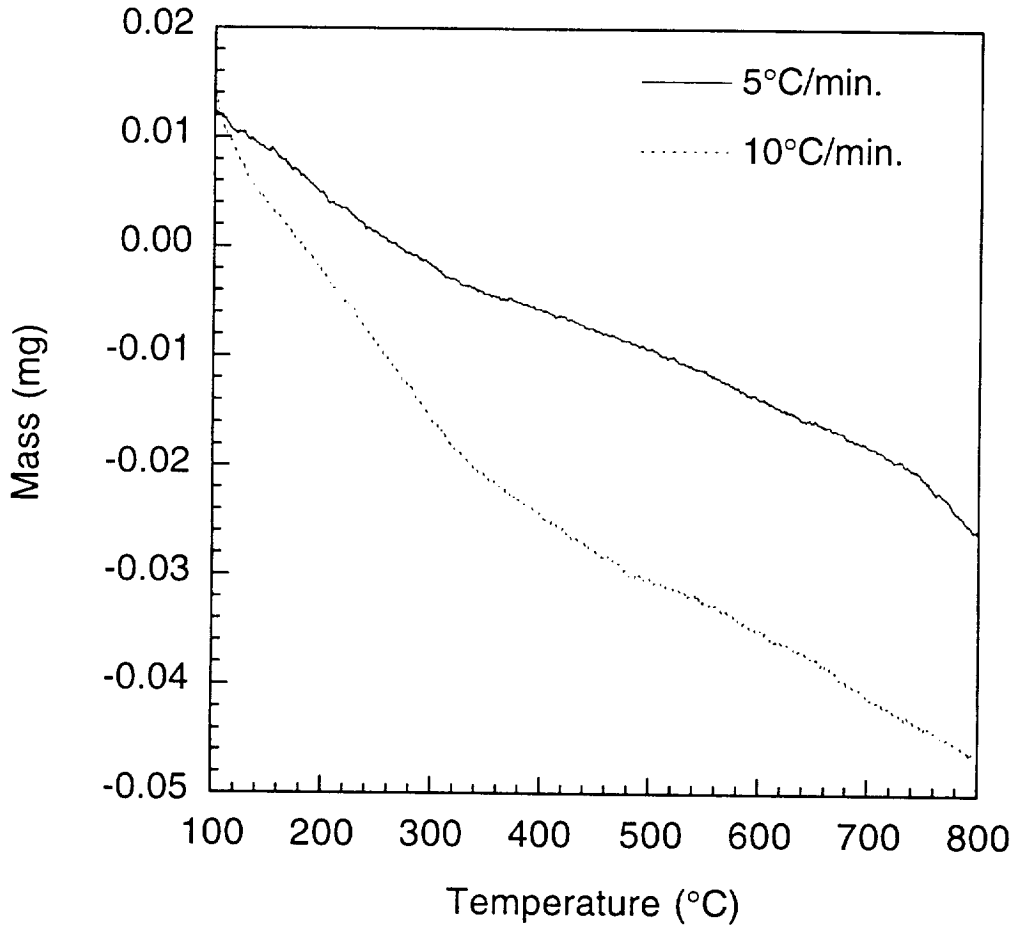

Figure 5.4 Microbalance zero-point variation at different heating rates.

were used in the air and oxygen atmospheres. Initial sample masses for all analyses ranged between 30 and 50 milligrams. Sample mass and mass loss rate profiles as functions of temperature were output from the system.

Due to the fact that the data acquisition system for the TGA uses a non-standard operating system (IDRIS), it was not possible to directly convert the data stored on this system to a convenient spreadsheet form which could then be used for data reduction. Instead, it was necessary to obtain printed plots of the mass and mass loss rate profiles which were required for data reduction. These profiles were converted to graphics files using a Hewlett Packard Scanjet 4C scanner and Adobe Photoshop [59] image editing software. Data from these plots was then collected using DataThief [60] , a public domain software package which allows the user to reverse engineer an accurate set of data from scanned plots. All mass and mass loss rate profiles were converted to spreadsheet form in this manner.

To ensure that this procedure did not result in a loss of the accuracy of the data, several data points from a number of samples aged in nitrogen were taken directly from the data acquisition computer and compared to those obtained from the plots recorded by the DataThief package. Both mass and mass loss rate data for several samples subjected to different heating rates in nitrogen were compared. Table 5.3 shows a comparison between the actual data, taken directly from the data-acquisition computer screen, and that measured by DataThief at 450°C. Both the mass and mass loss rates change rapidly in this region and so comparisons between the two sets of data from this temperature region should be indicative of the accuracy of the data retrieval method. As shown in Table 5.3, a maximum discrepancy of 1% exists between the actual data and that captured by the DataThief software, allowing confidence that the data presented in the DataThief-derived

Table 5.3 Mass Loss and Mass Loss Rates at 450°C in Nitrogen

	Actual		DataThief		Difference (%)	
	Mass (mg)	Rate (mg/min.)	Mass (mg)	Rate (mg/min.)	Mass	Rate
10°C/min.						
Sample 1	37.05	-0.497	36.92	-0.496	-0.35	-0.20
Sample 2	38.04	-0.547	38.08	-0.546	0.11	-0.18
Sample 3	42.16	-0.661	42.10	-0.667	-0.14	0.90
15°C/min.						
Sample 1	42.95	-0.726	42.98	-0.731	0.09	0.69
Sample 2	46.25	-0.764	46.19	-0.771	-0.13	0.90
Sample 3	44.96	-0.763	44.60	-0.769	-0.83	0.79
20°C/min.						
Sample 1	49.37	-0.943	49.25	-0.945	-0.24	0.21
Sample 2	48.00	-0.844	47.77	-0.843	-0.48	-0.12
Sample 3	48.08	-0.855	48.03	-0.864	-0.10	1.05

spreadsheets is an accurate representation of the TGA data.

Typically, between 600 and 800 data points were collected by DataThief from each of the sample profiles. The data collected in this manner was then linearly interpolated so that a total of 701 data points, one data point for each degree Celsius between 100°C and 800°C, was stored for each profile. Means and standard deviations for each set of samples at each of the heating rates were calculated. The TGA data reduction procedure, described in Chapter 4, was then applied to this data to determine the required kinetic parameters.

5.3.3 Isothermal TGA Experiments

Three isothermal tests, having a total of 10 hours exposure time, were also carried out in nitrogen. In the case of isothermal tests, it is desirable to achieve the required temperature as quickly as possible in order to avoid mass loss at temperatures other than that being considered. To achieve this, high heating rates were used to reach the exposure temperature in a minimum amount of time. Samples were initially heated to 125°C where they were held for 10 minutes to eliminate any residual moisture which may have diffused back into the material during storage. Several test runs indicated that this time was sufficient to remove any moisture which may have been absorbed. This additional step is necessary in the isothermal test because of the initially high heating rates which may not allow all of the moisture to be baked out of the specimen before it reaches its target temperature if the sample is heating directly from room temperature. Samples were then heated from 125°C to the test temperature at a rate of 50°C/min. and held at the required exposure temperature for a total of 10 hours.

Because of the very high heating rate used to achieve the exposure temperature, an initial overshoot ranging from 25°C and 40°C was experienced

in each of the isothermal tests. Figure 5.5 shows the programmed and actual temperature profiles for the first 30 minutes of the 300°C isothermal run, as measured by the thermocouple near the sample pan. Overshoots are experienced at the beginning of both the 125°C and 300°C isothermal hold portions of the profile. In both cases the overshoot was corrected within 10 minutes of the time at which the overshoot first occurred. This behavior is seen at all isothermal temperatures, with the overshoot being compensated for in less than 10 minutes, regardless of the final exposure temperature. The actual temperature profiles from each run were used in subsequent modeling of the data in order to ensure that any significantly accelerated degradation which may have occurred at the higher temperatures could be accounted for.

5.4 ISOTHERMAL AGING OF MACROSCOPIC SPECIMENS

5.4.1 Isothermal Aging Test Procedure

All macroscopic neat resin and composite samples were aged in a thermal environment chamber. The chamber used electric resistance rods for heating and a maximum temperature of 427°C could be achieved. A stainless steel wire rack was used to support the specimens within the chamber. Specimens were closely grouped in the central region of the chamber in order to minimize the temperature gradients across the specimens at the high exposure temperatures. Internal chamber dimensions were 30.2 cm x 10.2 cm x 10.2 cm (12" x 4" x 4"), and specimens were grouped within a 10.2 cm x 7.6 cm x 10.2 cm (4" x 3" x 4") region in the middle of the oven. Care was taken to ensure that all surfaces of the specimens were exposed to the aging atmosphere. The specimens were shielded from direct heat radiation from the heating rods and were heated and cooled by fan-circulated air only. The temperature of the chamber was controlled through the use of an Omega

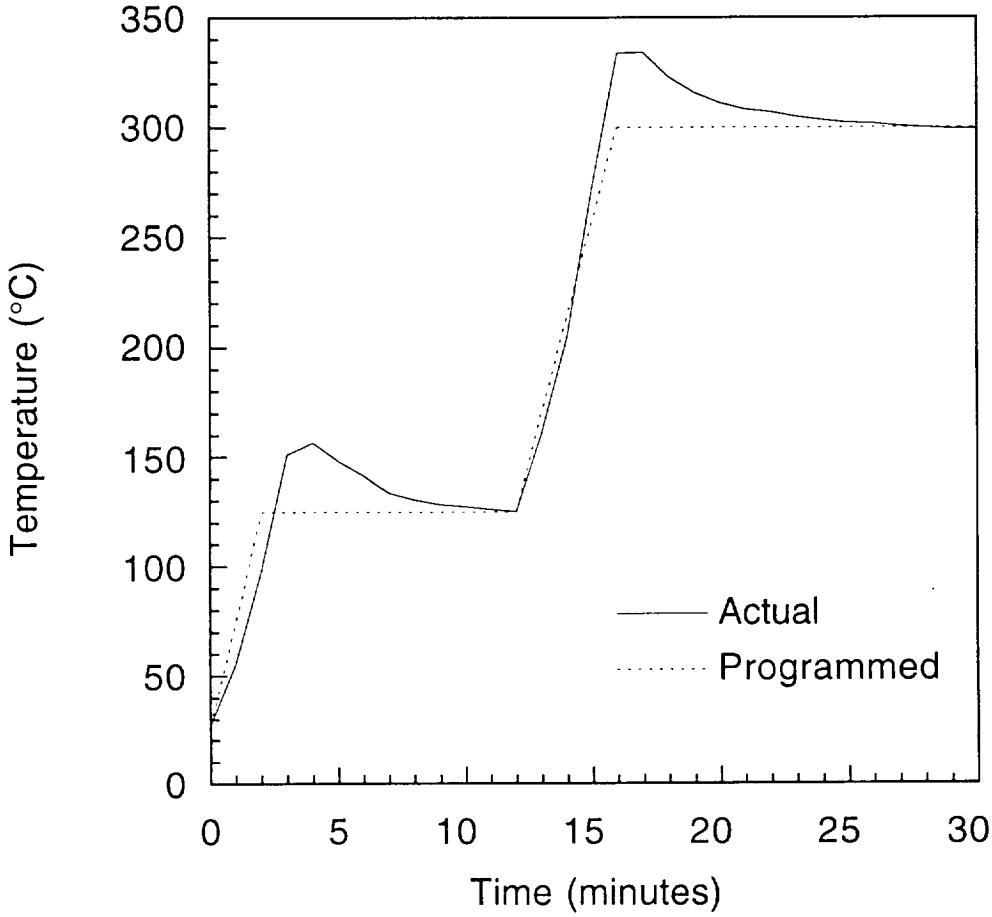

Figure 5.5 Temperature profile for 300°C isothermal run.

temperature controller. This microprocessor-based controller could be programmed to any user-defined thermal profile consisting of a series of linear segments. A single J-type thermocouple provided feedback to the controller. Over 100 tuning runs had been carried out in a previous study to determine the optimum controller tuning settings and feedback thermocouple location [61]. These settings were not altered in the current study.

Three additional K-type thermocouples were mounted within the chamber in order to monitor the temperature gradients across the region in which the specimens were placed. The thermocouples were arranged vertically with a single thermocouple at the top, middle and bottom of the sample arrangement. Because of the extended isothermal exposure times, and small thermal mass of the specimens, it was possible to assume that at steady state the samples would have the same temperature as the surrounding environment and so it was not necessary to mount thermocouples directly onto the specimens. Thermocouple outputs were fed into a National Instruments breakout box, which was in turn interfaced with an Apple PowerMacintosh through a National Instruments analog-to-digital converter. Thermocouple readings were recorded and displayed in a virtual strip chart by the LabVIEW®3 data acquisition software. The thermocouples were used to record temperatures at the different locations across the specimens during the isothermal-hold portions of the run. As it was not feasible to record the data output from these thermocouples for the entire duration of the tests (in excess of 250 hours in total) only a single short period during one of the isothermal portions of each run was monitored in this manner. This was sufficient to determine the thermal gradients in the region of interest at each of the different exposure temperatures. A single J-type thermocouple, mounted near the control thermocouple, was connected to an Omega chart recorder which

ran for the duration of the test runs. This provided a record of the temperature profile for the chamber over the entire exposure time.

Table 5.4 shows the temperature gradients across the specimen arrangement for each of the isothermal exposure temperatures. The temperatures shown in this table were recorded over a four hour period during one of the isothermal hold portions of each of the runs. The temperatures at these thermocouples fluctuated by less than 2°C from the temperatures shown in Table 5.4 over the entire four hour period. At both exposure temperatures, a temperature gradient of approximately 10°C is experienced across the specimen arrangement. The highest temperature is experienced at the bottom of the specimen grouping which is closest to the location of the heating elements. The temperature decreases in an approximately linear fashion as we move further away from the heat source. Efforts to decrease the gradient across the specimens through repositioning of the specimen rack, or reorganization of the manner in which the specimens were grouped, were unsuccessful. Figure 5.6 shows a schematic of the specimen and thermocouple locations in the environmental chamber. Only the H type samples experience the temperature gradients shown in Table 5.4. All other samples are grouped close to the bottom of the specimen rack where a temperature very close to the target temperature is maintained.

5.4.2 Measurement of Mass Loss and Dimensional Changes

Dimensional and mass measurements were taken for each of the test specimens immediately after drying, prior to being placed in the oven, as described in Section 5.2. Specimens were then heated to the required isothermal exposure temperature (316°C or 343°C) and held at that temperature for 24 hours. The heating elements were then turned off and oven

Table 5.4 Thermal Chamber Steady-State Temperature Gradients

	Thermocouple Readings		
Target Temperature	Thermocouple 1	Thermocouple 2	Thermocouple 3
316°C	304°C	309°C	315°C
343°C	332°C	337°C	340°C

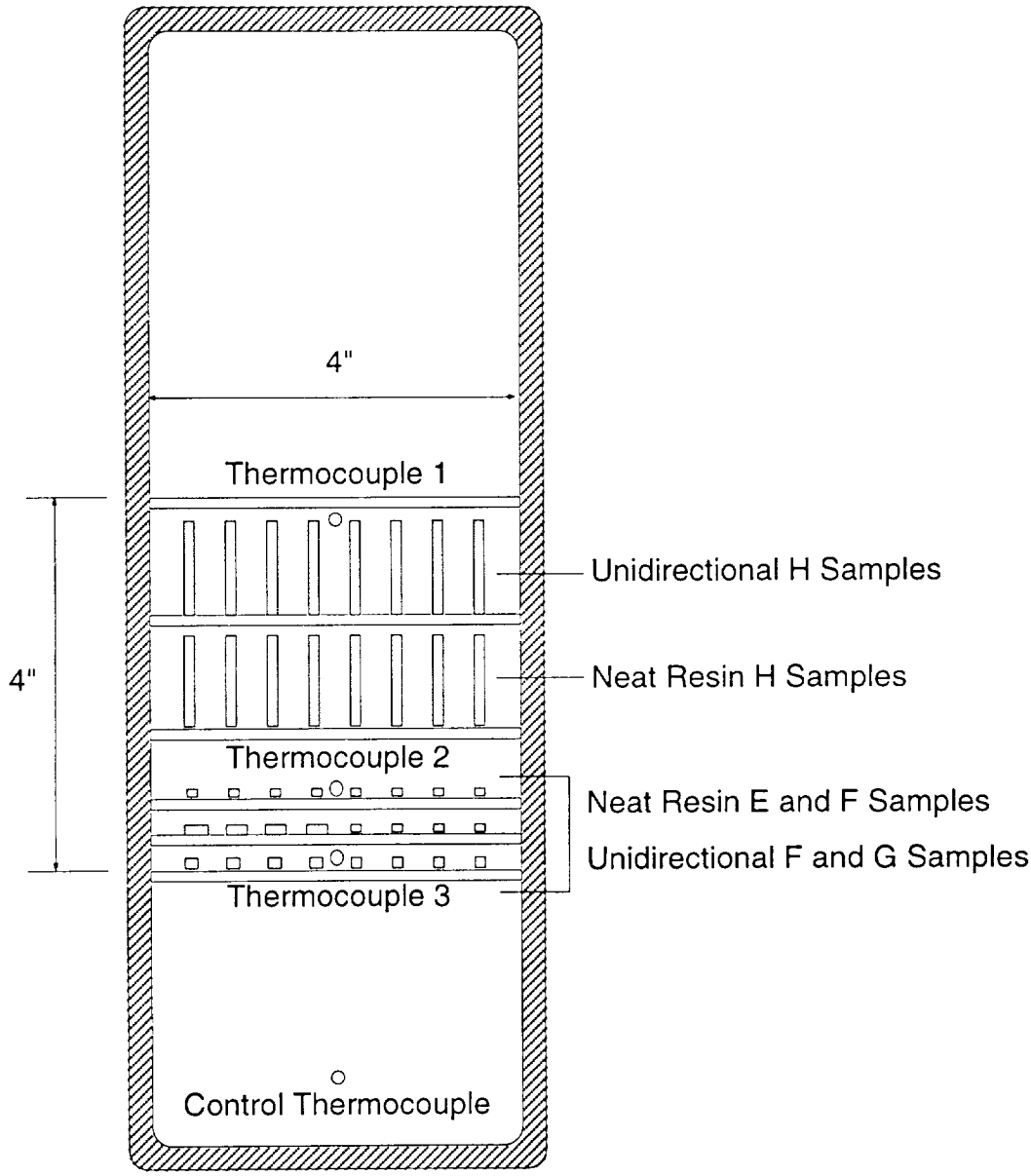

Figure 5.6 Schematic of specimen and thermocouple locations in thermal environment chamber.

was cooled gradually by fan-circulated air to 125°C. By cooling to 125°C before removing the samples it was possible to avoid thermally shocking the specimens while at the same time preventing any additional moisture from being absorbed from the environment before the samples were extracted. Once the oven had cooled to 125°C all samples were removed and their dimensional and mass measurements were recorded. At each extraction time, a single sample from each of the specimen groups was removed permanently and stored immediately in a sealed container along with desiccant to prevent any moisture uptake. These samples were later sectioned and analyzed to determine the formation of degraded surface layers as discussed in Section 5.4.3. The remaining samples were then placed back into the oven and heated to the exposure temperature where they were held for an additional 24 hours, after which the procedure was repeated. After a total isothermal exposure time of 144 hours, the isothermal hold portions were extended to 48 hours between extractions. Samples cut from alternate panels were removed permanently at consecutive extraction times, e.g. if samples from unidirectional panel A were extracted at time t, then samples from unidirectional panel B would be extracted at time $t+\Delta t$.

Mass losses from the neat resin and unidirectional samples were both expressed in terms of the volumetric mass loss percent and the mass loss per unit area. The mass loss percent was determined by dividing the total change in mass by the original (dry) mass. The mass loss per unit area was determined by dividing the total change mass by the total surface area of the specimen. Additionally, the mass lost from the unidirectional specimens was expressed in terms of a mass loss per unit surface area from each of the principal surfaces (molded, parallel to fibers, and cut fiber ends). This mass loss was calculated using the following set of simultaneous equations which

describe the mass lost from the composites as a function of the mass lost in each of the principal directions

$$\begin{aligned}(\Delta M)_F A_F &= \Delta M_1 A_{1F} + \Delta M_2 A_{2F} + \Delta M_3 A_{3F} \\ (\Delta M)_G A_G &= \Delta M_1 A_{1G} + \Delta M_2 A_{2G} + \Delta M_3 A_{3G} \\ (\Delta M)_H A_H &= \Delta M_1 A_{1H} + \Delta M_2 A_{2H} + \Delta M_3 A_{3H}\end{aligned} \tag{5.1}$$

where ΔM represents the total mass loss per unit surface area from each of the respective sample sizes, and ΔM_1, ΔM_2, and ΔM_3 are the mass losses per unit surface area for each of the principal surfaces. A is the total surface area, and A_1, A_2, and A_3 are the exposed surface areas in each of the principal directions.

5.4.3 Optical Microscopy

A study of the surface layer growth and changes in the surface features of the neat resin and unidirectional composites was carried out through the optical examination of sectioned specimens after extraction from the oven. A single neat resin sample (type E) and two unidirectional samples (one each of type F and G) from each extraction group were sectioned perpendicular to the long dimension of the specimen and examined. The neat resin sample provided information for the surface layer growth when no fibers are present. Unidirectional sample type F provided information on both the *S1* and *S2* surfaces, while unidirectional sample type G provided information on the *S3* surface. Figure 5.1 illustrates the location of each of these surfaces.

In order to obtain high quality photomicrographs of the sectioned specimens it was first necessary to obtain a highly polished finish on the surface which was to be examined. All sectioned samples were mounted in a transparent bakelite medium before polishing. The bakelite sample mount allows samples to be polished using automatic polishing/grinding machines

while also providing good optical contrast at the sample edges. The sample mounts were manufactured using a Streurs Prontopress-2 automatic hydraulic mounting press. The sectioned samples were placed on a sample stage, with the sectioned edge resting on the staging platform. The stage was lowered into a cylindrical cavity, 32 mm in diameter, which was surrounded by heating and cooling elements. Buehler Transoptic Powder was added and the entire assembly was sealed. The chamber was then heated to 150°C and a compressive force of 25 kN was applied. After 10 minutes at 150°C, the assembly was cooled and the mounted sample removed from the chamber. This produced a hard cylinder of transparent bakelite surrounding the specimen, with the sectioned surface of interest lying flush with the bottom surface of the cylinder.

Samples were then loaded into a Streurs Rotopol-1 grinding/polishing machine equipped with a Pedemat automatic specimen mover. Up to six samples could be ground at the same time. Samples were ground using incrementally finer silicon-carbide grinding papers. A force of 40N is applied to the rear face of each specimen during the polishing process to ensure that contact is maintained between the specimen and grinding paper at all times. Initially, samples were polished for 60 seconds using a 1200 grit (14 micron) paper to obtain a planar surface. Samples were then polished with 2400 grit (8 micron) and 4000 grit (5 micron) grinding papers. Two sheets of each grit size were used and specimens were polished for 45 seconds on each sheet before it was changed. Specimens were thoroughly rinsed in distilled water between each change of polishing paper. This ensured that a clean surface was maintained at all times. In all cases, the lubricant used during polishing was water and the grinding wheel was operated at 150 rpm.

Once grinding with the 4000 grit papers had been completed, the

samples were rinsed in distilled water and then placed in an ultrasonic bath for three minutes to remove any residual particles. Upon removal from the bath, the specimens were rinsed once again and then mounted in a Rotopol-1 polisher equipped with a 0.3 micron polishing cloth. The samples were then polished for 45 seconds at 150 rpm, using an aluminum-oxide particulate slurry as the lubricant, with a force of 40N being applied to the rear face of each specimen. The cleaning procedure was repeated in its entirety after which the samples were polished for an additional 45 seconds on the 0.3 micron polishing wheel. Finally, the samples were cleaned thoroughly once more in preparation for the required photomicrographs. At each intermediate stage in the grinding process, the samples were placed under a microscope to ensure that the scratches from the previous (larger) grit size paper had been eliminated. If scratches from the previous grit size still remained then the polishing procedure was repeated until they had been completely removed before moving on to the next grit size. This ensured that a very smooth, uniform, high-quality surface finish was achieved.

Photomicrographs of the degraded layers were taken using an Olympus BH-2 microscope. This microscope allows for the polarization of both the light from the light source before it strikes the sample surface and the light reflected from the sample surface. The required light source strength and polarization differed depending on the type of sample being analyzed. All samples from a particular specimen group were analyzed under the same conditions to ensure consistency between photomicrographs of the individual specimens. For each specimen group, the polarization of both the incoming and reflected light was adjusted, along with the power of the light source, until the degraded layer (or other features such as surface cracks) could clearly be seen on the specimen which had been exposed for the longest period of time. A photomicrograph of

the sectioned surface was then taken. Photomicrographs of the remaining specimens in that group were taken with no further adjustments being made to the apparatus, apart from focus adjustment.

Polaroid 55 Instant Sheet Film was used for all photomicrographs. This film yields a high-contrast positive print which allows features such as the degraded layer to be clearly seen. All photomicrographs were converted to graphics files using a Hewlett Packard Scanjet 4C and the Adobe Photoshop software. The scanned images were then analyzed using NIH Image 1.60 [62], an easy-to-use public domain image processing and analysis program for the Macintosh. Image allows the accurate measurement of lengths, areas and grayscale levels within user-defined regions of interest. Both degraded layer thicknesses and grayscale levels across the degraded layers were measured using this software. All grayscale levels recorded using Image were normalized to allow a direct comparison between different samples. A total of 256 levels of gray were used in each analysis. The grayscale analysis is highly sensitive to small variations in the coloration of adjacent and so a considerable amount of noise is present in the resulting grayscale data. However, in the case of the analyses carried out on the neat resin, the noise was not sufficient enough to mask the trends of the observed data.

Layer thicknesses were measured at three locations on each of the photomicrographs - one each at the left and right hand sides of the photograph and one in the center of the picture. Layers were measured by increasing the contrast and brightness levels of the scanned image until the surface layer was extremely well defined, with a high contrast existing between the surface layer and the core material. A narrow area traversing the surface layer was then selected and its length recorded by NIH Image. The surface layer thickness recorded in this manner was compared to the surface layer thickness

determined by the grayscale analysis for a number of specimens. Both methods returned exactly the same values for the layer thickness.

CHAPTER 6

RESULTS AND DISCUSSION

Experimental and analytical results are presented and discussed in this chapter. First, the results of the preliminary analytical model are reviewed. Experimentally measured thermogravimetric data is then presented, reduced to the reaction coefficients required by the analytical model, and correlated with analytical predictions. Results from the short-term isothermal exposure of macroscopic specimens and the relevant correlations follow. At each stage the correlation between the data and the analytical models are discussed. The validity of the mechanism-based analytical model and its assumptions are also addressed.

6.1 PRELIMINARY MODEL

A preliminary model was used to analytically simulate tests on neat resin specimens which had been isothermally exposed to oxidative environments [6]. Neat resin specimens measuring 75 mm x 6.4 mm x 2.5 mm were isothermally aged and weight loss, shrinkage, and the depth of the visible surface layer were recorded. The tests were analytically simulated using a coupled diffusion and chemical reaction model which considered only a single oxidative reaction. The constants required to use the model were estimated from available literature. Bowles [8] estimated the activation energy for the mass loss mechanism to be 128 kJ/mol. Kiefer *et al.* [22] performed thermogravimetric analyses on similar thermoplastic polyimides.

The powdered specimens used in these tests returned an activation energy (121 kJ/mol) which was very close to that reported in [8]. As a result it was decided to use the pre-exponential rate constant from this data as a starting point for determining the actual constants for the PMR-15 resin. Some limited information on the gas diffusivity of polymer matrix composites may be found in [26]. As moisture diffusion has been more widely studied, values of D_o and C which were reported in [56] were used as a starting point for further calculations.

The preliminary values shown in Table 6.1 were taken as a starting point and then actual constants were established through fits to existing mass loss data [6]. The resulting fit constants are also given in Table 6.1. The purpose of this exercise was not to generate coefficients which could be used in predictive calculations, but rather to establish a baseline for further parametric calculations. No information on the quantity of oxygen which is absorbed through the polymer surfaces is currently available, and so the concentration of oxygen at a point in the polymer, c_{ox}, was left as a relative, dimensionless parameter. A value of c_{ox}=1 represents the material's equilibrium concentration. It is assumed that the surface concentration is always equal to the equilibrium concentration.

Similarly no information was available in the consumption rate (R_{ox} in the case of a single oxidative reaction). Two extreme conditions exist in this respect. The first case considers a situation where the consumption rate is very small and oxygen diffuses through the structure relatively unaffected by consumption, or immobilization, of oxygen as reactions are initiated. The second extreme involves a situation where the consumption rate is very high, with the diffusion of oxygen into the material bulk being slowed by the digestion of oxygen molecules by the chemical reactions. Both of these

Table 6.1 Preliminary Study Reaction/Diffusion Data

	E_{ox} (kJ/mol)	$E_{ox}/R^{\dagger}$ (K)	k_{ox} (s^{-1})	D_o (m^2/s^{-1})	C (K)
Starting Point Data	128	15,395	6.46×10^{7}	1.61×10^{-5}	5,690
Model Fit R_{ox}= 0.01	128	15,395	6.46×10^{6}	4.31×10^{-2}	18,000
Model Fit R_{ox}= 165,000	128	15,395	6.46×10^{6}	2.20×10^{-7}	3,741

† Real gas constant.

limiting cases will be considered separately in the following subsections. Finally, the initial density of the material was set to 1300 kg/m^3, and the final density of the material, after the completion of the oxidative reaction, was taken to be 1066 kg/m^3 based on the data presented in [6]. The value for the final density represents an oxidative reaction mass fraction of y_{ox}=0.18 and was arrived at by assuming that all mass loss reported in [6] occurs within the visible degraded layer on the specimens. It is also assumed that an approximately uniform degradation state occurs across the entire degraded layer.

6.1.1 Low Consumption Rate

R_{ox} was set to a nominal value of 0.01. The coefficients which provided the best fit to the data at two different exposure temperatures are shown in Table 6.1. These coefficients were determined by a manual search of the variable space for the diffusion coefficients and the reaction rate pre-exponential constant, using the preliminary values in Table 6.1 as a starting point. A first order Arrhenius reaction was assumed and the activation energy was set to that reported by Bowles in [8]. The fit achieved in this manner is shown in Figure 6.1. The fit to the data at 288°C is very tight, however, the fit to data at 316°C is less so, particularly at the extended aging times. A possible reason for this is that at the longer aging times at the higher temperature the onset of cracks from the surfaces causes an increase in the exposed surface area. As this model was generated for the purpose of gaining insight into the mechanisms at hand, rather than obtaining exact numbers, the coefficients used to obtain the fit illustrated in Figure 6.1 are sufficient to allow parametric studies to be carried out.

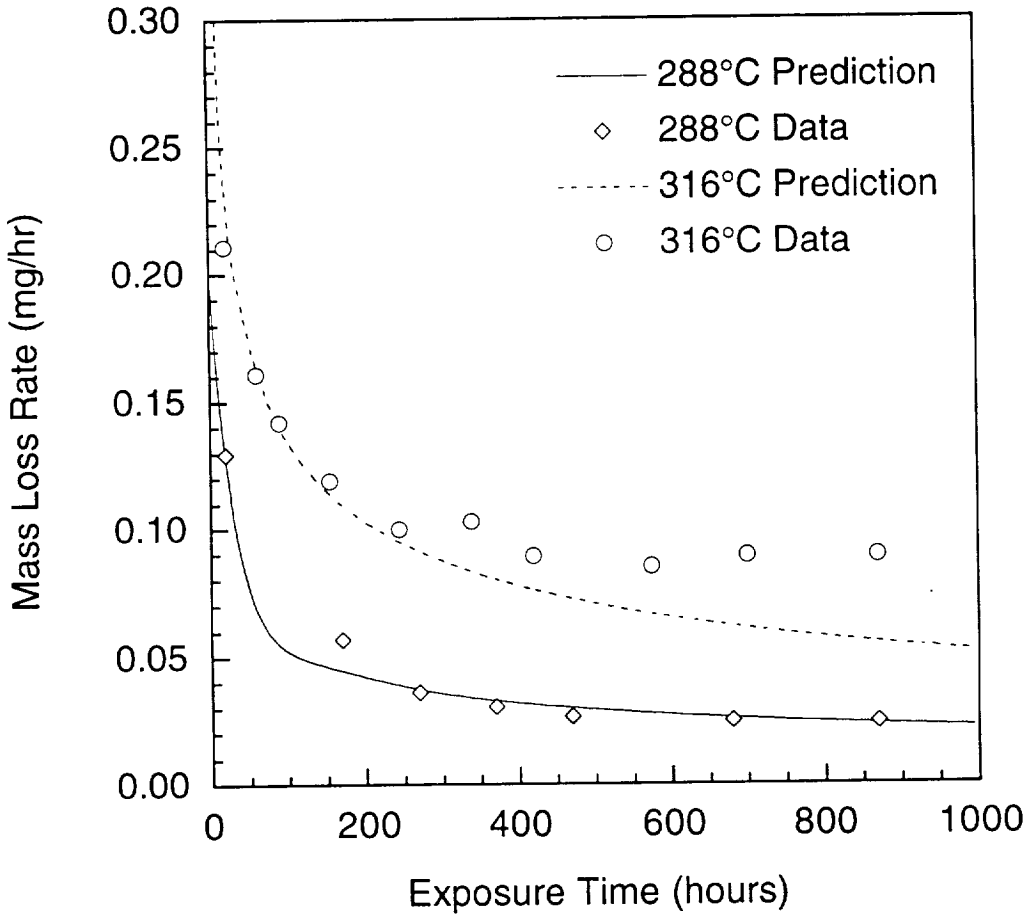

Figure 6.1 Preliminary model mass loss rates at 288°C and 316°C.

6.1.2 Parametric Study

To compare the relative importance of the diffusion and reaction mechanisms, a non-dimensional parameter ζ was defined as

$$\zeta = \frac{k_{ox} h^2 \exp\left(\frac{-E_{ox}}{RT}\right)}{D_z^{ox}} \tag{6.1}$$

The parameter ζ represents the ratio of the rate determining terms of the reaction and diffusion processes, normalized by the specimen dimension h. Large values of ζ indicate that mass loss will be limited by diffusion of oxygen into the material bulk, while small values indicate that the mass loss will be limited by the rate at which the reaction occurs. The speed of these processes may vary by many orders of magnitude depending on exposure conditions, in particular temperature due to the exponential dependency of both the reaction and diffusion, and so a wide range of values of ζ may be encountered. In cases where the consumption of the diffusing substance (R_{ox}) is small, ζ can be shown to fully characterize the shape of the mass loss curve.

A parametric study was carried out, with the 75 mm x 6.4 mm x 2.5 mm specimens of Bowles [6] being considered. Mass loss calculations were repeated for each set of D_z^{ox} and k_{ox} values given in Table 6.2. For the purposes of comparison these values were normalized such that the total mass loss from a specimen (ΔM in Eq. 4.15) at 1,000 hours was held constant at 37 mg in each set of calculations. Figures 6.2 and 6.3 show the mass loss and mass loss rates, respectively, for each of the values of ζ which were considered. It can be seen in Figure 6.2 that the parameter ζ has a strong effect on the shape of the mass loss curve, with a clear distinction existing between the low and high values of ζ. The mass loss curves for very high and

Table 6.2 Parametric Study Values for R_{ox} = 0.01

ζ	k_{ox} (s^{-1})	D_z^{ox} (m^2/s^{-1})
0.1	3.02×10^{4}	5.37×10^{-13}
10	1.35×10^{5}	2.57×10^{-14}
100	3.24×10^{5}	6.17×10^{-15}
1,000	8.91×10^{5}	1.74×10^{-15}
10,000	3.46×10^{6}	6.61×10^{-16}
20,000	5.50×10^{6}	5.37×10^{-16}
24,000	6.46×10^{6}	5.01×10^{-16}

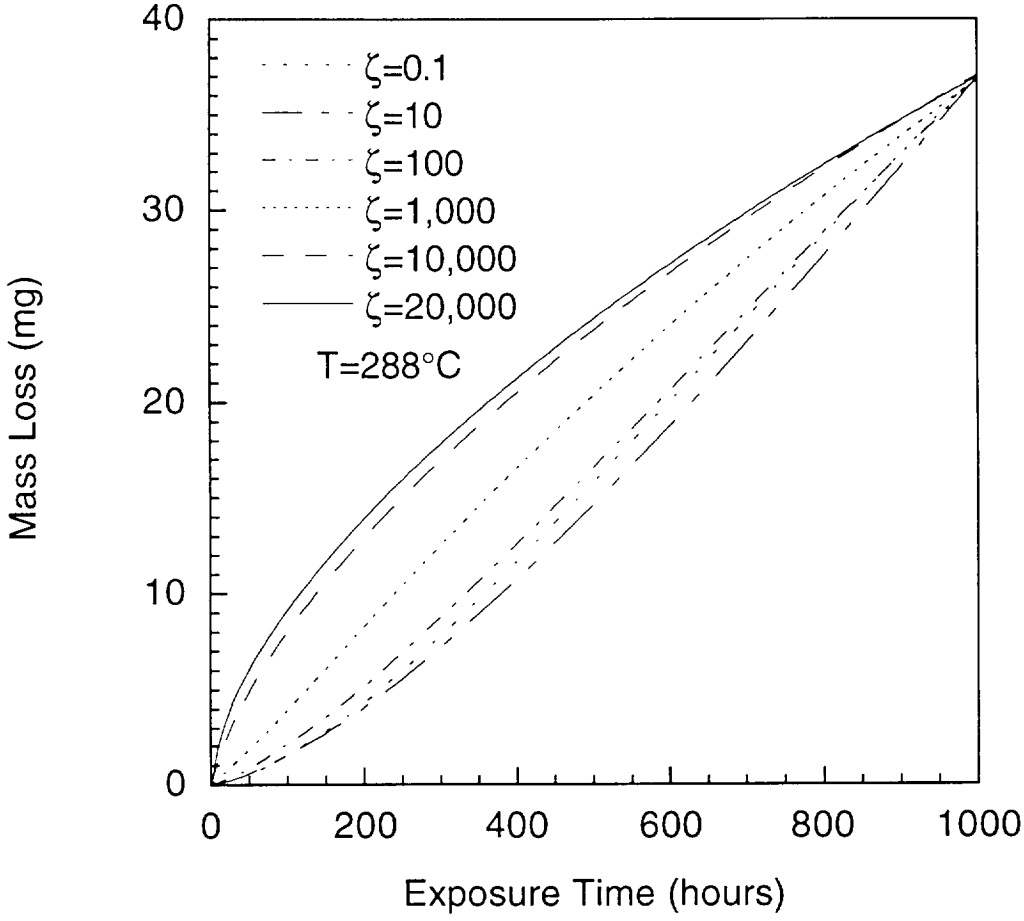

Figure 6.2 Mass losses for different values of ζ at 288°C.

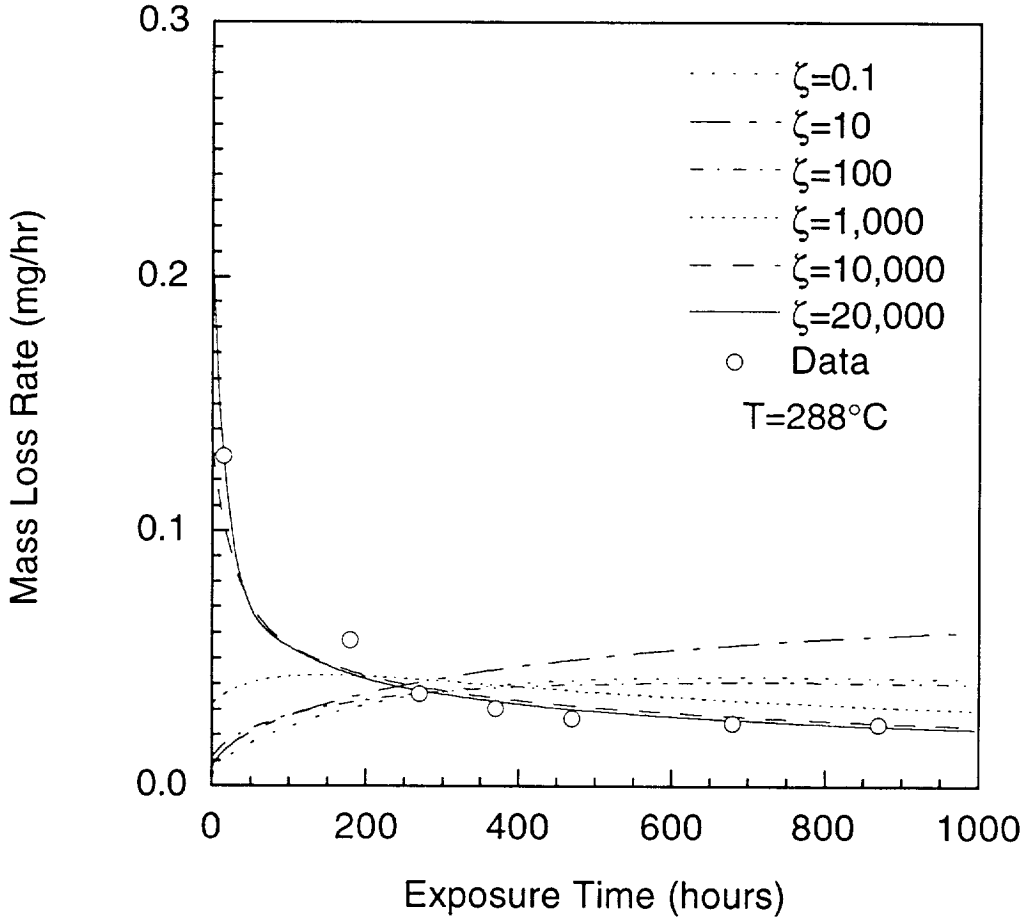

Figure 6.3 Mass loss rates for different values of ζ at 288°C.

very low values of ζ tend to asymptote to the same values, while a definite transition region occurs across the intermediate values (between ζ=100 and ζ=10,000).

The effect of ζ on the mass loss from a system can be more clearly seen in Figure 6.3, which shows the mass loss rates. This figure includes the data of Bowles. Two extremes are apparent. At very high values of ζ, the mass loss rate is initially very high and gradually decreases over time to a lower, steady rate. For these values of ζ the diffusion rate is slow while the reaction rate is very fast. Hence, when the specimen is initially exposed to the environment, the mass loss rate will be high because of the large surface area of undegraded material which may be attacked by the oxidative reactions. As time progresses, the reactions exhaust the material at the surface. The oxygen has not yet progressed very far into the material bulk, resulting in a rapid drop in the mass loss rate. As the slow diffusion of oxygen into the material begins to control the mass loss, the rate asymptotes to a steady-state value. In the case of a low ζ, the situation is completely reversed. The diffusion rate is now extremely fast, while the reaction rate is slow. When a specimen is exposed to the environment, oxygen diffuses rapidly into the material, saturating the specimen in a relatively short period of time. The mass loss rate increases rapidly from zero as the oxygen penetrates deeper into the material. However, this rate remains small by comparison to the initial mass loss rates seen in the high ζ case due to the slow reaction rates. Once all points within the sample have reached the equilibrium concentration, the mass loss is then completely controlled by the reaction rate.

Correlation between the model predictions and the data, plotted in Figure 6.3, suggests that mass loss from neat resin specimens is controlled by

diffusion of oxygen into the material bulk. Figures 6.4 and 6.5 illustrate the internal distribution of both the relative oxygen concentration, c_{ox}, and degradation state, α_{ox}, for the case of $\zeta = 24{,}000$, the value which corresponds to the coefficients used in the fit to Bowles data. A value of $\alpha_{ox} = 1$ represents an 18% mass loss from the material at that point. Degradation proceeds in from the surface, with the reactions being controlled by the availability of oxygen. The reactions proceed at a much faster rate than the oxygen can diffuse into the material. As a result, even in areas where the oxygen concentration is low the reactions proceed very quickly, rapidly degrading any available polymer. This leads to a sharp wall of degraded material which moves in towards the center of the specimen as time progresses, as shown in Figure 6.5. The degraded state within the surface layer is approximately uniform. Bowles also recorded the progression of the observed degraded layer [6]. Figure 6.6 shows a comparison between an empirical fit to the recorded data and the predictions of the model. It was assumed that the degradation at a point in the specimen would be visible when $\alpha_{ox} \geq 0.25$ at that point. The similarity between the data and the model increases confidence that the model is capable of capturing the correct phenomenon.

Figures 6.7 and 6.8 show the internal distributions of the relative oxygen concentration and degradation state for the case where $\zeta = 0.1$. This cases represents the extreme situation where mass loss is completely controlled by a slow degradative reaction. Oxygen diffuses very rapidly into the material, with the concentration throughout the specimen approaching the equilibrium (surface) level in approximately 1,000 hours at 288°C. Although not entirely uniform, degradation occurs slowly throughout the sample. In this case a uniform degraded layer would appear across the entire thickness, contradicting the empirically observed phenomenon. Through the

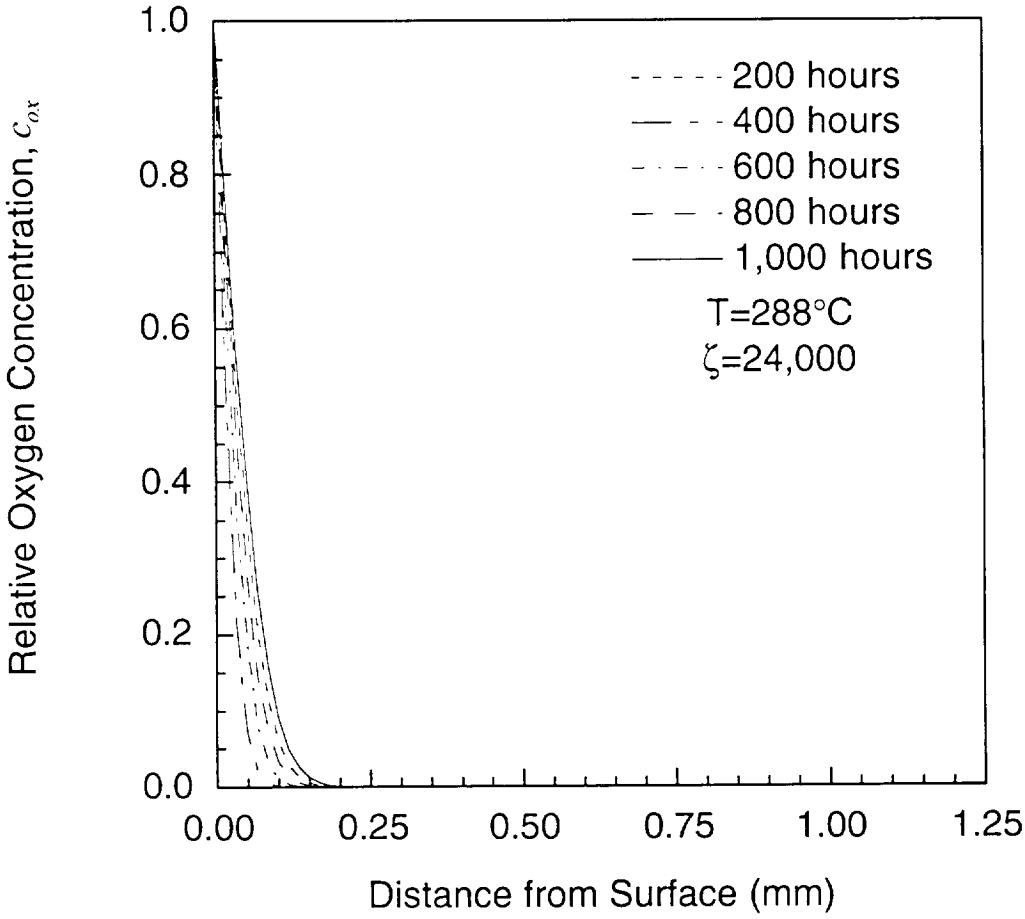

Figure 6.4 Concentration profile for $\zeta = 24{,}000$ at 288°C.

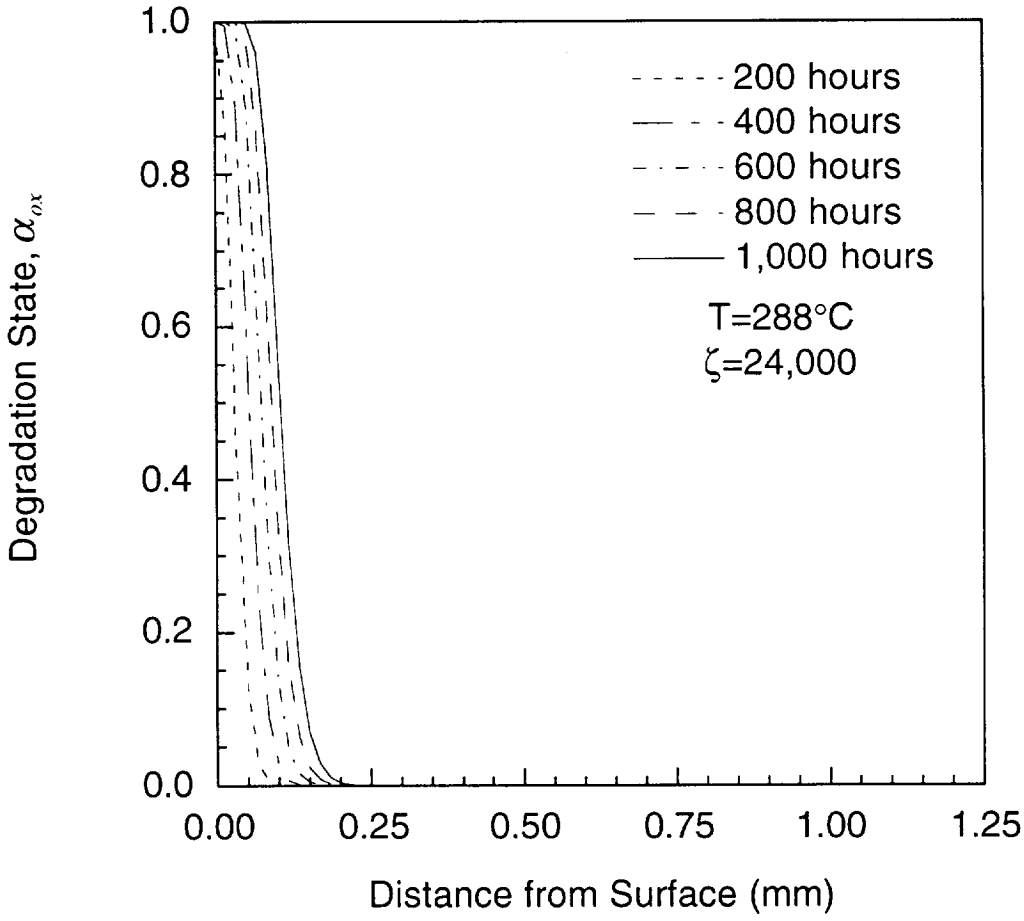

Figure 6.5 Degradation state profile for ζ = 24,000 at 288°C.

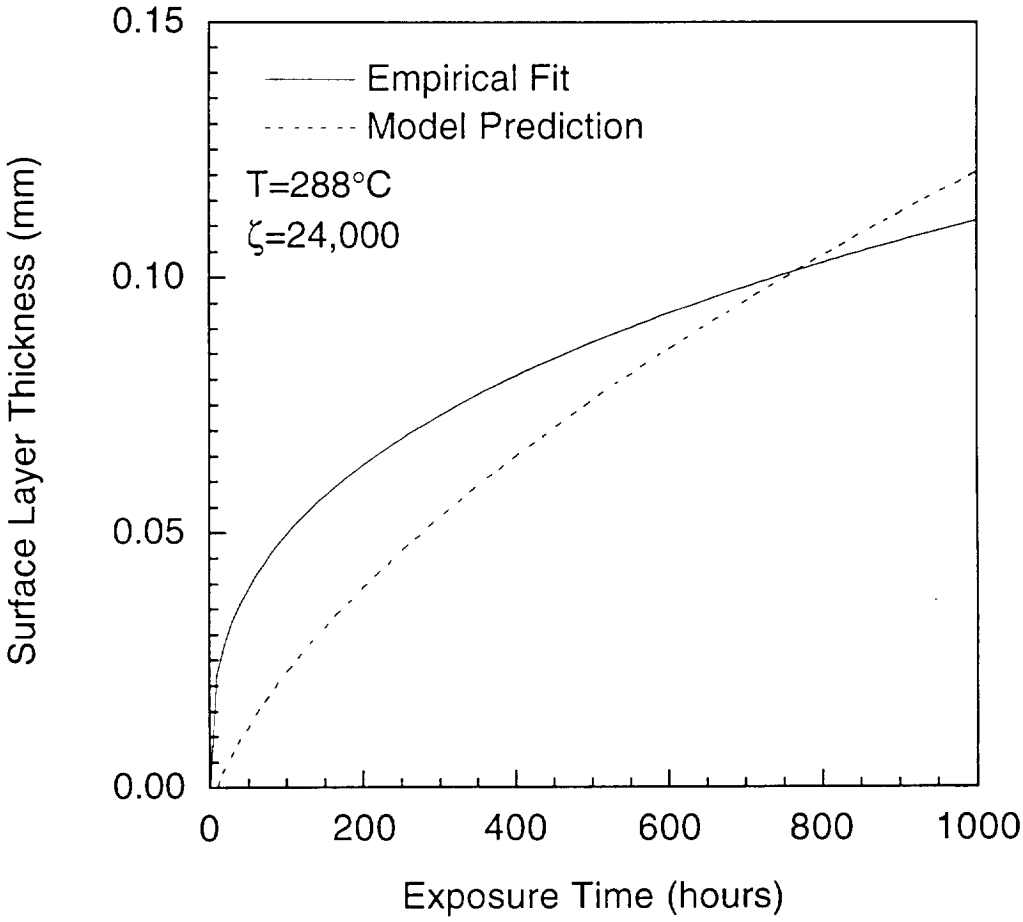

Figure 6.6 Surface layer growth for $\zeta = 24{,}000$ at 288°C.

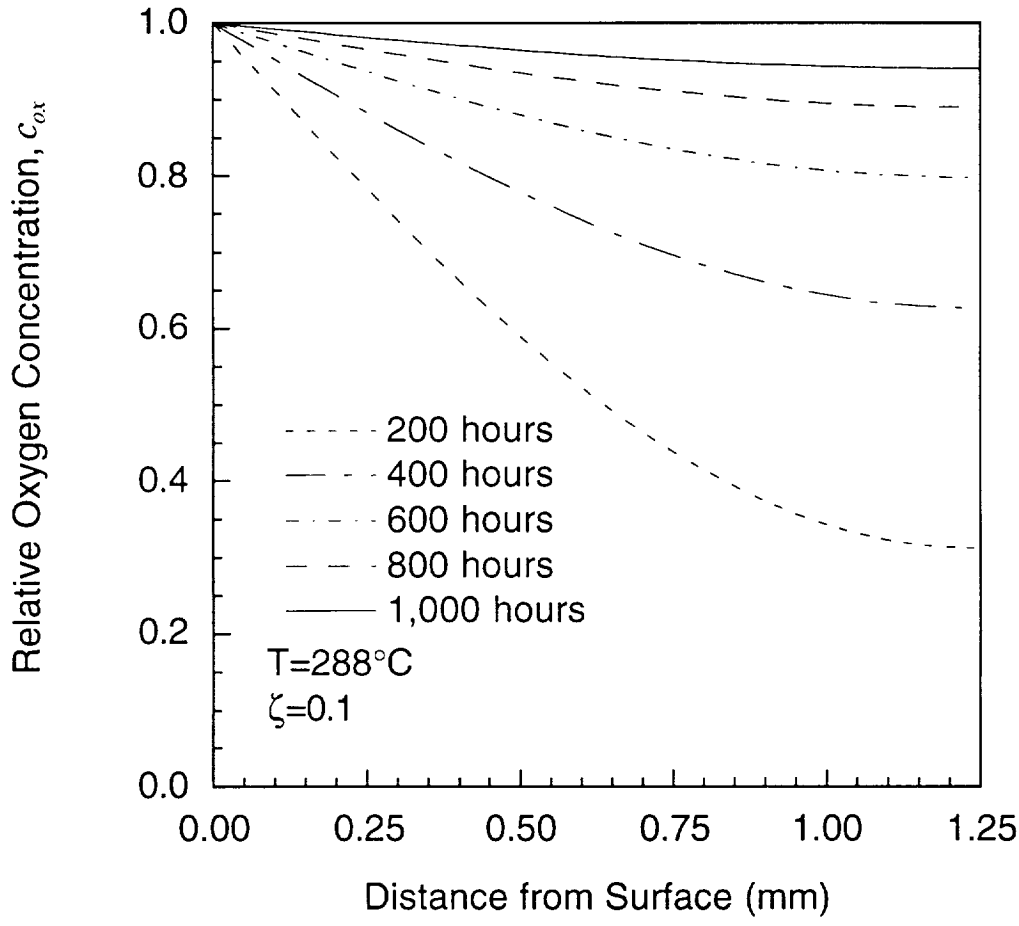

Figure 6.7 Concentration profile for $\zeta = 0.1$ at 288°C.

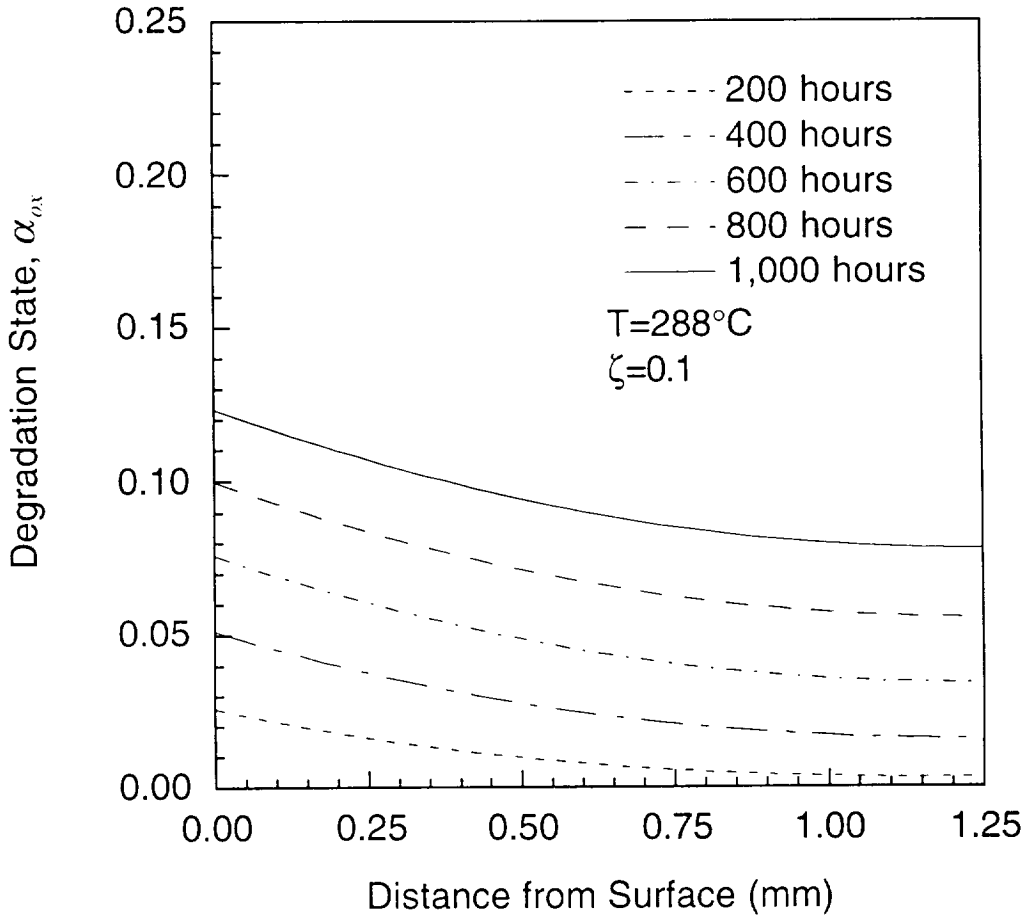

Figure 6.8 Degradation state profile for $\zeta = 0.1$ at 288°C.

study of a complete set of such figures, it was determined that for values of ζ below 1,000 the degradation process is limited by the reaction rate; for values between 1,000 and 5,000 it is dependent on both reaction rate and oxygen diffusion, and at values above 5,000 it is limited by the availability of the diffusing oxygen.

As both the diffusion coefficient and reaction rate have strong temperature dependencies, then the relative influence of these mechanisms will change with temperature. To parametrically study the effects of different temperatures, the dimensionless parameter ζ is reconsidered. Rewriting Eq. 6.1 so that the temperature dependency of the diffusion coefficient is illustrated, as noted in Eq. 4.6, yields

$$\zeta = \frac{k_{ox} h^2}{D_o} \exp\left[\frac{-(E_{ox}/R - C)}{T}\right] \tag{6.2}$$

A parametric study was carried out across a range of temperatures using the coefficients reported for R_{ox} = 0.01 in Table 6.1. The results of this are shown in Figure 6.9. In this case, $E_{ox}/R < C$ and so the exponential term in equation 6.2 is positive. This results in a rapid decrease in ζ as the temperature increases. As a result, the process remains diffusion limited across the entire test regime, from upper use temperatures to accelerated test temperatures. As can be seen in Figure 6.9, the phenomenon becomes increasingly diffusion limited at lower temperatures.

A different situation exists when $E_{ox}/R > C$. Figure 6.10 illustrates the case where $C = 13{,}500$ and E_{ox} remains the same as before. Physically, this corresponds to a system in which the reactions proceed at the same rate as before, but diffusion is now much faster at lower temperatures. At the low temperatures the reaction proceeds very slowly while the diffusion proceeds

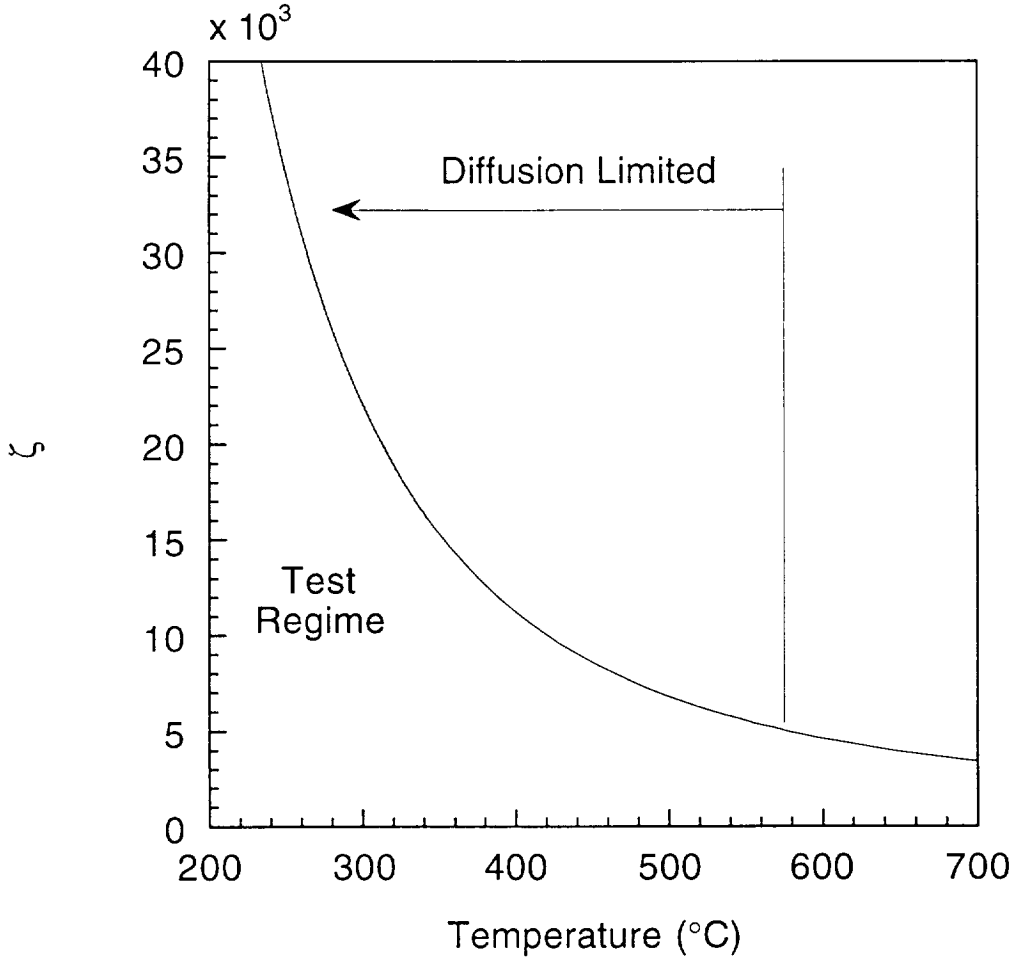

Figure 6.9 Variation of ζ with temperature for $E_{ox}/R < C$.

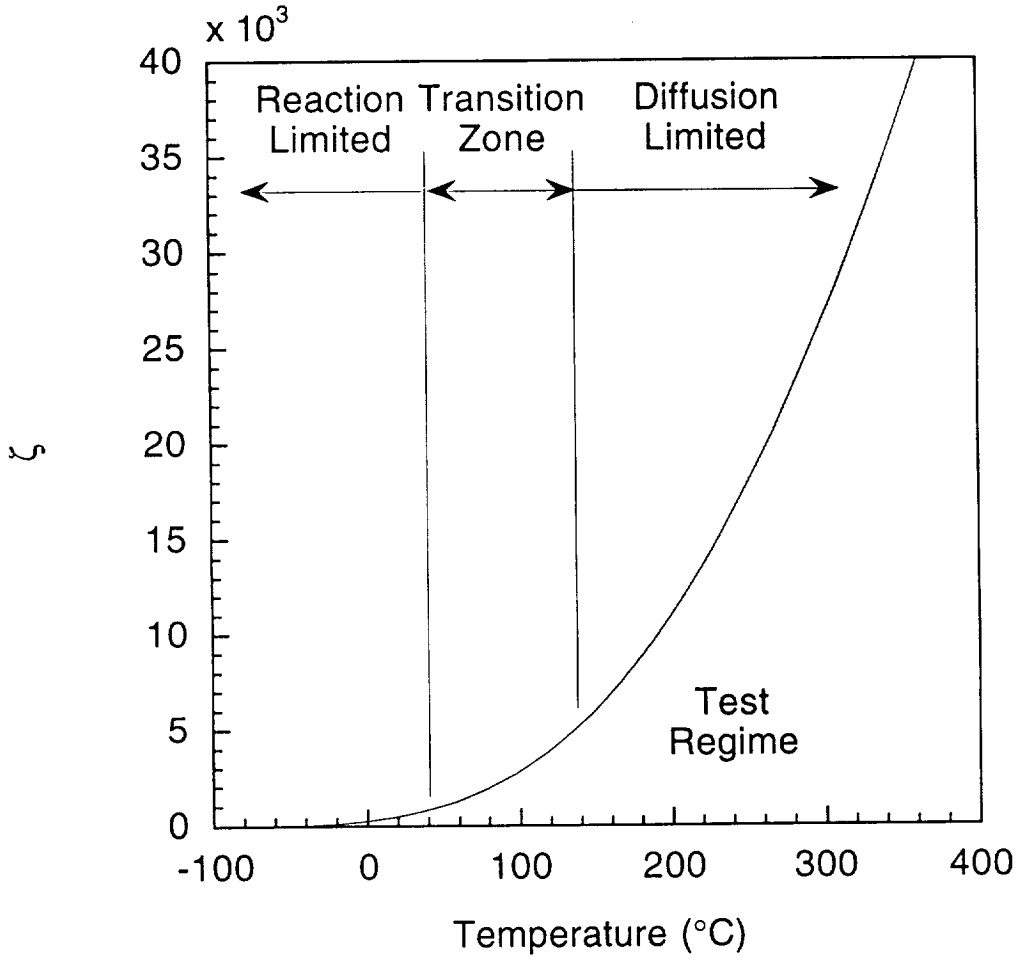

Figure 6.10 Variation of ζ with temperature for $E_{ox}/R > C$.

more rapidly, resulting in a reaction controlled process. As the temperature is increased the reaction rate rises very rapidly and soon overtakes the diffusion rate resulting in a diffusion controlled process at high temperatures. For this case, the exponential term in Eq. 6.2 is now negative, resulting in an increase in ζ as the temperature is increased. Unlike the case where $E_{ox}/R < C$, the entire test regime no longer clearly lies within a diffusion limited zone. A transition zone, defining a change from diffusion to reaction limited processes, now exists in the use temperature region, with the process becoming increasingly reaction limited as temperature is decreased. The marked differences between these two cases highlights the need for reliable material coefficients if the model is to be used for predictive calculations.

6.1.3 High Consumption Rate

The coefficients which allowed a fit to the data for a low consumption rate suggest that the degradation process is controlled by the very slow diffusion of oxygen into the material. However, there is some debate as to the validity of this diffusion limited mechanism. A recent preliminary study by Grayson [63] on the transport of oxygen in neat K3B resin, a polymer similar to that of PMR-15, suggests that the diffusion of oxygen proceeds at a very fast rate. Tests which traced the diffusion of Oxygen-18 into neat K3B between 45°C and 120°C resulted in the Fickian diffusion parameters shown in the last row of Table 6.1. Figure 6.11 shows a comparison between this diffusion coefficient and the diffusion coefficient derived in Section 6.1.1. As can be seen in the figure, the diffusion coefficient for K3B closely resembles that of the starting point data which was determined from moisture diffusion coefficients. The diffusion coefficient derived from the data fit in the previous section is much slower at all temperatures of interest.

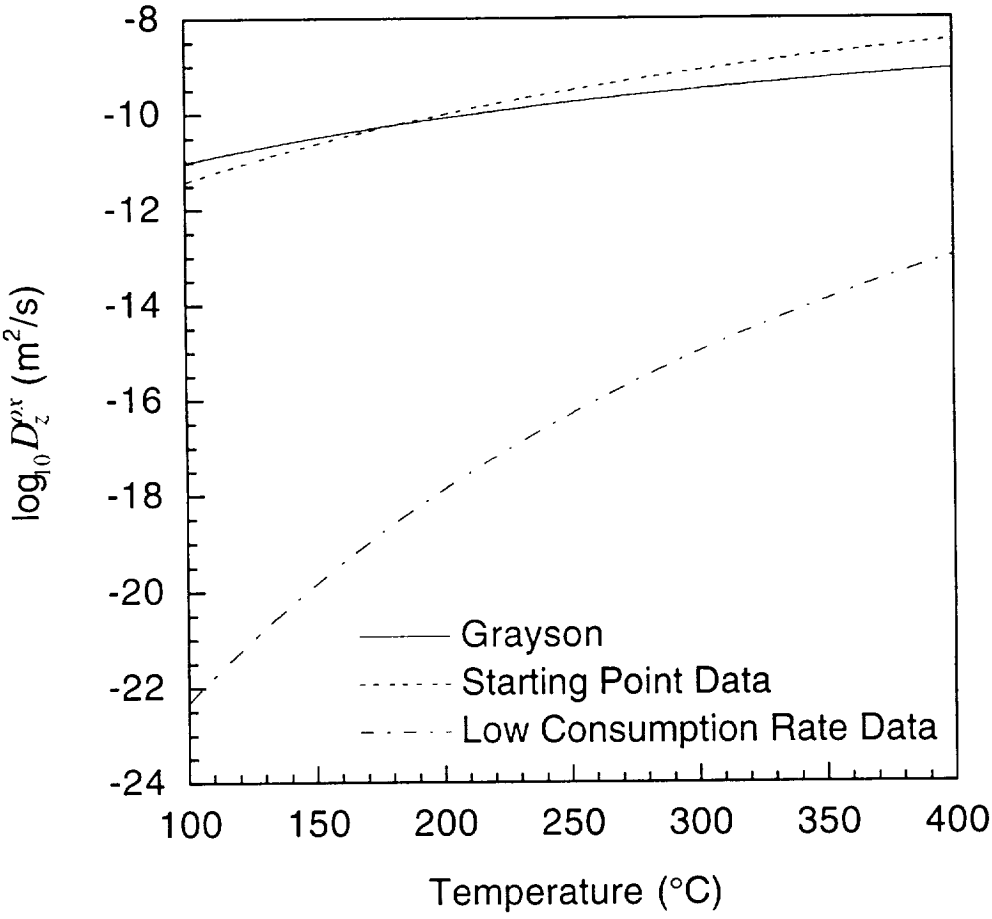

Figure 6.11 Neat resin diffusion coefficients as a function of temperature.

If the highly accelerated diffusion coefficients of Grayson are to be used in the simulation of the experimental data of Bowles then it is necessary to use a very high consumption rate. The reason for this is that without a high consumption rate, oxygen will diffuse through the thickness in a very short amount of time resulting in a uniform degradation of the entire specimen rather than the formation of a degraded layer. The diffusion time required for a substance, in this case oxygen, to diffuse across a distance h can be approximated by

$$\tau = \frac{h^2}{D_z^{ox}} \tag{6.3}$$

If we consider a plate 2.5 mm thick, exposed to oxygen at a temperature of 288°C, then Grayson's coefficients indicate that oxygen will have diffused into the mid-plane of the plate in a time of 1.5 hours. Clearly, this is not the case as this would result in a spatially uniform degradation of the material at longer aging times.

However, if a sufficiently high proportion of the diffusing oxygen is immobilized by the reactions this will result in an effective slowing down of the diffusion of oxygen into material. The diffusion rate is still very high but the oxygen is consumed so quickly by the reactions that reactions at a point in the material must effectively run to completion before the oxygen can diffuse beyond that point. In order to investigate this phenomenon, the diffusion coefficients reported by Grayson were used, along with the reaction coefficients already used in Section 6.1.1. A best fit to the data was then achieved by varying the value of R_{ox}. The final values which were used are reported in Table 6.1.

Figure 6.12 and 6.13 show the mass loss rate and surface layer growth predictions at 288°C, respectively. Excellent agreement with the data is

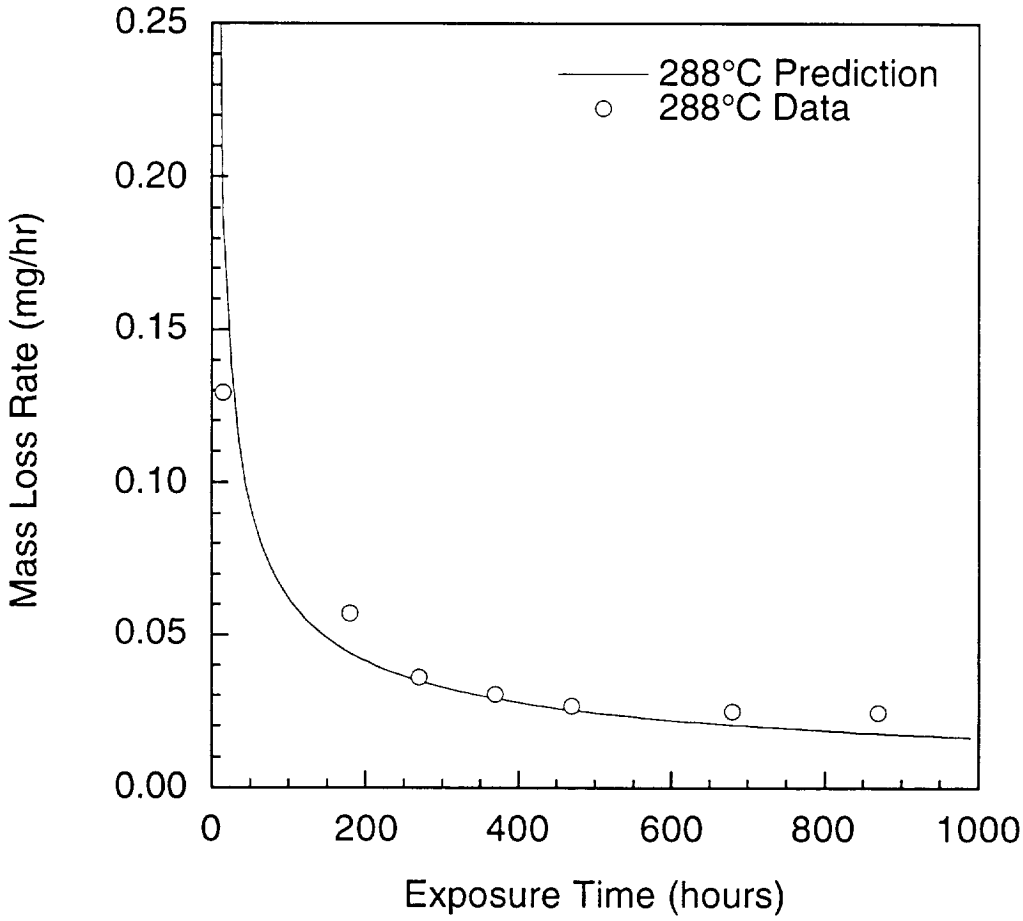

Figure 6.12 High consumption factor mass loss rate prediction at 288°C.

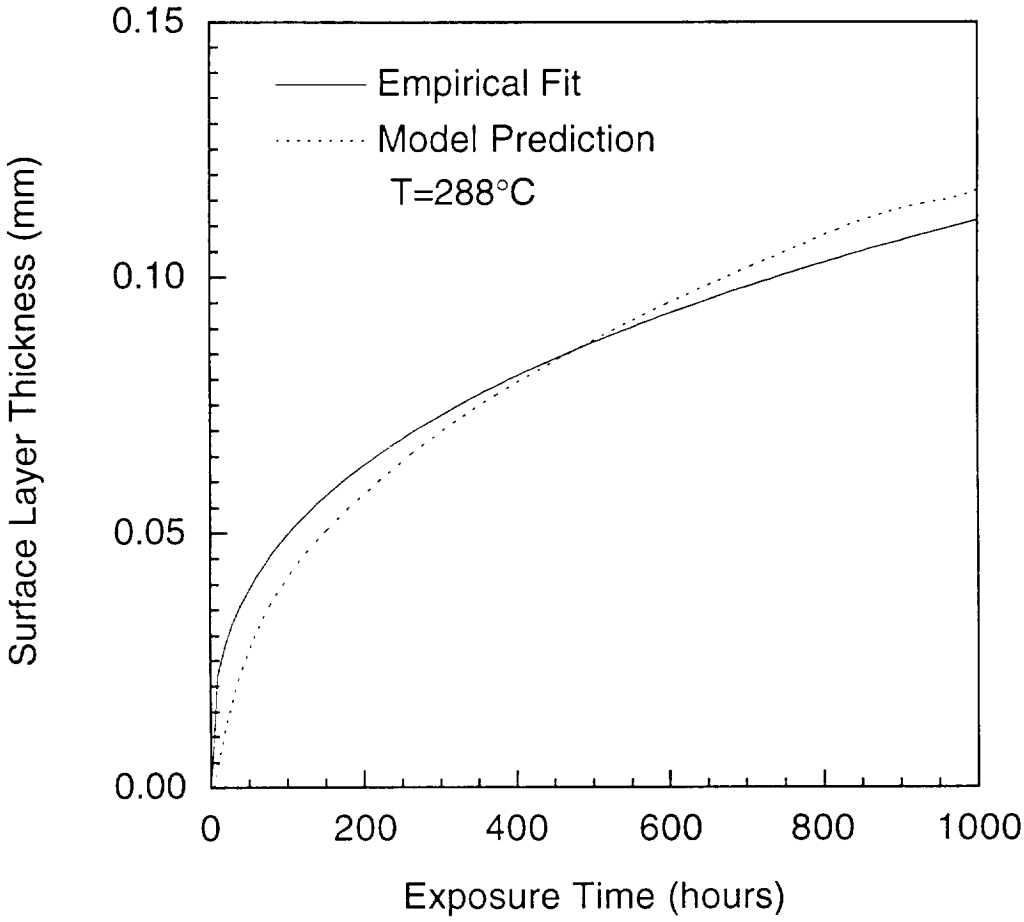

Figure 6.13 High consumption factor surface layer prediction at 288°C.

found in both cases. The internal distribution of the relative oxygen concentration and degradation state for the high consumption rate are shown in Figures 6.14 and 6.15. As in the case of the low consumption rate data, a very sharp wall of degradation moves into the material bulk, the degradation state being approximately uniform throughout the degraded region. The agreement between the analysis and the data shows that we can in fact accurately capture the phenomenon at a single temperature using a very fast diffusion rate coupled with a high consumption factor.

However, it was not possible to obtain a similar fit to the data at 316°C using the same diffusion coefficients and consumption factor. As can be seen in Figure 6.11, the diffusion coefficient of Grayson is highly insensitive to temperature. As a result the thickness of the degraded layer changes only by a trivial amount at the higher temperature. Efforts to compensate for this by increasing the rate at which the oxidative reaction progressed, in order to bring the reaction at a point to completion in a shorter amount of time and hence decrease the consumption of oxygen at that point, were unsuccessful. The reason that this approach will not work is that, for a given consumption factor, the amount of oxygen required to bring the reaction to completion at a point is always the same. If we increase the reaction rate then we simply consume the oxygen more quickly as it passes through that point. The rate at which new oxygen diffuses in to replace the consumed oxygen has not increased however and so the thickness of the degraded layer, as a function of time, will remain the same. The shape of the mass loss rate curve changes slightly, but the overall mass loss remains approximately the same. A fit to the 316°C data can only be achieved by changing either the consumption factor or the temperature dependence of the diffusion coefficient, however changing either of these coefficients will invalidate the fit to the data at

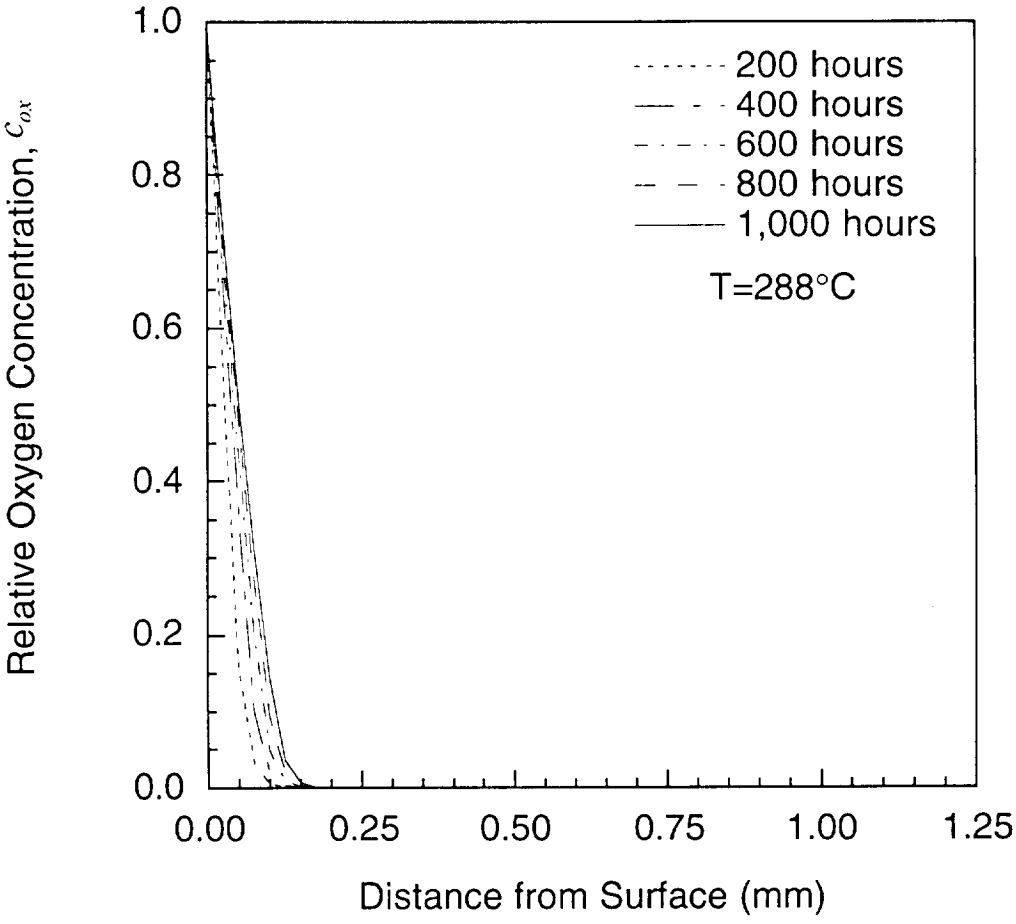

Figure 6.14 Concentration profile for high consumption rate at 288°C.

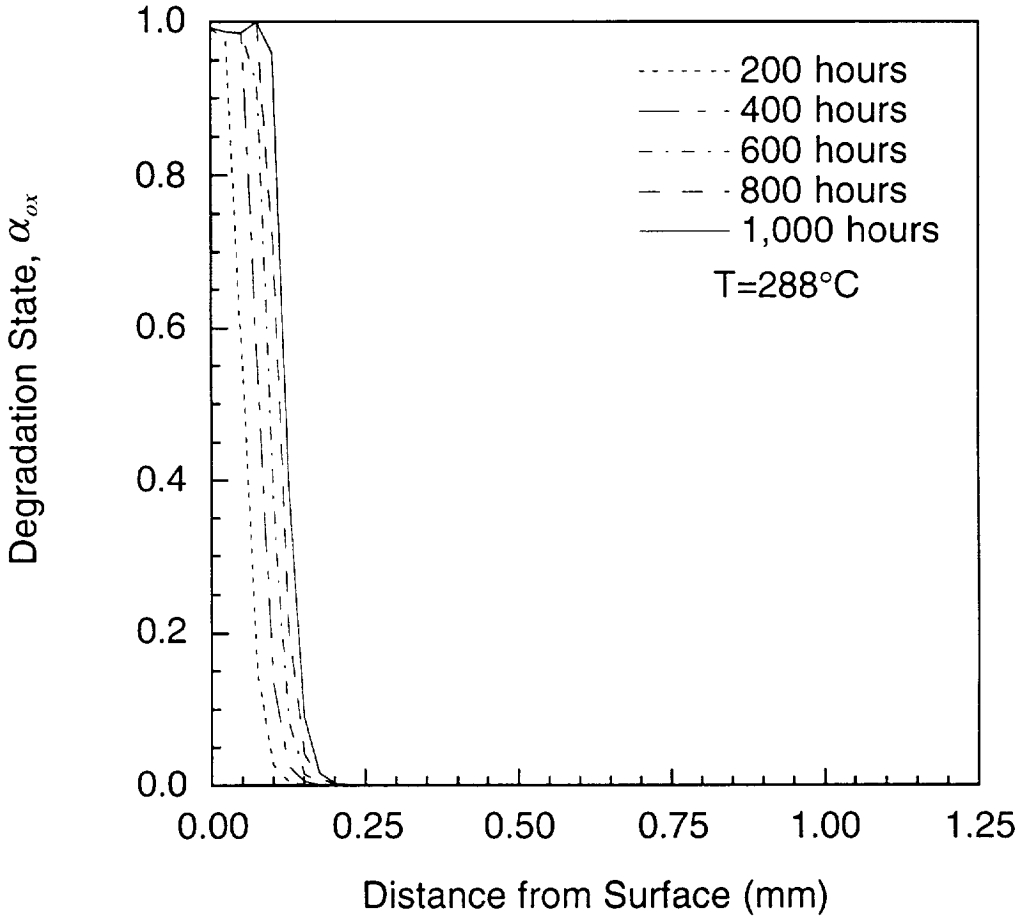

Figure 6.15 Degradation state profile for high consumption rate at 288°C.

288°C. This problem again highlights the lack of any true understanding of the physics of the degradation mechanisms.

6.1.4 Conclusions

It is possible to capture the mass loss behavior of neat resin specimens using a simple one-dimensional reaction/diffusion model. Two separate hypotheses are capable of providing good approximations to the data, the overall effect of both being the same. While one scenario requires a very slow diffusion of oxygen into the material combined with a fast reaction and limited consumption of the diffusing species, this slow diffusion is simply another way of expressing the fast diffusion and very high consumption rate seen in the second case. Each model tries to suppress the diffusion of oxygen in a different way to allow accurate simulation of the data. What is clear, however, is that without accurate material coefficients for the reaction rates and diffusion coefficients, and a more profound understanding of the physics, it is not possible to completely validate either of these hypotheses.

The remainder of this chapter addresses the efforts carried out in the current work to address these some of these issues. Extensive empirical and analytical studies were carried out with the ultimate goal being to establish a firm groundwork which would offer insight, both quantitatively and qualitatively, into the degradation mechanisms and aid in the future development of both design tools and accelerated tests.

6.2 DYNAMIC HEATING TESTS IN NITROGEN

All results in this section are presented in the form of normalized mass losses and mass loss rates. In the experimental results the change in the mass of the sample ΔM is measured. The powdered samples are assumed to

degrade uniformly, so $\Delta m = \Delta M/V$. Eqs. 4.18 and 4.20 are used to reduce the results to normalized form. The analysis predicts Δm, and the results are normalized in the same way as the data. A complete set of the empirical data gathered in the course of these tests may be found in Appendix C.

6.2.1 TGA Empirical Data

A typical dynamic heating thermogram in nitrogen, generated at a heating rate of 10°C/min., is shown in Figure 6.16. Both the normalized mass loss and mass loss rates are illustrated. Approximately 60% of the original mass remains in the sample pan as char at 800°C and so, in this case, a normalized mass loss equal to one represents a mass loss of 40% of the original mass. No significant mass loss is evident below 300°C. As the temperature is increased above this value the mass loss increases rapidly. As more of the material is consumed then the mass loss begins to slow down, due to the decreasing availability of material for consumption. By 800°C the reactions which are responsible for the mass loss have essentially burned themselves out.

Figure 6.17 shows the mean mass loss rates for five sets of data at a heating rate of 10°C/min., and also illustrates the extreme sets. The data across the entire temperature range is extremely consistent. This level of consistency is typical of all the TGA results in nitrogen at the high heating rates. Extremely good consistency is also found at the low heating rates for the later portions of the curve, however some scatter is evident in the height of the first mass loss rate peak at 5°C/min. and 7°C/min. (see Appendix C).

The mass loss rate curves for all heating rates are shown in Figures 6.18 and 6.19. The data is divided here into two sets: high heating rates and low heating rates. Figure 6.18 shows the three higher heating rates. As the

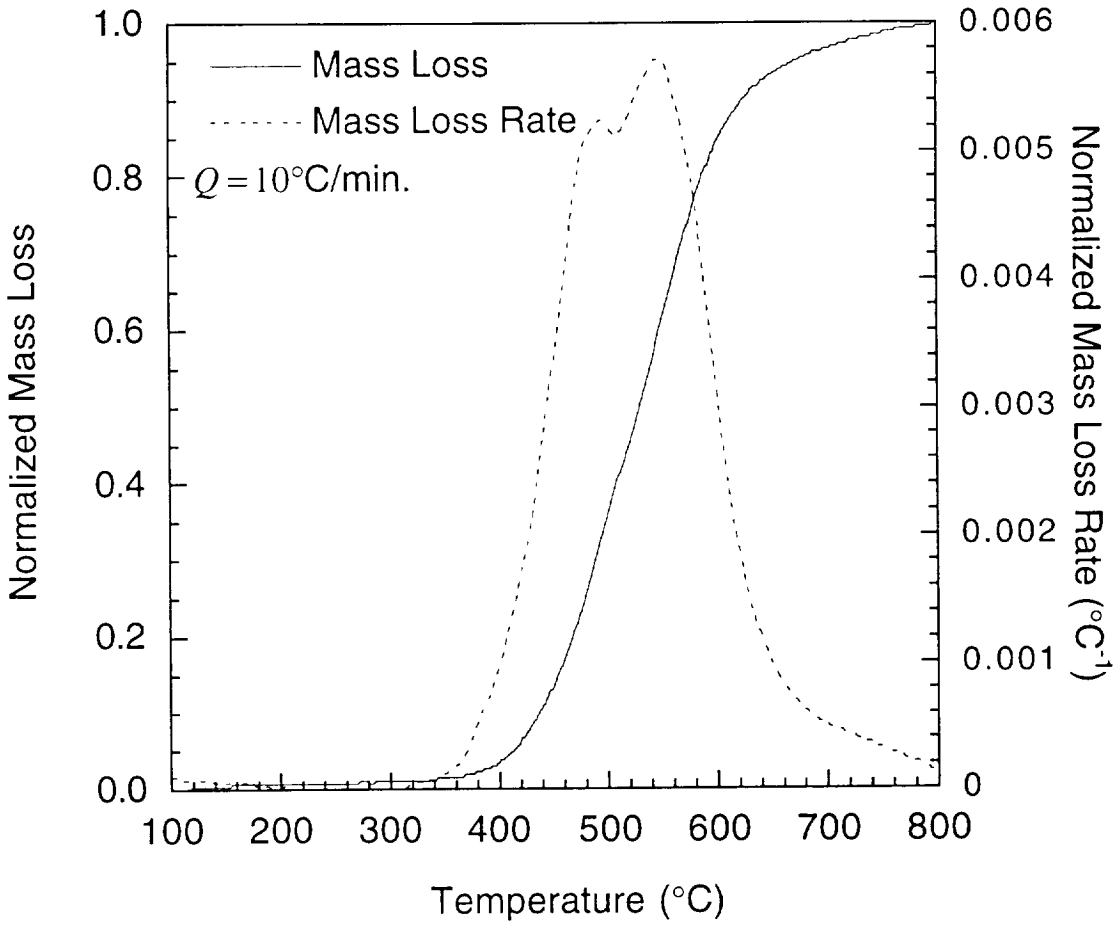

Figure 6.16 Normalized mass loss and mass loss rate in nitrogen.

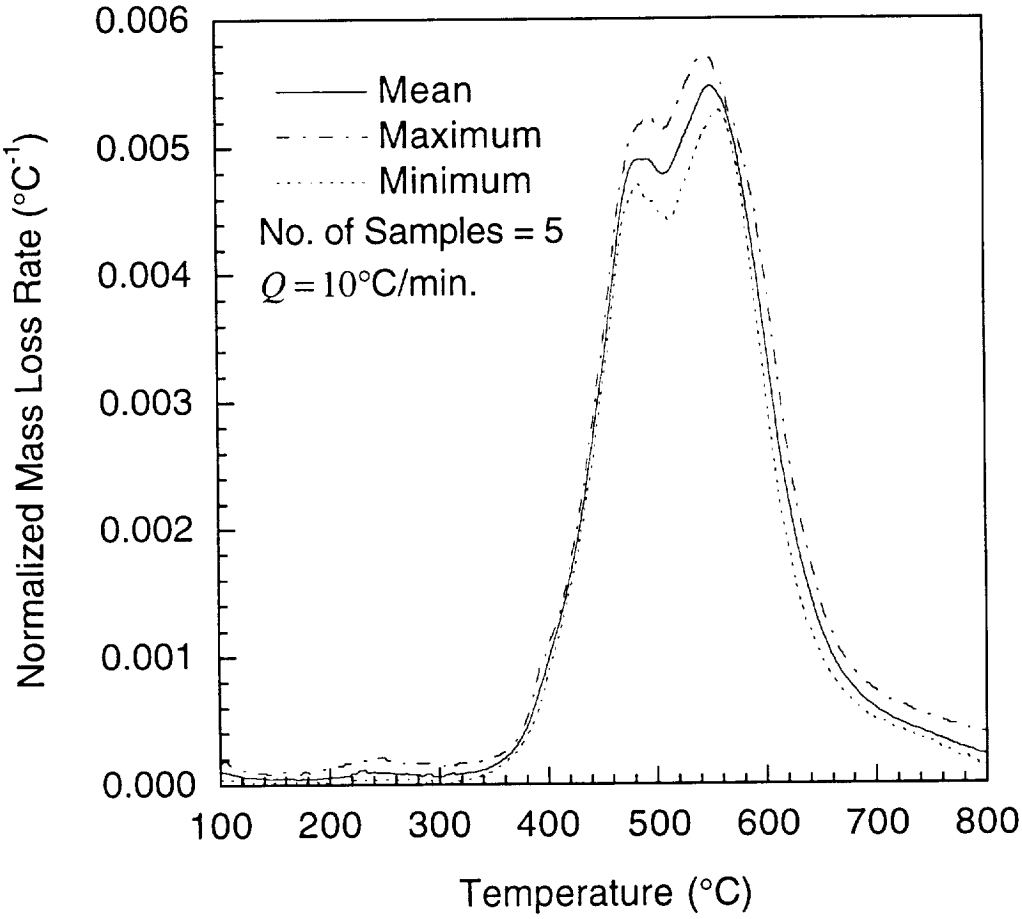

Figure 6.17 Normalized mass loss rates in nitrogen at Q=10°C/min.

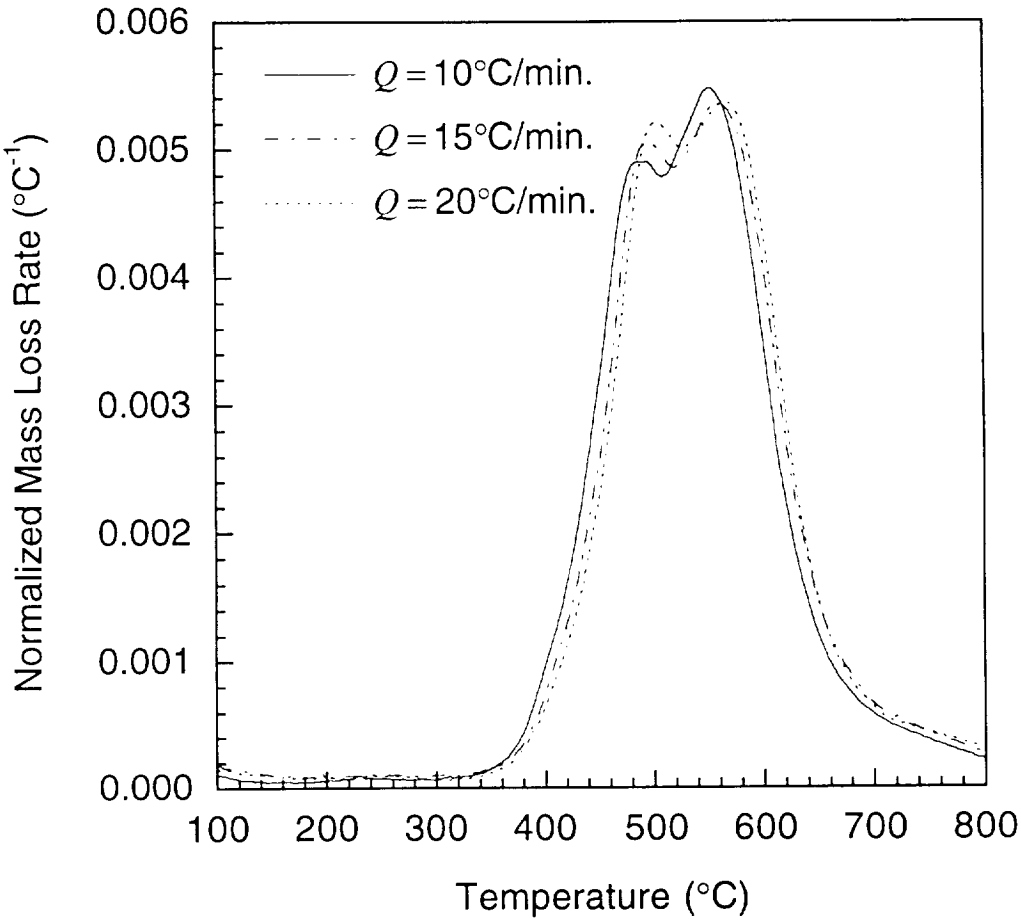

Figure 6.18 Normalized mass loss rates in nitrogen for high heating rates.

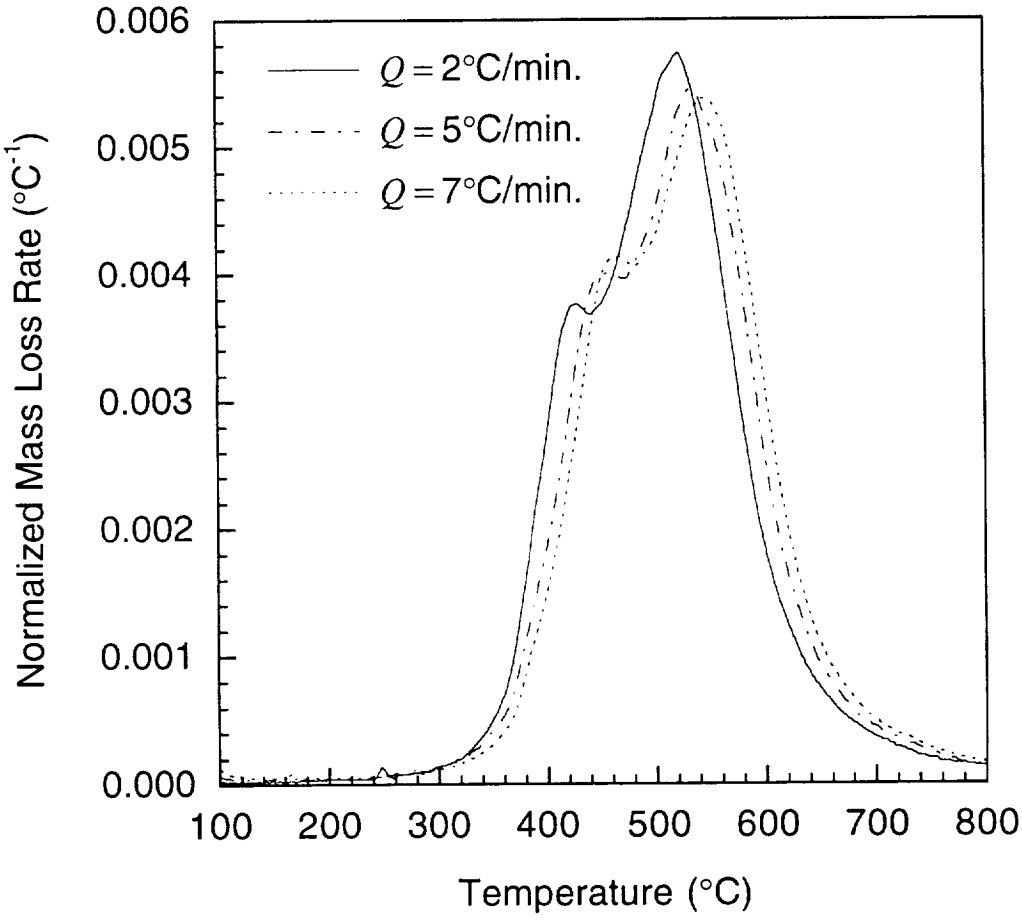

Figure 6.19 Normalized mass loss rates in nitrogen for low heating rates.

heating rate is increased, the mass loss rate curves shift to the right. However, the effects of heating rate on the data are relatively mild at these rates. Figure 6.19 shows the data at the three low heating rates, with each curve representing the mean of three samples. A distinct difference exists between the high and low heating rate data at the front end of the mass loss rate curve. While the high heating rate data possesses two peaks of almost equal magnitude, the first peak is considerably smaller in the case of the low heating rate data. In both high and low heating rate data the second peak is of approximately the same magnitude.

Typically, a single Arrhenius-type degradation reaction results in a single, clearly defined reaction peak in the mass loss rate curve as was previously illustrated in Figure 4.2. The presence of the second reaction peak in the mass loss rate curve suggests that two degradation reactions exist. The second reaction peak exhibits classical Arrhenius-type behavior at all rates, shifting to the right and decreasing in magnitude as the heating rate is increased. While the first peak also shifts to the right, it tends to increase in magnitude, rather than decrease, as the heating rate is increased. This feature is evident in both sets of heating rate data and it is significantly more pronounced at the lower heating rates.

6.2.2 Nitrogen TGA Data Reduction

Based on the empirical data presented in Section 6.2.1, it was decided to model the mass loss behavior in nitrogen as two n-th order Arrhenius reactions acting on two separate material components. This hypothesis is supported by the empirical observations which suggest that the degradation of PMR-15 resin is attributable to the breakdown of both the MDA and NE monomers [5, 34, 36]. The coefficients for this model for both sets of heating

rates were derived using the data fit procedure described in Section 4.4, and are shown in Table 6.3. For each set of heating rates, the data reduction procedure resulted in a number of local minima across a range of mass fractions. The reaction coefficients corresponding to the mass fractions which produced the global minima in these regions are presented here. A complete presentation of the reduction of this data is given in Appendix B. The second reaction in each set of coefficients is the same, however it was not possible to achieve a single set of reaction coefficients for the first reaction which could be applied across all heating rates. Note also that the mass fractions used to achieve the best fits to the data are different for the high and low heating rates, with a lower mass fraction being necessitated for the first reaction at the low heating rates.

Figures 6.20-6.23 show the relevant fits to the low and high heating rate data. The fits to the data, for the respective sets of coefficients, is extremely good. Comparisons between the predicted peak magnitudes and locations and the data at all heating rates are given in Tables 6.4 and 6.5. Attempts to fit to the low heating rates using the coefficients for the high heating rate data resulted in a large overestimation of the height of the first peak. Similarly, attempts to fit to the high heating rate data using the coefficients for the low heating rate data resulted in a large underestimation of the first peak. A comparison between the behavior of the first reaction derived at the optimum mass fractions for both the low and high heating rate data sets is shown in Figure 6.24. The sensitivity of the peak location to heating rate is approximately the same for each reaction, however the magnitude of the peaks for the two reactions differ considerably. This suggests that a single Arrhenius reaction cannot accurately capture the complicated behavior of the assumed first reaction.

Table 6.3 Optimum Nitrogen TGA Data Fit Reaction Coefficients

y_1	y_2	E_1 (kJ/mol)	E_2 (kJ/mol)	k_1 (s^{-1})	k_2 (s^{-1})	n_1	n_2
Low Rates†							
0.33	0.67	140	239	2.78×10^{7}	7.90×10^{12}	1.87	3.20
High Rates††							
0.40	0.60	182	239	3.12×10^{10}	7.90×10^{12}	1.61	3.20

† Low heating rates are 2°C/min., 5°C/min., and 7°C/min.

†† High heating rates are 10°C/min., 15°C/min., and 20°C/min.

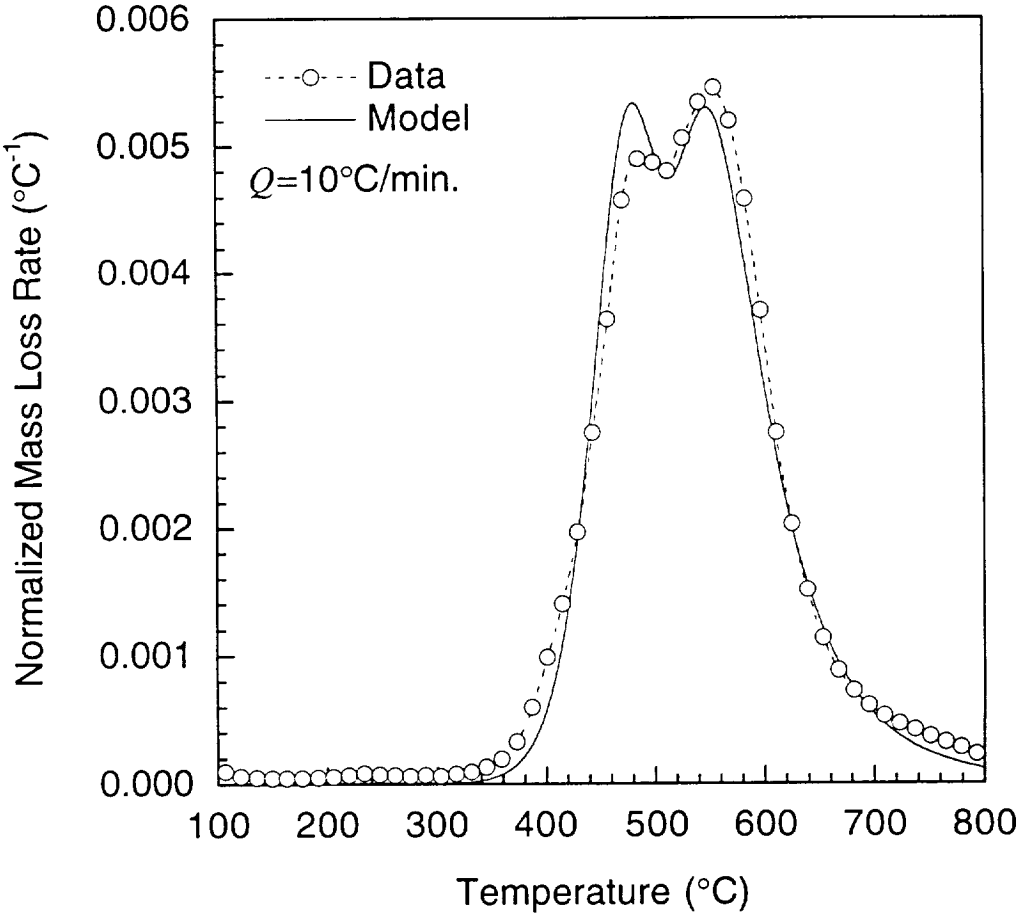

Figure 6.20 Model prediction versus data at 10°C/min. in nitrogen.

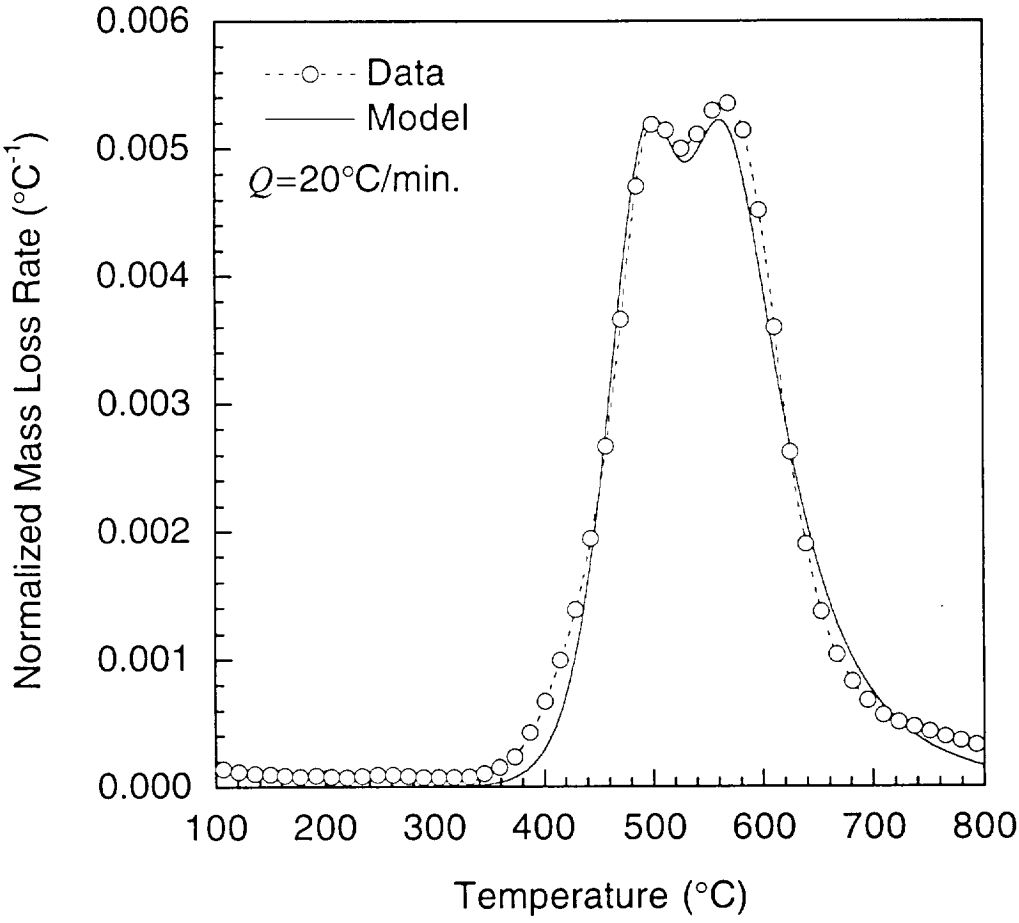

Figure 6.21 Model prediction versus data at 20°C/min. in nitrogen.

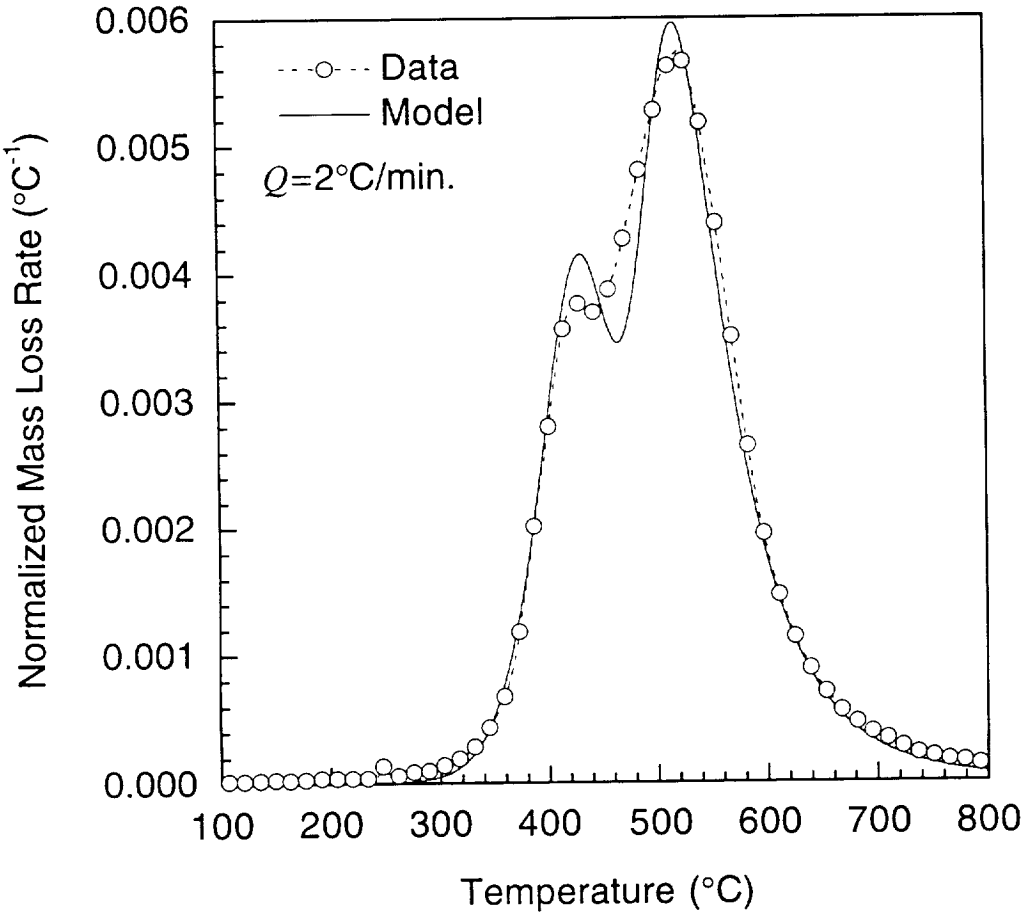

Figure 6.22 Model prediction versus data at 2°C/min. in nitrogen.

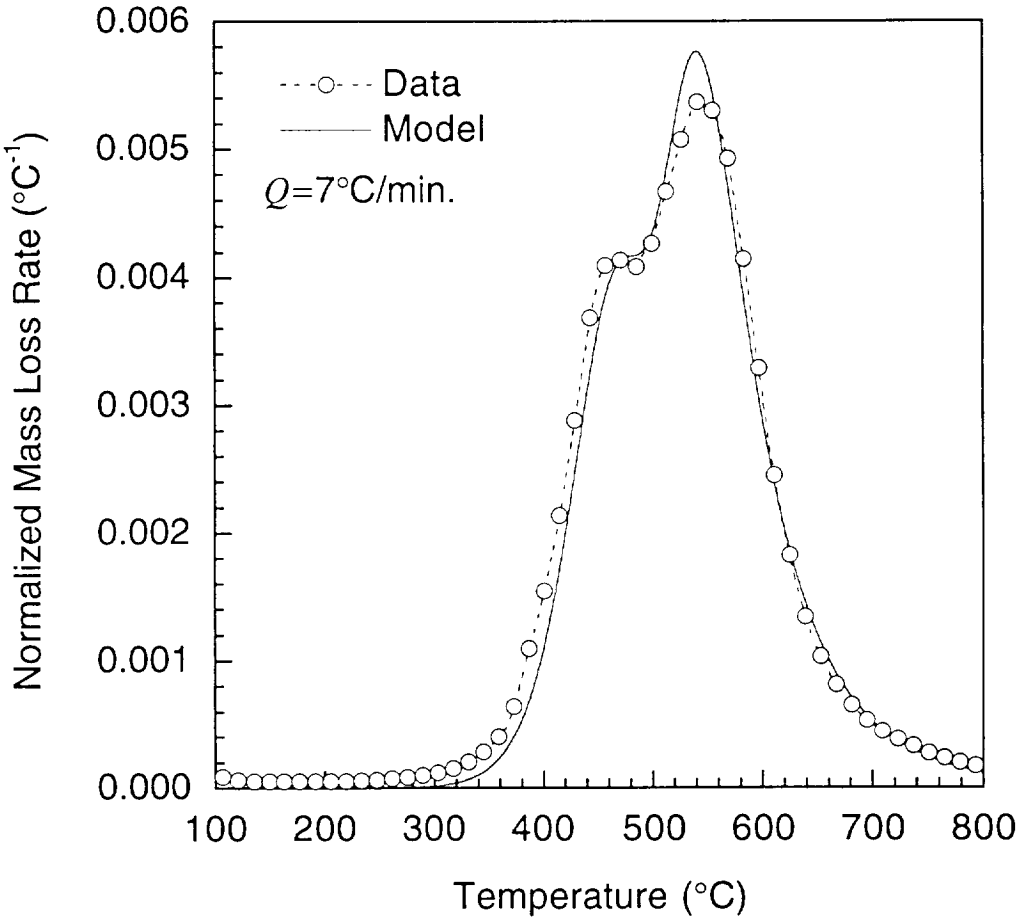

Figure 6.23 Model prediction versus data at 7°C/min. in nitrogen.

Table 6.4 Nitrogen TGA High Heating Rates - Model vs. Data

	Data	Model Predictions
Q=10°C/min.		
$T_{1,max}$ †	493	481
$T_{2,max}$ ††	553	548
$(\partial\alpha/\partial T)_{1,max}$	0.0049	0.0053
$(\partial\alpha/\partial T)_{2,max}$	0.0055	0.0053
Q=15°C/min.		
$T_{1,max}$ †	495	492
$T_{2,max}$ ††	561	556
$(\partial\alpha/\partial T)_{1,max}$	0.0051	0.0053
$(\partial\alpha/\partial T)_{2,max}$	0.0055	0.0053
Q=20°C/min.		
$T_{1,max}$ †	503	500
$T_{2,max}$ ††	565	561
$(\partial\alpha/\partial T)_{1,max}$	0.0052	0.0053
$(\partial\alpha/\partial T)_{2,max}$	0.0054	0.0052

† Temperature, in °C, at which the first peak in the *combined* mass loss rate curve occurs.

†† Temperature, in °C, at which the second peak in the *combined* mass loss rate curve occurs.

Units for $(\partial\alpha/\partial T)$ are in $°C^{-1}$.

Table 6.5 Nitrogen TGA Low Heating Rates - Model vs. Data

	Data	Model Predictions
Q=2°C/min.		
$T_{1,max}$ †	428	431
$T_{2,max}$ ††	522	517
$(\partial\alpha/\partial T)_{1,max}$	0.0038	0.0041
$(\partial\alpha/\partial T)_{2,max}$	0.0057	0.0060
Q=5°C/min.		
$T_{1,max}$ †	457	462
$T_{2,max}$ ††	535	534
$(\partial\alpha/\partial T)_{1,max}$	0.0040	0.0041
$(\partial\alpha/\partial T)_{2,max}$	0.0055	0.0058
Q=7°C/min.		
$T_{1,max}$ †	471	480‡
$T_{2,max}$ ††	546	540
$(\partial\alpha/\partial T)_{1,max}$	0.0041	0.0042
$(\partial\alpha/\partial T)_{2,max}$	0.0054	0.0058

† Temperature, in °C, at which the first peak in the *combined* mass loss rate curve occurs.

†† Temperature, in °C, at which the second peak in the *combined* mass loss rate curve occurs.

‡ This temperature represents an inflection point, not a maximum. No first peak was apparent in the combined predicted mass loss rate curve at this heating rate.

Units for $(\partial\alpha/\partial T)$ are in $°C^{-1}$.

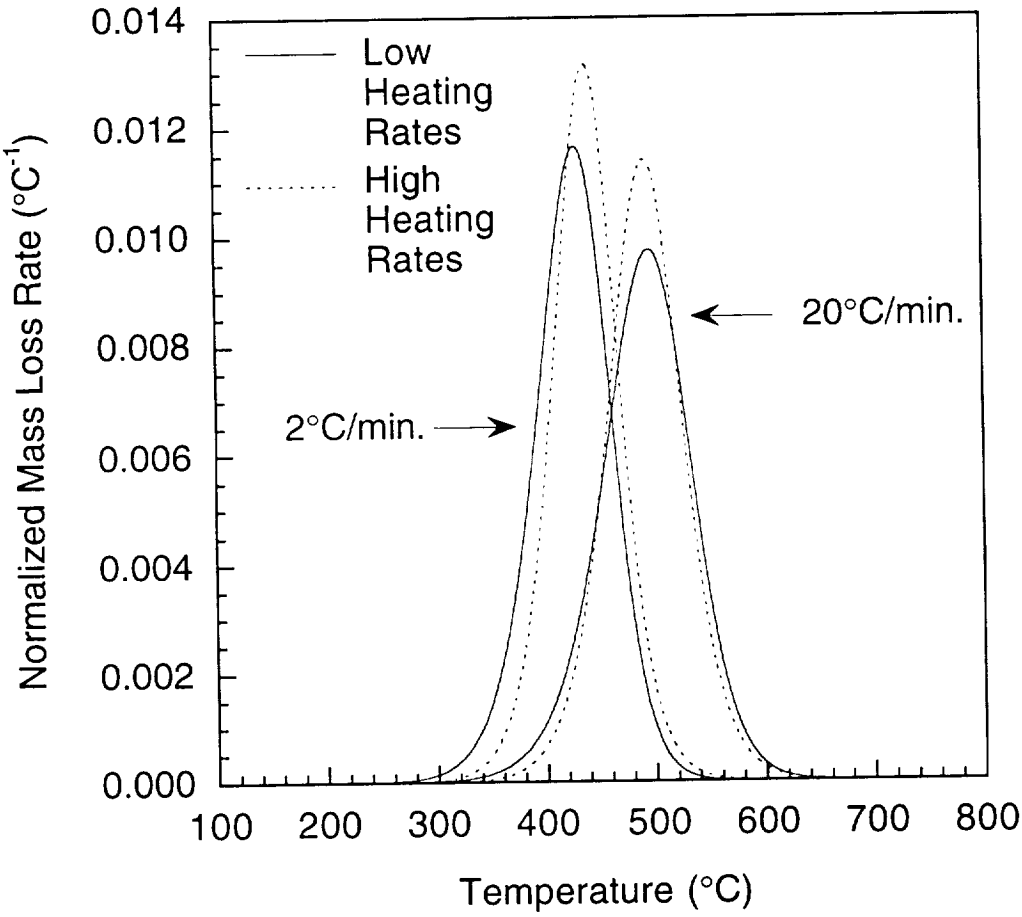

Figure 6.24 Predicted mass loss rate curves for first thermal reaction at optimum high and low heating rate mass fractions.

6.2.3 Discussion

A detailed presentation of the cost function data fit to the thermal TGA data is presented in Appendix B. From this study, it became apparent that the reduction method is not very sensitive to realistic data which possesses an inherent scatter in both the magnitudes and locations of reaction peaks. The best solution is shown here, however multiple good solutions for the reaction coefficients were found across a range of mass fractions at both the low and high heating rates. In fact, at the high heating rates there is a very large number of solutions with approximately the same value cost function, making the choice of solution rather arbitrary. The number of good solutions for the low heating rate data is considerably less, however, multiple solutions with similar cost functions do still exist. The application of any of these other solutions to the current model will not significantly decrease the accuracy of the fits shown here, and because of this a more in-depth investigation of these solutions is warranted.

For the optimum parameters used in this study, the coefficients for the second reaction produced exactly the same mass loss behavior (see Appendix B) across the entire range of heating rates, suggesting that the second reaction is in fact a well behaved Arrhenius-type reaction. On the other hand, while there is a consistency in the behavior of the first reaction within each of the heating rate groups, that consistency is not evident across the heating rate groups.

The most likely explanation for the discrepancies in the behavior of the first reaction across a wide range of heating rates is that there are in fact a large number of closely grouped, low mass fraction reactions occurring in this region. This hypothesis is supported by empirical studies on the degradation of PMR-15 which recorded the desorption of a large variety of low molecular

mass volatiles from specimens during TGA/FTIR studies [24]. These multiple reactions may have some statistical distribution of activation energies, reaction rates and reaction orders, which for a given heating rate result in a mass loss rate curve which appears to be the product of a single Arrhenius-type reaction.

An example of three reactions masquerading as one is shown in Figure 6.25. Three closely grouped n-th order Arrhenius reactions are shown along with their combined effect. The coefficients used to generate these curves are given in Table 6.6. The combined mass loss rate of the individual reactions closely resembles that of a single Arrhenius-type reaction. A best fit to the data using a single Arrhenius reaction is also shown in this figure. The coefficients derived for this reaction are given in Table 6.6. While the location of the mass loss rate peak is captured at each heating rate, the details of the reaction are not. Both the magnitudes of the mass loss rate peaks and the shape of the front end of the curves are significantly different. Both of these errors are evident at the front of the fits to the data shown in Figures 6.20-6.23. As the number of closely grouped reactions increases then these discrepancies will become more and more apparent due to the inability of a single Arrhenius reaction to accurately capture the combined behavior of multiple reactions.

Several other hypotheses may be used to try to explain this phenomenon, however they all tend to simply be different expressions of the same basic hypothesis. Bowles [8] suggested the use of a temperature dependent activation energy to capture the mass loss behavior of Celion 6000/PMR-15 composites, with the activation energy increasing with temperature. The use of an increasing activation energy allows the model to capture the behavior at different temperatures by effectively smearing

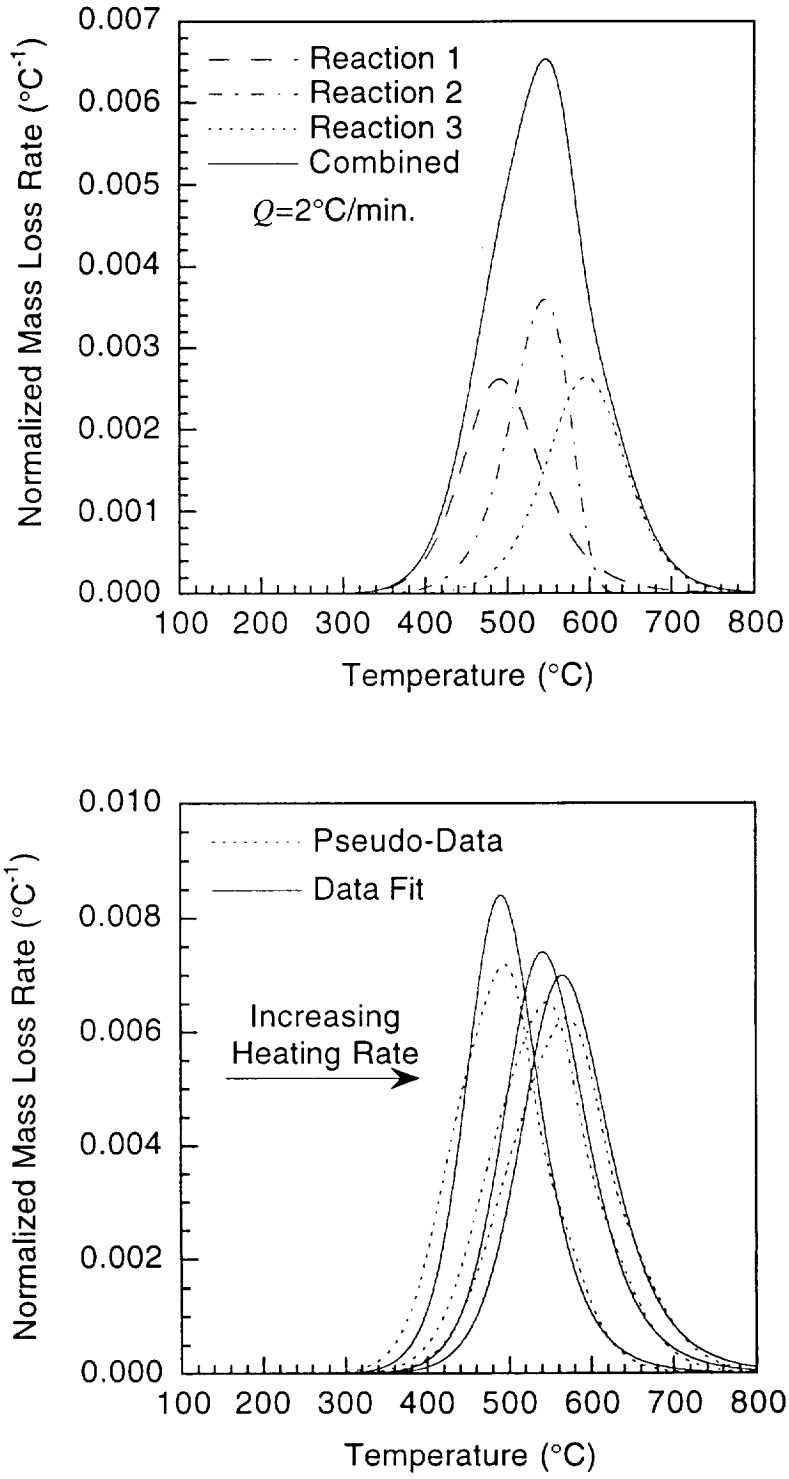

Figure 6.25 Mass loss rate curves and data fit for closely grouped multiple reactions.

Table 6.6 Multiple Arrhenius Reaction Coefficients

	y	E (kJ/mol)	k (s^{-1})	n
Reaction 1	0.33	140.0	1.67×10^7	2.00
Reaction 2	0.33	150.0	1.67×10^7	1.00
Reaction 3	0.33	160.0	1.67×10^7	1.60
Data Fit	1.00	149.7	1.65×10^7	1.98

together all of the reactions which have been activated at a particular temperature.

Despite the fact that it is not possible to accurately predict the behavior of the data at all heating rates using the model at its current level of sophistication (nor can we extrapolate very far outside of the temperature and heating regimes considered here), we do possess a model which works extremely well at the high heating rates. This model provides a very good fit to the data in the test regime which was used to determine the mass loss behavior of the neat resin in air and oxygen. Hence, it is still possible to use this model with reasonable confidence to separate out the purely oxidative effects from the combined thermal/oxidative TGA data.

6.3 DYNAMIC HEATING TESTS IN AIR AND OXYGEN

6.3.1 TGA Empirical Data in Air

Figure 6.26 compares the mass loss rates measured in air and in nitrogen atmospheres. The contrast between the air results, assumed to be dominated by oxidative reactions, and the nitrogen results is dramatic. A new reaction peak is notable at lower temperatures. Later reactions are initially somewhat suppressed by comparison to the thermal reactions at similar temperatures, however at higher temperatures (above 500°C) the reactions proceed extremely rapidly. At very high temperatures a constant rate process takes place. This rate is maintained until all of the material has been consumed. Unlike the TGAs in nitrogen, no char residue remains in the sample pan at 800°C at a heating rate of 10°C/min. suggesting that the high temperature constant rate reactions are in fact ablative. Hence all mass loss rates presented here have been normalized such that a normalized mass loss equal to one represents a 100% loss of the original specimen mass. The

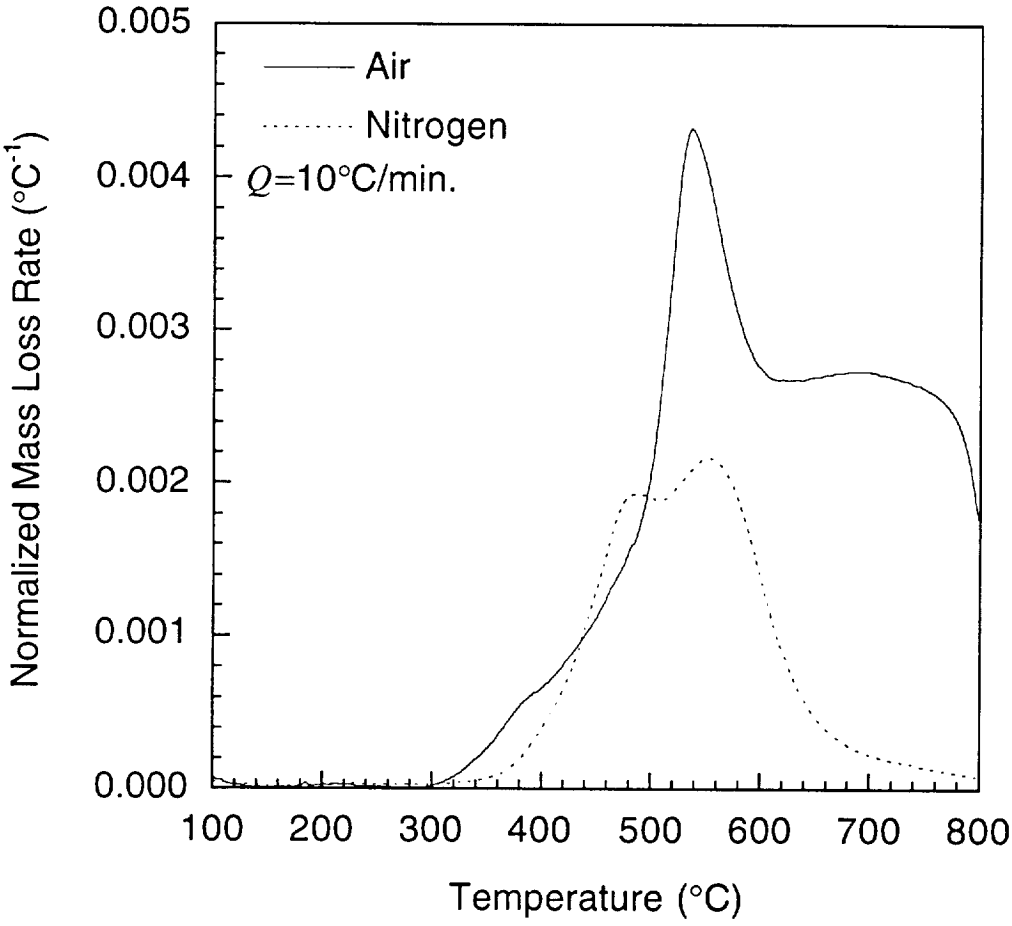

Figure 6.26 Mass loss rates in air and nitrogen at 10°C/min.

nitrogen data plotted in Figure 6.26 has been renormalized to reflect this.

Figure 6.27 show the test results in air at three different heating rates. The data presented here represents the mean of three separate samples. As in the case of the nitrogen data, the data from the three test specimens is extremely consistent across the entire temperature range with the exception of some scatter in the region of the new, early reaction peak and the later reaction peak at 550°C (see Appendix C). The early response of the samples is relatively insensitive to heating rate. The second peak, as well as the high-temperature ablative plateau, are rate dependent in ways that are not compatible with Arrhenius reaction models. The location of the second peak does not change with heating rate even though very large changes in magnitude are evident, and therefore cannot be fit to using the Arrhenius reaction.

6.3.2 TGA Empirical Data in Oxygen

Figure 6.28 shows the behavior of two samples which were tested in oxygen at 10°C/min. In the presence of pure oxygen the later exothermic reactions completely dominate the mass loss behavior. All of the material is consumed across a very small temperature range, with the reactions being extremely aggressive. The height of the reaction peak is approximately an order of magnitude higher than that recorded for exposures in air. Little consistency exists between the behavior of the individual samples above a temperature of 450°C. This lack of consistency at higher temperatures is evident at all heating rates. The behavior of the samples at temperatures below 400°C is considerably more consistent however. Figure 6.29 shows the mass loss rate behavior of the two samples at 10°C/min. up to 400°C. The consistency between samples shown here is typical of the data in this

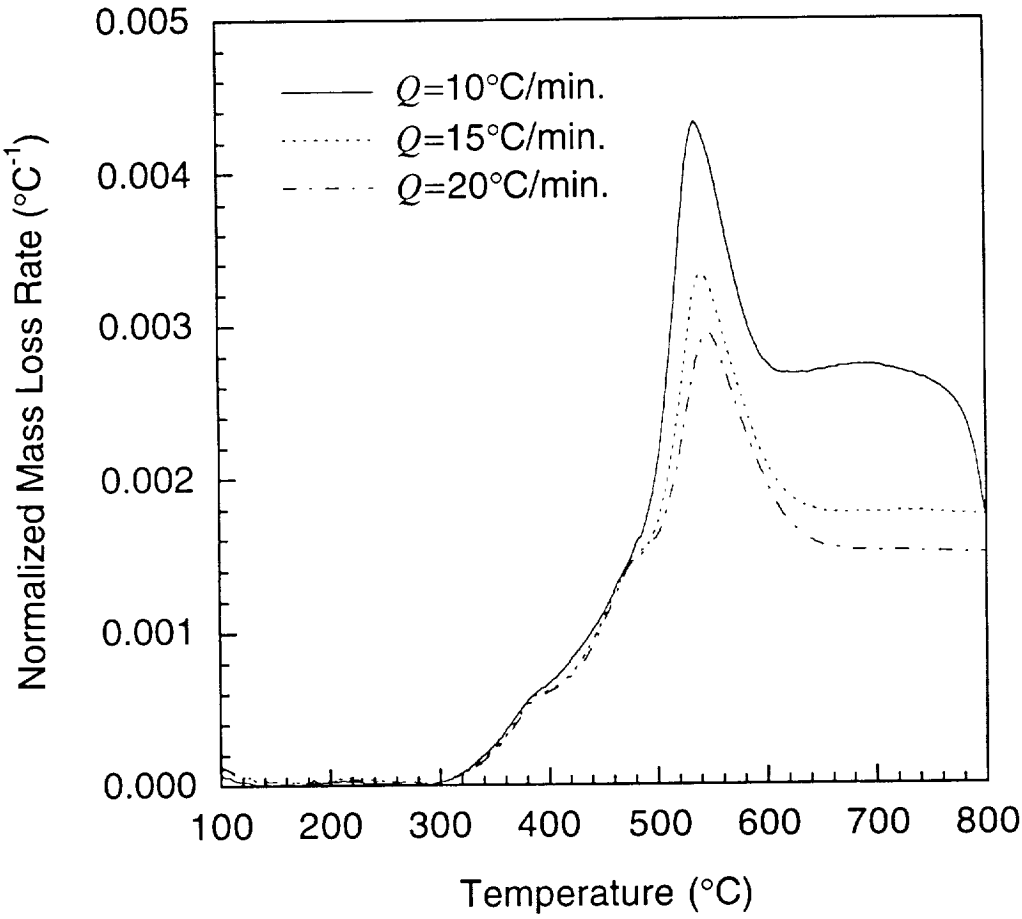

Figure 6.27 Normalized mass loss rates in air at 10°C/min., 15°C/min. and 20°C/min.

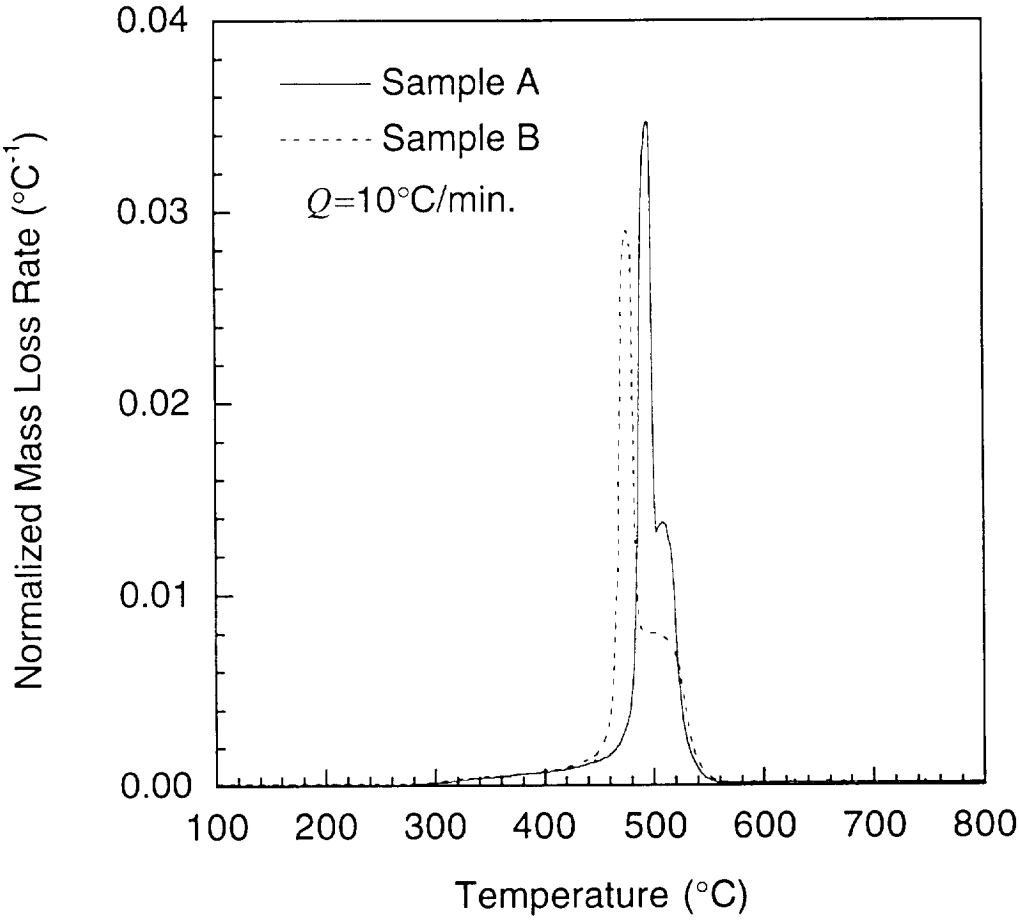

Figure 6.28 Normalized mass loss rates for samples A and B in oxygen at 10°C/min.

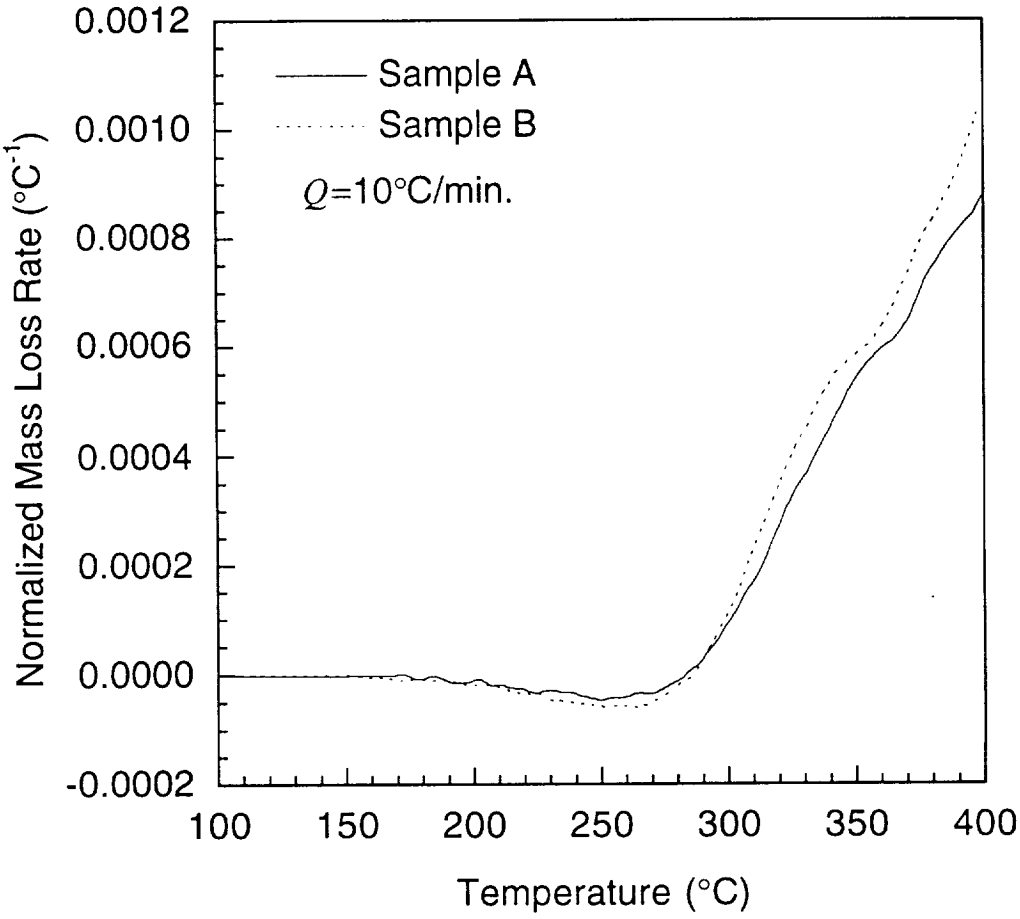

Figure 6.29 Normalized mass loss rates for samples A and B in oxygen at 10°C/min. up to 400°C.

temperature range at all heating rates.

6.3.3 Reduction of TGA Data in Air and Oxygen

As the later reactions which occur in air and oxygen are not compatible with the simple engineering models under development here, and as they only take place at temperatures much higher than those in the range of interest, no attempt was made to model them. Instead a model of the low-temperature oxidative reactions, and their interaction with the thermal reactions, was developed.

A single oxidative reaction and two thermal reactions were assumed to occur. The coefficients for the thermal reactions were not modified. Due to the fact that the first thermal reaction appears to be suppressed in the oxidative atmosphere, it was assumed that the oxidative reaction consumes some of the same material components as the first thermal reaction. As a result, the mass fraction for the first thermal reaction was broken into two components – one component shares material with the oxidative reaction while the other component is consumed only by the first thermal reaction. The best-fit to the data in air was achieved through the evaluation of the χ^2 cost function over a range of mass fractions for the first oxidative reaction, as described in Section 4.4. The optimum set of oxidative reaction coefficients derived in this manner are shown in Table 6.7 along with the thermal reaction coefficients for the three reaction model. Figure 6.30 and 6.31 show the analytical fit to the region between 100°C and 450°C at heating rates of 10°C/min. and 20°C/min. The fit to the initial portion of the mass loss rate curve is very good in both cases.

The reaction coefficients derived for the oxidative and thermal reactions were then applied to the data in oxygen in order to determine a

Table 6.7 Optimum Parameters for Three Reaction Model

Thermal Reactions			
$y_1 = 0.07$	$E_{11} = 182$	$k_{11} = 3.12 \times 10^{10}$	$n_{11} = 1.61$
$y_2 = 0.09$	$E_{21} = 182$	$k_{21} = 3.12 \times 10^{10}$	$n_{21} = 1.61$
$y_3 = 0.24$	$E_{31} = 239$	$k_{31} = 7.90 \times 10^{12}$	$n_{31} = 3.20$
$y_4^{\dagger} = 0.60$			
Oxidative Reactions			
$y_1 = 0.07$	$E_{12} = 135$	$k_{12} = 1.67 \times 10^{8}$	$n_{12} = 2.30$
$y_2 = 0.09$			
$y_3 = 0.24$			
$y_4^{\dagger} = 0.60$			

† Unreacted in nitrogen (remains as char residue), reacts completely (through unmodeled ablation) in the presence of oxygen.

Units for E_{ij} are kJ/mol.

Units for k_{ij} are s^{-1}.

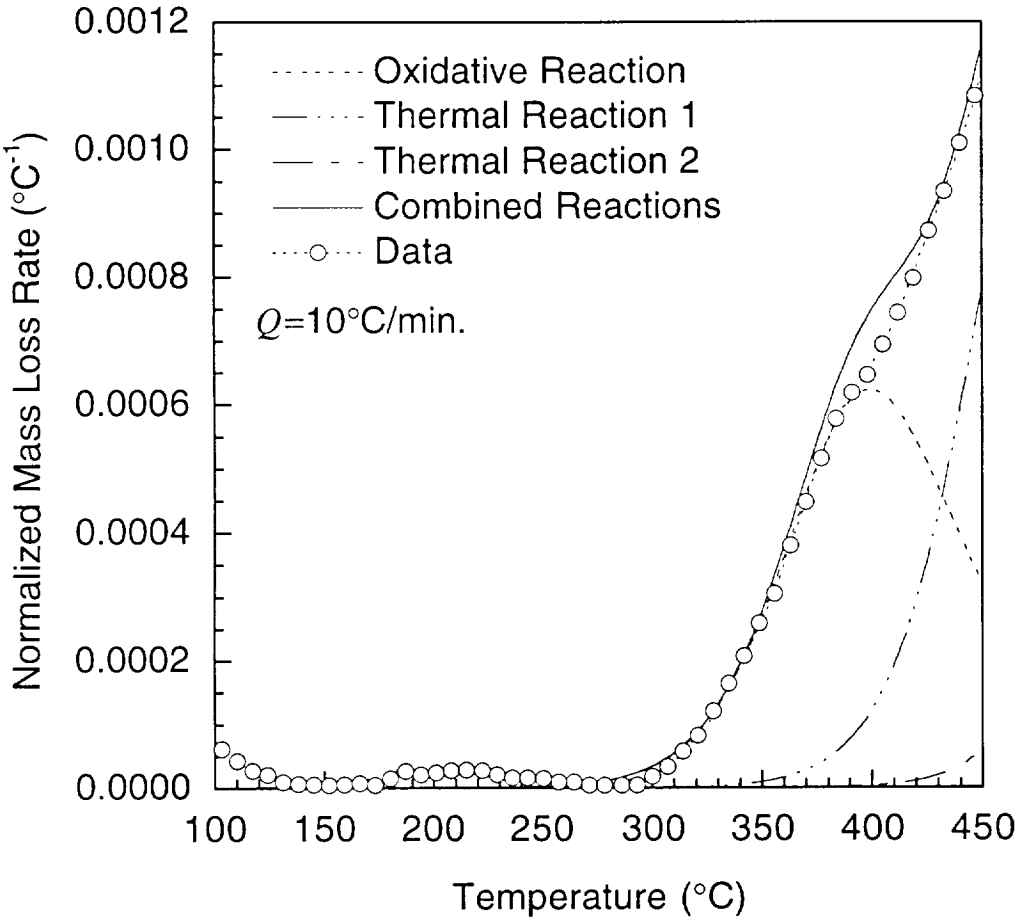

Figure 6.30 Three reaction model prediction versus data in air at 10°C/min.

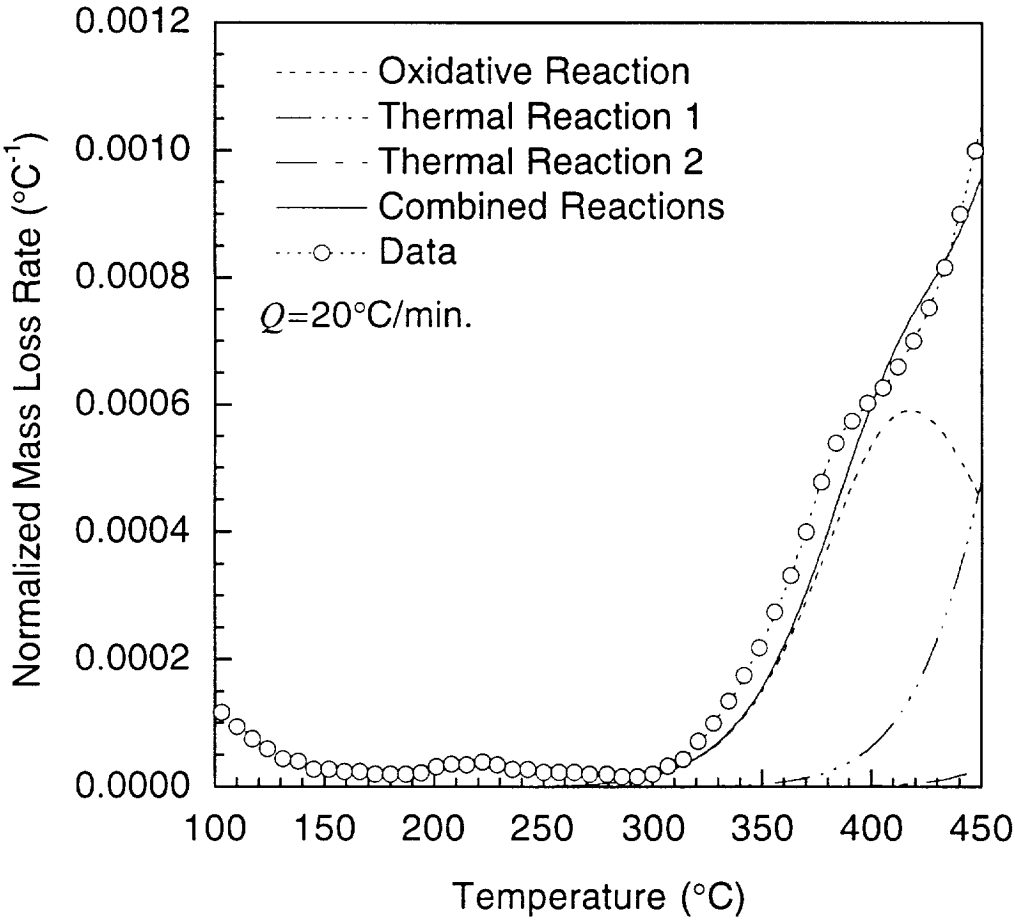

Figure 6.31 Three reaction model prediction versus data in air at 20°C/min.

concentration dependency for the oxidative reaction. The oxidative reaction which was derived from the data in air appears to have a concentration dependency with m_{12}= 1.0, however it was not possible to replicate the data across the temperature range between 100°C and 400°C using only a single oxidative reaction. The reasons for this are discussed in the following section.

6.3.4 Discussion

Figures 6.32 and 6.33 show the very early mass loss rate behavior (up to 400°C) of the neat resin in air and oxygen. In the case of the mass loss rates in air, the first reaction displays very little rate sensitivity, with the three curves being almost identical. In pure oxygen, the initial portion of the curve appears to very rate insensitive while the rates above 325°C tend to demonstrate some divergence at the higher heating rates. In particular a peak begins to become more evident in the region of 340°C as the heating rate in increased. It is also worth noting that there is a small initial mass gain below 300°C at each of the heating rates. This is most likely due to oxygen binding to the polymer before the mass loss mechanisms have initiated.

A clearer picture of what is happening is shown in Figure 6.34 which compares the behaviors in nitrogen, air and oxygen at 20°C/min. As the concentration of oxygen is increased, the front end of the mass loss rate curve appears to gradually separate from the rest of the data. This suggests that the oxidative reaction, like the thermal reactions, is possibly composed of, not one, but several similar reactions. Not only are the heating rate dependencies of these reactions different, but their concentration dependencies are also different. The data presented in Figures 6.33 suggests at least two reactions. The first is highly concentration dependent, but rate insensitive. A second which is more sensitive to heating rate, and less

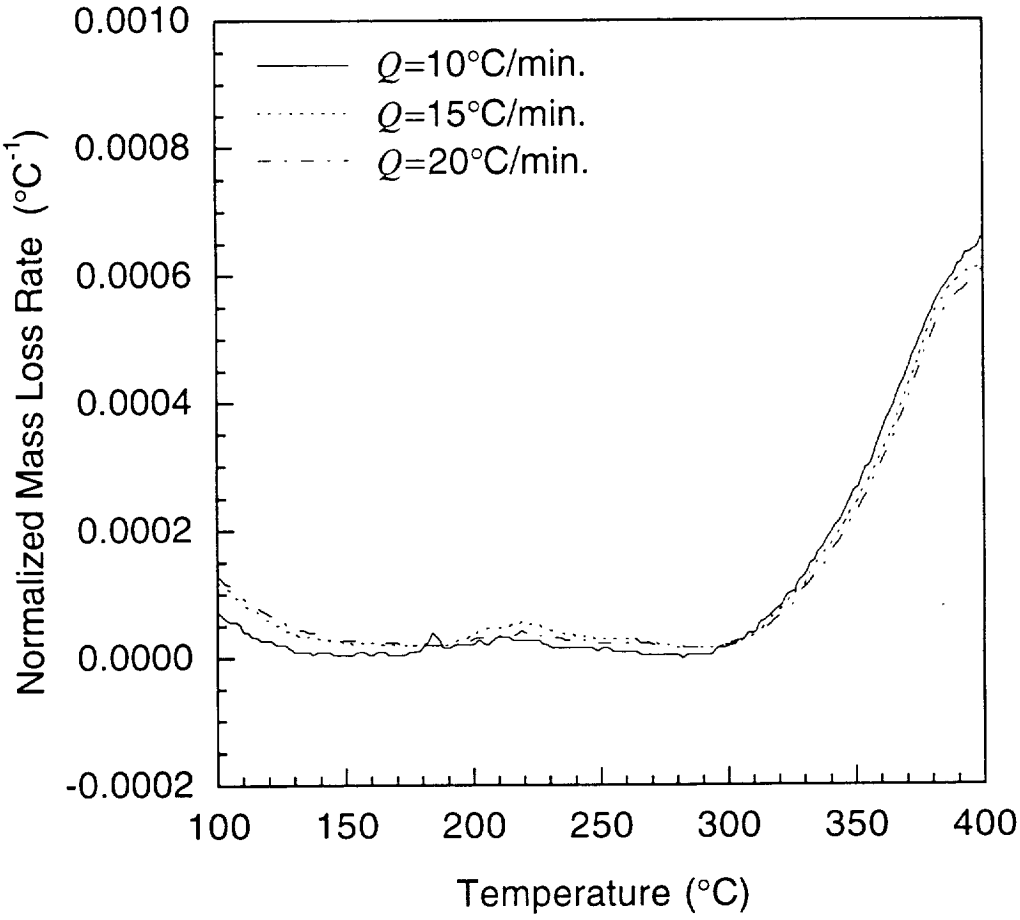

Figure 6.32 Normalized mass loss rates in air at 10°C/min., 15°C/min. and 20°C/min. up to 400°C.

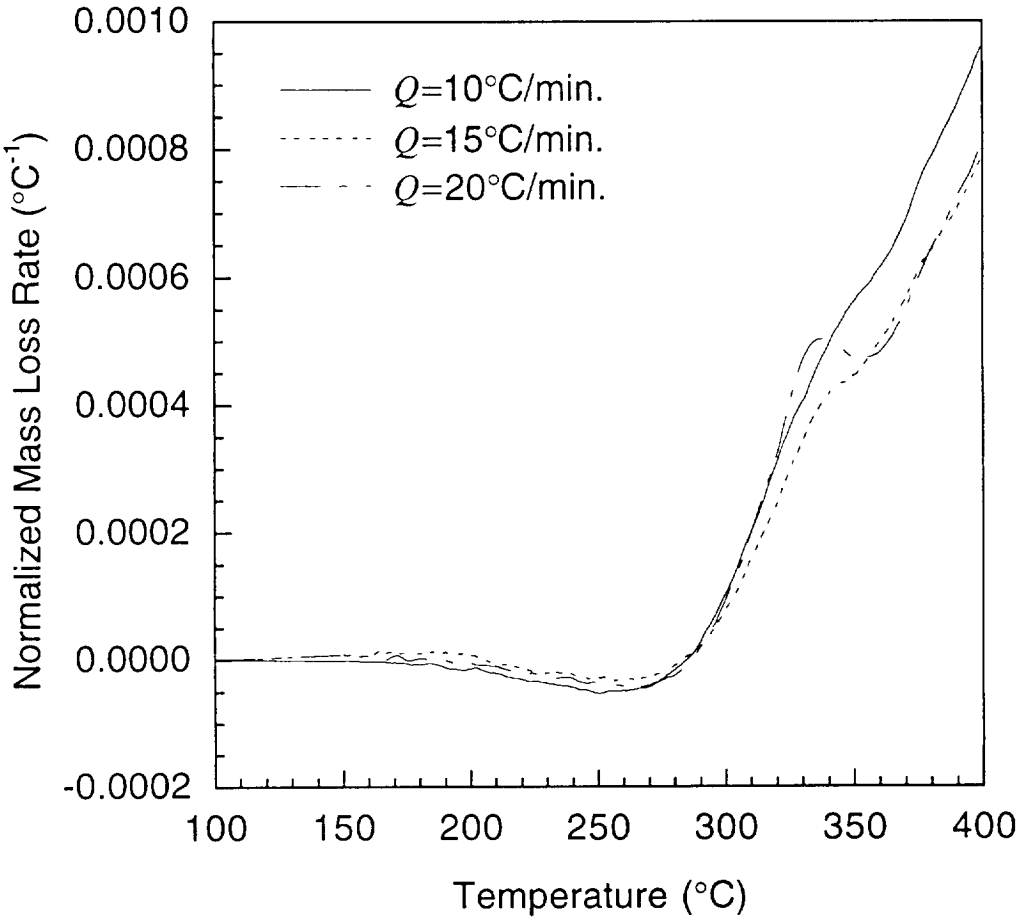

Figure 6.33 Normalized mass loss rates in oxygen at 10°C/min., 15°C/min. and 20°C/min. up to 400°C.

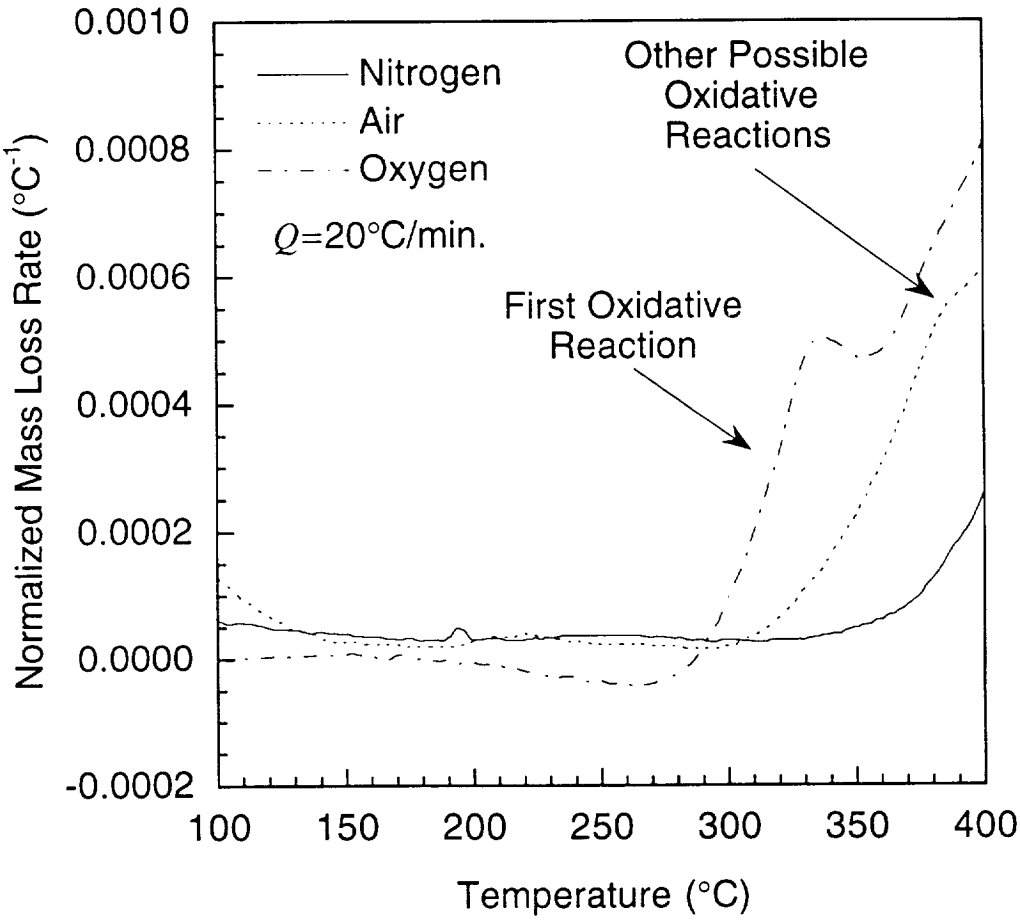

Figure 6.34 Mass loss rates in nitrogen, air and oxygen at 20°C/min.

concentration dependent, shifts to the right as heating rate increases, leaving the first reaction isolated. These details are not as evident in air. In air, the later oxidative reaction appears to be severely confounded with the thermal reactions. The later oxidative reaction(s) was not modeled in this work. However, the model used captures the trend of the data in air, and allows us to establish at least a first-order estimate of the concentration and rate dependence of the first oxidative reaction for the heating rates considered here.

6.4 ISOTHERMAL AGING TESTS

6.4.1 Isothermal TGAs in Nitrogen

The data for each of the three isothermal TGAs are presented in Figure 6.35. Only a single sample was tested in each case. The mass loss has been normalized so that a normalized mass loss equal to one represents a 40% reduction in the original sample mass. The total mass loss after an exposure time of 10 hours increases rapidly with temperature. The mass loss at 380°C is more than twice that at 340°C, and eight times greater than that at 300°C, after 10 hours. The initial jump in the mass loss curves is most likely due to the relatively large temperature overshoot in the TGA furnace which was caused by the initial rapid ramp up to the test temperatures. This overshoot would tend to greatly accelerate the reactions operating in this regime.

The mass loss curves at each of the temperatures appear to want to asymptote to different final values. Again this behavior is suggestive of the presence of many small mass fraction reactions which are closely grouped together in this temperature regime. As the temperature is increased, more and more of the mass fractions will be consumed by reactions resulting in an increase in the overall mass loss.

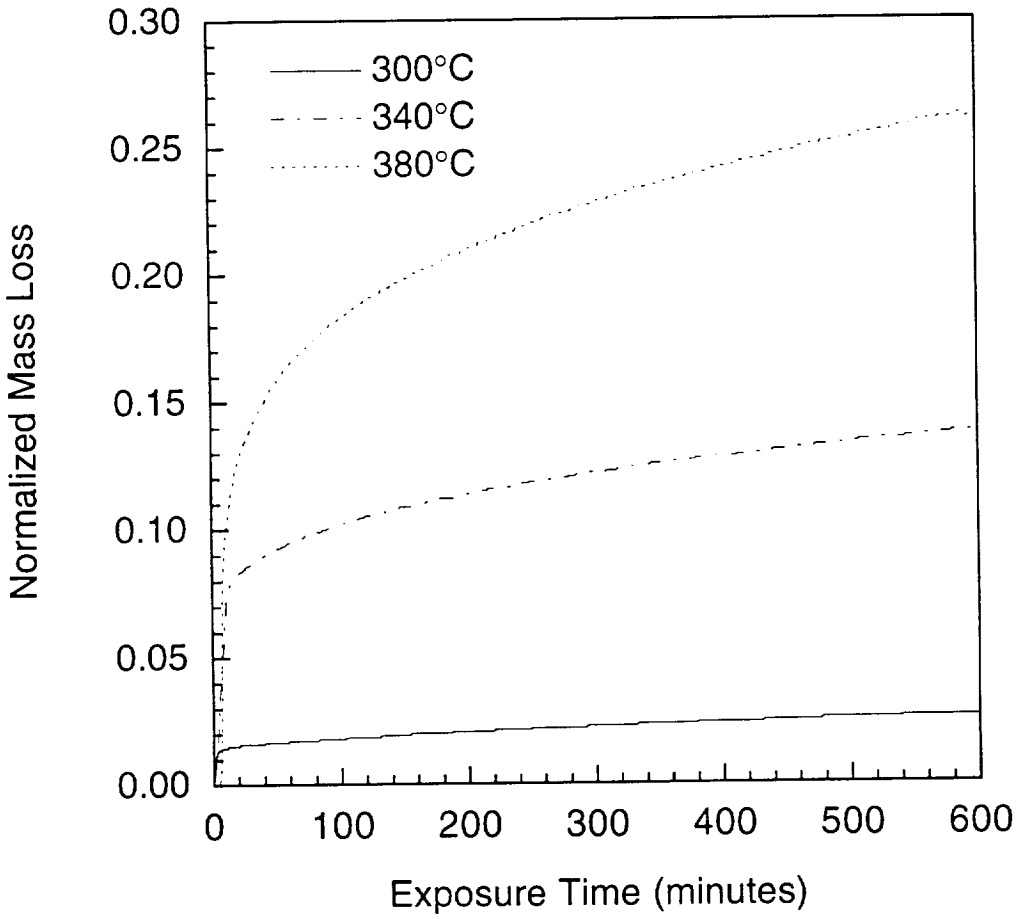

Figure 6.35 Isothermal TGA data at 300°C, 340°C and 380°C.

6.4.2 Isothermal Aging of Neat Resin

Figures 6.36 and 6.37 show plots of the percentage mass loss from all neat resin groups for the 316°C and 343°C isothermal runs respectively. All data presented at 316°C been corrected for moisture absorption as described in Chapter 5. All raw, uncorrected data may be found in Appendix D. A total of eight samples from each resin group are represented by the data points at 24 hours, while the data at 240 hours represents only a single sample from each group. The number of samples represented by each data point between these two times decreases by one at each sampling time due to the extraction of a single sample from each group at each time. A considerable amount of scatter is present in the data at 316°C. The data is much tighter at 343°C where the mass losses are greater.

All mass loss curves, for each sample type and each exposure temperature, are approximately linear in shape. The increase in mass loss at the higher temperature in quite dramatic, with mass losses from all specimens being greater than twice those recorded at 316°C. The trend of the data at 316°C indicates that a higher mass loss occurs from specimens with a higher surface area to volume ratio. The trend is less clear at 343°C, where sample groups E and F have approximately the same mass loss percentage at each time while that of sample group H is considerably lower. Figures 6.38 and 6.39 show the mass loss per unit surface area for each of the sample groups at 316°C and 343°C. The data at 316°C suggests that the mass loss from the samples is controlled by the amount of surface area exposed to the environment. The data at 343°C again is less clear, with the mass loss per unit surface area of samples E and F, which were quite similar when plotted on a volumetric basis, diverging at 343°C. This suggests that the mass loss at 343°C tends to shift from a surface area controlled effect to a volume

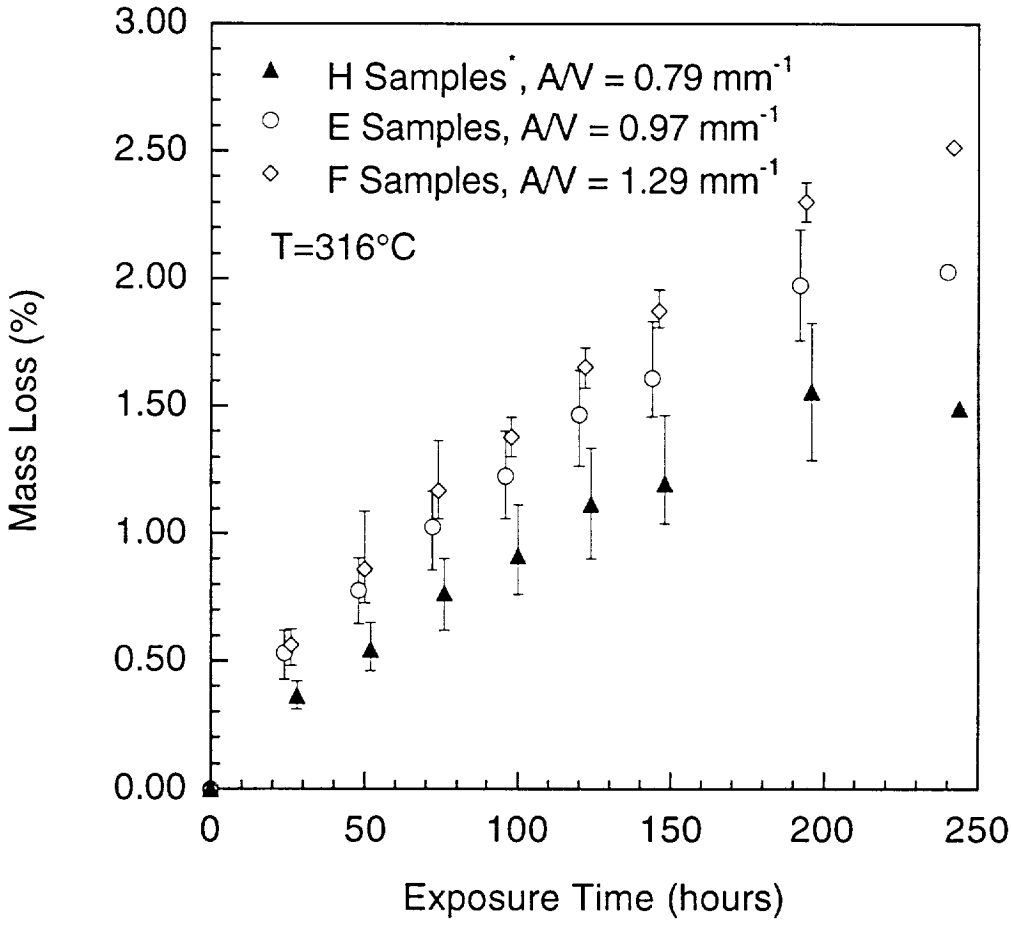

Figure 6.36 Volume mass loss percentage versus exposure time of neat resin samples for 316°C isothermal run (*Actual temperature of H samples was 306°C).

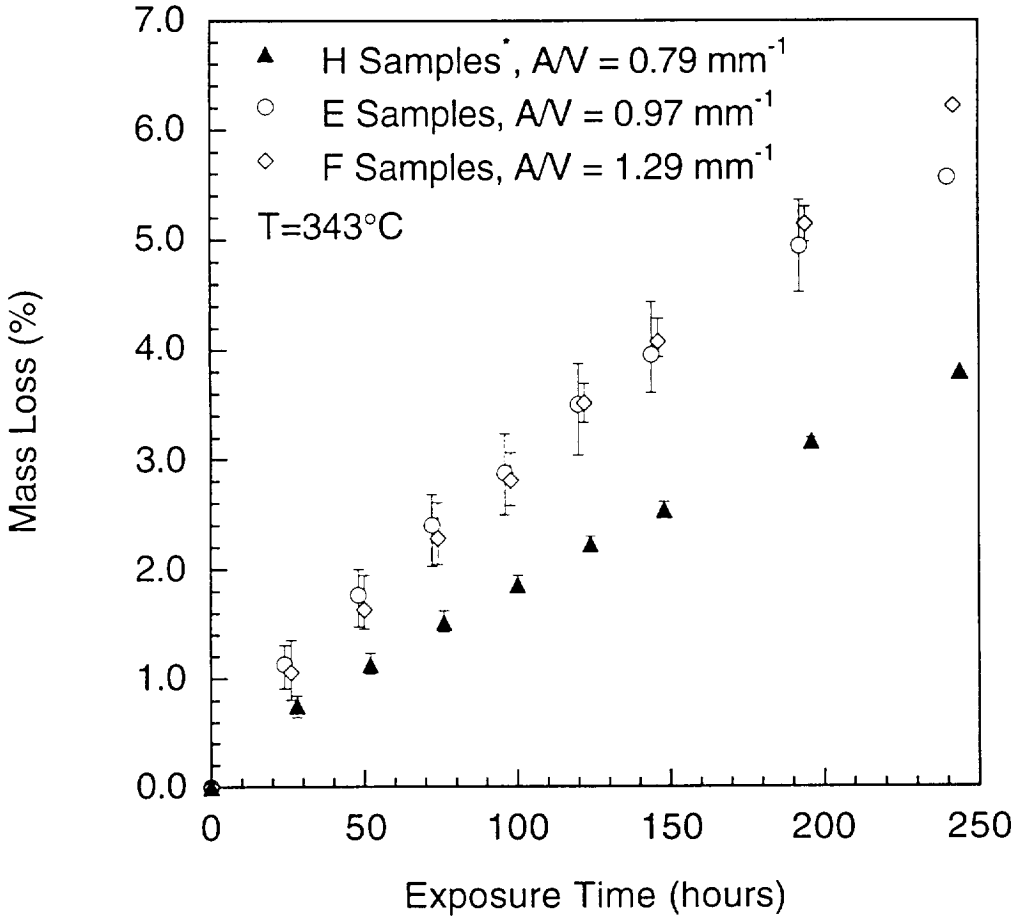

Figure 6.37 Volume mass loss percentage versus exposure time of neat resin samples for 343°C isothermal run (*Actual temperature of H samples was 333°C).

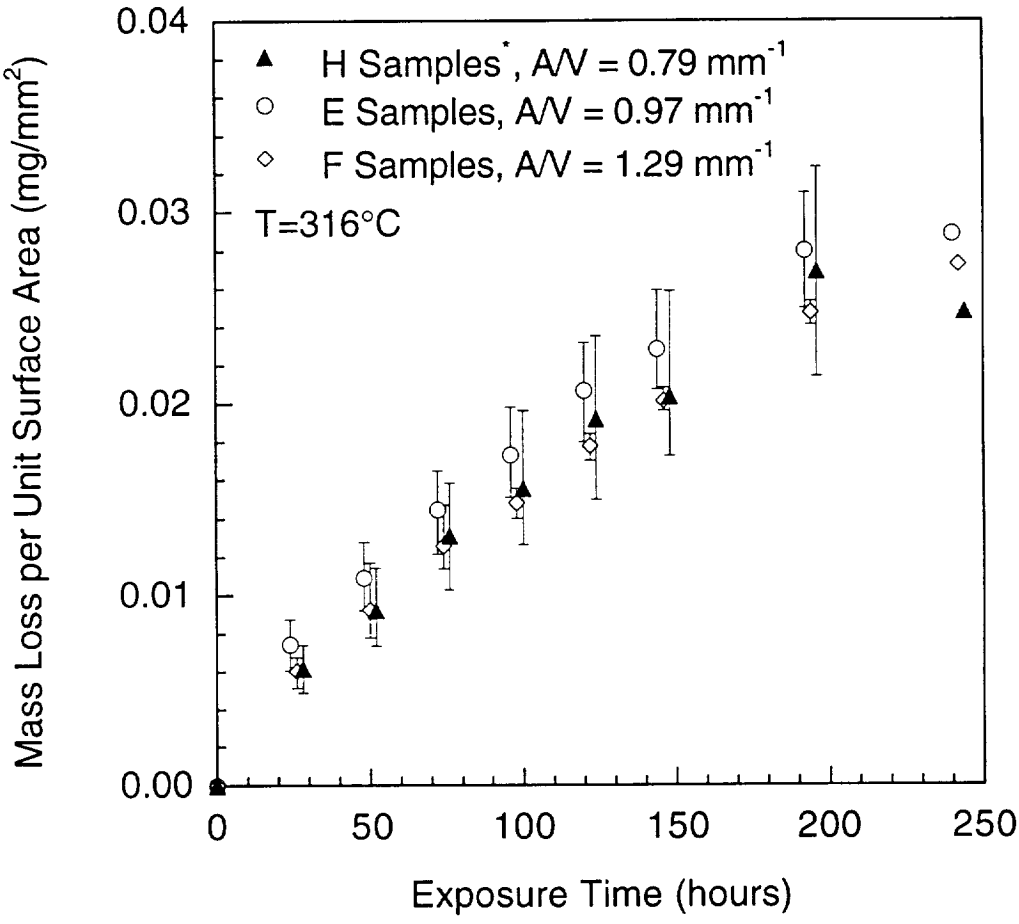

Figure 6.38 Mass loss per unit surface area versus exposure time of neat resin samples for 316°C isothermal run (*Actual temperature of H samples was 306°C).

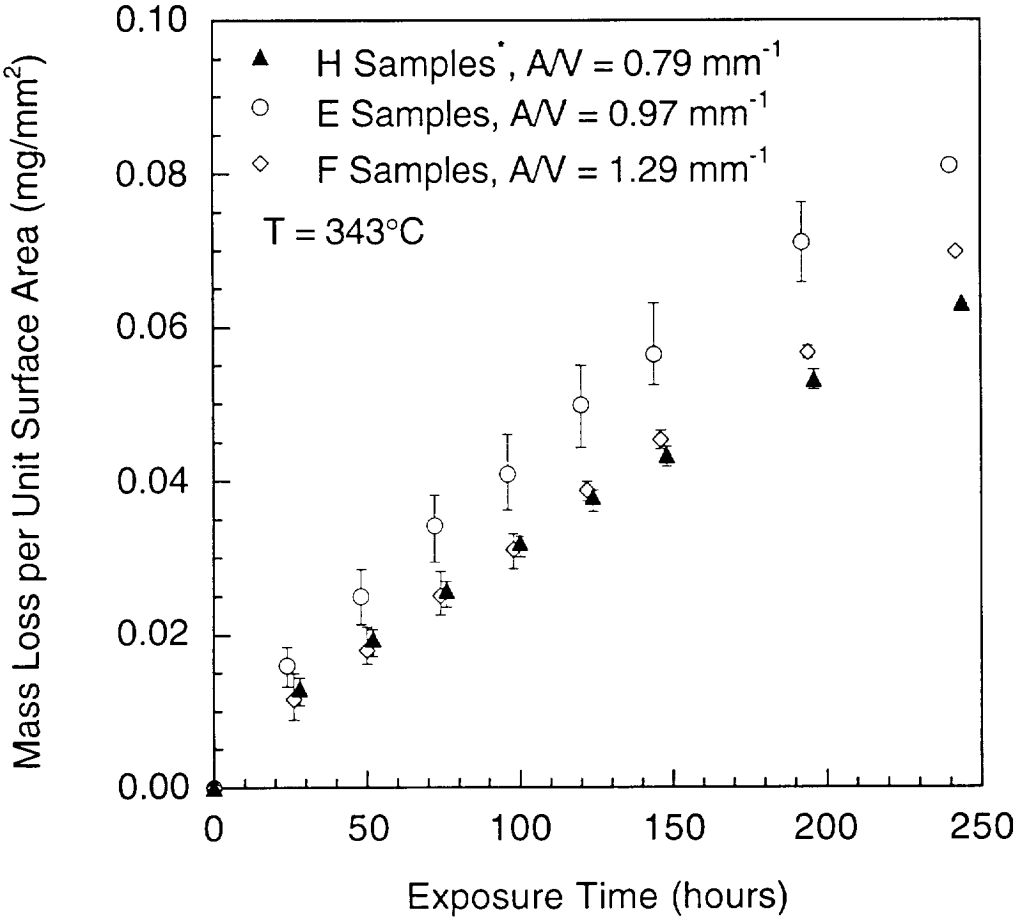

Figure 6.39 Mass loss per unit surface area versus exposure time of neat resin samples for 343°C isothermal run (*Actual temperature of H samples was 333°C).

controlled effect.

Figures 6.40 and 6.41 show the percentage shrinkage in each of the three principal directions for neat resin sample group E. The data presented here is representative of the other sample groups. A large amount of scatter is evident at both 316°C and 343°C. While the overall trend of the data suggests that shrinkage occurs in all directions at longer aging times, the scatter in the data is so large that no definite conclusions may be drawn.

Figures 6.42 and 6.43 show the evolution of the degraded surface layer on specimens aged in air at 343°C. All neat resin photomicrographs were taken from the neat resin E group specimens. A complete set of these photomicrographs is given in Appendix E. A distinct, lighter surface layer is present in all of the photomicrographs and the progression of the layer into the material core can be clearly seen. The thickness of the layer is uniform in each photomicrograph. At longer aging times, the formation of voids in the surface layer begins, with the size and density of these voids increasing over time. No voids are evident in the core of the material. No surface cracking was observed in any of the neat resin specimens which were examined.

Figure 6.44 shows the results of a grayscale analysis carried out across the degraded layer for samples aged for 144 and 240 hours at 343°C. Two distinct levels exist, with a sharp front dividing these levels. The surface layer corresponds to the higher plateau. No gradient is evident across this layer, nor is there a gradient across the core material. This data suggests that degradation near the surface is characterized by a uniformly degraded layer which progresses into the material over time.

The surface layer thickness is plotted as a function of exposure time in Figure 6.45. Also plotted in this figure is the data previously recorded by Bowles [6]. Bowles' data is shown here as two continuous lines due to the fact

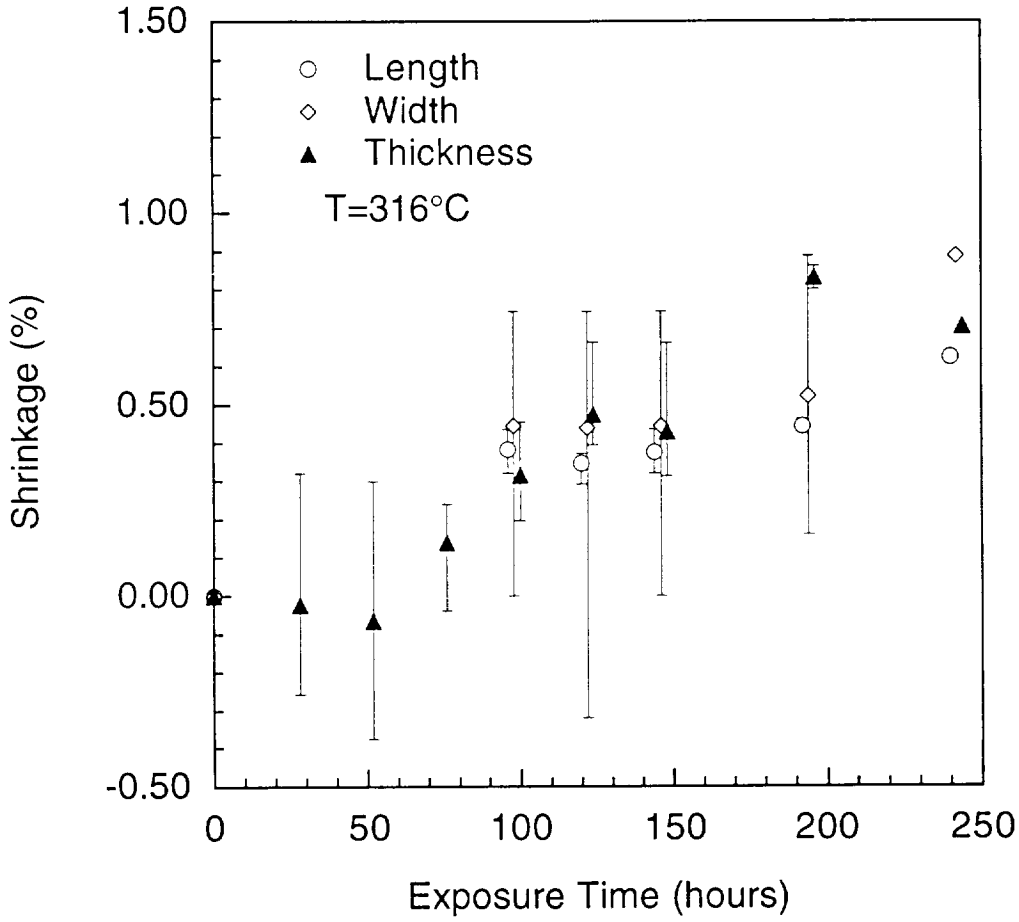

Figure 6.40 Dimensional shrinkage versus exposure time for neat resin E group at 316°C.

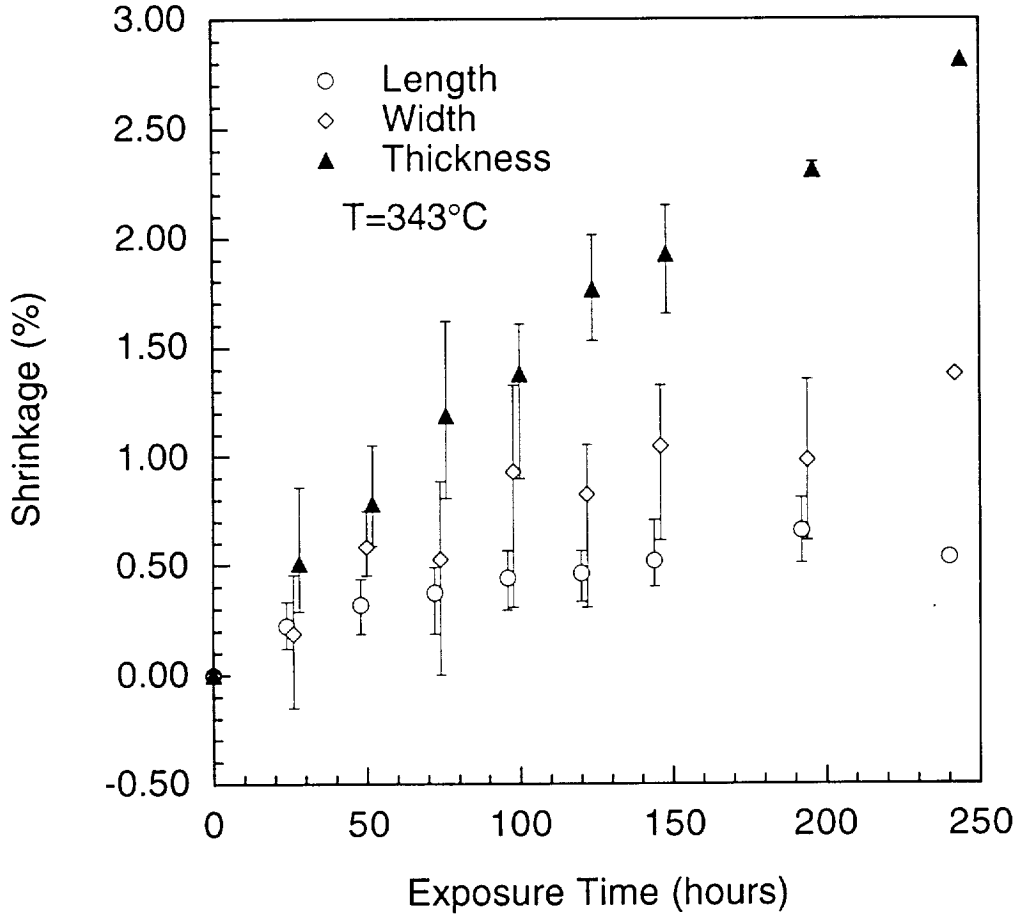

Figure 6.41 Dimensional shrinkage versus exposure time for neat resin E group at 343°C.

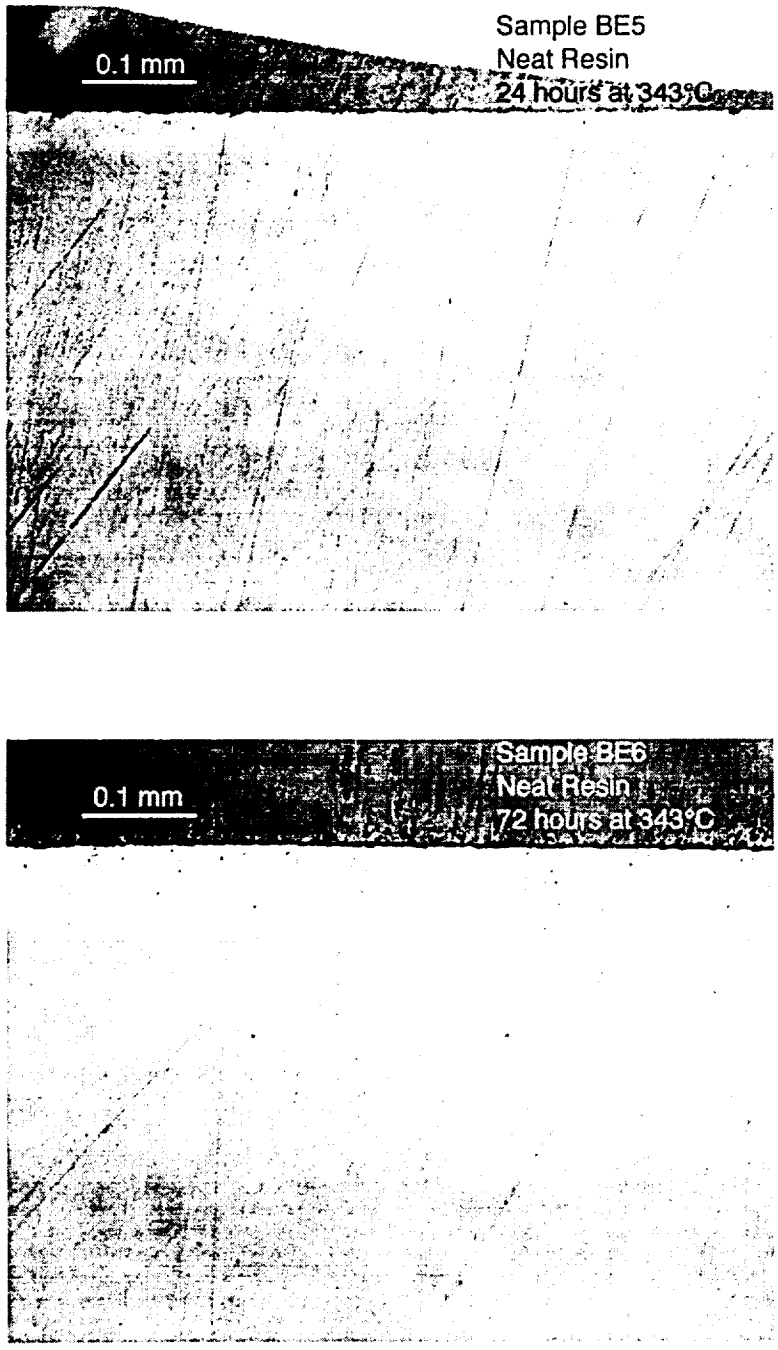

Figure 6.42 Photomicrographs of surface layer on neat resin samples exposed to air for 24 hours (*top*) and 72 hours (*bottom*) at 343°C.

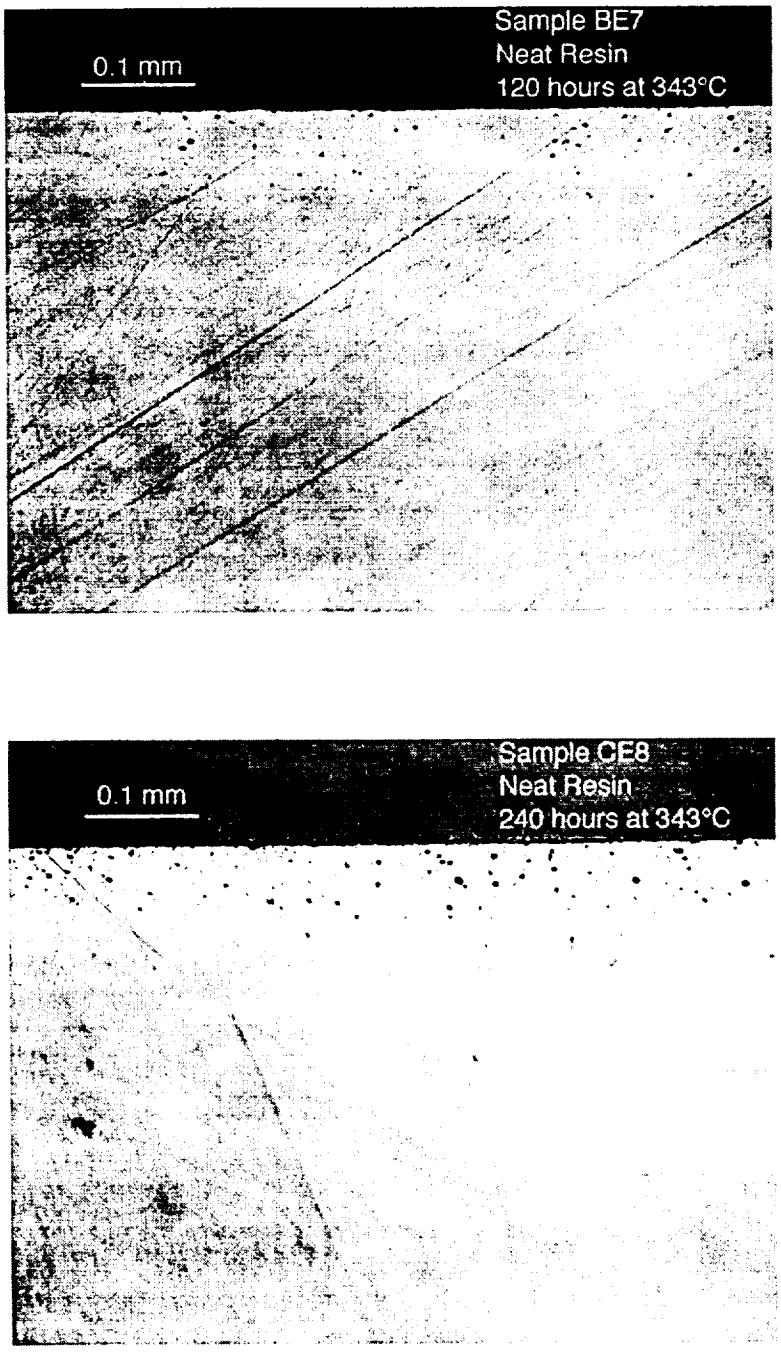

Figure 6.43 Photomicrographs of surface layer on neat resin samples exposed to air for 120 hours (*top*) and 240 hours (*bottom*) at 343°C.

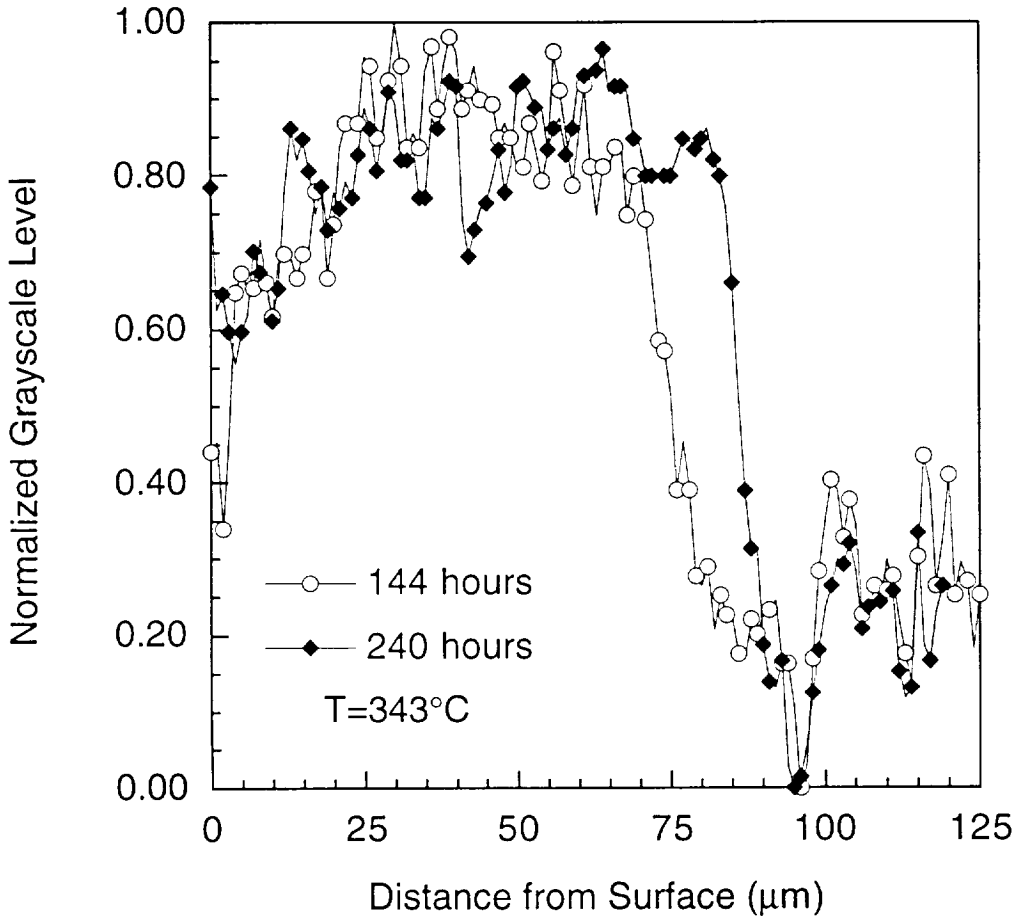

Figure 6.44 Normalized grayscale levels across degraded surface layer at 343°C.

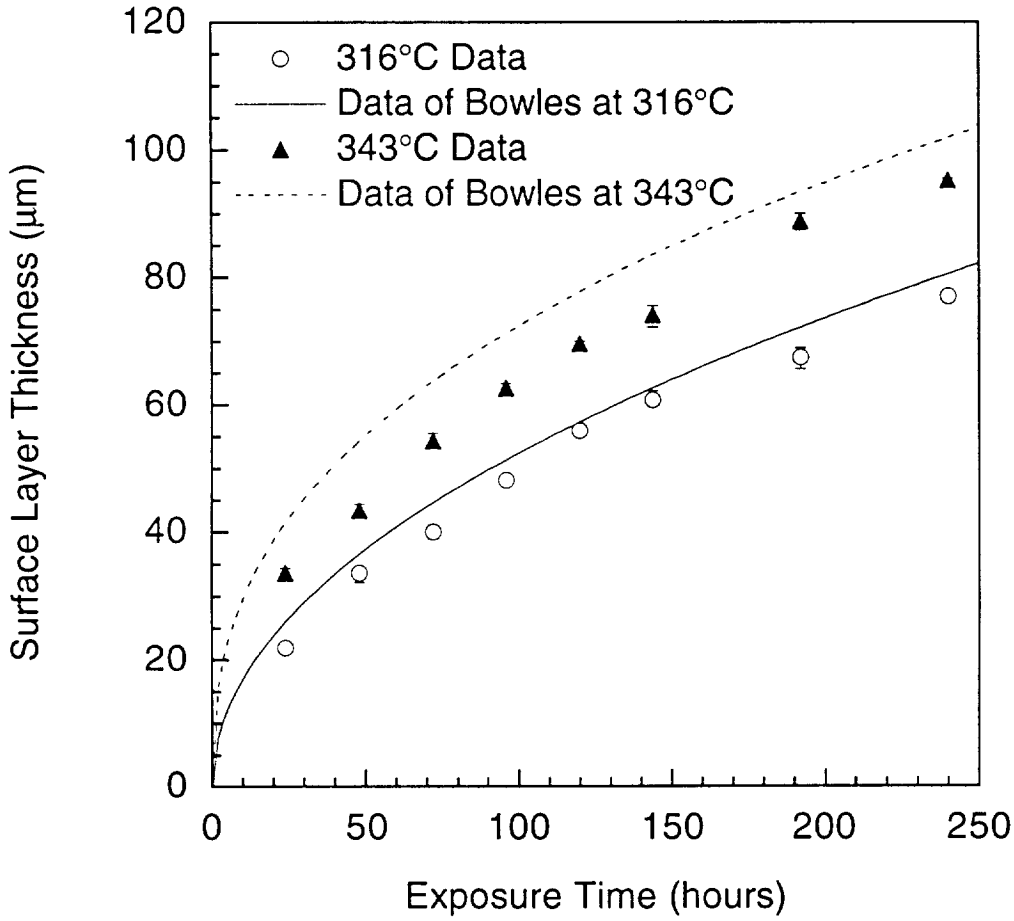

Figure 6.45 Surface layer thickness versus exposure time for neat resin samples exposed to air at 316°C and 343°C.

that he reported his surface layer data in the form of power-law fits to the recorded measurements. Very good agreement is found between the data recorded here and that of Bowles. Each data point presented here represents the mean of three separate measurements taken from each photomicrograph. Very low scatter is observed.

6.4.3 Reduction of Neat Resin Isothermal Data

A fit to the neat resin surface layer data was achieved using the oxidative reaction coefficients derived from the TGA experiments. It was assumed that the diffusion rate through each of the specimen surfaces was the same. An effective diffusion coefficient for the oxidative reactions was found by matching the predicted surface layer growth to the data at 316°C and 343°C. A low consumption factor, $R_{ox} = 0.01$, was used. The surface layer was considered to be visible when $\alpha_{ox} \geq 0.25$. The choice of the value at which the surface layer becomes visible is rather arbitrary due to the fact that the surface layer degrades uniformly. This insensitivity to α is caused by the fact that the reaction progresses much more quickly than the oxygen can diffuse into the structure, with the reaction proceeding to completion even in regions with a very low concentration of oxygen. Hence, as long as the coefficients for the oxidative reaction are in the correct regime, then a reasonable estimate of the diffusion coefficient may be achieved. The values for the diffusion coefficient derived in this manner are shown in Table 6.8. Figure 6.46 shows the fit to the data at 316°C and 343°C. The fit at both temperatures is excellent.

6.4.4 Isothermal Aging of Unidirectional Composites

Figures 6.47 and 6.48 show the percentage mass loss from all

Table 6.8 Parameters for Analytical Fit to Neat Resin Specimens

Thermal Reactions - 316°C			
$y_1 = 0.16$	$E_{11} = 182$	$k_{11} = 1.36 \times 10^{9}$	$n_{11} = 1.61$
$y_2 = 0.24$	$E_{21} = 239$	$k_{21} = 7.90 \times 10^{12}$	$n_{21} = 3.20$
$y_3^{\dagger} = 0.60$			
Thermal Reactions - 343°C			
$y_1 = 0.16$	$E_{11} = 182$	$k_{11} = 0.84 \times 10^{9}$	$n_{11} = 1.61$
$y_2 = 0.24$	$E_{21} = 239$	$k_{21} = 7.90 \times 10^{12}$	$n_{21} = 3.20$
$y_3^{\dagger} = 0.60$			
Oxidative Reactions			
$y_1 = 0.16$	$E_{12} = 135$	$k_{12} = 1.67 \times 10^{8}$	$n_{12} = 2.30$
			$m_{12} = 1.00$
Diffusion Coefficient			
Neat Resin		$D_o = 3.36 \times 10^{-11}$	$C = 6611$

† Unreacted in nitrogen (remains as char residue), reacts completely (through unmodeled ablation) in the presence of oxygen.

All coefficients derived for $R_{ox} = 0.01$.

Units for E_{ij} are kJ/mol.

Units for k_{ij} are s^{-1}.

Units for D_o are m^2/s.

Units for C are Kelvin.

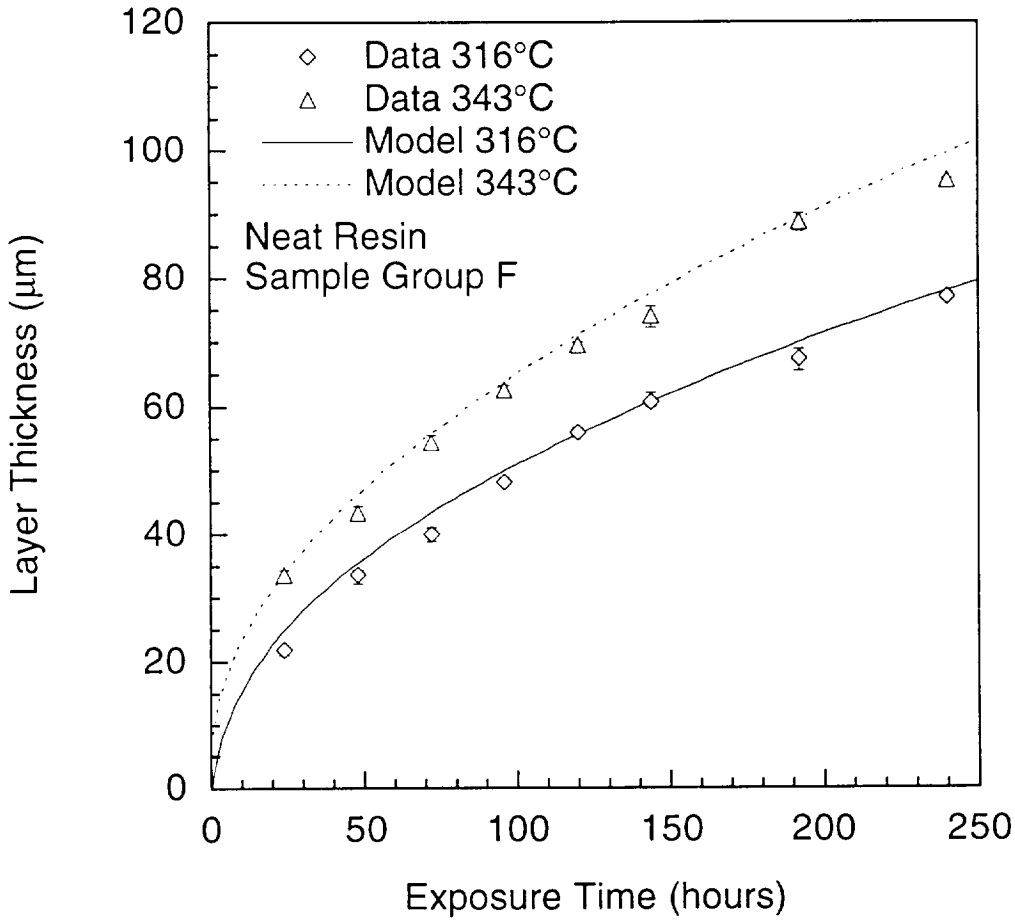

Figure 6.46 Surface layer thickness data and analytical predictions for neat resin sample group F at 316°C and 343°C.

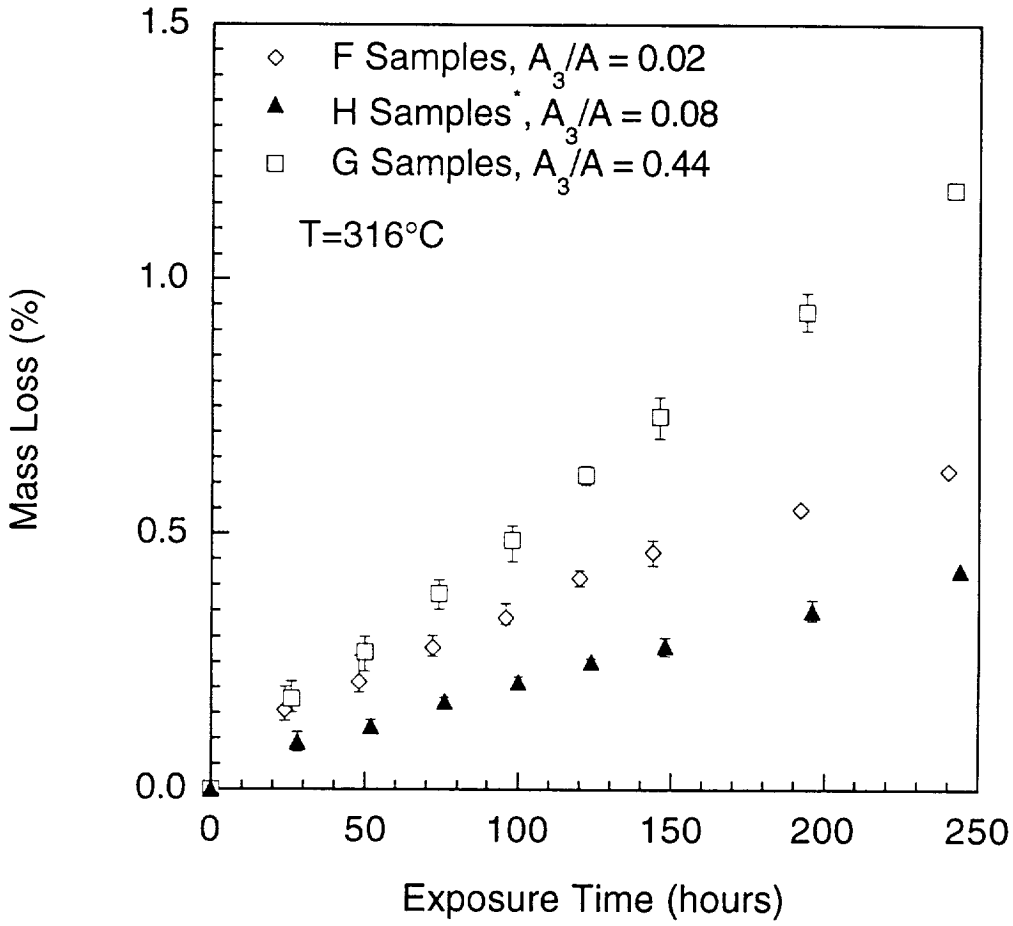

Figure 6.47 Mass loss percentage versus exposure time for unidirectional samples at 316°C (*Actual temperature of H samples was 306°C).

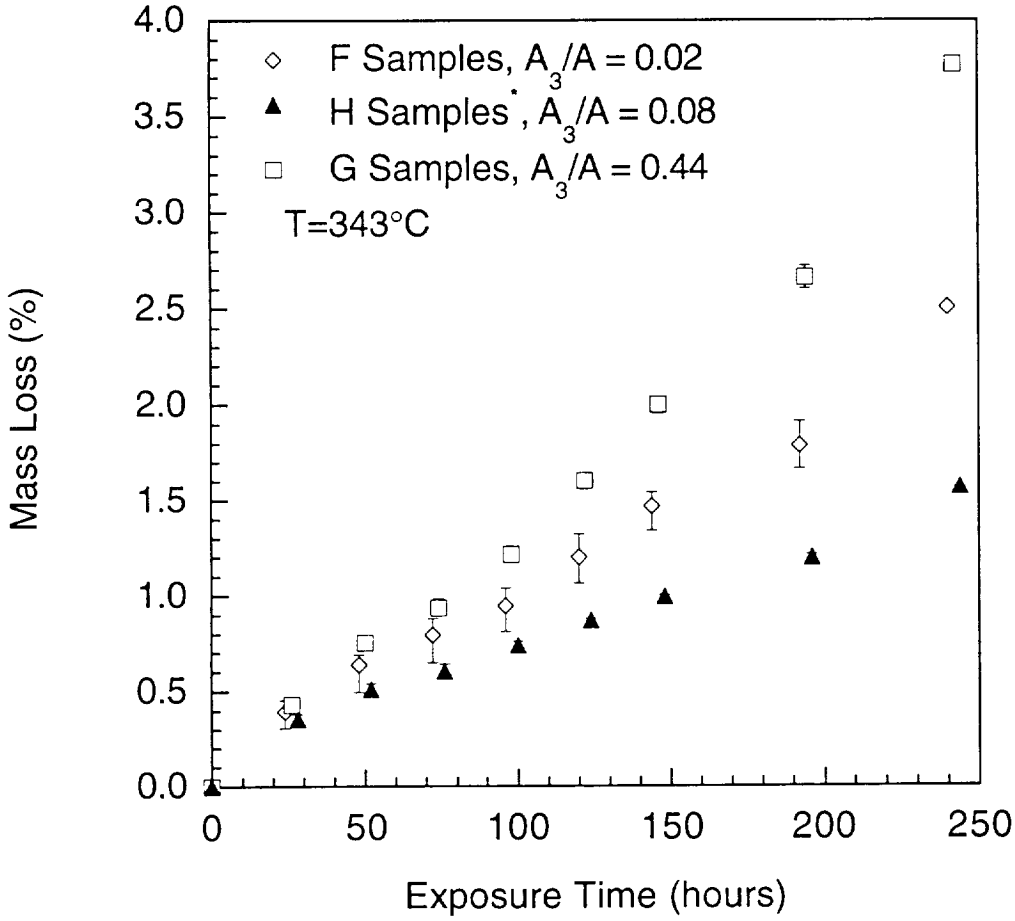

Figure 6.48 Mass loss percentage versus exposure time for unidirectional samples at 343°C (*Actual temperature of H samples was 333°C).

unidirectional composite groups at 316°C and 343°C respectively. A similar data collection method was employed here as was used in the case of the neat resin specimens, with the data points at 24 hours representing a total of eight individual samples from each group while those at 240 hours represents only a single sample from each group. All 316°C data presented here has been corrected to account for residual moisture, as described in Chapter 5. The raw, uncorrected data may be found in Appendix D. As in the case of the neat resin the mass loss curves at both temperatures are all approximately linear. The trend of the data indicates that a higher mass loss results from specimens with a higher surface area to volume ratio. Similarly, a higher mass loss is evident for specimens with a higher surface area of exposed cut fiber ends. Specimens with the greatest surface area of cut fiber ends, demonstrate a much larger mass loss than either of the other two specimen types at both test temperatures. In all cases, the data is very tight at each data collection point, with little variation being evident.

Figures 6.49 and 6.50 show the mass loss per unit surface area at 316°C and 343°C. The mass loss per unit surface area from the samples with a low exposed area of cut fiber ends are very similar at both temperatures. The samples with a high exposed area of cut fiber ends consistently demonstrate a higher mass loss than the other two groups. Figures 6.51 and 6.52 show the mass loss per unit surface area from each of the three principal surfaces of the composites at 316°C and 343°C. In both cases the mass loss from the molded surface and the surface parallel to the fibers are approximately the same, while the mass loss through the surface with cut fiber ends is much higher.

Figures 6.53 and 6.54 show the percentage shrinkage in each of the three principal directions for unidirectional composite group F at 316°C and

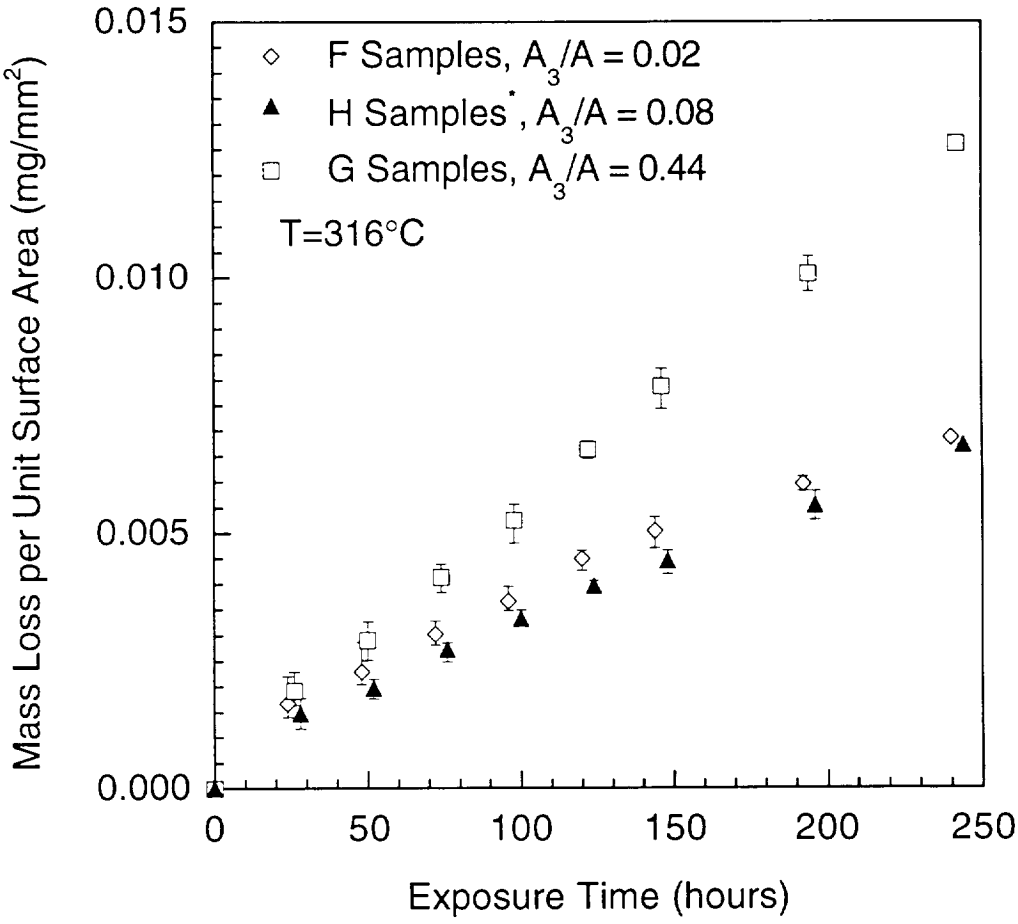

Figure 6.49 Mass loss per unit surface area versus exposure time for unidirectional samples at 316°C (*Actual temperature of H samples was 306°C).

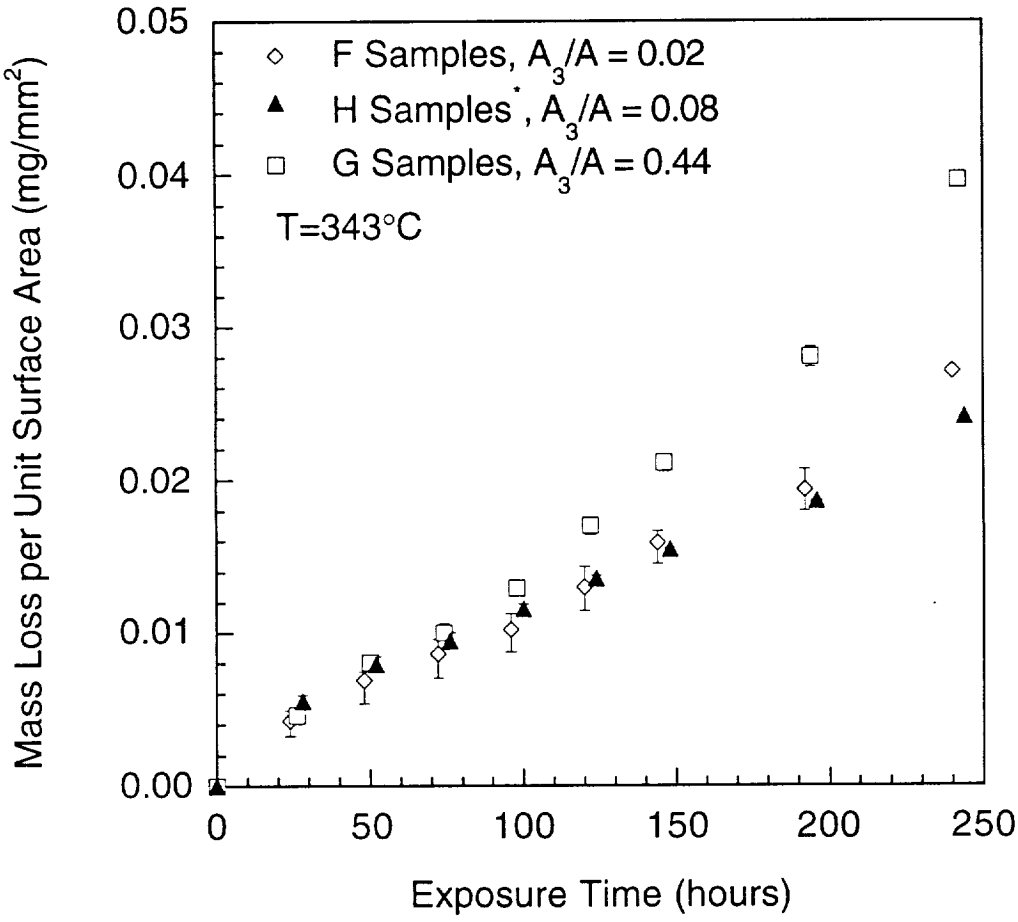

Figure 6.50 Mass loss per unit surface area versus exposure time for unidirectional samples at 343°C (*Actual temperature of H samples was 333°C).

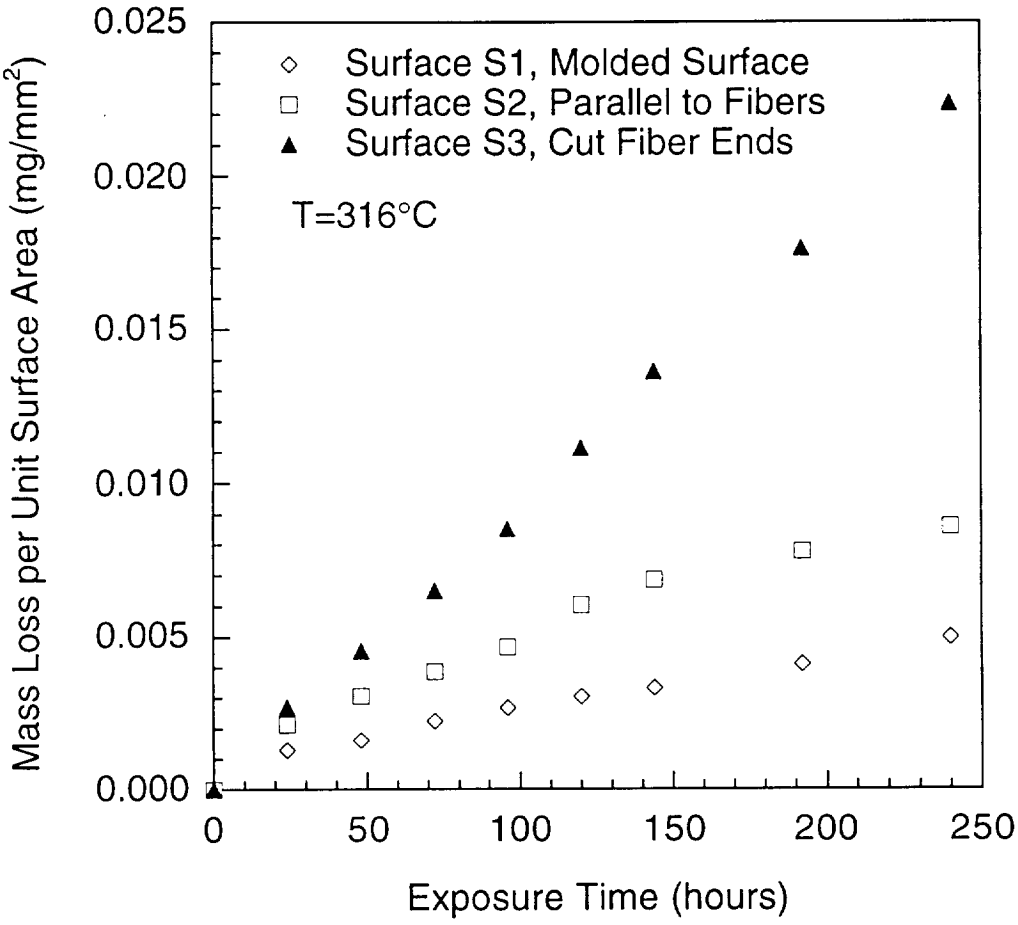

Figure 6.51 Mass loss per unit surface area from the three principal surfaces of the unidirectional composites at 316°C.

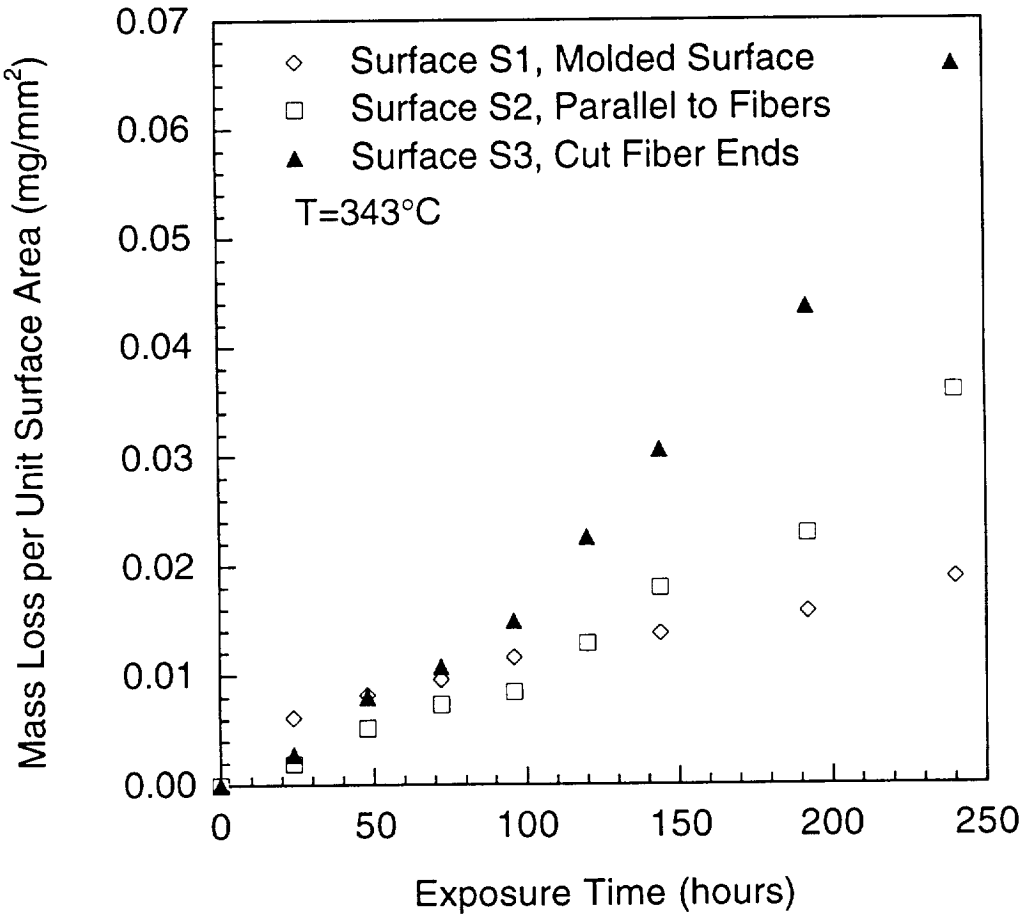

Figure 6.52 Mass loss per unit surface area from the three principal surfaces of the unidirectional composites at 343°C.

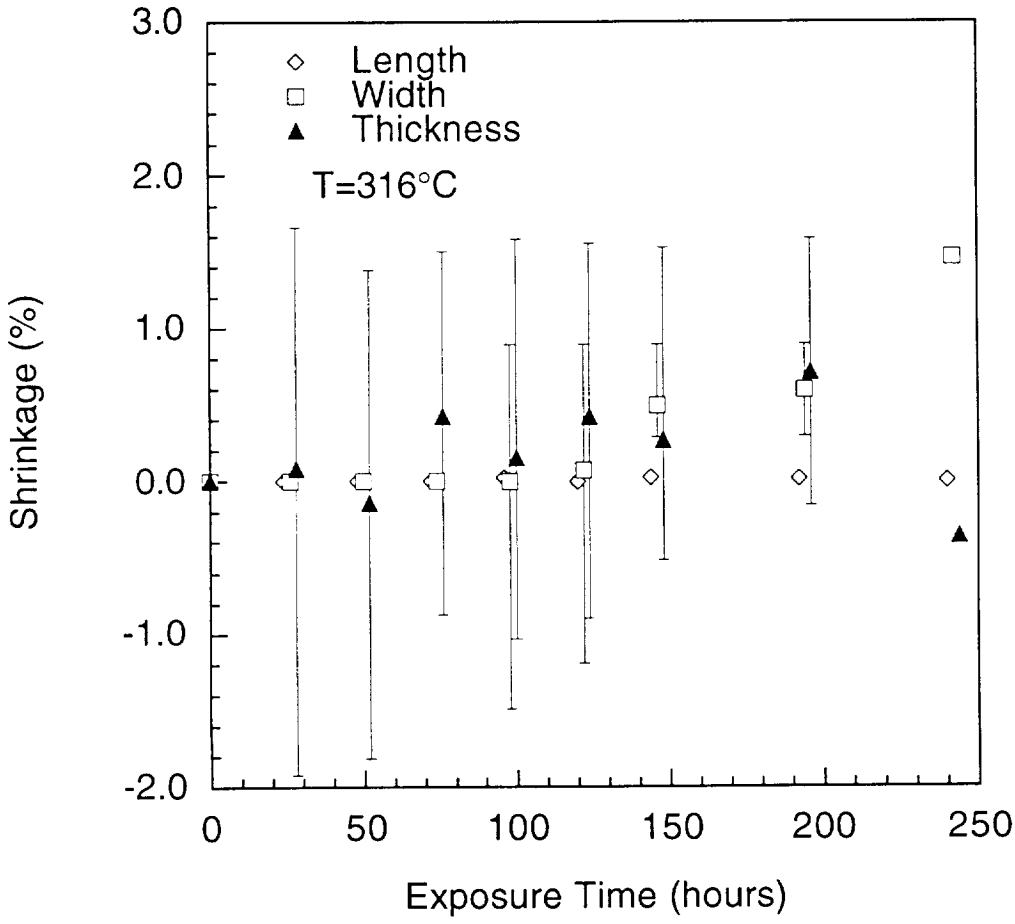

Figure 6.53 Dimensional shrinkage versus exposure time for unidirectional F group at 316°C.

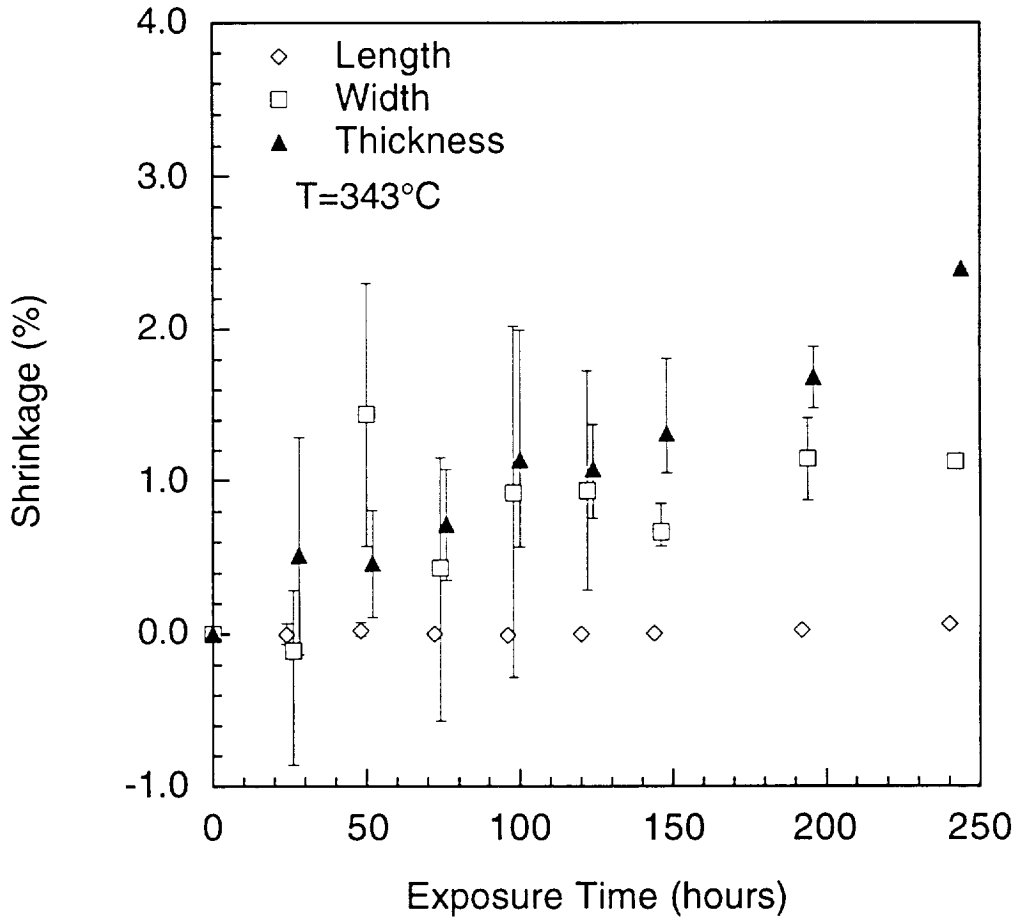

Figure 6.54 Dimensional shrinkage versus exposure time for unidirectional F group at 343°C.

343°C. The data presented here is representative of all the sample groups. The scatter in the data is on the order of the maximum change which was measured. Hence, as in the case of the neat resin, the large amount of scatter in the data prevents any conclusions from being drawn from this data.

Figure 6.55 shows a cross-section of a unidirectional composite sample illustrating the molded surface (*S1*) and the surface parallel to the fibers (*S2*). No excess resin is evident on the molded surface. This was typical of all cross-sectioned unidirectionals which were examined. Figure 6.56 shows photomicrographs, at two different magnifications, of a cross-sectioned composite specimen aged for 144 hours at 343°C. Unlike the neat resin samples, it is not possible to detect a clear degraded layer growing in from the surface. Possible reasons for this are illustrated in Figure 6.57 which shows the degraded layer formation on a neat resin specimen which has also been aged for 144 hours at 343°C. At a magnification of 150x, the degraded layer is clearly visible, however, at a magnification of 375x the transition from the degraded layer to the core material is much harder to determine. This difficulty is caused by the decrease in contrast which occurs as the magnification is increased. The lack of a visible degraded layer prevented the reduction of the data to a set of diffusion coefficients as was done in the case of the neat resin.

While the surface layer growth could not be measured, very clear pictures of the surface cracking which occurred in specimens aged for extended times at 343°C were obtained. Cracks were evident on the *S3* surface of all samples aged for greater than 120 hours at 343°C. No cracking was evident for aging times or aging temperatures less than this, and no cracks occurred on either the molded surface or surface parallel to the fibers on any of the samples. Figure 6.58 shows the network of crazing cracks

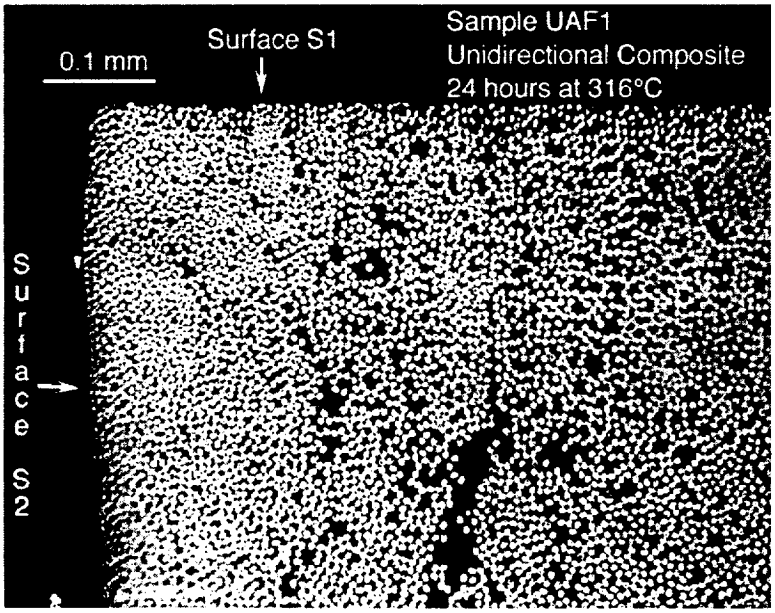

Figure 6.55 Cross-section of unidirectional composite sample illustrating surfaces *S1* and *S2*.

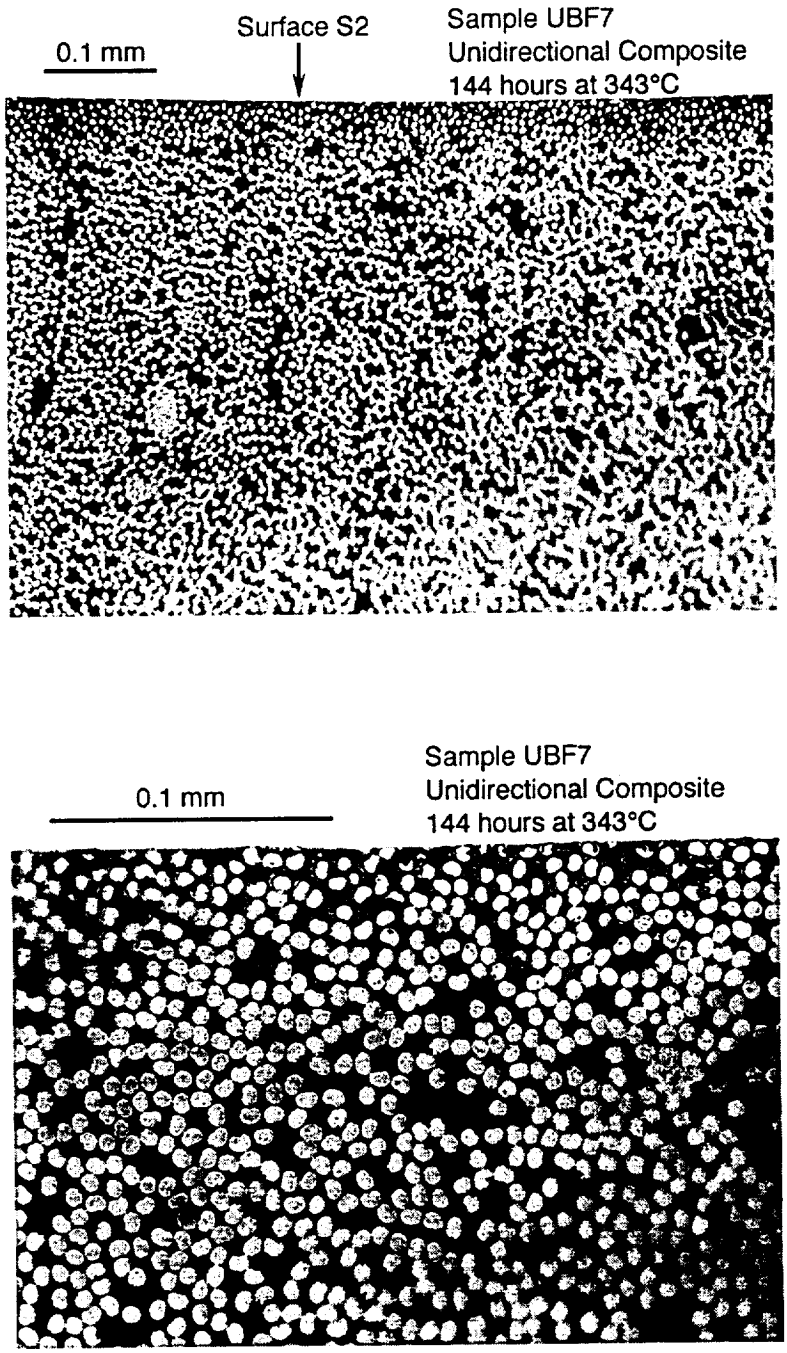

Figure 6.56 Photomicrographs, at magnifications of 150x (*top*) and 375x (*bottom*), showing surface *S2* for unidirectional composite exposed to air for 144 hours at 343°C.

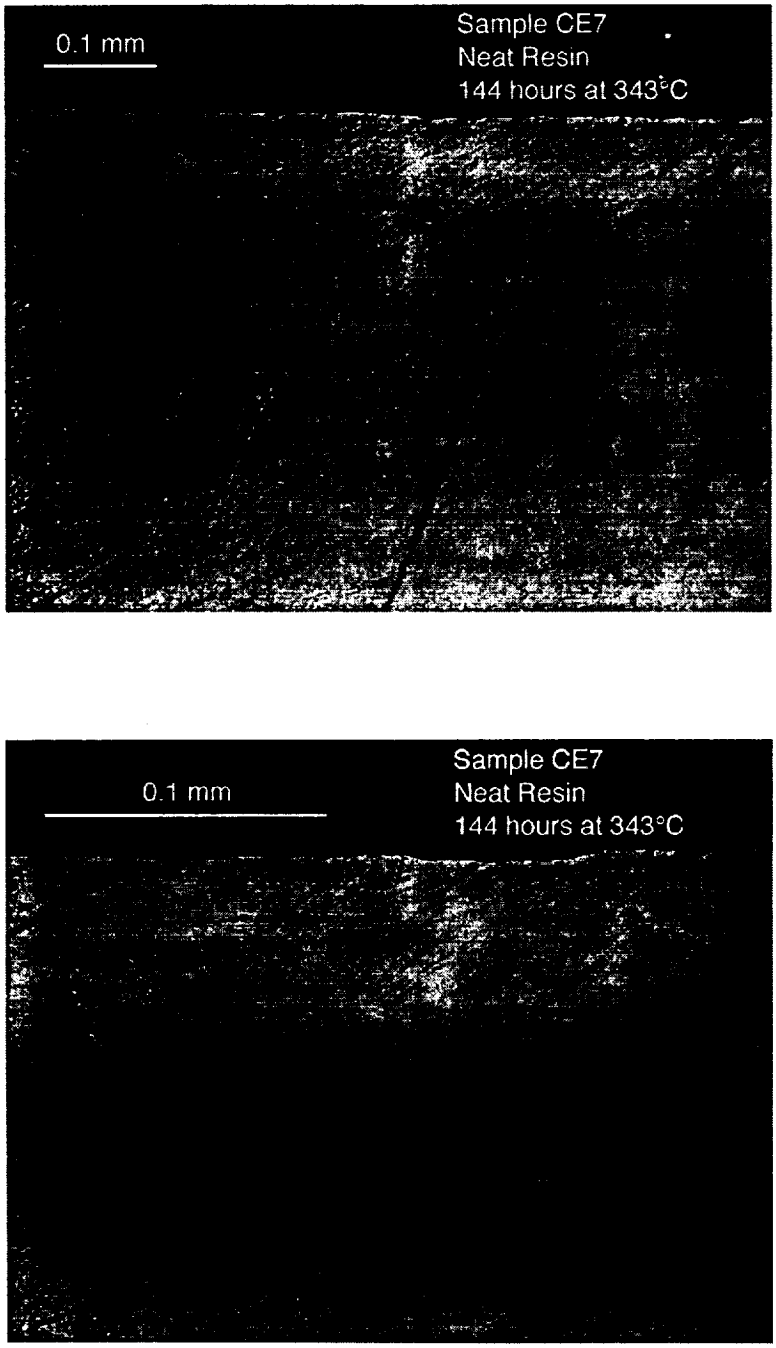

Figure 6.57 Photomicrographs, at magnifications of 150x (*top*) and 375x (*bottom*), of surface layer growth on neat resin sample exposed to air for 144 hours at 343°C.

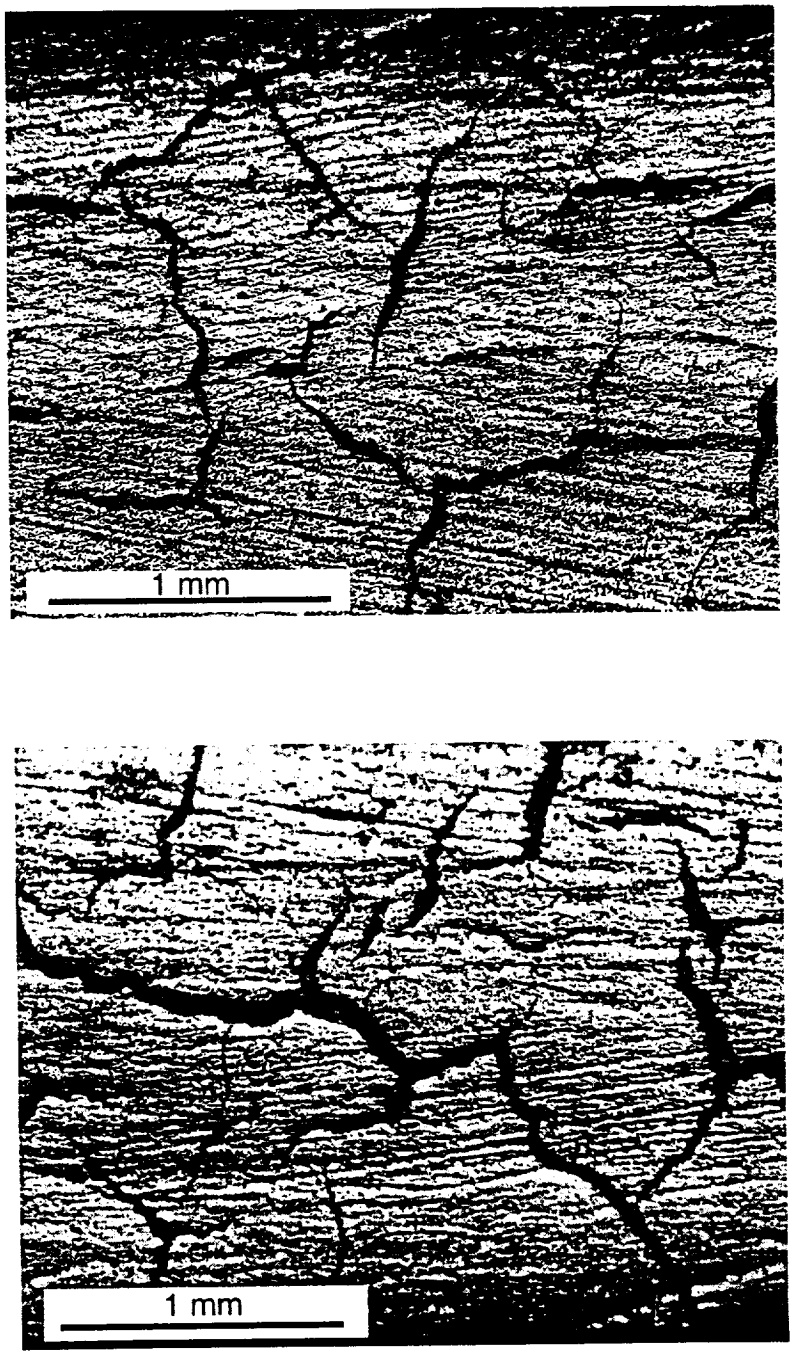

Figure 6.58 Cracks on *S3* surface of unidirectional composites exposed to air for 120 hours (*top*) and 240 hours (*bottom*) at 343°C.

which occur on the surface with exposed cut fiber ends (*S3*) at 120 and 240 hours. While the number of cracks on this surface does not increase significantly with time, an increase in the size and depth of the cracks is evident. Figures 6.59 and 6.60 show the propagation of these cracks from the surface, along the fiber direction, for aging times of 120, 144, 192 and 240 hours. The depth of penetration of the cracks formed at 120 hours is very small, with most cracks being arrested very close to the surface. As time increases, the depth of penetration increases dramatically as does the size of the crack opening near the surface.

6.4.5 Mass Loss Analytical Correlations

A fit to the mass loss data for the neat resin specimens was achieved by combining together the oxidative and thermal reactions, derived from the TGA data, and the diffusion coefficient, obtained from the reduction of the surface layer data for the neat resin specimens, into a single model. Preliminary analyses using this model revealed two very important facts. The first of these was that the reaction coefficients derived for the first thermal reaction through TGAs in nitrogen grossly overestimate the isothermal mass loss behavior of this reaction. Direct use of these coefficients resulted in thermal mass loss predictions which were greater than twice the total mass loss from the specimens at 316°C and 343°C. This effect is clearly illustrated in Figure 6.61 which shows a comparison between the predicted thermal mass loss and the isothermal TGAs in nitrogen. While the mass loss predictions up to 10 hours are conservative, the slopes of the predicted mass loss curves in are considerably steeper than the corresponding data, and at longer aging times will result in a large overestimation of the data as is the case in the macroscopic specimens. The second fact revealed by preliminary

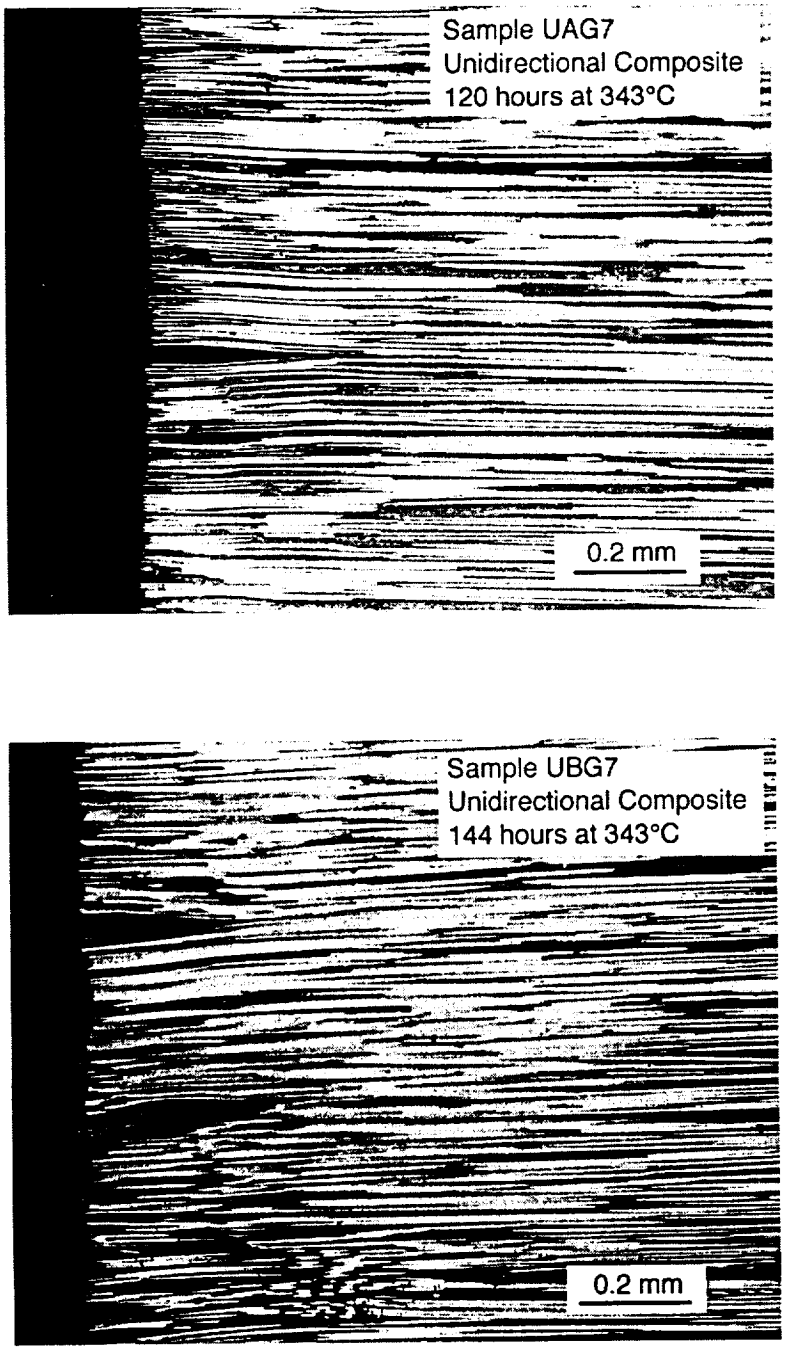

Figure 6.59 Propagation of cracks along the fiber direction for unidirectional composites exposed to air for 120 hours (*top*) and 144 hours (*bottom*) at 343°C.

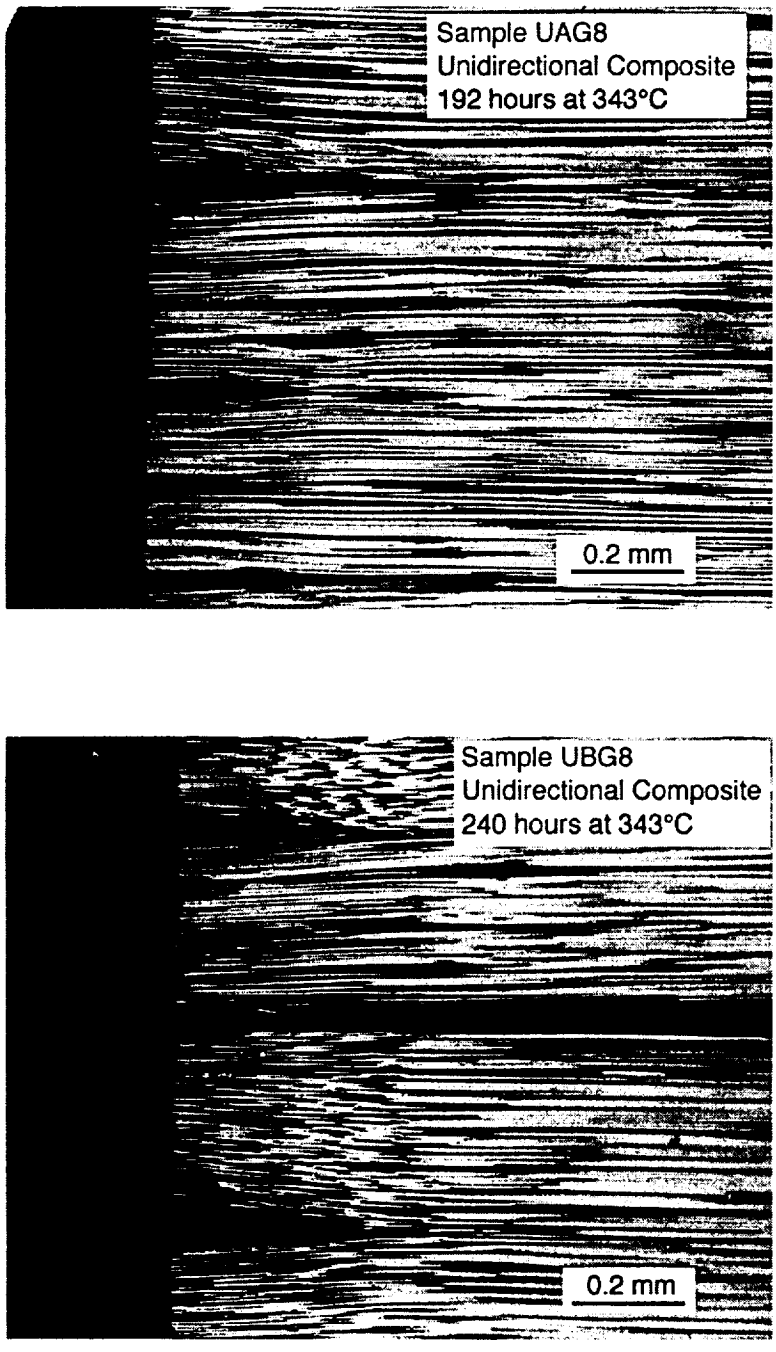

Figure 6.60 Propagation of cracks along the fiber direction for unidirectional composites exposed to air for 192 hours (*top*) and 240 hours (*bottom*) at 343°C.

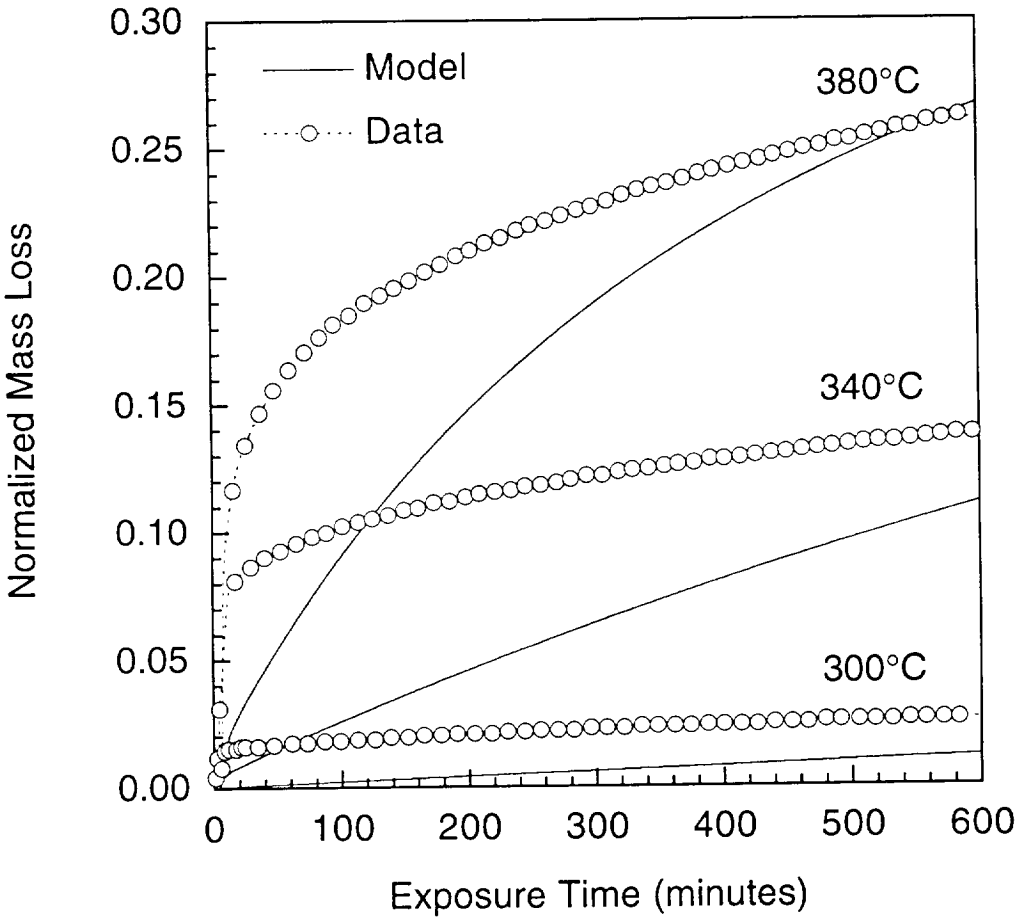

Figure 6.61 Analytical mass loss predictions versus isothermal TGA data in nitrogen.

studies is that the surface area effects which were noted for the neat resin could not be captured using the mass fraction (y_1= 0.07) derived for the first oxidative reaction from TGA data. For a mass fraction this low, the surface area effects can never account for a significant portion of the mass loss for the given surface layer thicknesses.

It is known from the TGAs carried out in air and oxygen that secondary oxidative reactions exist which are not accounted for in the TGA derived reaction model. These additional reactions are so confounded with the first thermal reaction that it was not possible to separate out their individual effects. However, as the preliminary analysis indicates, the neglection of their contribution to the mass loss mechanism results in an underestimation of the total contribution of the oxidative reactions. To account for this, it was decided to allow the oxidative reactions to act upon the entire mass fraction of the first thermal reaction. This is not an accurate model of all oxidative reactions, but it is a reasonable approach given that the diffusion-limited behavior is insensitive to the details of the oxidative reaction model as long as the reaction rate remains within a certain regime.

In order to obtain a reasonable estimate for the mass loss contribution of the thermal reactions at each of the aging temperatures, the reaction rate constant of the first thermal reaction was adjusted so that a fit to the data could be achieved. The TGA-derived reaction coefficients for the first thermal cause an overestimation of the mass loss due to the fact that we are most likely smearing together many low mass fractions into a single Arrhenius -type reaction. This results in an excessive temperature sensitivity as the single Arrhenius reaction assumes that, as temperature is increased, the entire mass fractions will respond in the same manner. However, only a certain number of the low mass fractions will experience a significant

acceleration in the mass loss rate for moderate increases in temperature. This can be compensated for by suppressing the reaction rate constant as temperature is increased.

Figures 6.62-6.64 show the correlations between the predicted mass losses and the data for each of the sample groups at the two test temperatures. The fit to the data is extremely good in all cases. Note that the H sample analytical prediction and data has been corrected to account for the lower temperature these sample experience in the oven. The coefficients used to obtain the fits to the data are shown in Table 6.8. It is also interesting to compare the reaction coefficients which were used for the first thermal reaction in order to achieve a fit to the data at the two test temperatures. In fitting to the data the activation energy for the first reaction was held constant while the reaction rate constant was varied until a fit to the data was achieved. The reaction rate constants for the thermal reactions acting on the first mass fraction are $1.36 \times 10^{9}\ s^{-1}$ and $0.84 \times 10^{9}\ s^{-1}$ at 316°C and 343°C respectively. The value for the reaction rate constant for these reactions derived from the TGA data in nitrogen was $3.12 \times 10^{10}\ s^{-1}$.

Figures 6.65 and 6.66 show the predicted distribution of degradation through the thickness of the resin samples at 316°C and 343°C respectively. At 316°C, the contribution from the thermal reactions starts to become significant after 150 hours. Prior to this, the mass loss is controlled by oxidative degradation in the surface layer. At 343°C, the situation is different. The thermal (volumetric) reactions now contribute much more significantly to the overall mass loss. The additional contribution from the oxidative reactions in the surface layer begins to become trivial by comparison to the volumetric effects at the longer aging times. This explains why the neat resin mass loss data at 343°C cannot be successfully expressed

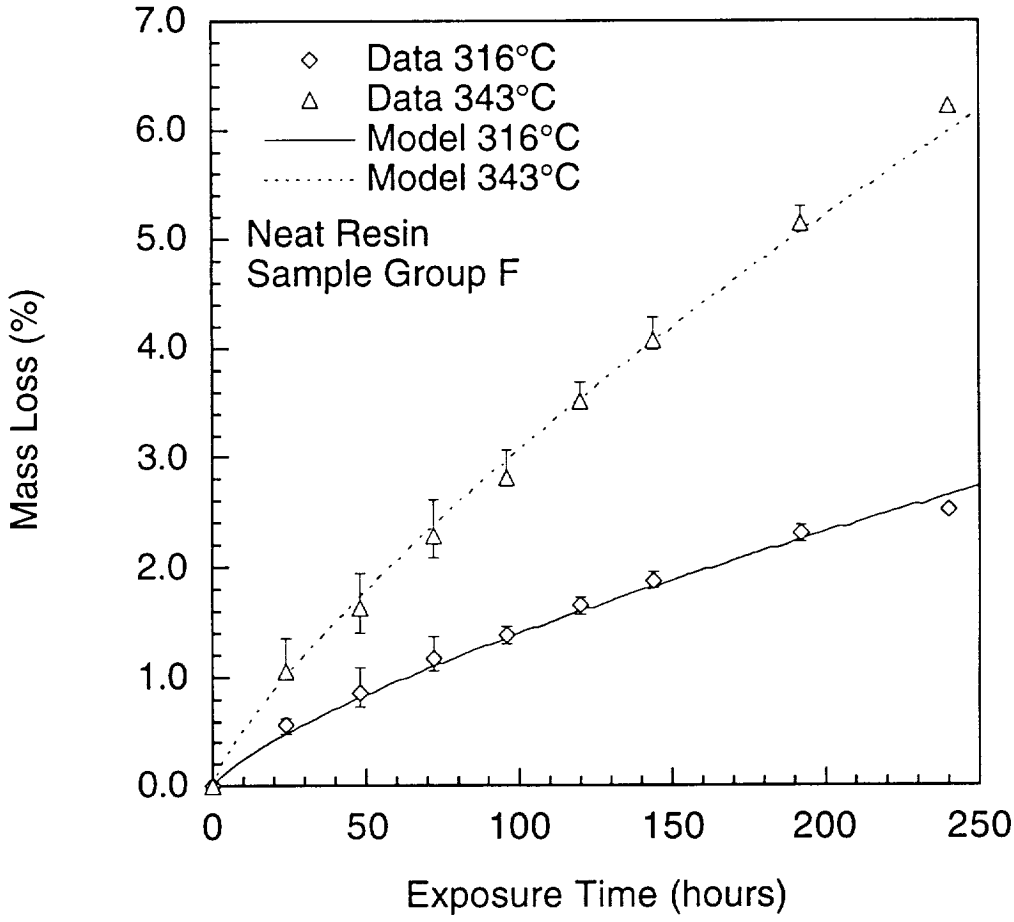

Figure 6.62 Mass loss data and analytical predictions for neat resin sample group F.

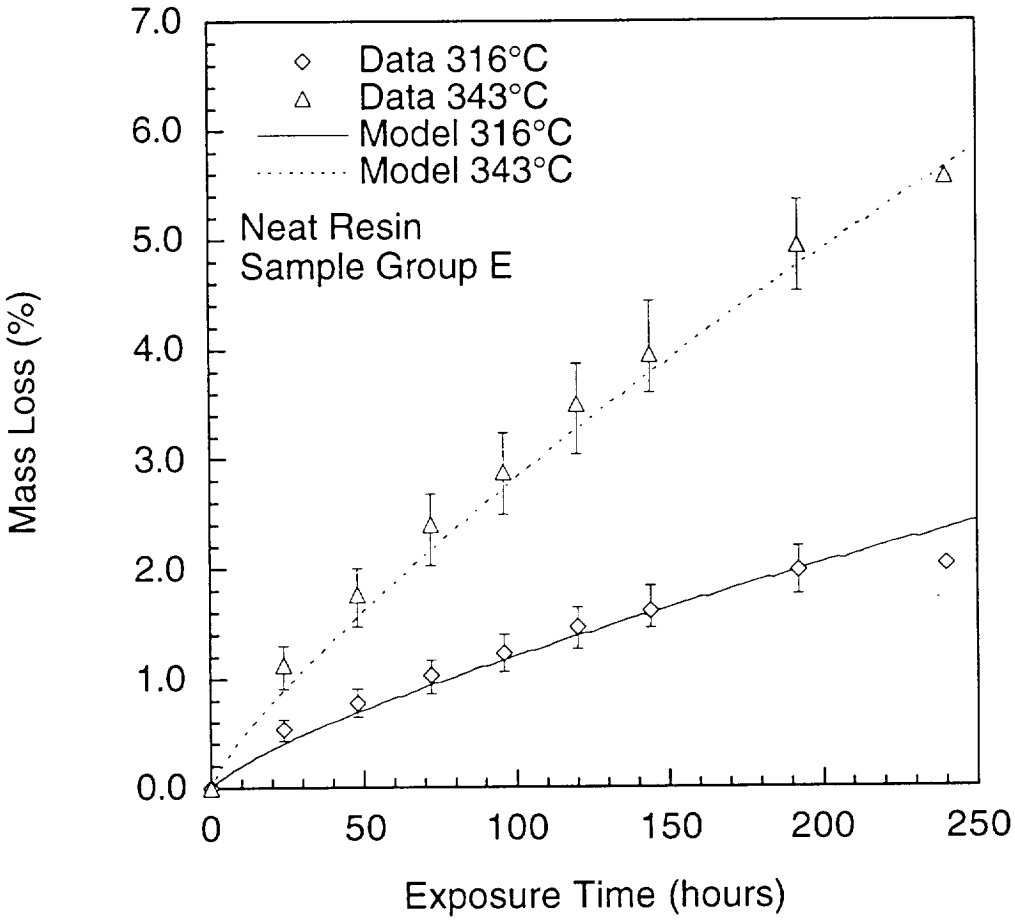

Figure 6.63 Mass loss data and analytical predictions for neat resin sample group E.

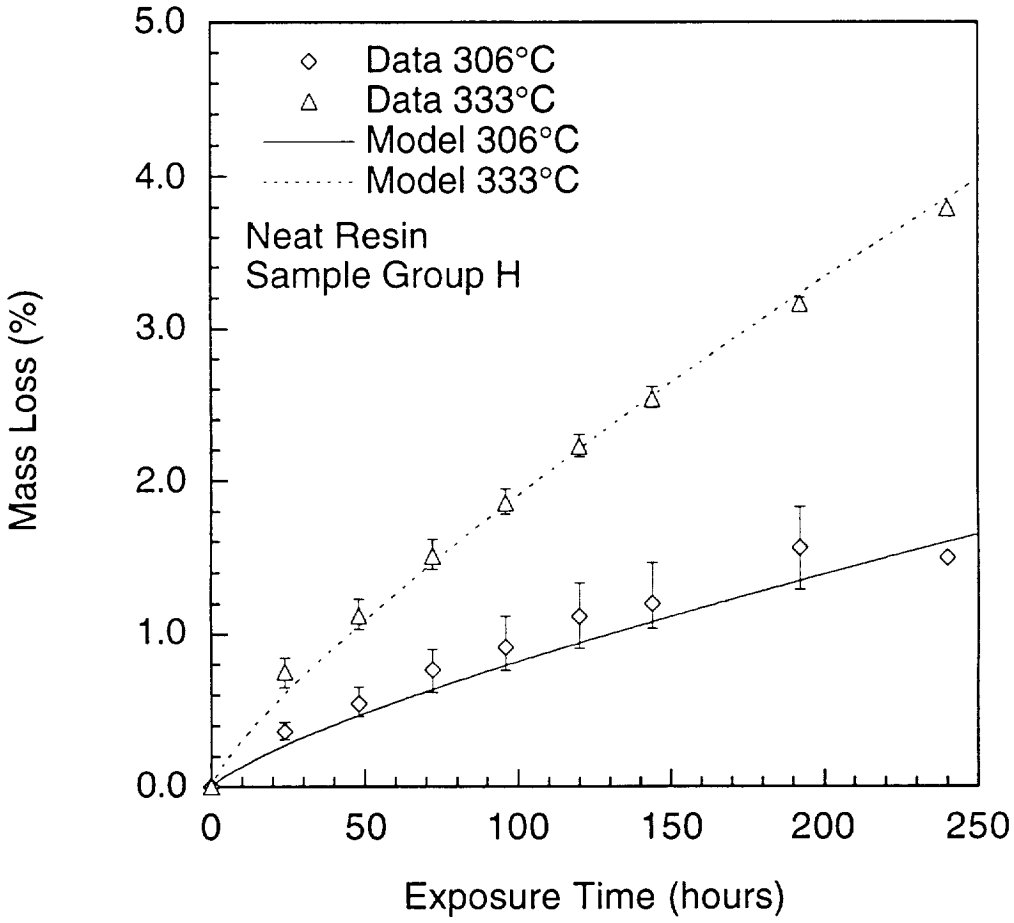

Figure 6.64 Mass loss data and analytical predictions for neat resin sample group H.

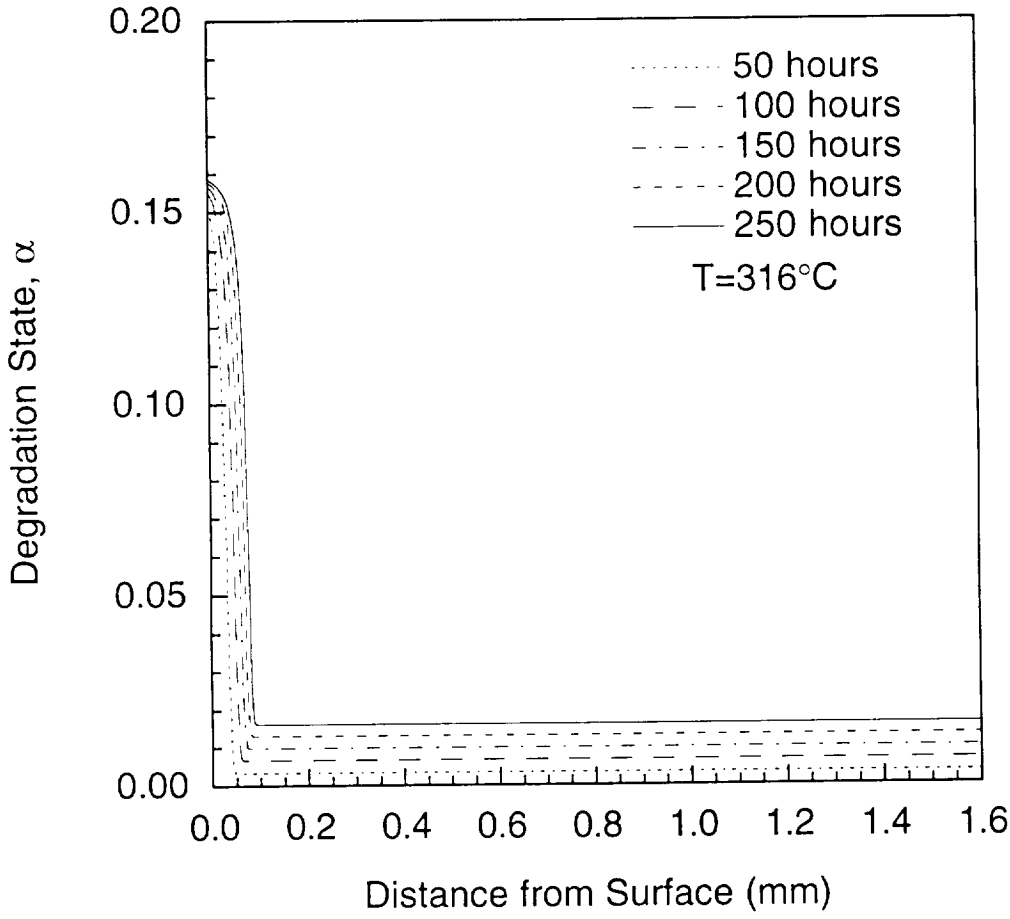

Figure 6.65 Degradation state profile in neat resin at 316°C.

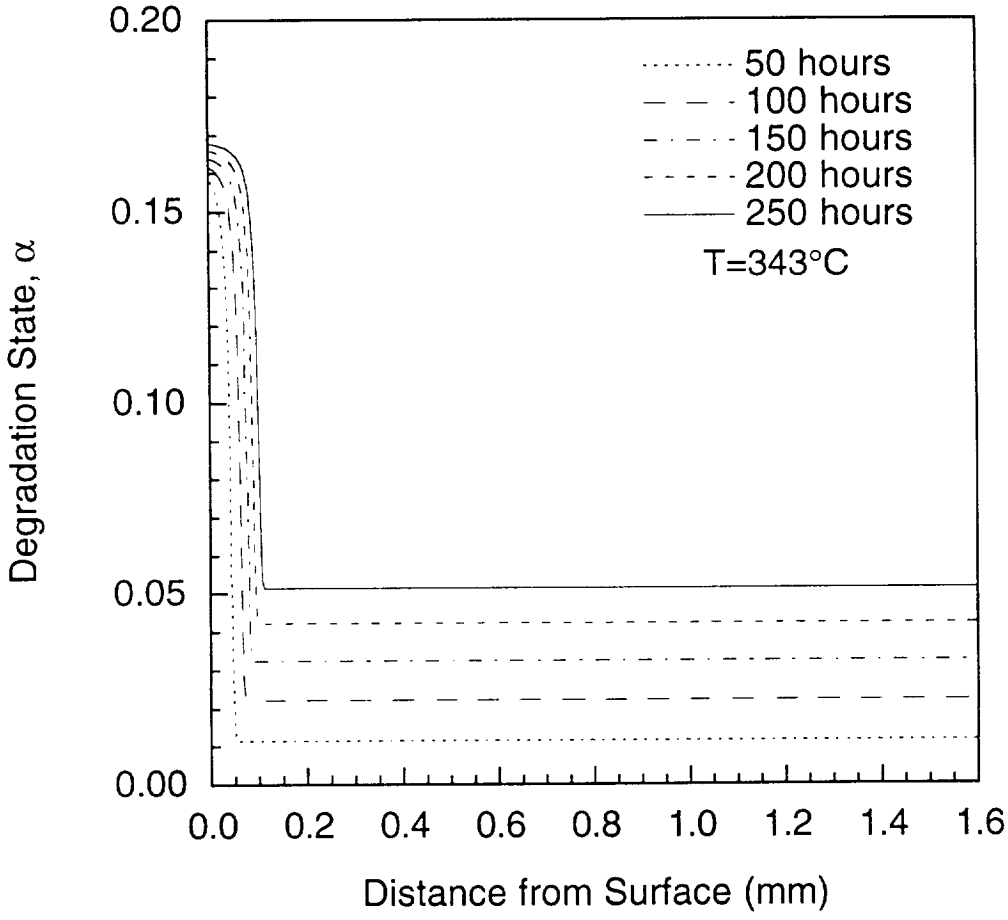

Figure 6.66 Degradation state profile in neat resin at 343°C.

as either a surface area or volumetric effect - the mass loss mechanism transitions from one to the other as aging time is increased. The data at 316°C can, however, be expressed in terms of a surface area effect in the time scale considered in these tests. The oxidative reactions dominate the behavior up to 250 hours.

Figure 6.67 shows the concentration profile at 343°C. The diffusion of oxygen through the material is very slow, with the depth of penetration being less than 100 microns after 250 hours. While, the diffusion may be slow, the oxidative reaction progresses very quickly as can be seen in the degradation profile at this temperature in which the oxidative reactions have almost reached completion even in the regions of very low oxygen concentration.

A similar fit to the composite data was not performed due to the lack of key information regarding the growth of the surface layers in the composite specimens. Without information as to the growth of these layers, and due to the significant changes which have to be made to the reaction coefficients to obtain a good fit to the neat resin data, realistic diffusion coefficients could not be rigorously obtained from the model. A preliminary fit to the unidirectional mass loss data, using a model which included anisotropic diffusion, suggested that diffusion through the molded surface and the surface parallel to the fibers is slower than that for the neat resin, while diffusion along the fiber direction is greatly accelerated. While this behavior is consistent with the observed empirical data, little confidence can be placed in these predictions without additional data.

6.5 SUMMARY

A preliminary analytical model was used to explore the physics of a degradation process involving a single oxidative reaction. Correlations

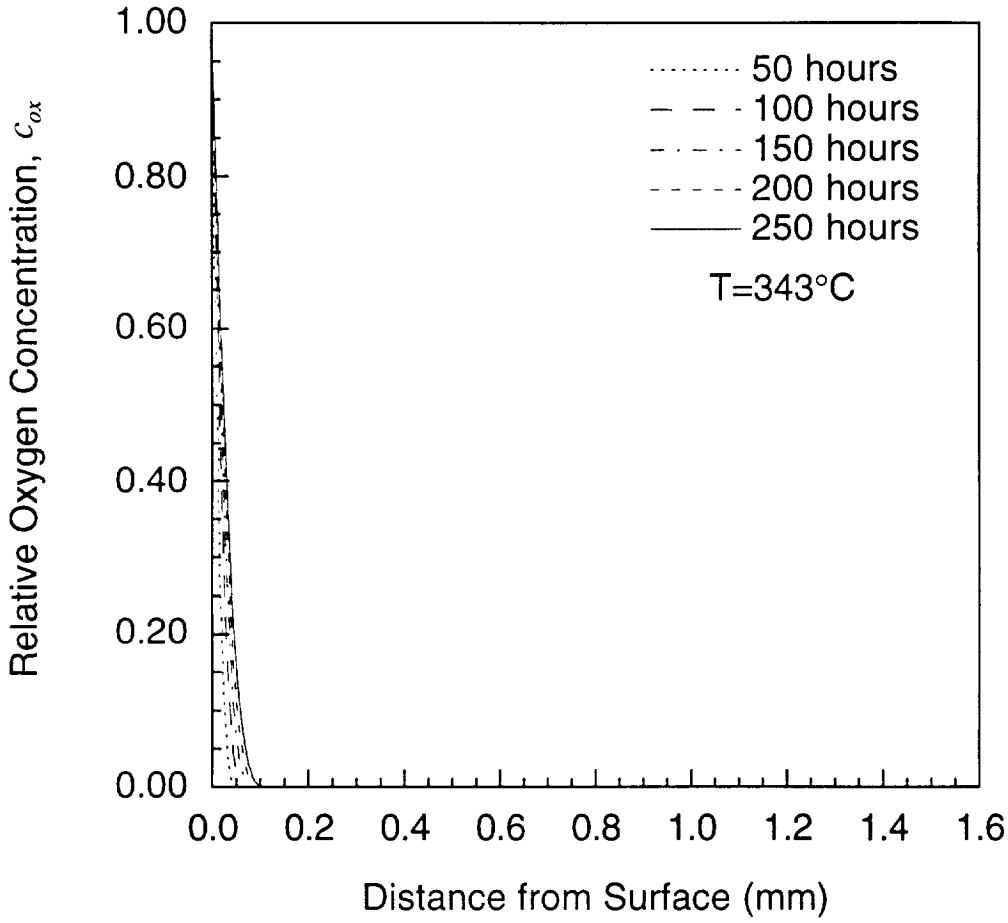

Figure 6.67 Concentration profile in neat resin at 343°C.

between the analysis and previously recorded data suggested that the mass loss due to oxidative reactions is a diffusion limited phenomenon. The diffusion may be limited either by the slow diffusion of oxygen into the material coupled with reactions which do not consume large amounts of oxygen, or through a very fast diffusion coupled with reactions which do consume large amounts of oxygen. However, both the quantitative and qualitative behavior depend on the details of both the reaction and diffusion mechanisms.

A set of carefully designed experiments were carried out to obtain the necessary coefficients for both the reaction and diffusion mechanisms. Thermogravimetric analyses were carried out on powdered neat resin specimens to determine the chemical reaction coefficients. The use of powdered samples allowed the mass transfer effects associated with diffusion to be minimized. Oxidative and thermal reactions were separated by carrying out tests in nitrogen and air. The concentration dependency of the oxidative reactions were determined through testing in a pure oxygen atmosphere.

Coefficients which allowed very good fits to the data in both nitrogen and air were obtained and are presented in Tables 6.6 and 6.7. While these coefficients provide extremely good fits to the data under test conditions, extrapolation outside of this regime is difficult. There are two primary reasons for this. The first of these is that the first thermal reaction is in fact a smeared effect, representing a number of closely grouped small mass fraction reactions rather than a single large mass fraction reaction. The second is that more than one oxidative reaction exists, and these additional reactions are severely confounded with the first thermal reaction, preventing the separation of their individual effects.

Diffusion effects were studied through the isothermal testing of both macroscopic neat resin and unidirectional composite specimens. Modeling of the surface layer growth allowed a reasonable set of effective diffusion coefficients to be obtained for the neat resin samples. The lack of a clearly visible surface layer on the composite specimens prevented the determination of diffusion coefficients for the unidirectional specimens.

Some modifications had to be made to the reaction coefficients in order to achieve a fit to the isothermal mass loss data from the neat resin samples. The thermal reactions proceed at a much slower rate than is predicted by the TGA model, while the oxidative reaction, because of the additional unmodeled reactions, consumes significantly more material than is suggested by the TGAs in air. However, very good fits to the mass loss data were achieved using the coefficients shown in Table 6.8.

CHAPTER 7

CONCLUSIONS AND RECOMMENDATIONS

7.1 PHYSICAL UNDERSTANDING ACHIEVED

This study has provided a much clearer picture of the physics involved in the degradation of PMR-15 and its composites than was previously available. Through the use of a mechanism-based analytical model and a carefully designed analysis driven experimental program it was possible to separate out, and quantify, many of the degradation phenomena observed to occur in polymer matrix composites. The analytical model, based on simple Arrhenius-type reactions and Fickian diffusion models, captures the key features of mass loss, the appearance and growth of degraded layers, and the relative contributions of both oxidative and thermal reactions as functions of time and exposure temperature in macroscopic specimens.

The analysis not only offers a method for quantifying the degradation mechanisms but also allows considerable insight into the physics of these mechanisms. The matrix material appears to be aged by a variety of mechanisms. Short term, low temperature degradation includes physical aging, and chemical aging in the form of additional crosslinking. These effects are covered in other work, for example [48], and are not the subject of this study. At longer times and/or higher temperatures, chemical aging in the form of a breakdown of the polymer chains occurs which leads both to mass loss and shrinkage. This form of degradation has both thermal and oxidative components which were quantified in this work.

Thermal degradation appears to be highly complex, probably consisting of a large number of separate reactions, although the behavior at higher temperatures can be approximated through the use of two effective Arrhenius reactions. At low temperatures, these reactions are suppressed so significantly that their contribution to the mass loss in oxidative atmosphere is small.

Oxidative reactions are extremely active at test temperatures, and are also of concern at use temperatures. These reactions are concentration dependent and as such only occur where oxygen is available. In material without cracks, the oxidative reaction mechanisms are confined to a region near the surface. The oxygen supply is limited either by very slow diffusion of oxygen into the material, or its consumption by reactions – the exact physics have yet to be determined.

The reactions which occur in the material lead to changes in the material properties. Other studies suggest that these effects result in shrinkage and the generation of stresses [6], and ultimately cracking [13]. In composites, two complicating factors exist. Anisotropic diffusion results in accelerated oxidative degradation through surfaces with cut fiber ends. Also, stresses develop due to the mismatch in the coefficients of thermal expansion, Poisson's ratio, and shrinkage between the fibers and resin, and also between different plies in the composite. The stresses developed in this manner may result in the propagation of surface cracks deep into the interior of the material, and may also cause the formation of interior ply cracks. This allows the environment to invade the interior, resulting in runaway degradation of the specimen.

7.2 CONCLUSIONS

A mechanism-based analytical model can successfully capture the basic physics of polymer matrix composite degradation. Models incorporating simple Arrhenius and Fickian physics can replicate complex observed degradation behavior. Analysis-based test design allows the collection of data on the individual reactions which are responsible for degradation. Typically, available data represents the results of many confounded effects. Through the use of an analysis driven test program, good success was achieved here in the separation and quantification of the complicated and coupled mechanisms acting within the test regimes considered.

Even though it was possible to simulate the basic features of the degradation mechanisms, the details were found to be considerably more complex than was originally assumed. Specifically, both the thermal and oxidative reactions are difficult to model using one or two Arrhenius-type reactions. The thermal reactions appear to be made up of a spread of low mass fraction reactions. However, these reactions die out rapidly as the temperature is lowered towards the use condition and so the importance of accurately capturing the behavior of these reactions is not clear. The oxidative reactions also appear to consist of multiple reactions which have different rate and concentration dependencies. The confounded nature of these reactions makes it difficult to quantify the mass fractions which are associated with the oxidative reactions. These reactions dominate the low temperature behavior and so an accurate representation of their behavior is needed.

Several issues relating to the diffusion of oxygen into the material bulk also need to be addressed. The issue of whether oxidative reactions are limited by very slow diffusion of oxygen, or faster diffusion which is coupled

with a high rate of consumption of oxygen by reactions, must be resolved. It is also likely that, while the current model does not include these effects, the diffusion coefficient and consumption factor are both functions, not only of temperature, but also of the degraded state of the material.

The understanding gained here is very useful and has interesting consequences. The models developed here are useful even in the presence of uncertainties in the mechanisms and material properties. The success achieved with analysis driven testing shows that tests must be designed in a manner which allows quantitative data for the correct mechanisms to be determined. The mechanisms shown here, and the data collected, suggests that the durability of PMR-15 is limited by oxidative reactions at the surface. This suggests that the materials may be durable in oxidative environments if they are protected from the environment. Hence the use of surface coatings warrant considerable investigation as a means for extending the useful lifetimes of parts exposed to these conditions. This also points out the importance of microcracking in composites as it allows the environment to penetrate into the material. An in-depth understanding of both the initiation and the arrest of microcracking is crucial in order to gain a full understanding of the durability issues.

7.3 RECOMMENDATIONS FOR FUTURE WORK

Based on the understanding gained through this work, it is obvious that improved models and test procedures must be developed. Two different courses of action may be taken. The first is to try to develop a better understanding of the details of the chemical degradation through, for example, a more in-depth study of the thermal and oxidative reactions, and by determining whether the surface degradation mechanism is diffusion or

consumption limited.

Additional studies of reaction mechanisms which would attempt to separate out the individual effects of multiple reactions, both oxidative and thermal, would be part of this approach. Such a program should include a large number of isothermal TGA studies over a large range of temperatures, coupled with very low rate (below 1°C/min.) dynamic heating tests. The use of variable heating rate TGAs which attempt to maintain a constant mass loss rate rather than a constant heating rate, slowing the heating rate down as the mass loss rate accelerates, should also be investigated. Tests such as these should allow the isolation of at least some of the low mass fractions reactions.

An improved understanding of both the oxidative reactions and the diffusion mechanism must also be developed. TGAs or long term isothermal tests of neat resin and composites in a number of atmospheres, with various concentrations of oxygen, should allow the concentration dependencies of the individual reactions to be determined. Consideration should also be given to tests which use traceable Oxygen-18 isotopes as a means of determining the nature of oxygen diffusion into the resin. Tests carried out at low temperatures, where the reactions are suppressed, should allow the determination of the diffusion coefficient, while tests at a number of elevated temperatures, where the oxidative reactions are active, should allow a quantification of the oxygen consumption factor as a function of temperature.

The second course of action is to concentrate on the development of better engineering models of the phenomena. A trade-off exists between the complexity and accuracy of the model and its overall usefulness from an engineering point of view. More complexity is not necessarily better, particularly when many of the effects noted for the high temperatures are

suppressed at use temperatures. While the current model certainly needs tuning, it is not necessarily the case that more elaboration would offer significant advantages. For example, better engineering models of the degradation could be developed using temperature dependent activation energies or reaction rate constants. Such approaches are necessarily semi-empirical, but have been used previously to fit to the mass loss curves from PMR-15 composite specimens [8]. Similarly, surface layer growth could be predicted using effective diffusion models. If an engineering model approach is to be taken, data must be collected to provide the necessary semi-empirical parameters which will allow predictions to be made for low temperature and long duration exposures. Sufficient generality of the model and the data collected is necessary to assure the applicability of the models to a wide range of aging conditions.

More generally, quantitative data on the effects of material degradation on the material properties is required. For example, information on material properties, such as tensile strength and stiffness, as functions of both temperature and degraded state are required. This poses a challenge for the model-based test philosophy given the non-uniform degradation observed in specimens which are sufficiently large to provide useful information on structural properties. Such data is vital in order to allow links to larger, more comprehensive models, which integrate the degradation effects with thermal, hygral and mechanical responses.

It is very important to understand that it has always been the intention of this work to improve the understanding of one particular weak link in a larger, more comprehensive model. The sub-model presented here must be integrated with other thermal [64] and environmental [65, 66] models to allow a full description of the environmental effects. These models

must in turn be integrated with stress [54] and damage [67, 68] models if a comprehensive predictive capability is to be achieved. Ultimately, links to comprehensive failure mechanism models must be established to achieve a design-for-durability capability for composite structures.

REFERENCES

1. Malarik, D. C. and Vannucci, R. D., "High Molecular Weight First Generation PMR Polyimides for 343°C Applications", *SAMPE Quarterly*, Vol. 23, No. 4, 1992, pp. 3-8.

2. Boyd, J. D. and Chang, G. E. C., "Bismaleimide Composites for Advanced High-Temperature Applications", *38th International SAMPE Symposium*, Covina, CA, 1993, pp. 357-365.

3. Bowles, K. J., "A Thermally Modified Polymer Matrix Composite Material With Structural Integrity to 371°C", NASA Technical Memorandum 100922, 1988.

4. Meador, M. A., Cavano, P. J., and Malarik, D. C., "High Temperature Polymer Matrix Composites for Extreme Environments", *Sixth Annual ASM/ESD Advanced Composites Conference*, Detroit, MI, 1990, pp. 529-539.

5. Alston, W. B., Gluyas, R. E., and Snyder, W. J., "Cyclopentadiene Evolution During Pyrolysis-Gas Chromatography of PMR Polyimides", NASA Technical Memorandum 105629, 1991.

6. Bowles, K. J., Jayne, D., and Leonhardt, T. A., "Isothermal Aging Effects on PMR-15 Resin", *SAMPE Quarterly*, Vol. 24, No. 2, 1993, pp. 3-9.

7. Bowles, K. J. and Nowak, G., "Thermo-Oxidative Stability Studies of Celion 6000/PMR-15 Unidirectional Composites, PMR-15, and Celion 6000 Fiber", *Journal of Composite Materials*, Vol. 22, No. 10, 1988, pp. 966-985.

8. Bowles, K. J., "Thermo-Oxidative Stability Studies of PMR-15 Polymer Matrix Composites Reinforced with Various Continuous Fibers", *SAMPE Quarterly*, Vol. 21, No. 4, 1990, pp. 6-13.

9. Bowles, K. J., "Effect of Fiber Reinforcements on Thermo-Oxidative Stability and Mechanical Properties of Polymer Matrix Composites", *SAMPE Quarterly*, Vol. 23, No. 3, 1992, pp. 2-12.

10. Wong, M. S., Skontorp, A., and Wang, S. S., "Thermal Oxidation of Carbon Fibers and Carbon-Fiber Reinforced High-Temperature Polyimide Composite at Elevated Temperatures", *ASC 9th Technical Conference*, Newark, DE, 1994, pp. 458-467.

11. Bowles, K. J. and Meyers, A., "Specimen Geometry Effects on Graphite/PMR-15 Composites During Thermo-Oxidative Aging", NASA Technical Memorandum 87204, Cleveland, OH, 1986.

12. Beckwith, S. W. and Wallace, B. D., "Effects of Aging and Environmental Conditions on Kevlar/Epoxy Composites", *SAMPE Quarterly*, Vol. 14, No. 4, 1983, pp. 38-45.

13. Bowles, K. J., Jayne, D., Leonhardt, T. A., and Bors, D., "Thermal Stability Relationships Between PMR-15 Resin and Its Composites", *Journal of Advanced Materials*, Vol. 26, No. 1, 1994, pp. 23-32.

14. Delvigs, P., Alston, W. B., and Vannucci, R. D., "Effects of Graphite Fiber Stability on the Properties of PMR Polyimide Composites", NASA Technical Memorandum 79062, Cleveland, OH, 1979.

15. Skontorp, A., Wong, M., and Wang, S., "High-Temperature Anisotropic Thermal Oxidation of Carbon-Fiber Reinforced Polyimide Composites: Theory and Experiment", *ICCM-10*, Whistler, Canada, 1995, pp. 375-382.

16. Alston, W. B., "Resin/Fiber Thermo-Oxidative Interactions in PMR Polyimide/Graphite Composites", NASA Technical Memorandum 79093, Cleveland, OH, 1979.

17. Martin, R. H., Siochi, E. J., and Gates, T. S., "Isothermal Aging of IM7/8320 and IM7/5260", *American Society for Composites 7th Technical Conference on Composite Materials*, University Park, PA, 1992, pp. 207-217.

18. Nam, J. C. and Seferis, J. C., "Anisotropic Thermo-Oxidative Stability of Carbon-Fiber Reinforced Polymeric Composites", *SAMPE Quarterly*, Vol. 24, No. 1, 1992, pp. 10-18.

19. Salin, I. M. and Seferis, J. C., "Anisotropic Effects in

Thermogravimetry of Polymeric Composites", *Journal of Polymer Science: Part B: Polymer Physics*, Vol. 31, 1993, pp. 1019-1027.

20. Madhukar, M. S., Bowles, K. J., and Papadopolous, D. S., "Thermo-Oxidative Stability of Graphite/PMR-15 Composites: Effect of Fiber Surface Modification on Composite Shear Properties", NASA Technical Memorandum 4608, 1994.

21. Grayson, M. A. and Fry, C. G., "On the Use of a Kinetic Map to Compare the Thermal Stability of Polymeric Materials Undergoing Weight Loss", McDonnell Douglas Co. preprint, 1994.

22. Kiefer, R., Yue, J. J., and Hinkley, J. A., "Kinetic Mapping of Oxidative Weight Loss in Polyimide Composites", *Journal of Advanced Materials*, Vol. 26, No. 3, 1995, pp. 55-59.

23. Bamford, C. H. and Tipper, C. H. F. (eds.), *Comprehensive Chemical Kinetics*, Elsevier, 1980.

24. Ansari, A. S., Turk, M. J., Alston, W. B., Frimer, A. A., and Scheiman, D. A., "TGA/FTIR Determination of Polyimide Thermal-Oxidative Degradation Kinetics", NASA preprint, 1996.

25. Hipp, R. C., Harmon, D. M., and McClellan, P. S., "Accelerated Aging and Methodology Development for Polymeric Composite Material Systems", McDonnell Douglas Co. preprint, 1994.

26. Kim, H. J., Harmon, D. M., Wanthal, S. P., and Saff, C. R., "Integrated Physical/Mechanical Analysis of Aged Polymer Matrix Composites", McDonnell Douglas Co. preprint, St. Louis, MO, 1994.

27. Nam, J. D. and Seferis, J. C., "Generalized Composite Degradation Kinetics for Polymeric Systems Under Isothermal and Nonisothermal Conditions", *Journal of Polymer Science: Part B: Polymer Physics*, Vol. 30, No. 5, 1992, pp. 455-463.

28. Pederson, C. L., "The Effect of Temperature on Transverse Cracking in High Performance Composites", CCM Report 92-28, University of Delaware Center for Composite Materials, Newark, DE, June, 1992.

29. Zocher, M. A., Allen, D. H., and Groves, S. E., "Analysis of the Effects of Matrix Cracking in a Viscoelastic Composite at Elevated Temperatures", *ASC 9th Technical Conference*, Newark, DE, 1994, pp. 442-449.

30. Gates, T. S. and Brinson, L. C., "Acceleration of Aging in Graphite/Bismaleimide and Graphite/Thermoplastic Composites", *36th AIAA/ASME/ASCE/AHS/ASC Structures, Structural Dynamics and Materials Conference*, Hilton Head, SC, 1994, pp. 2096-2105.

31. Chamis, C. C., "Simplified Composite Micromechanics for Predicting Microstresses", NASA Technical Memorandum 87295, 1986.

32. Chamis, C. C., "Simplified Composite Micromechanics Equations for

Hygral, Thermal, and Mechanical Properties", *SAMPE Quarterly*, Vol. 15, 1984, pp. 14-23.

33. Chamis, C. C. and Ginty, C. A., "Fiber Composite Structural Durability and Damage Tolerance: Simplified Predictive Methods", NASA Technical Memorandum 100179, 1987.

34. Roberts, G. D. and Lauver, R. W., "Quantitative Analysis of PMR-15 Polyimide Resin by HPLC", *Journal of Applied Polymer Science*, Vol. 33, No. 8, 1987, pp. 2893-2913.

35. Scola, D. A. and Vontell, J. H., "High Temperature Polyimides, Chemistry and Properties", *Polymer Composites*, Vol. 9, No. 6, 1988, pp. 443-452.

36. Alston, W. B., "Characterization of PMR-15 Polyimide Resin Composition in Thermo-Oxidatively Exposed Graphite Fiber Composites", NASA Technical Memorandum 81565, 1980.

37. Bowles, K. J., Roberts, G. D., and Kamvouris, J. E., "Long-Term Isothermal Aging Effects on Carbon Fabric-Reinforced PMR-15 Composites: Compression Strength", NASA Technical Memorandum 107129, 1995.

38. Pater, R. H., Whitley, K., Morgan, C., and Chang, A., "Crosslinking-Property Relationships in PMR Polyimide Composites, Part I", *Polymer Composites*, Vol. 12, No. 2, 1991, pp. 126-132.

39. Alston, W. B., "Replacement of MDA with More Oxidatively Stable Diamines in PMR-Polyimides", *High Temperature Polymer Matrix Composites*, Cleveland OH, 1985, pp. 187-205.

40. Roberts, G. D. and Vannucci, R. D., "Effect of Solution Concentration and Aging Conditions on PMR-15 Resin", *SAMPE Journal*, Vol. 22, 1986, pp. 24-28.

41. Alston, W. B., "Structure-to-Property Relationships in Addition Cured Polymers. IV - Correlations Between Thermo-Oxidative Weight Losses of Norbornenyl Cured Polyimide Resins and Their Composites", NASA Technical Memorandum 105553, 1992.

42. Torrecillas, R., Regnier, N., and Mortaigne, B., "Thermal Degradation of Bismaleimide and Bisnadimide Networks - Products of Thermal Degradation and Type of Crosslinking Points", *Polymer Degradation and Stability*, Vol. 51, No. 3, 1996, pp. 307-318.

43. Simpson, M., Jacobs, P. M., and Jones, F. R., "Generation of Thermal Strains in Carbon Fibre-Reinforced Bismaleimide (PMR-15) Composites Part 3: A Simultaneous Thermogravimetric Mass Spectral Study of Residual Volatiles and Thermal Microcracking", *Composites*, Vol. 22, No. 2, 1991, pp. 105-112.

44. Salin, I. M. and Seferis, J. C., "Kinetic Analysis of High-Resolution TGA Variable Heating Rate Data", *Journal of Applied Polymer Science*,

Vol. 47, No. 5, 1993, pp. 847-856.

45. Tsotsis, T. K., "Thermo-Oxidative Aging of Composite Materials", *Journal of Composite Materials*, Vol. 29, No. 3, 1995, pp. 410-422.

46. Prian, L., Pollard, R., Shan, R., Mastropietro, C. W., Gentry, T. R., Bank, L. C., and Barkatt, A., "Use of Thermogravimetric Analysis to Develop Accelerated Test Methods to Investigate Long-Term Environmental Effects on Polymer Composites", *ASTM Second Symposium on High Temperature and Environmental Effects on Polymeric Composites*, 1995, Norfolk, VA, preprint.

47. Xiang, Z. D. and Jones, F. R., "Thermal Degradation of an End-Capped Bismaleimide Resin Matrix (PMR-15) Composite Reinforced with Pan-Based Carbon Fibers", *Composites Science and Technology*, Vol. 47, No. 3, 1993, pp. 209-215.

48. Kamvouris, J. E., Roberts, G. D., Pereira, J. M., and Rabzak, C., "Physical and Chemical Aging Effects in PMR-15 Neat Resin", *ASTM Second Symposium on High Temperature and Environmental Effects on Polymeric Composites*, 1995, Norfolk, VA, preprint.

49. Parvatareddy, H., Wang, J. Z., Dillard, D. A., Ward, T. C., and Rogalski, M. E., "Environmental Aging of High-Performance Polymeric Composites: Effects on Durability", *Composites Science and Technology*, Vol. 53, No. 4, 1995, pp. 399-409.

50. Pederson, C. L., Gillespie, J. W., McCullough, R. L., Rothschilds, R. J., and Stanek, S. L., "The Effect of Isothermal Aging on Transverse Crack Development in Carbon Fiber Reinforced Cross-Ply Laminates", CCM Report 93-42, University of Delaware Center for Composite Materials, Newark, DE, November, 1993.

51. Hipp, R. C., Grayson, M. A., Mallow, A. R., and Dow, M. B., "Thermal Aging Effects on Candidate Polymeric Matrix Composites for HSCT Applications", McDonnell Douglas Co. preprint, St. Louis, MO, 1994.

52. Hipp, R. C., Mallow, A. R., McClellan, P. S., and Renieri, M. P., "Accelerated Test Methodology Development for Polymer Composite Materials", McDonnell Douglas Co. preprint, St. Louis, MO, 1994.

53. Bank, L. C., Gentry, T. R., and Barkatt, A., "Accelerated Test Methods to Determine the Long-Term Behaviour of FRP Composite Structures: Environmental Effects", *Journal of Reinforced Plastics and Composites*, Vol. 14, No. 6, 1995, pp. 559-587.

54. McManus, H. L. and Chamis, C. C., "Stress and Damage in Polymer Matrix Composite Materials Due to Material Degradation at High Temperatures", NASA Technical Memorandum 4682, 1996.

55. Crank, J., *The Mathematics of Diffusion*, First ed., Oxford University Press, Oxford, 1956.

56. Tsai, S. W., *Composites Design*, Fourth ed., Think Composites, Ohio,

1988.

57. Vannucci, R. D., "PMR-15 Polyimide Modifications for Improved Prepreg Tack", *1982 National Technical Conference of the Society of Plastics Engineers: The Plastic ABC's*, Bal Harbour, FL, 1982, pp. 131-133.

58. "TGA 7 Thermogravimetric Analyzer", User's Guide, Perkin Elmer, U.S.A., 1985.

59. "Adobe Photoshop LE", User's Guide, Adobe, U.S.A., 1995.

60. Huyser, K. and van der Laan, J., "DataThief 2.0b", User's Guide, National Institute for Nuclear Physics and High Energy Physics (NIKHEF-K), The Netherlands, 1994.

61. Maddocks, J. R., "Microcracking in Composite Laminates Under Thermal and Mechanical Loading", Massachusetts Institute of Technology, S. M. Thesis, 1995.

62. Rasband, W., "NIH Image Version 1.60", User's Guide, National Institutes of Health, U.S.A., 1996.

63. Grayson, M. A., McDonnell Douglas Co., personal communication.

64. Kucner, L. K., "Experimental Investigation of Fire Damage to Composite Materials", Massachusetts Institute of Technology, S. M.

Thesis, 1995.

65. Czepiela, S., Massachusetts Institute of Technology, S. M. Thesis, 1997 (expected).

66. Foch, B. J., Massachusetts Institute of Technology, S. M. Thesis, 1997 (expected).

67. McManus, H. L. and Maddocks, J. R., "On Microcracking in Composite Laminates under Thermal and Mechanical Loading", *Polymers and Polymer Composites*, in press.

68. Park, C. H. and McManus, H. L., "Thermally Induced Damage in Composite Laminates: Predictive Methodology and Experimental Investigation", *Composites Science and Technology*, Vol. 56, No. 10, 1996, pp. 1209-1219.

APPENDIX A

DIFFUSE SCRIPT

INTRODUCTION

DIFFUSE is an easy-to-use computer code which will calculate the distribution of degradation in a composite laminate in a given environment as a function of distance from the surface and exposure time. All equations used in this code are given in Chapter 4. The code use an explicit finite difference scheme to predict degradation at a point within the laminate. The distribution of oxygen concentration is also predicted, as is the total mass loss from the specimen. The thicknesses of degraded surface layers are also predicted as a function of time. Both isotropic and anisotropic diffusion may be accounted for. The current code allows for two different diffusion coefficients to be accounted for. As many as three thermal reactions and one oxidative reaction may be included.

INPUTS

All necessary input coefficients are contained in data statements at the beginning of the code. Each reaction requires a mass fraction, y_i, activation energy, E_i, reaction rate constant, k_i, and reaction order, n_i. The oxidative reaction also requires a concentration dependency term, m_{ox}. Each diffusion coefficient requires a pre-exponential diffusivity constant, D_i, and a diffusivity exponential coefficient, C_i. It is assumed in the code that the oxidative reaction acts on the same material component as the first thermal

reaction.

OUTPUTS

The code outputs three ASCII files. The first of these, CPROFILE, contains concentration and degradation profiles, as functions of distance from the surface and exposure time, in each of the directions with different diffusion coefficients. The file MASSLOSS contains the mass loss percentage and surface layer thicknesses as a function of time. Finally, the matrix ALPHA contains the individual degraded state profiles for each of the chemical reactions as functions of distance from the surface and exposure time.

```
C     Diffusion and Reaction code
C     Program to predict the distribution of degradtion in a composite laminate
      PROGRAM diffuse
      character*1 tab
      character*2 title(4)
      parameter  (maxnodes=500)
      parameter  (nplts=10)
      parameter  (splts=20)
      dimension  save(splts,maxnodes),tp(nplts),aprof(splts,maxnodes)
      dimension  r(4),rdt(4),atot(2,maxnodes)
      dimension  E(3),rk(3),y(3),n(3)
      real  h,nstep,D(2),b,dt,dlt(2),massIsfrac,w,l,rthermdt(2)
      real  volume,mass,geom,density,roxy(2),roxydt(2),nox,mox,dlt2prime
      real  vouter1,vinner1,alphaavg1,valphavg1,valpha1,massls
      real  valphaavg2,alphaavg2,valpha2,vfiber,vol1,vol2,valphatot1,valphatot2
      integer   nspp,nspm,ntime,j
C     Define initial values and constants - alpha is the degradation metric at each
C     node, c is the concentration, rgc is the gas constant, h is the half thickness of
C     the laminate, k is the reaction rate pre-exponential constant, E is the
C     activation energy, D is the diffusion constant and b is the proportion of
C     oxygen that is consumed by the reaction at each step. The variable thold
C     represents the percentage degradation which must be present at a point in
C     order for the degradation to be visible. The thickness of the visible surface
C     layer, dlt, is found through the application of this criteria in the main
C     routine.
      common/stuff/ c(2,maxnodes), alpha(4,maxnodes),alphaoxy(2,maxnodes)
      data  c/1000*0./,alpha/2000*0./,atot/1000*0./,alphaoxy/1000*0./
C     Data statements containing mass fractions, activation energies, reaction rate
C     constants, reaction orders, diffusioncoefficients and fiber volume fraction
      data  E/127.87e3,127.87e3,239e3/,rk/2.16e4,2.16e4,7.9e12/
      data  y/0.16,0.00,0.24/,n/1.61,1.61,3.20/,vfiber/0.5/
      data  Eox,kox,nox,mox/135e3,1.67e8,2.30,0.5/
      data  D/3.363e-13,2.52e-6/
```

```
      data  title/'C1','C2','A1','A2'/
      tab=char(9)
      c(1,1)=1.
      c(2,1)=1.
      rgc=8.3144
      density=1300
      h=1.24e-3
      w=3.2e-3
      l=76.2e-3
      volume=2*h*l*w
      mass=volume*density
      geom=(w+2*h)/w
      nstep=251.0
      dz=h/(nstep-1)
      type *,'Value for T'
      read *,temp
      D(1)=D(1)*exp(-6611/temp)
      D(2)=D(2)*exp(-13223/temp)
      b=0.01
      IF (D(1).GT.D(2)) THEN
         Dmax=D(1)
      ELSE
         Dmax=D(2)
      ENDIF
      type *,'Time step must always be less than ',dz**2/(2*Dmax)
      type *,'Enter the time step, dt, and number of steps'
      read(5,*) dt,ntime
      thold=0.25
      type *,'Store profiles every how many steps?'
      read(5,*) nspp
      type *,'Print mass loss every how many steps?'
      read(5,*) nspm
      npp=ntime/nspp
      open (23,file='massloss',status='new')
      open (20,file='alpha',status='new')
      WRITE(23,10) 'Time','Mass Loss %','Layer Thickness 1 (mic)','Layer Thickness 2 (mic)'
10    FORMAT(a4,',',a11,',',a23,',',a23)
C     Main routine - the degradation at each time step for each node is
C     calculated based on the concentration of the oxygen at each node for the
C     given time step.  The  progression of the oxygen through the material is
C     calculated using a forward Euler finite difference scheme.  As a result the
C     system must conform to the following time step criterion - the time step
C     must always be less than dx^2/(2*D).  A time step of approximately one
C     tenth of this value will ensure stability of the system always.
      ns=0
      t=0
      oldcmi1=1.
      oldcmi2=1.
      dlt(1)=0
      dlt(2)=0
      DO 100 j=1,ntime
         t=t+dt
         alphatot=0
C     If a spatially varying D is to be used then put a comment (C) prompt in
C     front of the following  line and remove the comment prompt from the next
C     line.  This will set the concentration at all nodes which have degraded
C     beyond a certain threshold to a normalized value of one.
         kfirst=1
```

```
C       kfirst=int(dlt/dz)+1
        dlt(1)=0.0
        dlt(2)=0.0
        DO 90 k=1,nstep
           DO 50 i=1,4
           IF (i.LE.2) THEN
              roxy(i)=c(i,k)**mox*(1.0-alpha(i,k))**nox*kox*exp(Eox/(rgc*temp))
              roxydt(i)=min(roxy(i)*dt,1.0-alpha(i,k),c(i,k)/b)
              alphaoxy(i,k)=alphaoxy(i,k)+roxydt(i)
              r(i)=(1.0-alpha(i,k)-roxydt(i))**n(1)*rk(1)*exp(E(1)/(rgc*temp))
              rthermdt(i)=min(r(i)*dt,1.0-alpha(i,k)-roxydt(i))
              rdt(i)=roxydt(i)+rthermdt(i)
           ELSE
              r(i)=(1.0-alpha(i,k))**n(i-1)*rk(i-1)*exp(-E(i-1)/(rgc*temp))
              rdt(i)= min(r(i)*dt,1.0-alpha(i,k))
           ENDIF
           alpha(i,k)=alpha(i,k)+rdt(i)
50         CONTINUE
           atot(1,k)=atot(1,k)+(y(1)*rdt(1)+y(2)*rdt(3)+y(3)*rdt(4))
           atot(2,k)=atot(2,k)+(y(1)*rdt(2)+y(2)*rdt(3)+y(3)*rdt(4))
C       New concentration of oxygen at zk
        oldc1=c(1,k)
        oldc2=c(2,k)
        F (k.LE.kfirst) THEN
           c(1,k)=1.0
           c(2,k)=1.0
        ELSEIF (k.GT.kfirst.and.k.NE.nstep) THEN
           c(1,k)=c(1,k)+dt*(D(1)*(c(1,k+1)-2*c(1,k)+oldcmi1)/dz**2)-roxydt(1)*b
            c(2,k)=c(2,k)+dt*(D(2)*(c(2,k+1)-2*c(2,k)+oldcmi2)/dz**2)-roxydt(2)*b
        ELSEIF (k.eq.nstep) then
           c(1,k)=c(1,k-1)
           c(2,k)=c(2,k-1)
        ENDIF
        oldcmi1=oldc1
        oldcmi2=oldc2
90      CONTINUE
C       Degraded layer thickness (visible if alphaoxy>threshold)
        DO 93 k=1,nstep
        DO 92 i=1,2
        IF (alphaoxy(i,k).GT.thold.AND.k.NE.nstep) THEN
           IF (alphaoxy(i,k+1).NE.1) THEN
              dadz=(alphaoxy(i,k+1)-alphaoxy(i,k))/dz
              dlt(i)=(k-1)*dz-(alphaoxy(i,k)-thold)/dadz
           ELSE
              dlt(i)=k*dz
           ENDIF
        ENDIF
92      CONTINUE
93      CONTINUE
C       Calculate total mass loss and store
        valpha1=0.
        valpha2=0.
        DO 94 k=1,nstep-1
           alphaavg1=(atot(1,k)+atot(1,k+1))/2
           vouter1=(l-2*dlt(2))*(w-(2*dz*(k-1)))*(2*h-(2*dz*(k-1)))
           vinner1=(l-2*dlt(2))*(w-(2*dz*(k)))*(2*h-(2*dz*(k)))
           valphavg1=vouter1-vinner1
           valpha1=valpha1+alphaavg1*valphavg1
```

```
94      CONTINUE
        k=1
        DO 97 WHILE ((k-1)*dz.LT.dlt(2))
           alphaavg2=(atot(2,k)+atot(2,k+1))/2
           valphaavg2=4*h*w*dz
           valpha2=valpha2+alphaavg2*valphaavg2
           k=k+1
97      END DO
        vol1=(l-2*dlt(2))*w*2*h
        vol2=4*h*w*dlt(2)
        massls=(valpha1+valpha2)/volume
        masslsfrac=massls*(1-vfiber)
        IF (mod(j,nspm).EQ.0) THEN
           WRITE(23,91) t/3600,',',masslsfrac*100,',',dlt(1)*1e6,',',dlt(2)*1e6
91         FORMAT(E11.4,a1,3(1pE11.3,a1))
        ENDIF
        IF (mod(j,nspp).EQ.0) THEN
           ns=ns+1
           na=3*ns
           tp(ns)=t
        DO 95 k=1,nstep
           aprof(na-2,k)=alpha(1,k)
           aprof(na-1,k)=alpha(2,k)
           aprof(na,k)=alpha(3,k)
           save(ns,k)=c(1,k)
           save(ns+npp,k)=c(2,k)
           save(ns+(2*npp),k)=atot(1,k)
95         save(ns+(3*npp),k)=atot(2,k)
        ENDIF
100   CONTINUE
101   FORMAT(50(e11.2))
C     Profile storage
      IF (npp.NE.0) THEN
         OPEN(22,FILE='cprofile',STATUS='new')
         WRITE(22,490)',',((title(k),tp(i),',',i=1,npp),k=1,4)
490      FORMAT('Z',a1,20(a,E9.2,a1))
         ncols=4*npp
         DO 430 k=1,nstep
            WRITE(20,101) dz*float(k-1),',',(aprof(i,k),',',i=1,na)
430      WRITE(22,492) dz*float(k-1)*1000,',',(save(j,k),',',j=1,ncols)
492   FORMAT (2000(1pe11.4,a1))
      ENDIF
      CLOSE(22)
      CLOSE(23)
      STOP 'Analysis done'
      END
```

APPENDIX B

NITROGEN TGA DATA FIT

INTRODUCTION

In modeling the nitrogen TGA data, two n-th order Arrhenius reactions acting on two separate material components were assumed. The coefficients for this model were derived using the data fit procedure described in Section 4.4. This procedure was carried out using the MATLAB script REDUCE.M which is also presented here. This data fit procedure uses a cost function which evaluates the relative error between the analytical predictions and the data at each data point over a number of heating rates. The analysis surveys a user-defined range of mass fractions, returning the optimum set of parameters for each mass fraction based on the minimum cost function evaluation for that mass fraction. While this approach results in a single, clearly defined solution for pseudo-data involving well-behaved Arrhenius-type reactions, the reduction method is not particularly sensitive to realistic data which possesses a reasonable amount of scatter in both the locations and magnitudes of reaction peaks. The purpose of this appendix is to present the full results of the data fit to the nitrogen data and to discuss their implications.

DATA FIT RESULTS

The cost function for the high heating rates is shown in Figure B.1. While the shape of the cost function appears to be essentially concave, a

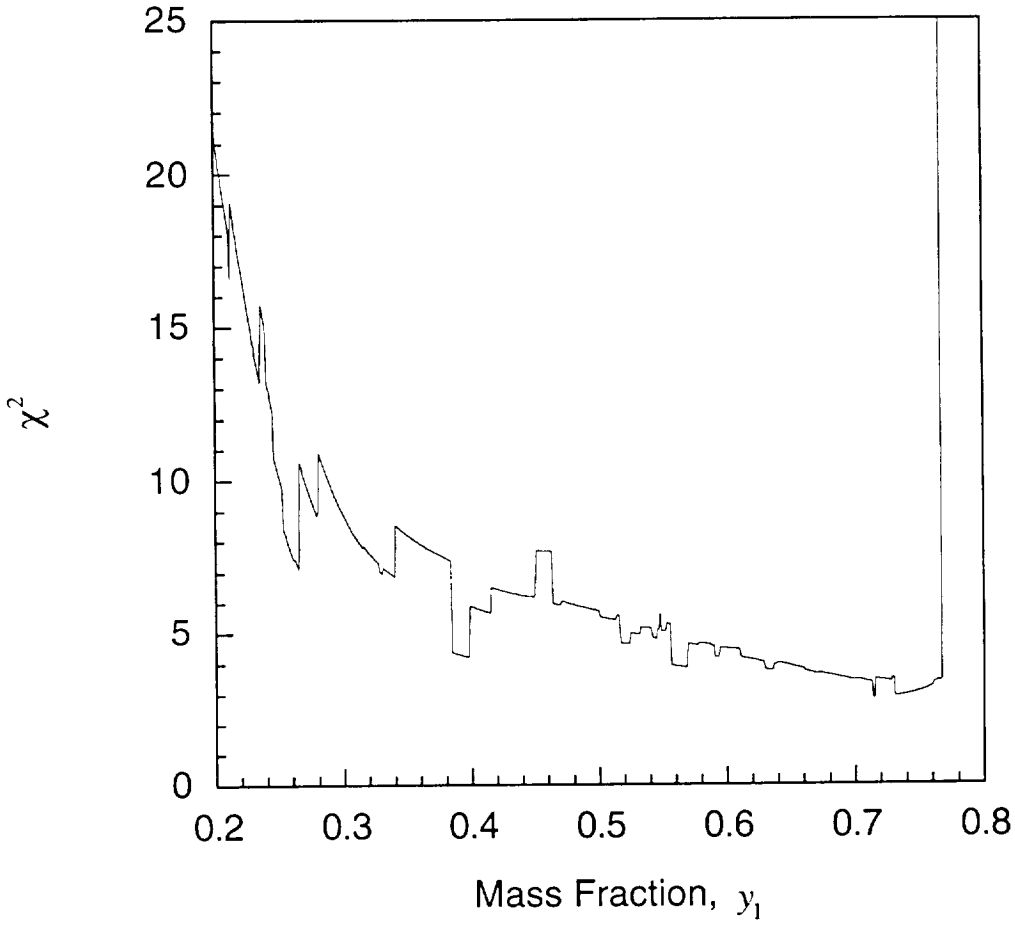

Figure B.1 Cost function for data fit to high heating rates in nitrogen.

considerable amount of discontinuities are present in the solution. This "noise" suggests that the solution technique is quite sensitive to the mass fraction itself. This sensitivity to the mass fraction is also apparent in the pseudo-data reduction presented in Section 4.5, where small variations of the mass fraction about the exact solution resulted in large increases in the cost function evaluation. For the case of real reactions, the inherent scatter in the data leads to an even greater sensitivity to small variations in the mass fraction resulting in a non-smooth solution. Unlike the case of the pseudo-data, there is no clearly defined minimum exhibited by this cost function. Instead, there appears to be a wide range of local minima which have approximately the same value cost function. A global minimum does exist at y_1=0.715, however, the difference between χ^2 for this global minimum and the other local minima is very small and no definite solution may be assumed.

The cost function determined from a data fit to the low heating rate data is illustrated in Figure B.2. As in the case of the high heating rates there are several local minima. However, the range of mass fractions across which these minima occur is much tighter then before. Previously local minima spanned almost the entire range of mass fractions which were searched. The band in which local minima occur for the low heating rates are confined to the region $0.30 < y_1 < 0.52$. Outside of these mass fractions the cost function increases rapidly due to the lack of any suitable reaction constants which may fit the data.

Several common local minima exist for both the high and low heating rates. The mass fractions and reaction coefficients for each of these local minima are given in Table B.1. The reaction coefficients corresponding to y_1=0.334 at the low heating rates and y_1=0.398 at the high heating rates will

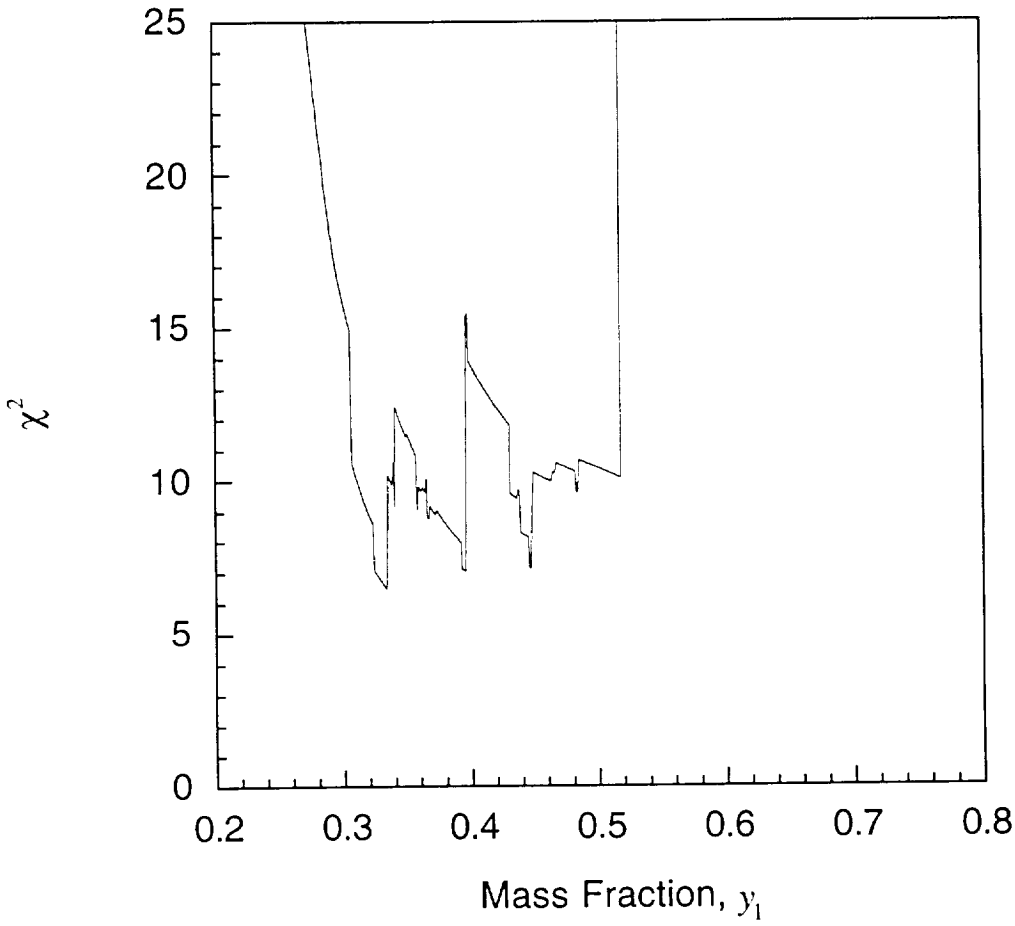

Figure B.2 Cost function for data fit to low heating rates in nitrogen.

Table B.1 Local Minima for Low and High Heating Rates

y_1	χ^2	E_1 (kJ/mol)	E_2 (kJ/mol)	k_1 (s^{-1})	k_2 (s^{-1})	n_1	n_2
Low Rates†							
0.334	6.49	142	243	4.07×10^{7}	1.51×10^{13}	1.38	3.34
0.396	7.05	140	222	2.78×10^{7}	4.77×10^{11}	1.87	2.97
0.447	7.14	135	220	1.16×10^{7}	3.30×10^{11}	2.23	2.92
High Rates††							
0.340	6.87	207	239	2.00×10^{12}	9.67×10^{12}	1.33	3.20
0.398	4.04	182	239	3.12×10^{10}	7.90×10^{12}	1.61	3.20
0.450	6.26	208	239	2.38×10^{12}	6.47×10^{12}	2.13	3.20

† Low heating rates are 2°C/min., 5°C/min., and 7°C/min.

†† High heating rates are 10°C/min., 15°C/min., and 20°C/min.

be referred to as the "global" minima for the low and high heating rate sets from here on. Several features of these minima are worth noting, the most interesting of which is the large difference between the reaction coefficients for the assumed first reaction at the different heating rates. For the high heating rates the cost function at y_1=0.398 is considerably lower than that at either of the other two minima. Both the activation energy and the reaction order for the second reaction are the same at each of the three minima for the high heating rates. The coefficients for the first reaction are less well behaved. While the activation energy and reaction rate constant at y_1=0.340 and y_1=0.450 are very similar, the reaction orders are vastly different. As the mass fraction for the first reaction increases, the reaction order also increases. The effect of this increase in n_1 is to give a broader tail to the first reaction. This allows the model to compensate for the resulting decrease in the mass fraction for the second reaction (and hence its contribution to the mass loss rate) while still providing a good fit to the data.

The fits to the low heating rate data are less consistent than those for the high heating rates. Reaction coefficients for both reactions are now subject to considerable variations across the range of minima. The reaction coefficients for the second reaction (with the exception of the reaction order) are now quite different at each of the minima. The best fit to this data was achieved for a mass fraction of y_1=0.334, although this "global" minimum is not as distinct, in terms of the cost function evaluation, as that for the high heating rates.

To allow a direct comparison between the different optimum reaction coefficients reported in Table B.1 for the second thermal reaction, data was generated at three different heating rates for each of set of coefficients corresponding to the local minima. Table B.2 shows compares the locations

Table B.2 Second Thermal Reaction - Mass Loss Rate Predictions

	$Q = 2$°C/min.		$Q = 10$°C/min.		$Q = 20$°C/min.	
y_1	$T^{\ddagger}_{max}$	$\left(\frac{\partial \alpha_2}{\partial T}\right)_{max}$	$T^{\ddagger}_{max}$	$\left(\frac{\partial \alpha_2}{\partial T}\right)_{max}$	$T^{\ddagger}_{max}$	$\left(\frac{\partial \alpha_2}{\partial T}\right)_{max}$
Low Rates†						
0.334	518	0.0088	552	0.0081	568	0.0078
0.396	522	0.0087	560	0.0079	577	0.0076
0.447	524	0.0087	562	0.0079	579	0.0076
High Rates††						
0.340	515	0.0090	549	0.0083	565	0.0080
0.398	519	0.0089	553	0.0082	569	0.0079
0.450	523	0.0088	558	0.0081	574	0.0078

† Low heating rates are 2°C/min., 5°C/min., and 7°C/min.

†† High heating rates are 10°C/min., 15°C/min., and 20°C/min.

‡ Temperature, in °C, at which the maximum mass loss rate occurs.

All reaction rates were calculated using the reaction coefficients reported for each local minimum in Table 6.3.

Units for $\left(\partial \alpha_2 / \partial T\right)_{max}$ are in $°C^{-1}$.

and magnitudes for these reaction coefficients across these heating rates. In all cases, the peak locations and magnitudes at each of the heating rates are very close to one another. It is interesting to note the strong similarity between the coefficients for the second reaction at the "global" minima for both the low and high heating rate data sets. A comparison between these two reactions at heating rates of 2°C/min. and 20°C/min. is shown in Figure B.3. Clearly, the second reaction is the same in both cases, with the differences in the reaction coefficients being attributable to scatter in the data and the high sensitivity of the reaction rate constant to any small variations in the value for the activation energy.

A similar comparison between the reaction coefficients derived for the first thermal reaction at each of the local minima was also carried out. Unlike the second thermal reaction, significant differences exist between all of the reaction coefficients derived at each of the local minima. Figure B.4 shows the behavior of each of the first reactions derived from the low heating rate data. The behavior at two different heating rates is illustrated. In all three reactions the maximum mass loss rate occurs at the same temperature, however the magnitudes of the peaks are different. The tails of each of the reactions are different, with a broader tail being required at the higher mass fractions. This is due to the fact that as the mass fraction for the first reaction increases, the mass fraction for the second reaction decreases. Hence, in order to compensate for the decreasing contribution of the second reaction to the second peak it is necessary to have a broader tail on the first reaction. The three sets of reaction coefficients derived for the first reaction at each of the high heating rate local minima behave in the same manner.

The data fit results presented here indicate that the data fit method is relatively insensitive to real data, allowing the determination of multiple

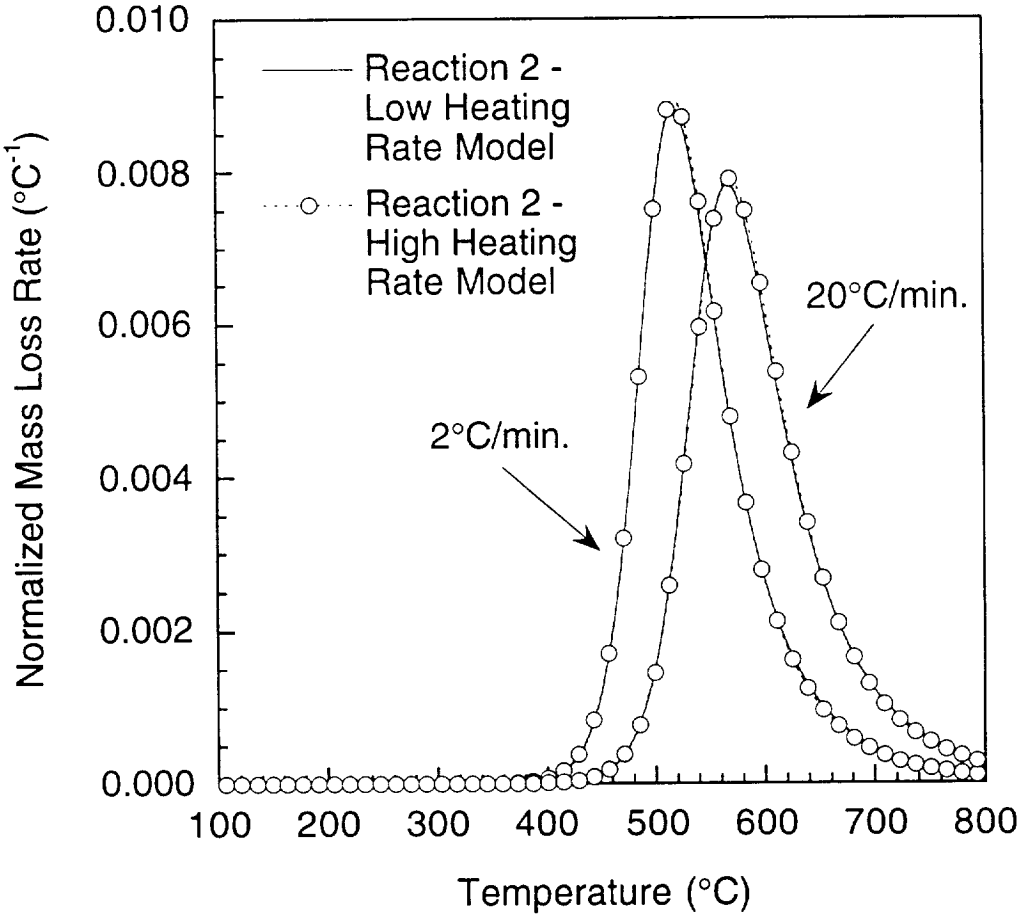

Figure B.3 Comparison between predicted mass loss rate curves for second thermal reaction derived from both high and low heating rate data sets.

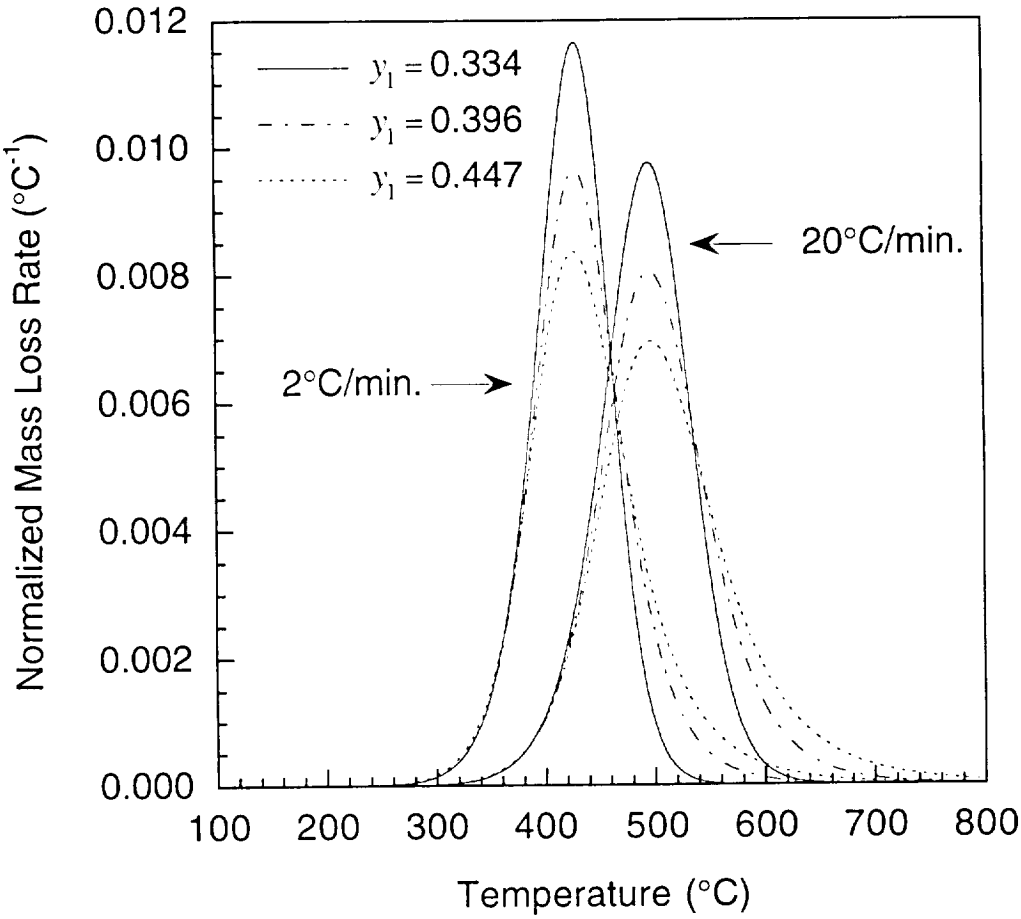

Figure B.4 Predicted mass loss rate curves for first thermal reaction derived at each of the local minima for the low heating rate data set.

good solutions rather than a single well defined minimum for each set of data. This is particularly true in the case of the high heating rates where the choice of solution becomes rather arbitrary. The data reduction method appears to be more sensitive to the low heating rate data. While multiple solutions are still presented, their number is greatly reduced and the range of mass fraction across which they occur is much tighter. It stands to reason that a true global minimum for the entire range of data must lie somewhere within the regions of local minima common to both the high and low heating rates. In this region the second reaction is very well behaved, with the different reaction coefficients reported by the reduction procedure at the local minima simply being different expressions of the same Arrhenius reaction. The first reaction, on the other hand, only demonstrates a consistency within the different sets of heating rates and can none of the coefficients reported here can be applied across the entire set of heating rates. This suggests that the true nature of the first reaction is more complex than was originally assumed and as such cannot be modeled using a single Arrhenius reaction.

REDUCE.M SCRIPT

REDUCE.M is an easy to use MATLAB script which allows the reduction of a set of empirical thermogravimetric data to a two reaction Arrhenius-type system. The code surveys a range of mass fractions and uses the data reduction technique described in Chapter 4 to generate a set of best-fit reaction coefficients through the evaluation of a cost function at each assumed mass fraction. The script given here surveys a range of mass fractions from $y_1 = 0.20$ to $y_1 = 0.80$. These parameters may be changed as desired. Cost functions are evaluated at each mass fraction increment and the set of parameters with the lowest cost function at each mass fraction is

returned to the main routine. All cost functions and optimum parameters are stored and may be viewed in graphical form or stored for further analysis.

Inputs

The code requires the input of five sets of data in matrix form within MATLAB before the code may be initiated. The first of these is an m x 1 matrix, "q", which specifies the heating rates (in °C/min.) for each of m sets of empirical data. Three n x m matrices containing the normalized mass loss rate, mass loss and standard deviations for each of the m heating rates at a total of n data points are then required. These matrices are called "rates", "mass" and "ratestd" respectively. Finally an n x 1 matrix, "temp", which contains the temperatures at which each of the n data points was recorded is required. The script shown here assumes a total of 701 data points for each set of data, however, this parameter may be changed to suit the user's needs.

Outputs

The code outputs a set of two matrices. The first matrix, "reactioncoeffs", contains the optimum activation energy, reaction rate constant, and reaction order for both reactions at each of the mass fractions. The second matrix, "costfn", contains the cost function value for the optimum reaction coefficients for each separate heating rate at each of the mass fractions surveyed. The mean of cost function value for the entire range of heating rates is also included. All matrices are in ASCII form and may be stored for further analysis or viewed graphically in the MATLAB code.

```
%       Reduce.m
%       Driver routine for reduction of TGA data to optimum set of two Arrhenius reactions
%       Increment y1 value and store optimum parameters for each value of y1
        ys=zeros(601,1);
```

```
chisquare=zeros(601,3);
chisquaremean=zeros(601,1);
Es=zeros(601,2);
ks=zeros(601,2);
ns=zeros(601,2);
y1=0.20
for w=1:601
        y2=1-y1;
        ys(w,1)=y1;
        TGAreduce;
        Es(w,1)=E1;
        Es(w,2)=E2;
        ks(w,1)=k1;
        ks(w,2)=k2;
        ns(w,1)=n1;
        ns(w,2)=n2;
        for i=1:f
                chisquare(w,i)=chisq(i,1);
                chisquaremean(w)=chisqmean;
        end
        y1=y1+0.001
end
reactioncoeffs=[ys Es ks ns];
costfn=[ys chisquare chisquaremean];

%       TGAreduce.m
%       Reduce TGA data using chisquared cost function
        [e,f]=size(rates);
        dadT1=zeros(701,f);
        dadT2=zeros(701,f);
        alpha1=zeros(701,f);
        alpha2=zeros(701,f);
        dadTtot=zeros(701,f);
        alphatot=zeros(701,f);
        E1=0;E2=0;k1=0;k2=0;n1=0;n2=0;
        R=8.3144;
        if y1<1.0
        for p=1:f;
                [i,j]=max(rates(:,p));
                dalphadTmax2(p,1)=i/y2;
                alphamax2(p,1)=(mass(j,p)-y1)/y2;
                Tmax(p,1)=temp(j,1)+273;
                Tmaxinv(p,1)=1/(Tmax(p,1));
                lnq(p,1)=log(q(p,1)/(Tmax(p,1)^2));
        end;
        [h,S]=polyfit(Tmaxinv,lnq,1);
        E2=-h(1,1)*R;
        for u=1:f
        n2prime(u,1)=(1/dalphadTmax2(u,1))*(-(h(1,1)/q(u,1))*exp(h(1,2))*(1-
        alphamax2(u,1))*exp(h(1,1)/Tmax(u,1)));
        end;
        n2=max(n2prime);
        k2=-h(1,1)*exp(h(1,2))*(1/(n2*(1-alphamax2(1,1))^(n2-1)));
        end
        E2old=E2;
        k2old=k2;
        n2old=n2;
        react2;
```

```
E1old=E1;
k1old=k1;
n1old=n1;
combined;
chisqmeanold=chisqmean;
react1;
flag=1;
count=1;
while flag==1
        combined;
        if chisqmean<chisqmeanold
                if abs(chisqmean-chisqmeanold)<1
                        flag=0;
                else
                        chisqmeanold=chisqmean;
                        E2old=E2;
                        k2old=k2;
                        n2old=n2;
                        react2;
                end
        else
                E2=E2old;
                k2=k2old;
                n2=n2old;
                flag=0;
        end
        if flag==1
                combined
                if chisqmean<chisqmeanold
                        if abs(chisqmean-chisqmeanold)<1
                                flag=0;
                        else
                                E1old=E1;
                                k1old=k1;
                                n1old=n1;
                                chisqmeanold=chisqmean;
                                react1;
                        end
                else
                        E1=E1old;
                        k1=k1old;
                        n1=n1old;
                        flag=0;
                end
        end
count=count+1;
if count>20
        flag=0
end
end
combined
end

%       React1
%       Generate predictions for first reaction and find new coefficients
%       for second reaction based on these predictions
        for i=1:f;
                rate=q(i,1);
```

```
            T=zeros(701,1);
            T(1,1)=100;
            dT=1;
for j=1:701
dadT1(j,i)=(1/rate)*k1*((1-alpha1(j,i))^n1)*exp(-E1/(R*(T(j,1)+273)));
dalpha1=dadT1(j,i)*dT;
if dalpha1>(1-alpha1(j,i))
            dalpha1=(1-alpha1(j,i));
dadT1(j,i)=dalpha1/dT;
end
if j==1
            alpha1(j+1,i)=dalpha1;
else if j<701
alpha1(j+1,i)=alpha1(j,i)+dalpha1;
end
end
if j<701
            T(j+1,1)=T(j,1)+dT;
end
end
end
dadT2=(rates-y1*dadT1)/y2;
alpha2=(mass-y1*alpha1)/y2;
for p=1:f;
            [i,j]=max(dadT2(:,p));
            dalphadTmax2(p,1)=i;
            alphamax2(p,1)=alpha2(j,p);
            Tmax(p,1)=temp(j,1)+273;
            Tmaxinv(p,1)=1/(Tmax(p,1));
            lnq(p,1)=log(q(p,1)/(Tmax(p,1)^2));
end;
[h,S]=polyfit(Tmaxinv,lnq,1);
E2=-h(1,1)*R;
for u=1:f
n2prime(u,1)=(1/dalphadTmax2(u,1))*(-(h(1,1)/q(u,1))*exp(h(1,2))*
                  (1-alphamax2(u,1))*exp(h(1,1)/Tmax(u,1)));
end;
n2=max(n2prime);
k2=-h(1,1)*exp(h(1,2))*(1/(n2*(1-alphamax2(1,1))^(n2-1)));

%     React2
%     Generate predictions for second reaction and find new coefficients
%     for first reactions based on these predictions
for i=1:f;
            rate=q(i,1);
            T=zeros(701,1);
            T(1,1)=100;
dT=1;
for j=1:701
dadT2(j,i)=(1/rate)*k2*((1-alpha2(j,i))^n2)*exp(-E2/(R*(T(j,1)+273)));
dalpha2=dadT2(j,i)*dT;
if dalpha2>(1-alpha2(j,i))
            dalpha2=(1-alpha2(j,i));
dadT2(j,i)=dalpha2/dT;
end
if j==1
            alpha2(j+1,i)=dalpha2;
else if j<701
```

```
alpha2(j+1,i)=alpha2(j,i)+dalpha2;
end
end
if j<701
        T(j+1,1)=T(j,1)+dT;
 end
end
end
dadT1=(rates-y2*dadT2)/y1;
alpha1=(mass-y2*alpha2)/y1;
for p=1:f;
        [i,j]=max(dadT1(:,p));
        dalphadTmax1(p,1)=i;
        alphamax1(p,1)=alpha1(j,p);
        Tmax(p,1)=temp(j,1)+273;
        Tmaxinv(p,1)=1/(Tmax(p,1));
        lnq(p,1)=log(q(p,1)/(Tmax(p,1)^2));
end;
[h,S]=polyfit(Tmaxinv,lnq,1);
E1=-h(1,1)*R;
for u=1:f
n1prime(u,1)=(1/dalphadTmax1(u,1))*(-(h(1,1)/q(u,1))*exp(h(1,2))*
                (1-alphamax1(u,1))*exp(h(1,1)/Tmax(u,1)));
end;
n1=max(n1prime);
k1=-h(1,1)*exp(h(1,2))*(1/(n1*(1-alphamax1(1,1))^(n1-1)));

%       Combined
%       Calculate mass loss and mass loss rate for  combined reactions and determine
%       resulting chisquared value
        alpha1=zeros(701,f);
        alpha2=zeros(701,f);
        dadT1=zeros(701,f);
        dadT2=zeros(701,f);
        dadTtot=zeros(701,f);
        alphatot=zeros(701,f);
        for i=1:f;
                rate=q(i,1);
                T=zeros(701,1);
                T(1,1)=100;
                dT=1;
        for j=1:701
        dadT1(j,i)=(1/rate)*k1*((1-alpha1(j,i))^n1)*exp(-E1/(R*(T(j,1)+273)));
        dadT2(j,i)=(1/rate)*k2*((1-alpha2(j,i))^n2)*exp(-E2/(R*(T(j,1)+273)));
        dalpha1=dadT1(j,i)*dT;
        dalpha2=dadT2(j,i)*dT;
        if dalpha1>(1-alpha1(j,i));
                dalpha1=(1-alpha1(j,i));
                dadT1(j,i)=dalpha1/dT;
        end
        if dalpha2>(1-alpha2(j,i));
                dalpha2=(1-alpha2(j,i));
                dadT2(j,i)=dalpha2/dT;
        end
        if j==1
                alpha1(j+1,i)=dalpha1;
                alpha2(j+1,i)=dalpha2;
        elseif j<701
```

```
        alpha1(j+1,i)=alpha1(j,i)+dalpha1;
        alpha2(j+1,i)=alpha2(j,i)+dalpha2;
end
if j<701
        T(j+1,1)=T(j,1)+dT;
end
end
dadTtot(:,i)=y1*dadT1(:,i)+y2*dadT2(:,i);
alphatot(:,i)=y1*alpha1(:,i)+y2*alpha2(:,i);
end
end
chisq=zeros(f,1);
for i=1:f;
for j=1:701;
        chisq(i,1)=chisq(i,1)+((rates(j,i)-dadTtot(j,i))/ratestd(j,i))^2;
end
end
chisqmean=mean(chisq);
```

APPENDIX C

THERMOGRAVIMETRIC ANALYSIS DATA

This appendix presents the thermogravimetric empirical data for all specimens in the TGA test matrix. The data is presented in the form of normalized mass loss rates. Tests carried out in nitrogen have been normalized such that a mass loss equal to one represents the loss of 40% of the original mass. Tests carried out in air and oxygen were normalized such that a mass loss equal to one represents the loss of 100% of the original volume. Specimens are denoted by the letter of the neat resin plaque from which they were manufactured.

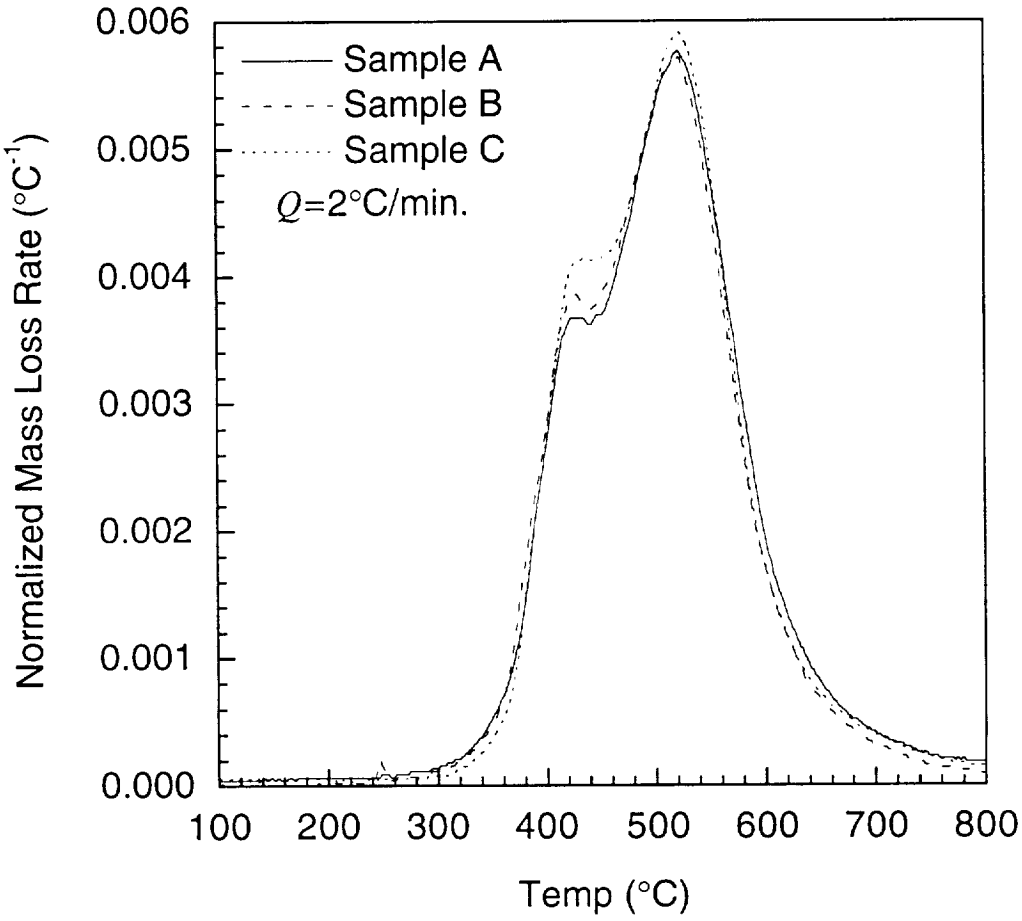

Figure C.1 Normalized mass loss rates for specimens in nitrogen at heating rate of 2°C/min.

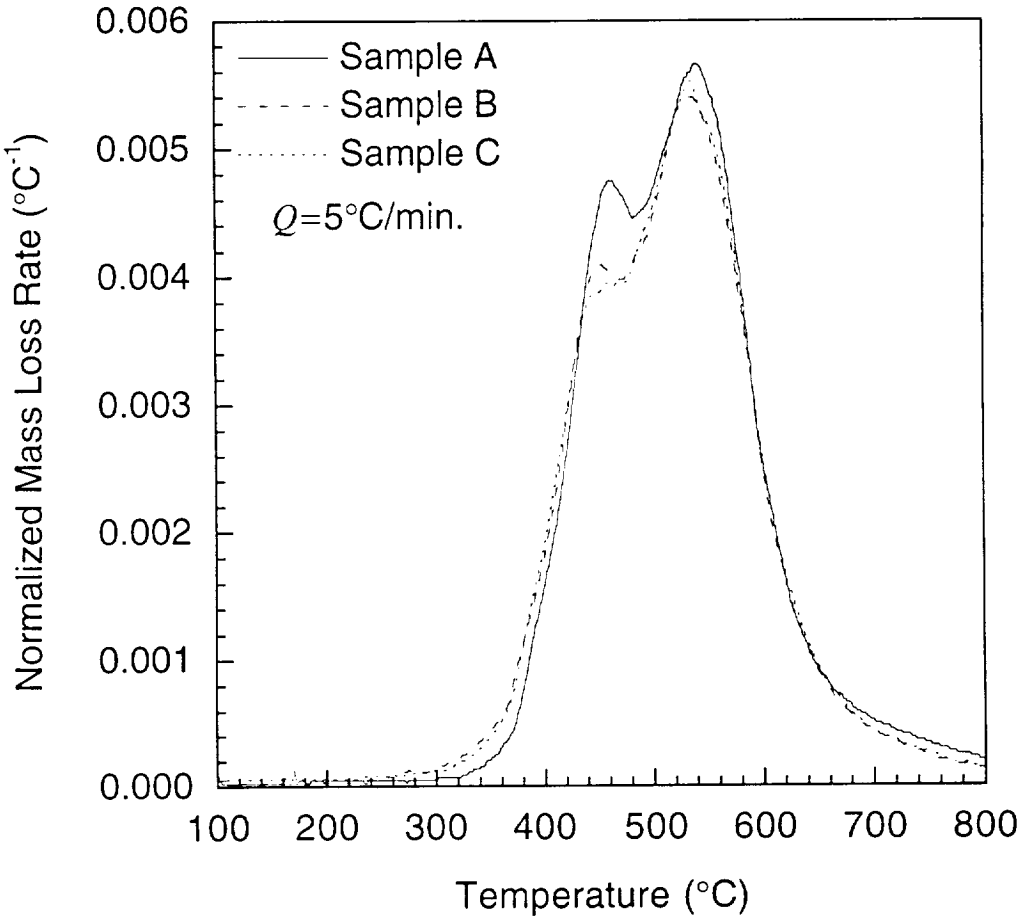

Figure C.2 Normalized mass loss rates for specimens in nitrogen at heating rate of 5°C/min.

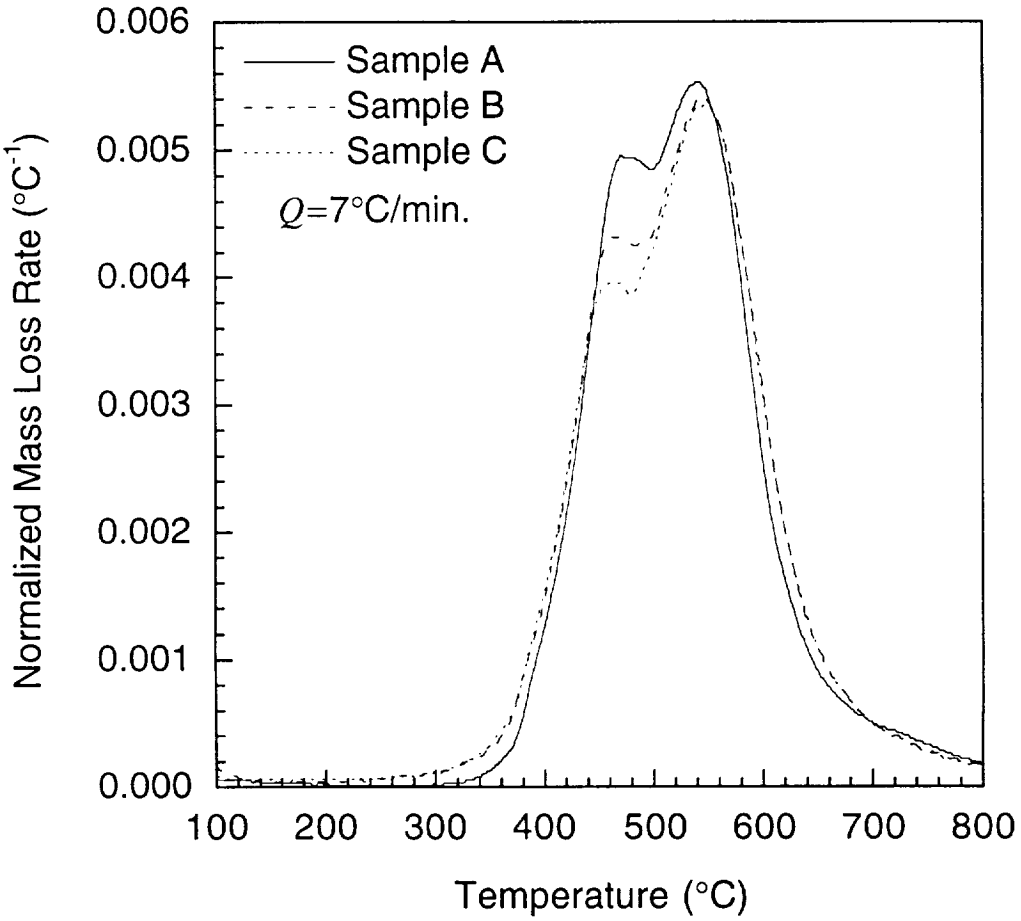

Figure C.3 Normalized mass loss rates for specimens in nitrogen at heating rate of 7°C/min.

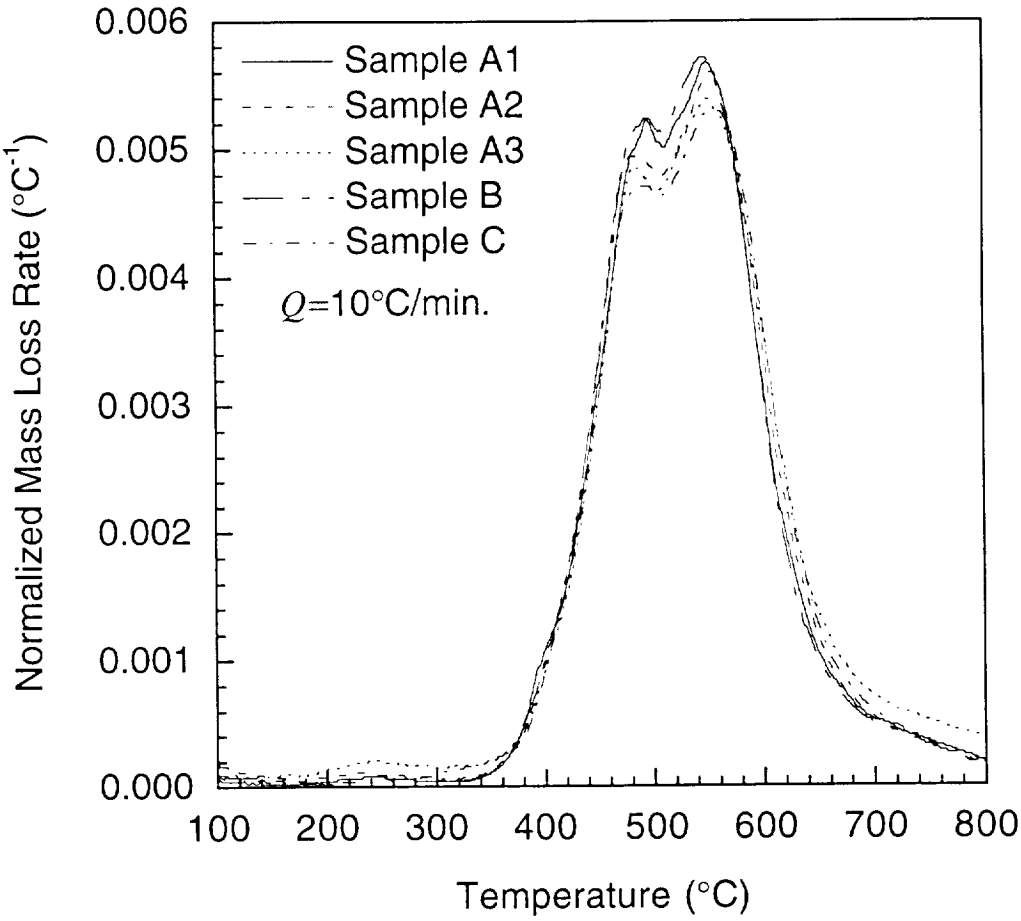

Figure C.4 Normalized mass loss rates for specimens in nitrogen at heating rate of 10°C/min.

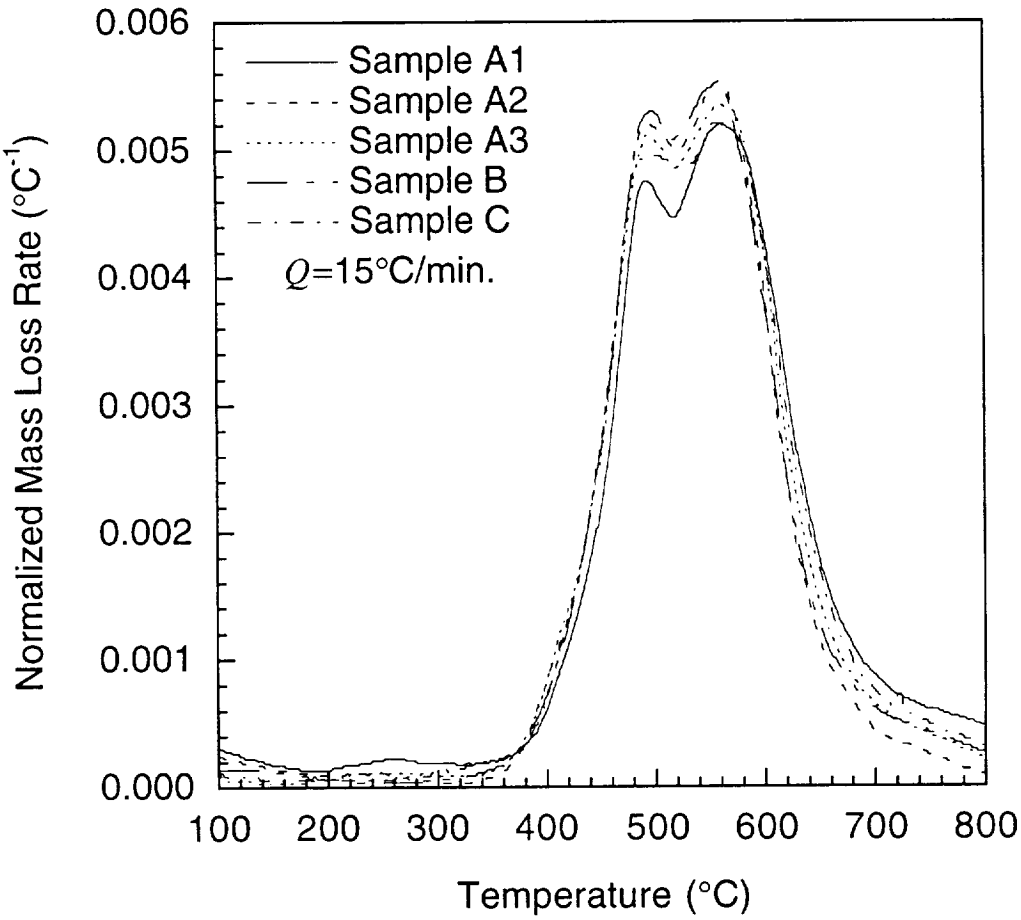

Figure C.5 Normalized mass loss rates for specimens in nitrogen at heating rate of 15°C/min.

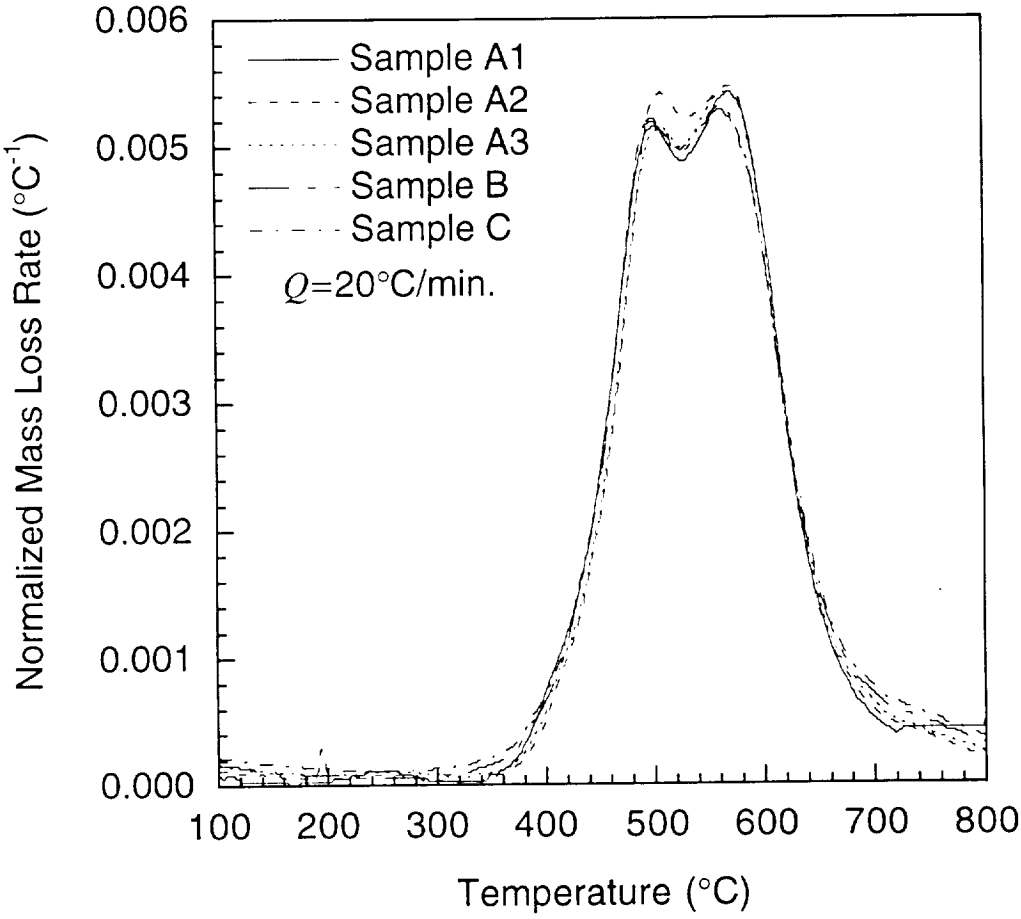

Figure C.6 Normalized mass loss rates for specimens in nitrogen at heating rate of 20°C/min.

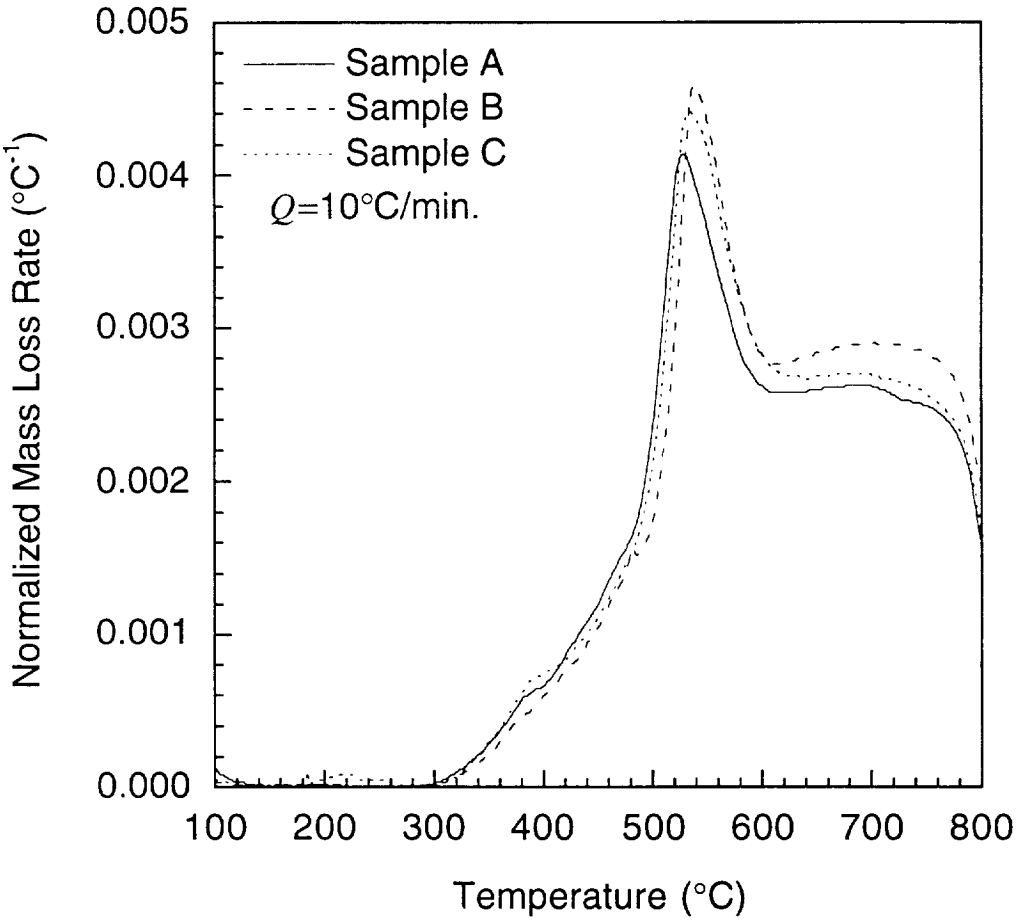

Figure C.7 Normalized mass loss rates for specimens in air at heating rate of 10°C/min.

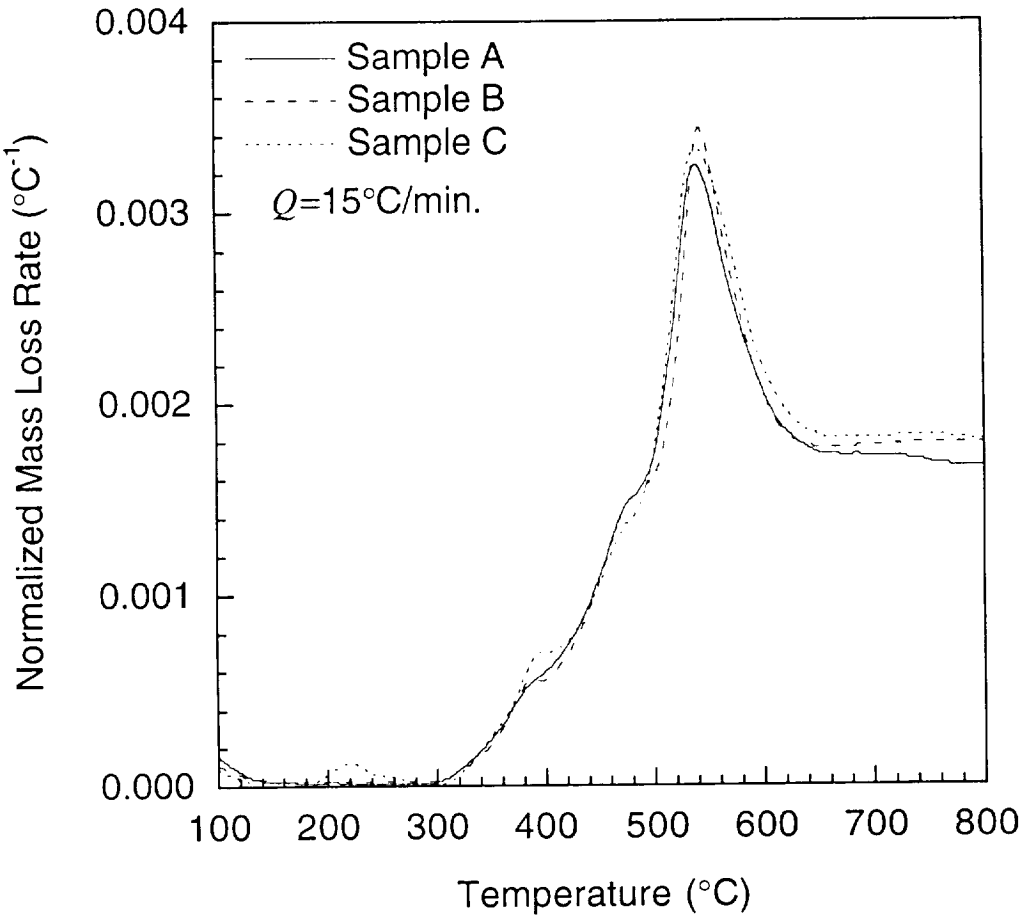

Figure C.8 Normalized mass loss rates for specimens in air at heating rate of 15°C/min.

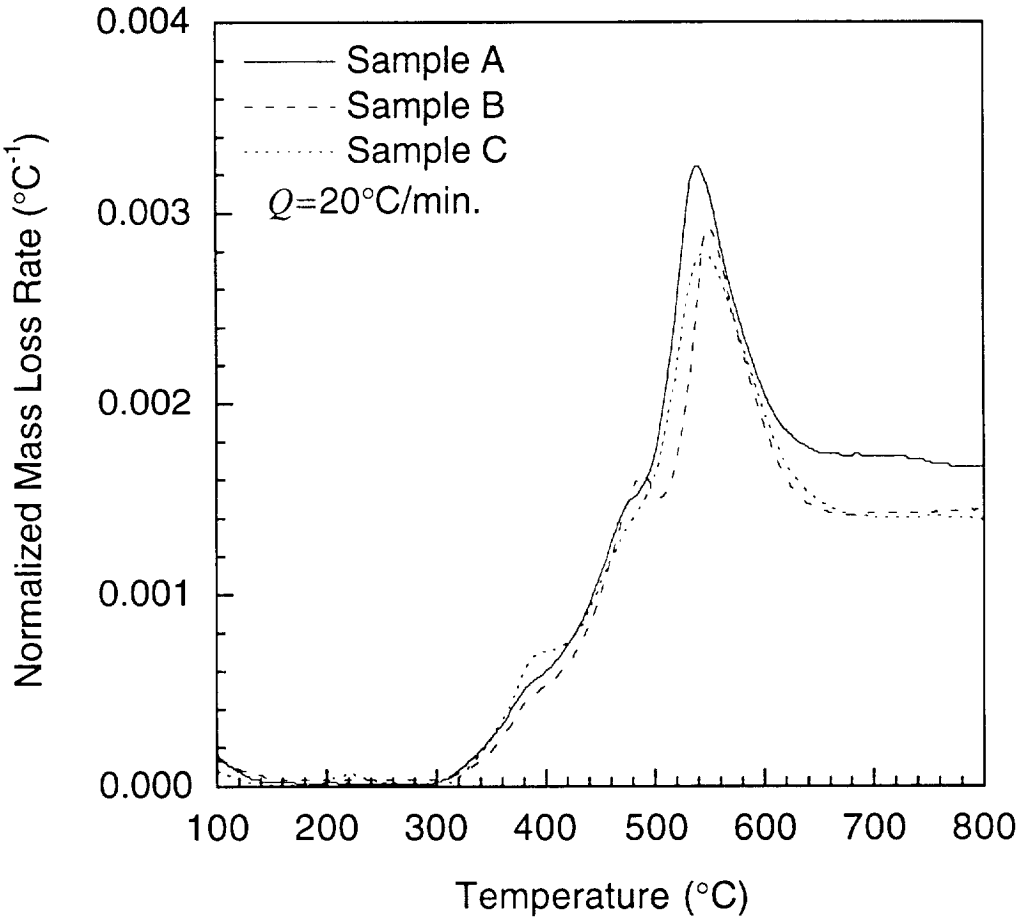

Figure C.9 Normalized mass loss rates for specimens in air at heating rate of 20°C/min.

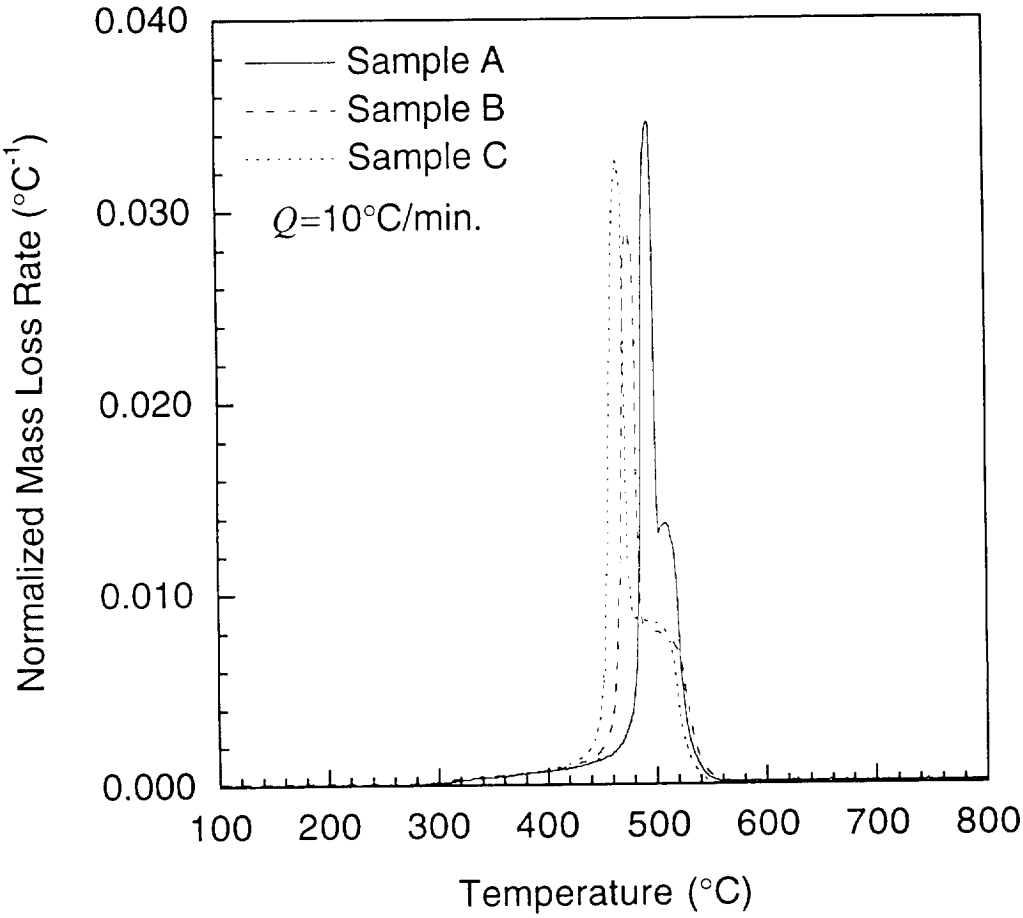

Figure C.10 Normalized mass loss rates for specimens in oxygen at heating rate of 10°C/min.

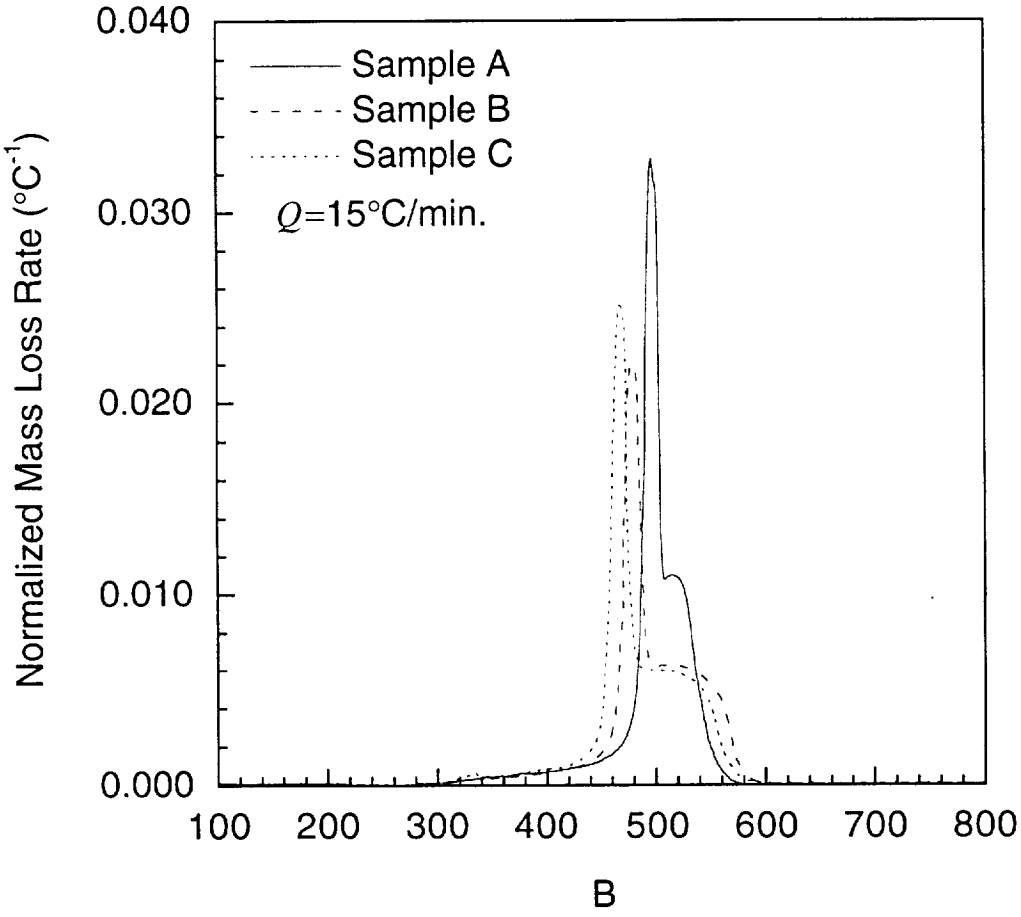

Figure C.11 Normalized mass loss rates for specimens in oxygen at heating rate of 15°C/min.

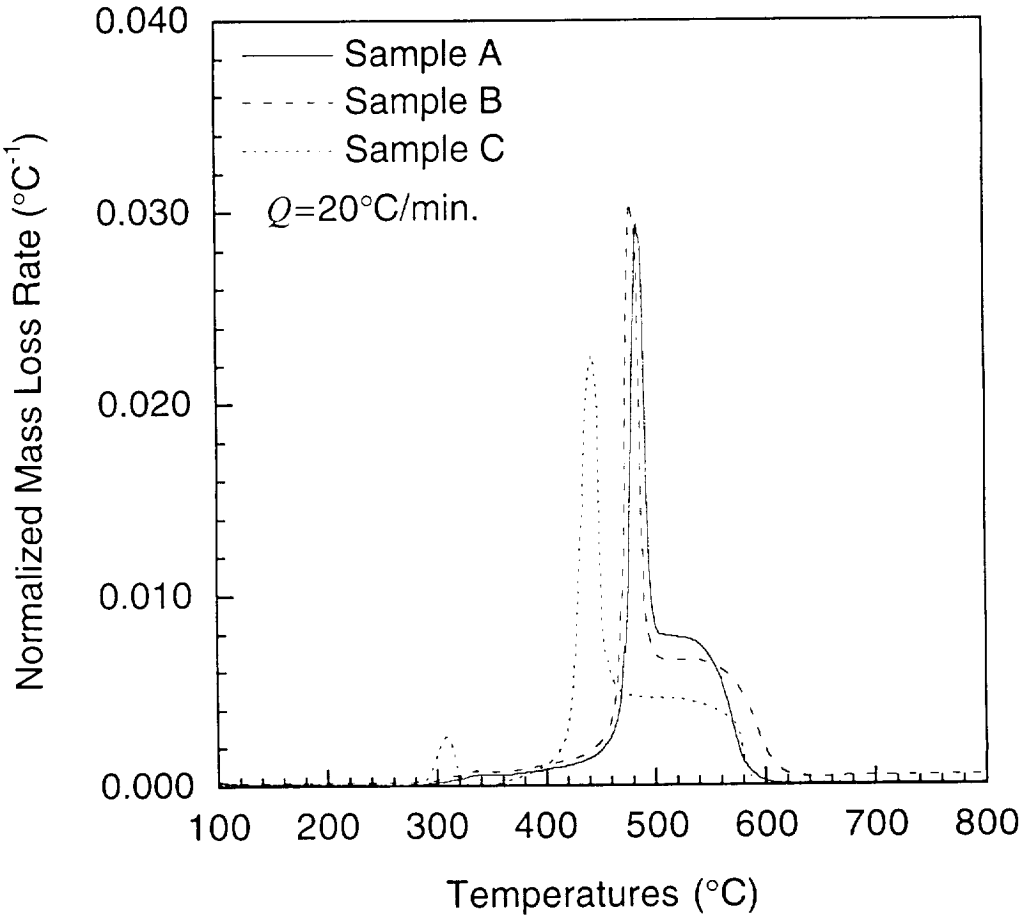

Figure C.12 Normalized mass loss rates for specimens in oxygen at heating rate of 20°C/min.

APPENDIX D

MACROSCOPIC SPECIMEN RAW DATA

This appendix presents raw experimental data for both the mass and dimensional measurements for all macroscopic specimens in the short term isothermal aging test matrix. The data is presented in tabular form. Data for each specimen group is presented at a total of eight aging times which correspond to the times at which a single sample was extracted from each specimen group. The thickness measurements provided here are the averages of three readings taken from each specimen. Units for the mass data are in grams. Units for the dimensional data are in millimeters.

Table D.1 Mass Data for Neat Resin E Group at 316°C

	0 hrs	24 hrs	48 hrs	72 hrs	96 hrs	120 hrs	144 hrs	192 hrs	240 hrs
BE1	2.0733	2.0581							
BE2	2.2671	2.2505	2.2443	2.2388					
BE3	2.2551	2.2385	2.2324	2.2267	2.2213	2.2162			
BE4	2.1781	2.1620	2.1558	2.1501	2.1450	2.1398	2.1356	2.1278	
CE1	2.1784	2.1655	2.1603						
CE2	2.2048	2.1922	2.1865	2.1811	2.1763				
CE3	2.2227	2.2104	2.2050	2.1999	2.1951	2.1900	2.1859		
CE4	2.2452	2.2329	2.2280	2.2233	2.2187	2.2141	2.2098	2.2031	2.1970

Table D.2 Mass Data for Neat Resin F Group at 316°C

	0 hrs	24 hrs	48 hrs	72 hrs	96 hrs	120 hrs	144 hrs	192 hrs	240 hrs
BF1	1.1172	1.1105							
BF2	1.1495	1.1423	1.1370	1.1338					
BF3	1.1461	1.1392	1.1359	1.1324	1.1295	1.1266			
BF4	1.1393	1.1322	1.1290	1.1257	1.1227	1.1196	1.1170	1.1122	
CF1	1.0993	1.0940	1.0913						
CF2	1.1132	1.1076	1.1047	1.1014	1.0987				
CF3	1.1173	1.1113	1.1080	1.1048	1.1022	1.0993	1.0966		
CF4	1.1325	1.1264	1.1233	1.1202	1.1174	1.1147	1.1120	1.1073	1.1040

Table D.3 Mass Data for Neat Resin H Group at 316°C

	0 hrs	24 hrs	48 hrs	72 hrs	96 hrs	120 hrs	144 hrs	192 hrs	240 hrs
BH1	2.9123	2.8957							
BH2	2.8380	2.8211	2.8145	2.8072					
BH3	2.9685	2.9502	2.9433	2.9359	2.9295	2.9230			
BH4	3.0716	3.0526	3.0458	3.0384	3.0322	3.0264	3.0206	3.0094	
CH1	2.5481	2.5351	2.5311						
CH2	2.6591	2.6451	2.6412	2.6367	2.6328				
CH3	2.7186	2.7039	2.7000	2.6952	2.6911	2.6872	2.6836		
CH4	2.6169	2.6033	2.5996	2.5955	2.5918	2.5881	2.5845	2.5780	2.5727

Table D.4 Mass Data for Neat Resin E Group at 343°C

	0 hrs	24 hrs	48 hrs	72 hrs	96 hrs	120 hrs	144 hrs	192 hrs	240 hrs
BE5	2.2542	2.2249							
BE6	2.2822	2.2533	2.2373	2.2214					
BE7	2.2745	2.2453	2.2290	2.2138	2.2009	2.1871			
BE8	2.2792	2.2499	2.2336	2.2181	2.2055	2.1910	2.1781	2.1570	
CE5	2.1785	2.1567	2.1416						
CE6	2.2297	2.2076	2.1935	2.1799	2.1680				
CE7	2.2393	2.2182	2.2043	2.1911	2.1798	2.1666	2.1538		
CE8	2.2677	2.2471	2.2344	2.2218	2.2112	2.1988	2.1860	2.1652	2.1414

Table D.5 Mass Data for Neat Resin F Group at 343°C

	0 hrs	24 hrs	48 hrs	72 hrs	96 hrs	120 hrs	144 hrs	192 hrs	240 hrs
BF5	1.1360	1.1216							
BF6	1.1780	1.1646	1.1551	1.1473					
BF7	1.1711	1.1586	1.1502	1.1428	1.1352	1.1279			
BF8	1.1852	1.1723	1.1644	1.1570	1.1496	1.1419	1.1344	1.1224	
CF5	1.1875	1.1715	1.1695						
CF6	1.2297	1.2198	1.2118	1.2046	1.1980				
CF7	1.2328	1.2222	1.2143	1.2065	1.994	1.1911	1.1836		
CF8	1.2594	1.2490	1.2411	1.2328	1.2255	1.2174	1.2099	1.1967	1.1811

Table D.6 Mass Data for Neat Resin H Group at 343°C

	0 hrs	24 hrs	48 hrs	72 hrs	96 hrs	120 hrs	144 hrs	192 hrs	240 hrs
BH5	2.4504	2.4298							
BH6	2.3669	2.3478	2.3380	2.3287					
BH7	2.3991	2.3796	2.3696	2.3609	2.3524	2.3439			
BH8	2.4350	2.4156	2.4061	2.3969	2.3882	2.3795	2.3714	2.3571	
CH5	2.7024	2.6832	2.6737						
CH6	2.6261	2.6075	2.5982	2.5886	2.5793				
CH7	2.5500	2.5328	2.5231	2.5137	2.5040	2.4950	2.4868		
CH8	2.3665	2.3512	2.3420	2.3329	2.3236	2.3152	2.3070	2.2927	2.2768

Table D.7 Mass Data for Unidirectional F Group at 316°C

	0 hrs	24 hrs	48 hrs	72 hrs	96 hrs	120 hrs	144 hrs	192 hrs	240 hrs
UAF1	0.8975	0.8963							
UAF2	0.9686	0.9673	0.9667	0.9661					
UAF3	0.9766	0.9750	0.9746	0.9740	0.9734	0.9726			
UAF4	0.9667	0.9654	0.9649	0.9642	0.9636	0.9629	0.9325	0.9615	
UBF1	0.9909	0.9889	0.9883						
UBF2	0.9931	0.9916	0.9909	0.9901	0.9895				
UBF3	1.0051	1.0037	1.0031	1.0022	1.0018	1.0008	1.0002		
UBF4	1.0088	1.0071	1.0068	1.0059	1.0054	1.0046	1.0041	1.0032	1.0025

Table D.8 Mass Data for Unidirectional G Group at 316°C

	0 hrs	24 hrs	48 hrs	72 hrs	96 hrs	120 hrs	144 hrs	192 hrs	240 hrs
UAG1	0.9803	0.9788							
UAG2	0.9751	0.9735	0.9726	0.9714					
UAG3	0.9720	0.9704	0.9696	0.9685	0.9675	0.9661			
UAG4	0.9894	0.9879	0.9871	0.9859	0.9850	0.9835	0.9826	0.9805	
UBG1	1.0013	0.9992	0.9983						
UBG2	0.9891	0.9870	0.9863	0.9851	0.9840				
UBG3	0.9928	0.9910	0.9900	0.9889	0.9878	0.9866	0.9855		
UBG4	0.9768	0.9750	0.9740	0.9728	0.9718	0.9706	0.9693	0.9673	0.9653

Table D.9 Mass Data for Unidirectional H Group at 316°C

	0 hrs	24 hrs	48 hrs	72 hrs	96 hrs	120 hrs	144 hrs	192 hrs	240 hrs
UAH1	2.5034	2.4948							
UAH2	2.5031	2.4944	2.4937	2.4925					
UAH3	2.4788	2.4699	2.4693	2.4682	2.4672	2.4663			
UAH4	2.5504	2.5415	2.5409	2.5398	2.5390	2.5380	2.5374	2.5357	
UBH1	2.4577	2.4498	2.4489						
UBH2	2.5019	2.4938	2.4928	2.4918	2.4907				
UBH3	2.4698	2.4615	2.4606	2.4593	2.4584	2.4575	2.4566		
UBH4	2.4635	2.4552	2.4543	2.4532	2.4521	2.4511	2.4501	2.4483	2.4469

Table D.10 Mass Data for Unidirectional F Group at 343°C

	0 hrs	24 hrs	48 hrs	72 hrs	96 hrs	120 hrs	144 hrs	192 hrs	240 hrs
UAF5	0.9782	0.9743							
UAF6	0.9892	0.9847	0.9828	0.9813					
UAF7	0.9852	0.9822	0.9803	0.9788	0.9772	0.9747			
UAF8	0.9838	0.9801	0.9781	0.9766	0.9750	0.9725	0.9706	0.9674	
UBF5	0.9846	0.9805	0.9778						
UBF6	0.9945	0.9906	0.9877	0.9860	0.9847				
UBF3	0.9912	0.9871	0.9844	0.9827	0.9812	0.9786	0.9761		
UBF8	0.9983	0.9943	0.9915	0.9895	0.9879	0.9851	0.9829	0.9792	0.9733

Table D.11 Mass Data for Unidirectional G Group at 343°C

	0 hrs	24 hrs	48 hrs	72 hrs	96 hrs	120 hrs	144 hrs	192 hrs	240 hrs
UAG5	0.9891	0.9845							
UAG6	0.9938	0.9894	0.9862	0.9846					
UAG7	0.9897	0.9856	0.9824	0.9807	0.9780	0.9738			
UAG8	0.9741	0.9700	0.9668	0.9651	0.9622	0.9582	0.9543	0.9476	
UBG5	0.9765	0.9723	0.9688						
UBG6	0.9827	0.9783	0.9750	0.9730	0.9704				
UBG7	0.9725	0.9682	0.9654	0.9632	0.9604	0.9567	0.9529		
UBG8	0.9612	0.9575	0.9543	0.9523	0.9498	0.9462	0.9424	0.9362	0.9250

Table D.12 Mass Data for Unidirectional H Group at 343°C

	0 hrs	24 hrs	48 hrs	72 hrs	96 hrs	120 hrs	144 hrs	192 hrs	240 hrs
UAH5	2.3637	2.3551							
UAH6	2.3386	2.3297	2.3262	2.3236					
UAH7	2.3480	2.3392	2.3353	2.3335	2.3301	2.3273			
UAH8	2.3732	2.3646	2.3608	2.3589	2.3559	2.3525	2.3498	2.3451	
UBH5	2.3507	2.3425	2.3387						
UBH6	2.3712	2.3634	2.3596	2.3572	2.3537				
UBH7	2.3394	2.3310	2.3278	2.3253	2.3220	2.3190	2.3160		
UBH8	2.3049	2.2974	2.2937	2.2915	2.2881	2.2850	2.2818	2.2769	2.2687

Table D.13 Lengths for Neat Resin E Group at 316°C

	0 hrs	24 hrs	48 hrs	72 hrs	96 hrs	120 hrs	144 hrs	192 hrs	240 hrs
BE1	77.96								
BE2	77.96								
BE3	77.96				77.64	77.68			
BE4	77.98				77.64	77.69	77.64	77.62	
CE1	75.18								
CE2	75.09				74.85				
CE3	75.20				74.91	74.98	74.96		
CE4	75.32				75.05	75.05	75.05	75.00	74.85

Table D.14 Lengths for Neat Resin F Group at 316°C

	0 hrs	24 hrs	48 hrs	72 hrs	96 hrs	120 hrs	144 hrs	192 hrs	240 hrs
BF1	77.81								
BF2	77.85								
BF3	77.91				77.54	77.55			
BF4	77.93				77.60	77.58	77.58	77.54	
CF1	74.87								
CF2	74.93				74.73				
CF3	74.98				74.76	74.76	74.75		
CF4	75.00				74.76	74.83	74.78	74.76	74.75

Table D.15 Lengths for Neat Resin H Group at 316°C

	0 hrs	24 hrs	48 hrs	72 hrs	96 hrs	120 hrs	144 hrs	192 hrs	240 hrs
BH1	25.64								
BH2	25.75								
BH3	25.70				25.62	25.67			
BH4	25.70				25.64	25.60	25.65	25.60	
CH1	25.57								
CH2	25.67				25.70				
CH3	25.74				25.64	25.58	25.59		
CH4	25.67				25.58	25.63	25.60	25.57	25.54

Table D.16 Lengths for Neat Resin E Group at 343°C

	0 hrs	24 hrs	48 hrs	72 hrs	96 hrs	120 hrs	144 hrs	192 hrs	240 hrs
BE5	77.83	77.59							
BE6	77.81	77.59	77.49	77.43					
BE7	77.79	77.57	77.47	77.44	77.36	77.35			
BE8	77.79	77.53	77.45	77.42	77.35	77.37	77.24	77.16	
CE5	75.08	74.98	74.89						
CE6	75.16	75.00	74.92	74.88	74.82				
CE7	75.12	75.03	74.96	74.92	74.87	74.82	74.78		
CE8	75.14	75.05	75.00	75.00	74.92	74.89	74.84	74.76	74.74

Table D.17 Lengths for Neat Resin F Group at 343°C

	0 hrs	24 hrs	48 hrs	72 hrs	96 hrs	120 hrs	144 hrs	192 hrs	240 hrs
BF5	77.83	77.63							
BF6	77.85	77.67	77.57	77.53					
BF7	77.83	77.65	77.57	77.54	77.50	77.44			
BF8	77.83	77.64	77.56	77.54	77.48	77.44	77.36	77.27	
CF5	75.14	75.09	75.00						
CF6	75.28	75.09	75.04	75.02	74.96				
CF7	75.18	75.11	75.04	75.05	74.95	74.94	74.85		
CF8	75.16	75.13	75.07	75.04	75.01	74.98	74.88	74.80	74.76

Table D.18 Lengths for Neat Resin H Group at 343°C

	0 hrs	24 hrs	48 hrs	72 hrs	96 hrs	120 hrs	144 hrs	192 hrs	240 hrs
BH5	25.22	25.17							
BH6	25.12	25.06	25.02	25.04					
BH7	25.16	25.13	25.09	25.08	25.06	25.06			
BH8	25.18	25.16	25.13	25.14	25.11	25.12	25.06	25.06	
CH5	25.30	25.26	25.24						
CH6	25.29	25.25	25.23	25.21	25.20				
CH7	25.30	25.27	25.25	25.26	25.23	25.19	25.16		
CH8	25.32	25.21	25.17	25.17	25.19	25.18	25.14	25.14	25.10

Table D.19 Widths for Neat Resin E Group at 316°C

	0 hrs	24 hrs	48 hrs	72 hrs	96 hrs	120 hrs	144 hrs	192 hrs	240 hrs
BE1	6.13								
BE2	6.73								
BE3	6.75				6.70	6.70			
BE4	6.28				6.28	6.30	6.28	6.27	
CE1	6.68								
CE2	6.73				6.70				
CE3	6.73				6.68	6.68	6.68		
CE4	6.76				6.74	6.72	6.72	6.70	6.54

Table D.20 Widths for Neat Resin F Group at 316°C

	0 hrs	24 hrs	48 hrs	72 hrs	96 hrs	120 hrs	144 hrs	192 hrs	240 hrs
BF1	3.40								
BF2	3.39								
BF3	3.39				3.36	3.36			
BF4	3.41				3.38	3.38	3.37	3.37	
CF1	3.45								
CF2	3.46				3.44				
CF3	3.45				3.42	3.42	3.41		
CF4	3.48				3.46	3.45	3.44	3.44	3.42

Table D.21 Widths for Neat Resin H Group at 316°C

	0 hrs	24 hrs	48 hrs	72 hrs	96 hrs	120 hrs	144 hrs	192 hrs	240 hrs
BH1	25.67								
BH2	24.81								
BH3	25.87				25.77	25.77			
BH4	26.71				26.68	26.64	26.67	26.61	
CH1	25.64								
CH2	25.78				25.68				
CH3	25.76				25.67	25.66	25.70		
CH4	24.36				24.28	24.27	24.25	24.25	24.23

Table D.22 Widths for Neat Resin E Group at 343°C

	0 hrs	24 hrs	48 hrs	72 hrs	96 hrs	120 hrs	144 hrs	192 hrs	240 hrs
BE5	6.60	6.57							
BE6	6.65	6.63	6.61	6.62					
BE7	6.63	6.63	6.60	6.60	6.57	6.57			
BE8	6.65	6.64	6.62	6.61	6.58	6.58	6.57	6.56	
CE5	6.49	6.48	6.45						
CE6	6.68	6.66	6.63	6.63	6.61				
CE7	6.78	6.76	6.73	6.72	6.69	6.71	6.69		
CE8	6.53	6.54	6.50	6.53	6.51	6.51	6.49	6.49	6.44

Table D.23 Widths for Neat Resin F Group at 343°C

	0 hrs	24 hrs	48 hrs	72 hrs	96 hrs	120 hrs	144 hrs	192 hrs	240 hrs
BF5	3.32	3.30							
BF6	3.50	3.47	3.46	3.46					
BF7	3.45	3.49	3.45	3.46	3.46	3.46			
BF8	3.51	3.49	3.47	3.46	3.46	3.46	3.44	3.44	
CF5	3.41	3.41	3.39						
CF6	3.64	3.64	3.61	3.62	3.60				
CF7	3.51	3.57	3.55	3.53	3.54	3.53	3.52		
CF8	3.71	3.71	3.68	3.68	3.68	3.66	3.66	3.66	3.64

Table D.24 Widths for Neat Resin H Group at 343°C

	0 hrs	24 hrs	48 hrs	72 hrs	96 hrs	120 hrs	144 hrs	192 hrs	240 hrs
BH5	21.94	22.05							
BH6	21.94	21.88	21.87	21.87					
BH7	21.97	21.94	21.89	21.91	21.86	21.90			
BH8	22.08	22.01	21.99	21.98	21.98	21.97	21.93	21.91	
CH5	21.94	21.93	21.86						
CH6	22.00	21.98	22.00	21.96	21.98				
CH7	22.02	22.02	21.99	22.01	22.00	21.96	21.98		
CH8	21.95	21.93	21.91	21.90	21.90	21.88	21.86	21.85	21.80

Table D.25 Thicknesses for Neat Resin E Group at 316°C

	0 hrs	24 hrs	48 hrs	72 hrs	96 hrs	120 hrs	144 hrs	192 hrs	240 hrs
BE1	3.330	3.319							
BE2	3.320	3.325	3.325	3.313					
BE3	3.327	3.323	3.328	3.319	3.317	3.313			
BE4	3.327	3.329	3.323	3.320	3.313	3.313	3.305	3.298	
CE1	3.350	3.345	3.340						
CE2	3.363	3.371	3.376	3.359	3.348				
CE3	3.387	3.395	3.395	3.388	3.380	3.373	3.376		
CE4	3.413	3.417	3.415	3.410	3.406	3.391	3.403	3.386	3.389

Table D.26 Thicknesses for Neat Resin F Group at 316°C

	0 hrs	24 hrs	48 hrs	72 hrs	96 hrs	120 hrs	144 hrs	192 hrs	240 hrs
BF1	3.320	3.319							
BF2	3.327	3.315	3.321	3.309					
BF3	3.313	3.317	3.321	3.311	3.303	3.297			
BF4	3.310	3.319	3.320	3.309	3.298	3.296	3.301	3.292	
CF1	3.263	3.269	3.274						
CF2	3.293	3.298	3.291	3.282	3.271				
CF3	3.313	3.306	3.301	3.312	3.287	3.288	3.289		
CF4	3.333	3.315	3.317	3.318	3.311	3.313	3.300	3.289	3.297

Table D.27 Thicknesses for Neat Resin H Group at 316°C

	0 hrs	24 hrs	48 hrs	72 hrs	96 hrs	120 hrs	144 hrs	192 hrs	240 hrs
BH1	3.410	3.397							
BH2	3.413	3.408	3.408	3.401					
BH3	3.433	3.425	3.420	3.421	3.413	3.410			
BH4	3.450	3.437	3.441	3.441	3.429	3.424	3.440	3.408	
CH1	2.993	2.987							
CH2	3.087	3.077	3.077	3.077	3.069				
CH3	3.160	3.147	3.153	3.153	3.143	3.139	3.144		
CH4	3.220	3.213	3.215	3.215	3.208	3.203	3.226	3.194	3.190

Table D.28 Thicknesses for Neat Resin E Group at 343°C

	0 hrs	24 hrs	48 hrs	72 hrs	96 hrs	120 hrs	144 hrs	192 hrs	240 hrs
BE5	3.347	3.337							
BE6	3.353	3.339	3.333	3.326					
BE7	3.365	3.345	3.334	3.322	3.311	3.303			
BE8	3.353	3.342	3.333	3.321	3.312	3.301	3.297	3.274	
CE5	3.474	3.464	3.450						
CE6	3.505	3.486	3.469	3.449	3.450				
CE7	3.522	3.496	3.485	3.475	3.465	3.451	3.446		
CE8	3.528	3.498	3.507	3.488	3.497	3.469	3.459	3.448	3.430

Table D.29 Thicknesses for Neat Resin F Group at 343°C

	0 hrs	24 hrs	48 hrs	72 hrs	96 hrs	120 hrs	144 hrs	192 hrs	240 hrs
BF5	3.330	3.327							
BF6	3.340	3.333	3.326	3.316					
BF7	3.343	3.338	3.325	3.319	3.307	3.301			
BF8	3.347	3.336	3.329	3.316	3.315	3.305	3.297	3.279	
CF5	3.551	3.531	3.517						
CF6	3.560	3.543	3.539	3.513	3.512				
CF7	3.561	3.549	3.533	3.527	3.521	3.508	3.501		
CF8	3.576	3.560	3.553	3.543	3.530	3.523	3.516	3.491	3.470

Table D.30 Thicknesses for Neat Resin H Group at 343°C

	0 hrs	24 hrs	48 hrs	72 hrs	96 hrs	120 hrs	144 hrs	192 hrs	240 hrs
BH5	3.412	3.398							
BH6	3.299	3.300	3.291	3.279					
BH7	3.341	3.333	3.325	3.317	3.309	3.302			
BH8	3.368	3.365	3.362	3.346	3.340	3.337	3.325	3.316	
CH5	3.741	3.731	3.723						
CH6	3.644	3.634	3.629	3.615	3.609				
CH7	3.533	3.511	3.506	3.497	3.491	3.484	3.485		
CH8	3.298	3.286	3.277	3.276	3.261	3.260	3.251	3.239	3.223

Table D.31 Lengths for Unidirectional F Group at 316°C

	0 hrs	24 hrs	48 hrs	72 hrs	96 hrs	120 hrs	144 hrs	192 hrs	240 hrs
UAF1	75.20								
UAF2	75.23								
UAF3	75.32				75.32	75.32			
UAF4	75.36				75.34	75.34	75.36	75.34	
UBF1	76.34								
UBF2	76.39				76.36				
UBF3	76.41				76.38	76.42	76.39		
UBF4	76.42				76.42	76.44	76.39	76.42	76.42

Table D.32 Lengths for Unidirectional G Group at 316°C

	0 hrs	24 hrs	48 hrs	72 hrs	96 hrs	120 hrs	144 hrs	192 hrs	240 hrs
UAG1	3.36								
UAG2	3.38								
UAG3	3.33				3.34	3.32			
UAG4	3.40				3.38	3.38	3.37	3.38	
UBG1	3.39								
UBG2	3.39				3.38				
UBG3	3.42				3.42	3.42	3.42		
UBG4	3.40				3.42	3.40	3.41	3.42	3.35

Table D.33 Lengths for Unidirectional H Group at 316°C

	0 hrs	24 hrs	48 hrs	72 hrs	96 hrs	120 hrs	144 hrs	192 hrs	240 hrs
UAH1	25.55								
UAH2	25.60								
UAH3	25.66				25.65	25.66			
UAH4	25.71				25.70	25.70	25.70	25.70	
UBH1	25.54								
UBH2	25.60				25.58				
UBH3	25.61				25.60	25.61	25.60		
UBH4	25.68				25.67	25.71	25.70	25.66	25.61

Table D.34 Lengths for Unidirectional F Group at 343°C

	0 hrs	24 hrs	48 hrs	72 hrs	96 hrs	120 hrs	144 hrs	192 hrs	240 hrs
UAF5	75.49	75.44							
UAF6	75.49	75.49	75.47	75.48					
UAF7	75.52	75.53	75.51	75.52	75.52	75.52			
UAF8	75.55	75.60	75.55	75.56	75.56	75.56	75.55	75.54	
UBF5	76.48	76.52	76.47						
UBF6	76.50	76.49	76.51	76.50	76.52				
UBF7	76.50	76.52	76.47	76.50	76.52	76.50	76.51		
UBF8	76.53	76.50	76.47	76.54	76.52	76.52	76.51	76.50	76.48

Table D.35 Lengths for Unidirectional G Group at 343°C

	0 hrs	24 hrs	48 hrs	72 hrs	96 hrs	120 hrs	144 hrs	192 hrs	240 hrs
UAG5	3.44	3.43							
UAG6	3.44	3.46	3.45	3.49					
UAG7	3.47	3.44	3.46	3.50	3.47	3.48			
UAG8	3.46	3.45	3.37	3.39	3.37	3.37	3.37	3.36	
UBG5	3.42	3.44	3.45						
UBG6	3.46	3.45	3.46	3.50	3.47				
UBG7	3.44	3.44	3.43	3.45	3.43	3.45	3.44		
UBG8	3.44	3.46	3.45	3.48	3.47	3.46	3.47	3.46	3.46

Table D.36 Lengths for Neat Resin H Group at 343°C

	0 hrs	24 hrs	48 hrs	72 hrs	96 hrs	120 hrs	144 hrs	192 hrs	240 hrs
UAH5	25.08	25.09							
UAH6	25.09	25.12	25.08	25.08					
UAH7	25.10	25.11	25.11	25.10	25.10	25.12			
UAH8	25.13	25.16	25.13	25.16	25.17	25.15	25.12	25.14	
UBH5	25.08	25.14	25.11						
UBH6	25.12	25.20	25.11	25.12	25.12				
UBH7	25.14	25.17	25.15	25.16	25.16	25.15	25.14		
UBH8	25.21	25.21	25.21	25.22	25.18	25.20	25.22	25.20	25.21

Table D.37 Widths for Unidirectional F Group at 316°C

	0 hrs	24 hrs	48 hrs	72 hrs	96 hrs	120 hrs	144 hrs	192 hrs	240 hrs
UAF1	3.16								
UAF2	3.37								
UAF3	3.36				3.41	3.40			
UAF4	3.37				3.34	3.34	3.34	3.34	
UBF1	3.43								
UBF2	3.42				3.40				
UBF3	3.46				3.47	3.45	3.45		
UBF4	3.43				3.42	3.42	3.42	3.42	3.38

Table D.38 Widths for Unidirectional G Group at 316°C

	0 hrs	24 hrs	48 hrs	72 hrs	96 hrs	120 hrs	144 hrs	192 hrs	240 hrs
UAG1	76.56								
UAG2	76.39								
UAG3	76.42				76.28	76.27			
UAG4	76.41				76.30	76.24	76.24	76.24	
UBG1	76.56								
UBG2	76.48				76.34				
UBG3	76.49				76.30	76.36	76.33		
UBG4	76.38				76.30	76.26	76.32	76.26	76.14

Table D.39 Widths for Unidirectional H Group at 316°C

	0 hrs	24 hrs	48 hrs	72 hrs	96 hrs	120 hrs	144 hrs	192 hrs	240 hrs
UAH1	25.80								
UAH2	25.74								
UAH3	25.61				25.58	25.58			
UAH4	26.07				26.04	26.00	26.02	26.00	
UBH1	25.45								
UBH2	25.78				25.75				
UBH3	25.74				25.76	25.70	25.70		
UBH4	25.67				25.63	25.64	25.61	25.65	25.69

Table D.40 Widths for Unidirectional F Group at 343°C

	0 hrs	24 hrs	48 hrs	72 hrs	96 hrs	120 hrs	144 hrs	192 hrs	240 hrs
UAF5	3.41	3.42							
UAF6	3.48	3.47	3.44	3.44					
UAF7	3.48	3.51	3.44	3.44	3.42	3.42			
UAF8	3.44	3.44	3.44	3.44	3.42	3.41	3.42	3.41	
UBF5	3.41	3.43	3.37						
UBF6	3.47	3.47	3.41	3.44	3.40				
UBF7	3.51	3.50	3.49	3.53	3.52	3.50	3.49		
UBF8	3.54	3.53	3.51	3.54	3.52	3.51	3.51	3.49	3.50

Table D.41 Widths for Unidirectional G Group at 343°C

	0 hrs	24 hrs	48 hrs	72 hrs	96 hrs	120 hrs	144 hrs	192 hrs	240 hrs
UAG5	76.36	76.20							
UAG6	76.36	76.21	76.13	76.10					
UAG7	76.39	76.25	76.21	76.09	76.10	76.03			
UAG8	76.39	76.24	76.17	76.12	76.08	76.03	76.00	75.92	
UBG5	76.39	76.25	76.13						
UBG6	76.40	76.27	76.15	76.12	76.08				
UBG7	76.39	76.29	76.18	76.11	76.10	76.02	75.97		
UBG8	76.42	76.29	76.23	76.15	76.10	74.08	76.06	75.96	75.90

Table D.42 Widths for Unidirectional H Group at 343°C

	0 hrs	24 hrs	48 hrs	72 hrs	96 hrs	120 hrs	144 hrs	192 hrs	240 hrs
UAH5	25.11	25.09							
UAH6	25.07	25.05	25.00	25.12					
UAH7	25.14	25.10	25.09	25.09	25.06	25.07			
UAH8	25.15	25.14	25.10	25.13	25.13	25.09	25.06	25.05	
UBH5	25.13	25.12	25.11						
UBH6	25.24	25.23	25.21	25.26	25.23				
UBH7	25.14	25.12	25.09	25.10	25.07	25.06	25.04		
UBH8	25.00	24.97	24.95	24.95	24.92	24.92	24.90	24.91	24.87

Table D.43 Thicknesses for Unidirectional F Group at 316°C

	0 hrs	24 hrs	48 hrs	72 hrs	96 hrs	120 hrs	144 hrs	192 hrs	240 hrs
UAF1	2.470	2.429							
UAF2	2.483	2.453	2.449	2.447					
UAF3	2.490	2.453	2.459	2.453	2.451	2.451			
UAF4	2.490	2.466	2.466	2.455	2.459	2.458	2.452	2.451	
UBF1	2.430	2.477	2.474						
UBF2	2.453	2.477	2.483	2.475	2.479				
UBF3	2.460	2.478	2.480	2.470	2.479	2.482	2.473		
UBF4	2.463	2.489	2.482	2.476	2.469	2.470	2.469	2.467	2.472

Table D.44 Thicknesses for Unidirectional G Group at 316°C

	0 hrs	24 hrs	48 hrs	72 hrs	96 hrs	120 hrs	144 hrs	192 hrs	240 hrs
UAG1	2.453	2.446							
UAG2	2.477	2.473	2.469	2.465					
UAG3	2.477	2.477	2.471	2.468	2.473	2.465			
UAG4	2.480	2.488	2.471	2.476	2.473	2.473	2.466	2.463	
UBG1	2.497	2.489	2.493						
UBG2	2.493	2.489	2.493	2.484	2.479				
UBG3	2.473	2.470	2.472	2.465	2.461	2.467	2.457		
UBG4	2.460	2.461	2.462	2.453	2.453	2.467	2.447	2.451	2.443

Table D.45 Thicknesses for Unidirectional H Group at 316°C

	0 hrs	24 hrs	48 hrs	72 hrs	96 hrs	120 hrs	144 hrs	192 hrs	240 hrs
UAH1	2.487	2.481							
UAH2	2.490	2.481	2.484	2.483					
UAH3	2.483	2.474	2.475	2.475	2.470	2.465			
UAH4	2.493	2.482	2.484	2.483	2.483	2.479	2.474	2.474	
UBH1	2.467	2.463	2.455						
UBH2	2.490	2.457	2.454	2.455	2.477				
UBH3	2.440	2.422	2.428	2.429	2.437	2.423	2.419		
UBH4	2.433	2.428	2.431	2.426	2.421	2.427	2.419	2.426	2.421

Table D.46 Thicknesses for Unidirectional F Group at 343°C

	0 hrs	24 hrs	48 hrs	72 hrs	96 hrs	120 hrs	144 hrs	192 hrs	240 hrs
UAF5	2.472	2.466							
UAF6	2.483	2.451	2.473	2.465					
UAF7	2.476	2.472	2.473	2.467	2.462	2.449			
UAF8	2.479	2.475	2.471	2.464	2.457	2.460	2.453		
UBF5	2.481	2.484	2.469						
UBF6	2.485	2.474	2.469	2.461	2.457				
UBF7	2.470	2.451	2.458	2.455	2.442	2.443	2.443		
UBF8	2.478	2.449	2.458	2.451	2.429	2.444	2.433	2.431	2.419

Table D.47 Thicknesses for Unidirectional G Group at 343°C

	0 hrs	24 hrs	48 hrs	72 hrs	96 hrs	120 hrs	144 hrs	192 hrs	240 hrs
UAG5	2.471	2.460							
UAG6	2.464	2.471	2.461	2.461					
UAG7	2.469	2.468	2.461	2.451	2.447	2.454			
UAG8	2.469	2.453	2.455	2.455	2.448	2.449	2.441	2.435	
UBG5	2.449	2.443	2.442						
UBG6	2.428	2.421	2.420	2.423	2.416				
UBG7	2.429	2.412	2.413	2.412	2.406	2.408	2.401		
UBG8	2.428	2.401	2.409	2.409	2.406	2.403	2.394	2.387	2.381

Table D.48 Thicknesses for Unidirectional H Group at 343°C

	0 hrs	24 hrs	48 hrs	72 hrs	96 hrs	120 hrs	144 hrs	192 hrs	240 hrs
UAH5	2.437	2.425							
UAH6	2.434	2.425	2.419	2.415					
UAH7	2.427	2.419	2.420	2.413	2.402	2.405			
UAH8	2.454	2.448	2.443	2.434	2.427	2.427	2.421	2.417	
UBH5	2.412	2.411	2.406						
UBH6	2.423	2.416	2.412	2.403	2.398				
UBH7	2.399	2.395	2.387	2.380	2.379	2.377	2.370		
UBH8	2.399	2.394	2.386	2.382	2.373	2.371	2.362	2.355	2.352

APPENDIX E

SURFACE LAYER PHOTOMICROGRAPHS

This appendix presents the photomicrographs illustrating the growth of the surface layer at 316°C and 343°C. All photomicrographs were taken from the neat resin E sample group. A single photomicrograph of each specimen was taken. All photomicrographs were taken at a magnification of 150x.

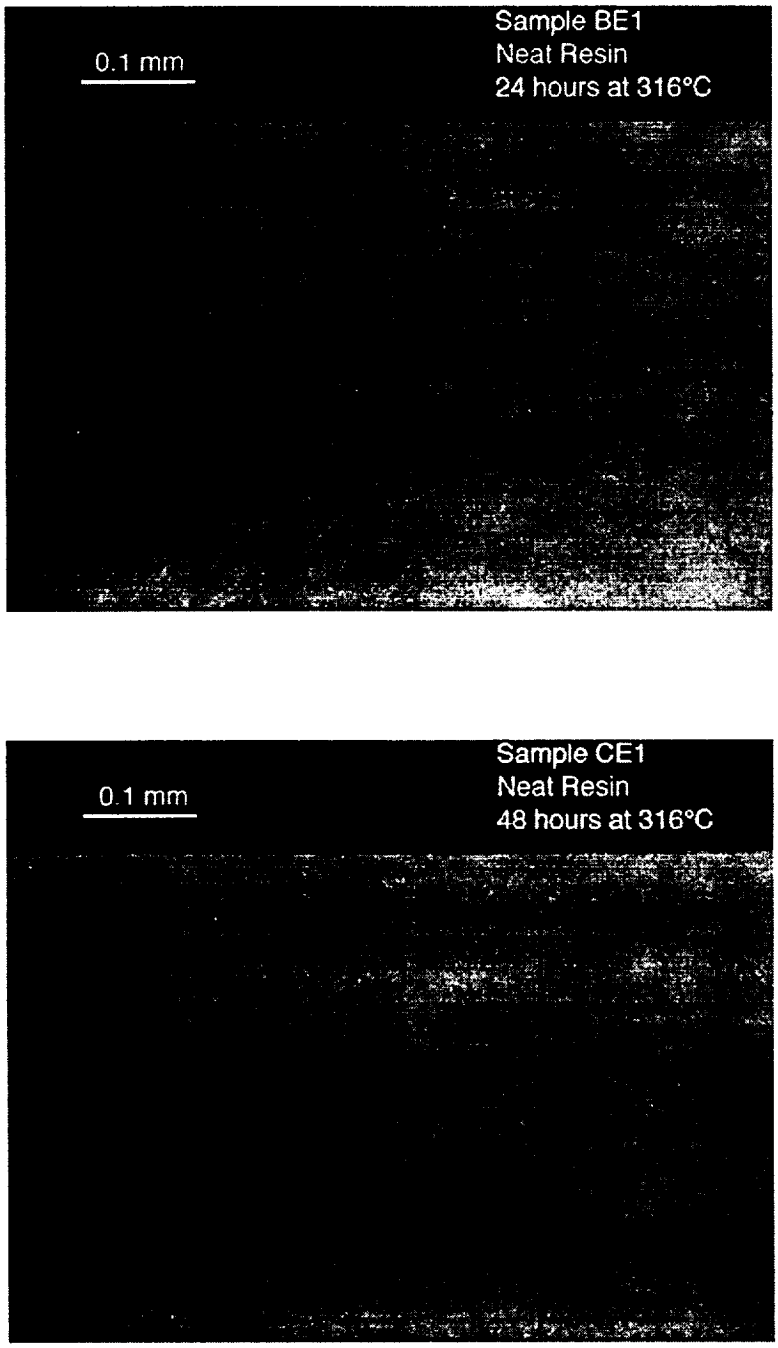

Figure E.1 Photomicrographs of surface layer on neat resin samples exposed to air for 24 hours (*top*) and 48 hours (*bottom*) at 316°C.

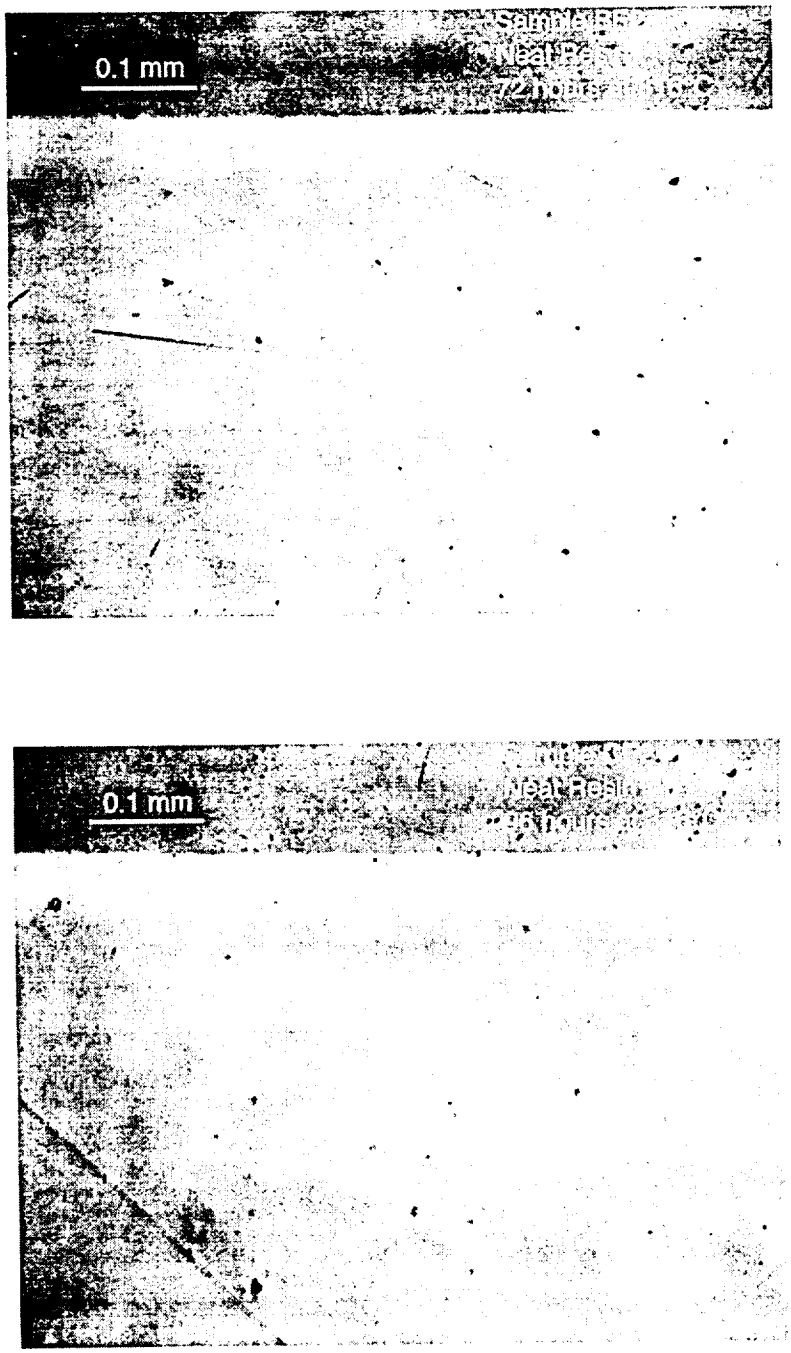

Figure E.2 Photomicrographs of surface layer on neat resin samples exposed to air for 72 hours (*top*) and 96 hours (*bottom*) at 316°C.

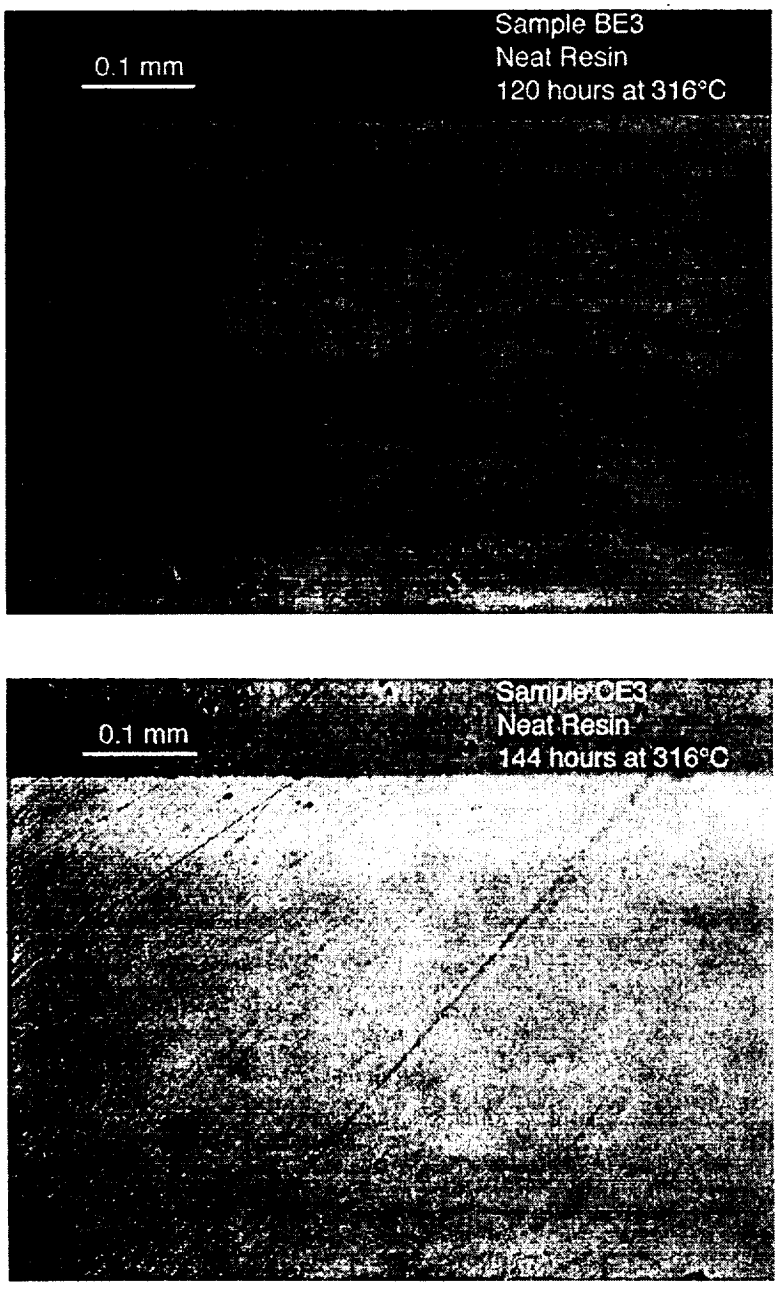

Figure E.3 Photomicrographs of surface layer on neat resin samples exposed to air for 120 hours (*top*) and 144 hours (*bottom*) at 316°C.

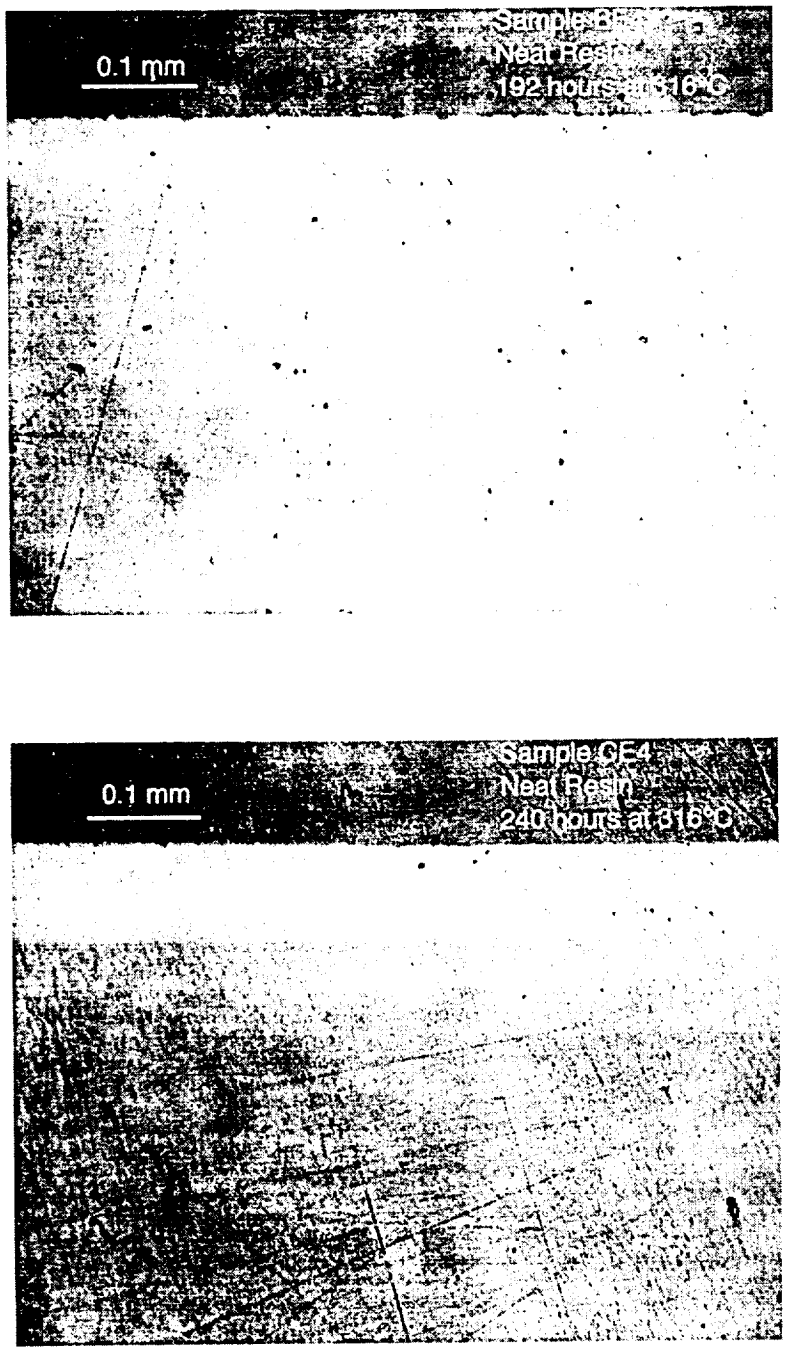

Figure E.4 Photomicrographs of surface layer on neat resin samples exposed to air for 192 hours (*top*) and 240 hours (*bottom*) at 316°C.

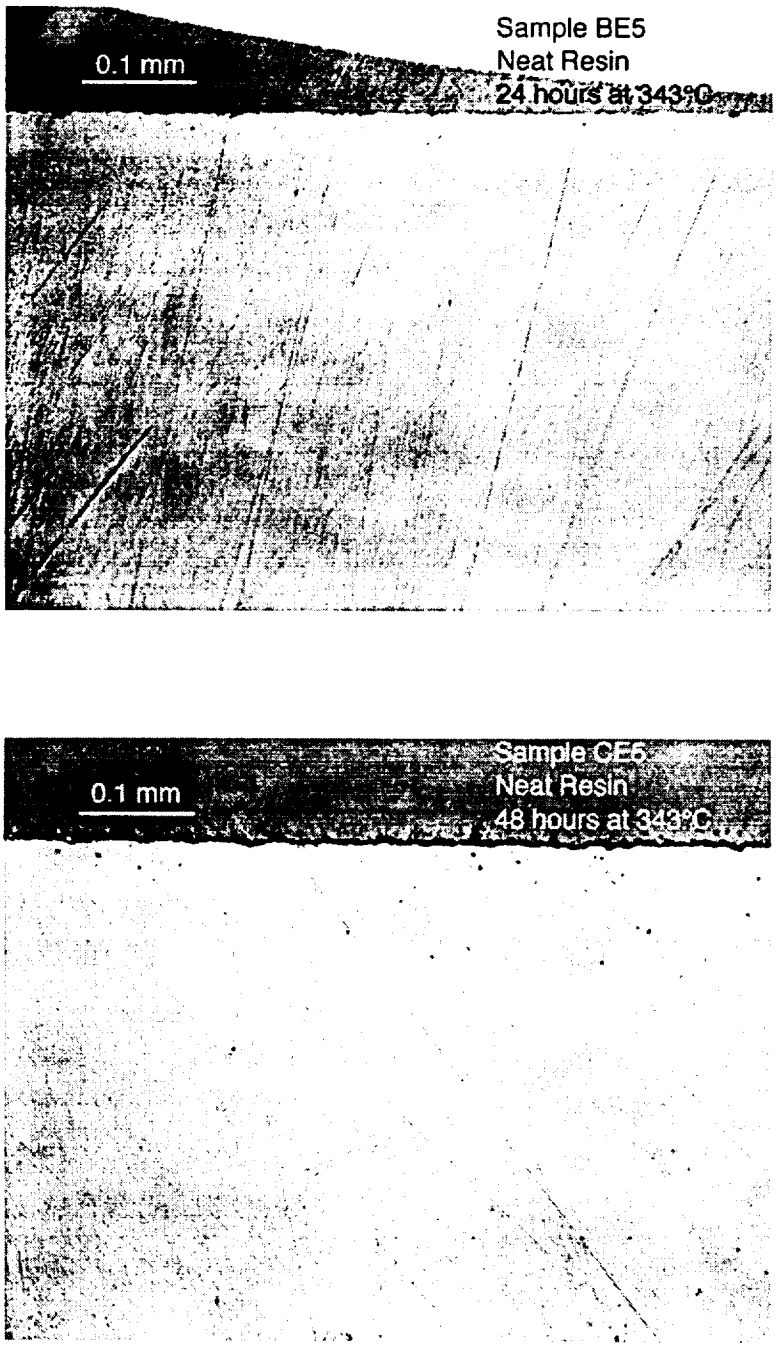

Figure E.5 Photomicrographs of surface layer on neat resin samples exposed to air for 24 hours (*top*) and 48 hours (*bottom*) at 343°C.

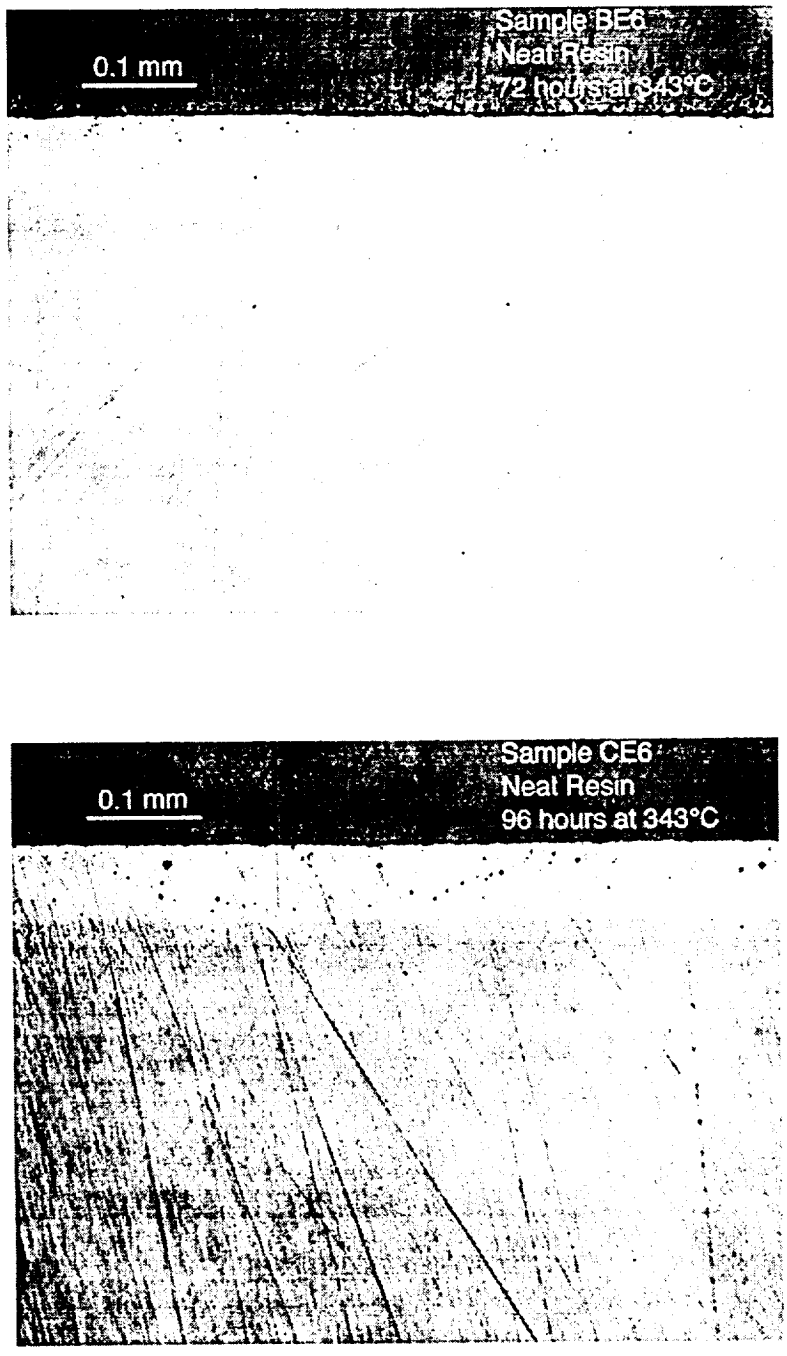

Figure E.6 Photomicrographs of surface layer on neat resin samples exposed to air for 72 hours (*top*) and 96 hours (*bottom*) at 343°C.

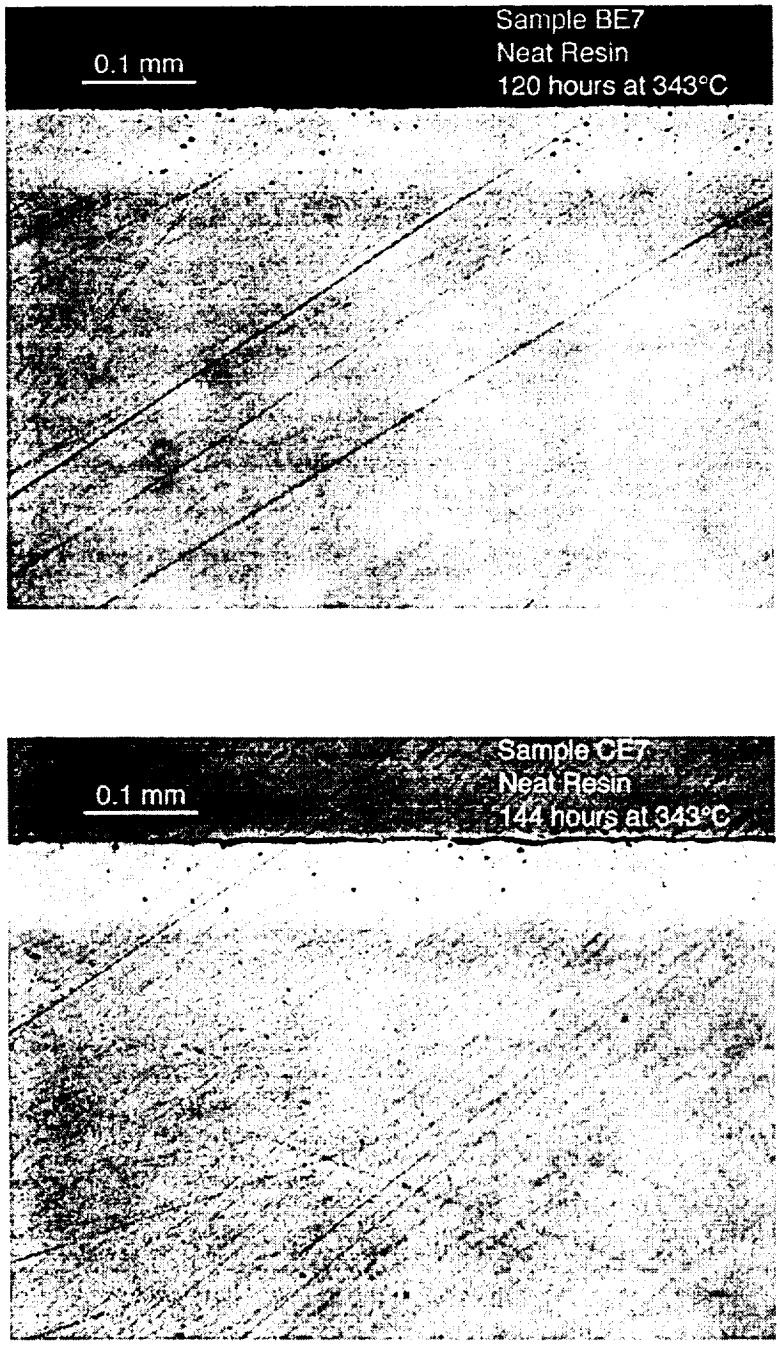

Figure E.7 Photomicrographs of surface layer on neat resin samples exposed to air for 120 hours (*top*) and 144 hours (*bottom*) at 343°C.

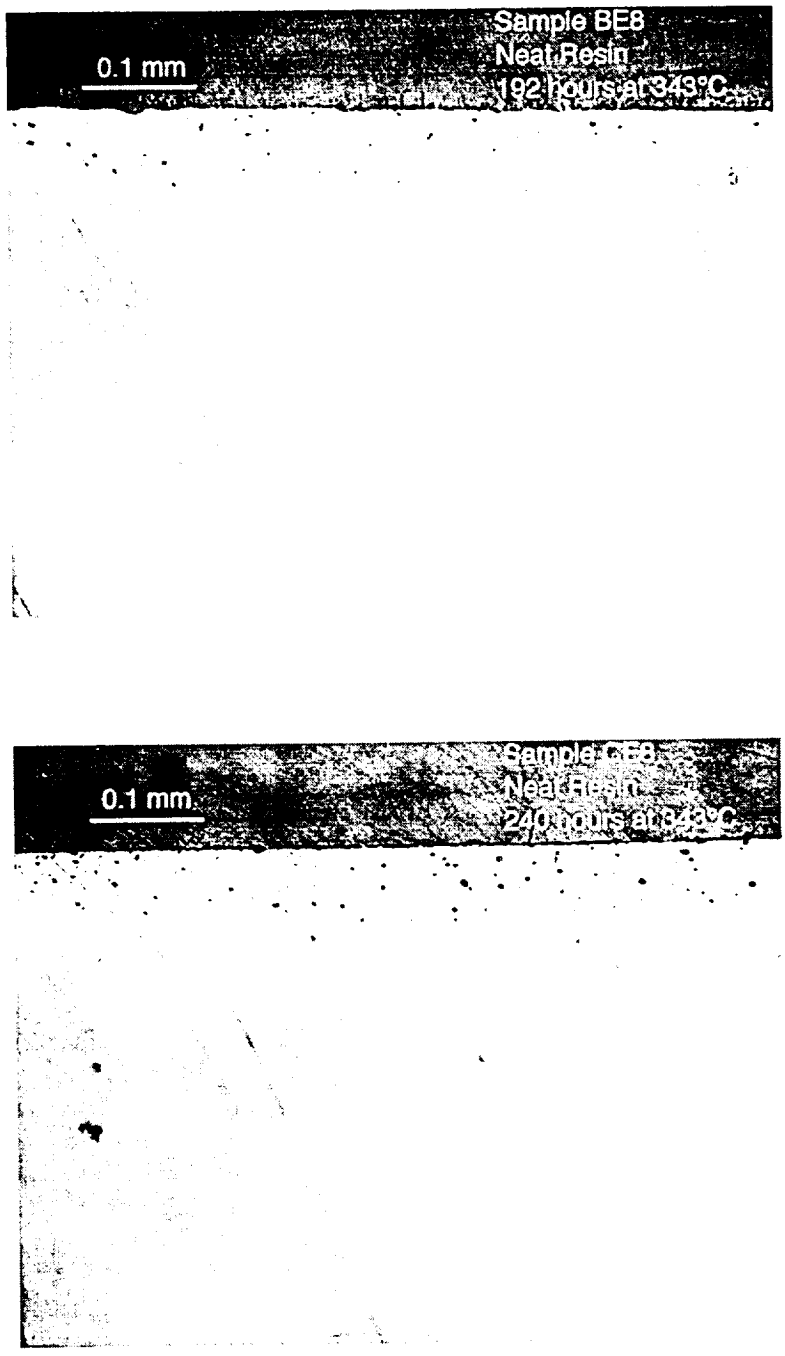

Figure E.8 Photomicrographs of surface layer on neat resin samples exposed to air for 192 hours (*top*) and 240 hours (*bottom*) at 343°C.